UNIVERSIDADE FEDERAL DO RIO DE JANEIRO

INSTITUTO DE FÍSICA

Disordered magnetic systems and fermions in optical lattices: numerical approaches

Tiago Mendes Santos

Tese de Doutorado apresentada ao Programa de Pós-Graduação em Física do Instituto de Física da Universidade Federal do Rio de Janeiro - UFRJ, como parte dos requisitos necessários à obtenção do título de Doutor em Ciências (Física).

Orientador: Raimundo Rocha dos Santos

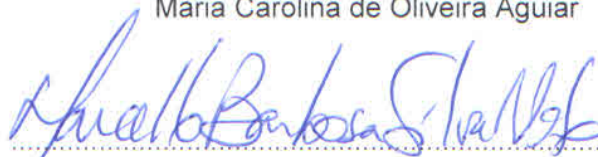**Coorientadora: Thereza Cristina de Lacerda Paiva**

Rio de Janeiro

September of 2017

Disordered magnetic systems and fermions in optical lattices: numerical approaches

Tiago Mendes Santos

Raimundo Rocha dos Santos
Thereza Cristina de Lacerda Paiva

Tese de Doutorado submetida ao Programa de Pós-Graduação em Física, Instituto de Física, da Universidade Federal do Rio de Janeiro – UFRJ, como parte dos requisitos necessários à obtenção do título de Doutor em Ciências (Física).
Aprovada por:

....
Raimundo Rocha dos Santos
(Presidente e Orientador)

....
Thereza Cristina de Lacerda Paiva
(Co-Orientadora)

....
Francisco Castilho Alcaraz

....
Maria Carolina de Oliveira Aguiar

....
Marcello Barbosa Silva Neto

....
André Luiz Saraiva de Oliveira

Rio de Janeiro, RJ – Brasil
Outubro de 2017

CIP - Catalogação na Publicação

Abstract

Disordered magnetic systems and fermions in optical lattices: numerical approaches

Tiago Mendes Santos

Orientador: Raimundo Rocha dos Santos

Coorientadora: Thereza Cristina de Lacerda Paiva

Abstract da Tese de Doutorado apresentada ao Programa de Pós-Graduação em Física do Instituto de Física da Universidade Federal do Rio de Janeiro - UFRJ, como parte dos requisitos necessários à obtenção do título de Doutor em Ciências (Física).

Heavy fermion and cuprate systems often exhibit a competition between antiferromagnetic (AF) and singlet ground states, and in this thesis we will explore its consquences in a number of problems. We first use Quantum Monte Carlo (QMC) simulations to examine the effect of impurities in the vicinity of the AF-singlet quantum critical point (QCP) described by the Heisenberg bilayer model. Our key finding is a connection, within a single calculational framework, between AF domains induced on the singlet side of the transition, and the behavior of the nuclear magnetic resonance (NMR) relaxation rate $1/T_1$. We then examine the strong coupling Heisenberg limit on a one-third depleted square lattice. This is the geometry occupied, after charge ordering, by the spin-$\frac{1}{2}$ Ni^{1+} atoms in a single layer of the nickelate materials $La_4Ni_3O_8$. Here we determine the location of the QCP when there is an onset of long range antiferromagnetic order, and the magnitude of the order parameter and compare with results of spin wave theory.

Another line of problems tackled in this thesis was motivated by experiments with

ultracold atoms in optical lattices. Here we employed the twist-averged boundary condition (TABC) method in the Lanczos diagonalization of relatively small systems. We investigate the harmonic-trap control of size and shape of Mott regions in the Fermi Hubbard model on a square optical lattice. The calculations in the grand canonical ensemble together with a local-density approximation (LDA) allow us to simulate the radial density distribution. We have found that as the trap closes, the atomic cloud goes from a metallic state, to a Mott core, and to a Mott ring; the coverage of Mott atoms reaches a maximum at the core-ring transition. A 'phase diagram' in terms of an effective density and of the on-site repulsion is proposed, as a guide to maximize the Mott coverage. We predict that the usual experimentally accessible quantities, the global compressibility and the average double occupancy (rather, its density derivative) display detectable signatures of the core-ring transition.

Motivated by experiments with dipolar atoms in optical lattice, we also considered the extended Hubbard model (EHM), where on-site (U), and nearest-neighbour (V) interactions are included. Using the TABC in the Lanczos diagonalization we show that the momentum distribution function $n(\mathbf{k})$ provides a signature for the AF-charge-density wave transition. And, finally, we investigate the single-particle spectral properties of the metal-insulator transitions described by the EHM.

Keywords: Antiferromagnetism, Quantum phase transitions, Optical Lattice, Quantum Monte Carlo

Agradecimentos

Em primeiro lugar, tenho muito a agradecer ao Raimundo por toda dedicação e disponibilidade nesses quase 10 anos de orientação. Por ter sempre confiado em mim, por ajudar a me manter instigado para lidar com os altos e baixos da atividade de pesquisa, e por todo conhecimento de física passado.

À Thereza, pela orientação e pelas excelentes ideias trazidas para esse trabalho, sem as quais boa parte dessa tese não teria se consolidado.

Ao Rubem Mondaini, por ter me concedido seu super *Lanczos Code* e ter me ajudado a quebrar *the Great Firewall of China* para usar seu cluster na reta final dessa tese.

À professora Belita Koiller, por ter me ensinado o bê-á-bá da Materia Condensada, e aos professores Sergio Queiroz e André Saraiva.

Aos parceiros de salinha e também colaboradores Natanael Carvalho e Tarik Cysne, por todas nossas discussões sobre física, a vida, o universo e tudo mais.

Aos amigos de IF, Elvis Soares, Álvaro Pimentel, Maurício Hippert, Rodrigo Coelho, Jilder Dandy, Arouca e Adriana. E aos funcionários, Casé, por me lembrar e perdoar meus esquecimentos de prazos e datas, e à Aninha, pelo café de todo dia, sem o qual essa tese não sairia do papel.

Também gostaria de agradecer as pessoas que colaboraram indiretamente para essa tese. Em primeiro lugar, meus familiares. Meu pai Joseilson, por desde sempre me incentivar a adquirir conhecimento, à minha mãe Luzia por sempre me apoiar em tudo, e aos irmãos Bruno e Lilian. Aos meus amigos Arthur Carvalho e Amaro Patrício. A minha querida namorada Luizianne Alves, pelo apoio e carinho na reta final dessa tese.

Acknowledgments

For the great year that I spent at UC Davis, I thank all Scalettar group. In special, I thank Richard for all the knowledge that he shared with me, and for his great enthusiasm to supervise me; and my friends Tyler Cary and Wei-Ting Chiu for useful discussions, and Huaimining Guo for help me with the Spin Wave calculations. I also thank Nick Curro for had presented me interesting problems of the heavy fermion materials.

Por fim gostaria de agradecer as agências de fomento CNPq, Capes e a FAPERJ.

Contents

List of Figures

Chapter 1

Introduction

Heavy-fermions and other strongly correlated systems often exhibit a competition between antiferromagnetic (AFM) and singlet ground states. One line of problems that we examine here is the effects of impurities in such a kind of systems. As an experimental example, we mention the spin-1/2 ladder system $SrCu_2O_3$ doped with Zn. In this system, a small fraction of non-magnetic impurities induces a magnetic response in the otherwise spin gapped system [1] [1]. More recently, a similar effect has been observed in experiments with Cd doped $CeCoIn_5$, in which a small percentage of Cd impurities induces an antiferromagnetic (AFM) state in the otherwise superconducting (nonmagnetic) system. However, as indicated by measurements of the NMR relaxation rate, $1/T_1$, the resulting phase is quite heterogeneous. In addition, the pristine $CeCoIn_5$ is considered a critical system, in the sense that it is in the vicinity of a quantum critical point (QCP) to an AFM state. Thus the plausible scenario is that in the Cd-doped $CeCoIn_5$, AFM emerges locally in the vicinity of the Cd impurities; and as the size of the regions of local AFM order grows and reaches the scale of the distance between impurities, the system can undergo long-range order [2].

Using quantum Monte Carlo (QMC) simulations, we examine the effects of impurities in the vicinity of such AFM-singlet QCP, through an appropriately defined impurity

---

[1]In bibliography, the numbers at the end of each reference indicate the pages in which they are cited.

susceptibility [3]. This is done in Chapter 4, where we consider the effects of impurities in the Heisenberg bilayer model; in this model the interlayer coupling between the layers induces an AFM-singlet QCP. Furthermore, the effects of non-magnetic impurities are described by removing spins in one of the layers of the system. We found that the impurity susceptibility captures both the inhibition of AFM order deep in the ordered phase and its sharp enhancement close to the QCP. We also obtain the spin relaxation rate, $1/T_1$, in both the clean and diluted system.

We also consider the Heisenberg model in a one-third-depleted lattice [4]. This is the geometry occupied, after charge ordering, by the spin-$1/2$ Ni^{1+} atoms in a single layer of the nickelate material $La_3Ni_2O_6$. In Chapter 5, we use QMC simulations to determine the location of the QCP where there is an onset of antiferromagnetic order, and the magnitude of the order parameter, and then compare with results of linear spin wave theory.

In both Chapters 4 and 5 we employ the quantum Monte Carlo (QMC) Stochastic Series Expansion (SSE). The SSE method has become the standard QMC method to study localized spin models in problems that are free from the sign problem; more about this issue will be discussed on Chapter 3. One reason for this success is that it is possible to achieve relatively very large systems with SSE; here we consider Heisenberg-like systems up to $N_s \approx 10^4$ spins. Systems sizes with $N_s \approx 10^4$ spins are particularly important in the study of disordered systems, for which a careful study of finite-size effects has to be performed. In Chapter 3 we review the SSE method for the isotropic Heisenberg model. The SSE code used was developed in the course of this thesis.

Another line of problems tackled in this thesis was motivated by experiments with ultracold atoms in optical lattices (OL). Optical lattice experiments have been used as a platform to emulate the fermionic Hubbard model (HM). In these cases, itinerant spin models are considered.

The fermionic HM can be stated as follows: fermionic particles can hop from site

to site of a lattice with kinetic energy, t, and two particles on the same site have an interaction energy, U, which can be positive or negative to represent repulsive or attractive interactions. Furthermore, particles on different sites do not interact. The repulsive HM on a square lattice is thought to contain the basic mechanism to explain high-T_c superconductivity. In this case, at half-filling, i.e., one particle per site, QMC simulations obtain that the ground state corresponds to a Mott insulator with AFM long-range order [5], [6]. When the temperature is higher than the interaction U, particles move freely around the lattice, despite the energy penalty for doubly occupied sites. At temperatures below U, they then freeze into the Mott insulating state, with each particle stuck to every site. At even lower temperatures, on the order of $4t^2/U$, the particles enter into the AFM state. The mechanism responsible for the magnetic ordering is known as virtual exchange. Further details of the HM are presented in Appendix A.

Doping the half-filled HM with holes or electrons induces a metal-insulator transition known as Mott transition. Numerical works have shown that some spectral properties observed in the cuprates, such as spectral weight redistribution upon doping, Fermi arcs, and hole pockets, can be explained by this model. Nevertheless in the doping regime in which superconductivity is observerd in the cuprates, there is still no conclusive answer about the nature of the ground state described by the HM. One reason for this is that QMC methods fail in this regime, due to the so called sign problem [7]. In view of this one, a motivation of OL is to answer open questions about the doped repulsive HM, such as the presence or not of a superconducting ground state.

In these experiments, an artificial OL is created by the interference pattern of counter-propagating lasers. Fermionic atoms (e.g.,^{6}Li and ^{40}K), prepared in two different hyperfine states, are then loaded in this artificial lattice. The basic physical ingredients of this system are the atomic tunnelling between next nearest-neighbour sites, characterized by the tunneling rate, t, and the contact (on-site) interaction, U, which occurs when two atoms meet at the same site. As an effect, cold-atoms experiments are designed to mimic the

fermionic HM, in a setup that both t and U are tunable parameters. One achievement in this direction was the realization of the Mott insulating state [8], [9], and, more recently, a state with AFM order [10]. Another advancing direction of ultracold systems deals with dipolar atoms (e.g., ^{161}Dy and ^{167}Er) and molecules in OL [11]. These experiments open up the possibilities towards the investigation of Hubbard-like models with additional long-ranged and anisotropic interactions [12].

One important experimental aspect of OL experiments is that in addition to the lattice potential, the atoms are also confined by a trapping potential. From the theoretical side, different techniques have been used to address this issue in the HM [13], [14], [15]. Dynamical mean field theory (DMFT) shows that the presence of a harmonic trap gives rise to inhomogeneous density profiles on a three dimensinal lattice, for instance, a Mott region in the center (Mott core) can coexist with a metallic region in the wings of the trap [15]. In this direction, QMC also shows that even when the average entropy per particle is larger than that required for AFM in the homogeneous system, the trap enables the formation of an AFM Mott phase in the center of the trap [13].

In Chapter 6, we consider a system of fermionic atoms confined in a two-dimendional OL and a harmonic trap [16]. The aim of this work is to characterize the size and form of the Mott region in a square OL as functions of the trap opening and of the on-site interaction. The choice of a square lattice is motivated both by the possibility of singling out some special features brought about by the van Hove singularity, and by the use of an unbiased calculational method (see below). We also connect our results with experimentally acessible global quantities, such as compressibility and average double occupancy.

We also consider extended Hubbard models (EHM's), in which not just the on-site, but next nearest-neighbour interactions are taken into account. The inclusion of a nearest-neighbour interaction, V, can give rise, for instance, to a charge density wave (CDW) ground state. Thus, depending on the relative magnitude of U and V, the ground state

at half-filling can display two insulating phases: (i) a spin density wave (SDW), and (ii) CDW. In Chapter 7, we use the Lanczos method to obtain the single-particle spectral function, $A(\mathbf{k}, \omega)$, of the one-dimensional EHM; this quantity is probed in angle resolved photoemission spectroscopy (ARPES). At half-filling, we investigate the spin-charge separation in both the SDW and CDW phases. In addition, we study the two metal-insulator transitions induced upon doping from half-filling: (i) the Mott transition, and (ii) the CDW-Metal transition. By calculating the density of states (DOS), we make quantitative predictions about the spectral weight transfer to the Fermi level upon doping in both transitions.

Two-dimensional extended Hubbard models are then considered in Chapter 8. In this case, the inclusion of nearest-neighbour interaction can give rise to a checkerboard CDW phase at half-filling. We also consider a case of current interest in the context of OL's, namely that of a ultracold dipolar atoms. The dipolar EHM incorporates both the long-range and anisotropic characters of the dipole-dipole interactions. In order to explore the ground state phase diagram of the dEHM, we use the Lanczos method to obtain the spin and charge correlation functions. Furthemore, we examine the momentum occupation function, $n_\sigma(\mathbf{k})$, across the phase transitions described by the dEHM. We show that the anisotropic character of the dipolar interaction can give rise to different kinds of CDW phases. Furthemore, by changing the dipole direction different AFM-CDW transitions can be induced.

The Lanczos diagonalization (LD) method is employed in the calculations of the ground state and spectral properties discussed in Chapters 6, 7 and 8. In addition to the LD method we consider the method of twist-averaged boundary conditions (TABC). Chapter 2 is devoted to discuss the TABC + LD method; also some comparison results of the LD + TABC results with calculations for larger systems using other methods is shown. The code used to obtain these results was developed in the course of this thesis.

Note to the reader.

I write this thesis in such a way that each Chapter with results could be read independently of the other. For the published works, we summarize the results in the body of the Chapter, and present the paper in the Appendix. Appendices D, E and F present the results of Chapter 4, 5, 6; respectively. Chapters 7 an 8 may be regarded as first drafts of future submissions.

Chapter 2

Twist-averaged boundary conditions in Lanczos diagonalization

The Lanczos diagonalization (LD) method is a standard technique for studying interacting localized and itinerant spin models [17], [18], [19]. This method can be used to obtain various ground state expectation values and dynamical spectral functions [20],[21]. In this thesis, the LD technique was used to obtain the ground state and the spectral density function, $A(\mathbf{k}, \omega)$, for both 1D chains and the 2D clusters of Fig. (2.1). This chapter is devoted to discussing the LD method. Further, we discuss the method of twist-averaged boundary conditions (TABC), used to minimize some finite-size effects (FSE) that would otherwise appear in the LD for the relatively small clusters of Fig. 2.1; and finally we show some tests of the LD + TABC method applied to the 1D and 2D Hubbard Model (HM).
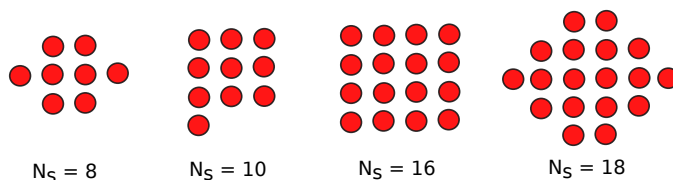
Figure 2.1: Two dimensional clusters considered in the thesis.

2.1 Ground state and spectral dynamical quantities

In the full Exact Diagonalization (ED) of the HM Hamiltonian, the eingenvalues and eingenvectors are obtained. To this end, a natural choice of basis is the occupation number representation, in which the fermion state on each site can be one of the following: $|0\rangle$, $|\uparrow\rangle$, $|\downarrow\rangle$, or $|\uparrow\downarrow\rangle$. Numerically, these site states can be represented by 2 bits, and the action of the terms in the Hamiltonian can be suitably implemented by bit manipulations [17]. Thus, one is able to construct the full Hamiltonian matrix, and, a numerical routine can be used to obtain the eigenvalues and eigenvectors. This strategy is hindered by the exponential growth of the Hilbert space. For the HM the dimension of the Hilbert space is $N_H = 4^{N_s}$, where N_s is the number of sites; using this strategy no more than $N_s = 8$ sites can be considered.

However, the effective size of the Hilbert space can be significantly reduced by the use of symmetries. In the canonical ensemble (CE) formulation, two symmetries that can be easily implemented are the conservation of particle number, N_e, and the conservation of the z component of the total spin S_z. Using these symmetries, we produce Hamiltonian blocks of size

$$N_B = \frac{N_s!}{N_\sigma!(N_s - N_\sigma)!},\tag{2.1}$$

where N_σ is the number of particles with spin σ. Another symmetry used here is the translation symmetry (TS), which typically reduces the size N_B by a factor of N_s [17]. Using these symmetries, we study systems up to $N_s = 18$ sites at half-filling with the LD method in the CE. In the grand canonical ensemble, we consider systems up to $N_s = 10$ sites.

The basic strategy of the LD method is to construct a subspace of the full Hamiltonian from which the lowest energy states can be obtained. As will be shown below, in this basis the Hamiltonian has a tridiagonal representation. The procedure is based on the fact that acting the Hamiltonian many times on an arbitrary state vector $|\Psi\rangle$ will project

out the eigenvector with the lowest energy (ground state), that is,

$$\mathcal{H}^n|\Psi\rangle = \sum_i c_i E_i^n |\psi_i\rangle = c_0 E_0^n |\psi_0\rangle \left(1 + \sum_{i \neq 0} \left(\frac{c_i}{c_0}\right)\left(\frac{E_i}{E_0}\right)^n |\psi_i\rangle\right), \qquad (2.2)$$

where $|\psi_i\rangle$ and E_i are the respective eigenvectors and eigenvalues of $\mathcal{H}$, i.e., $\mathcal{H}|\psi_i\rangle = E_i|\psi_i\rangle$. Assuming $|E_0| > |E_i|$ for any $i \neq 0$, and $n \to \infty$, we have $\mathcal{H}^n|\Psi\rangle \approx c_0 E_0^n |\psi_0\rangle$ [22].

The subspace of the Hilbert space spanned by the set of states $\mathcal{H}^m|\Psi\rangle$, with $m = 0, 1, 2, ..., n$, is known as the Krylov space. In the Lanczos procedure an orthogonal basis, $|f_i\rangle$, $i = 0, 1, ..., N_{steps}$, is obtained using linear combinations of the Krylov states. In such a basis the Hamiltonian has a tridiagonal form. Here we will give a brief description of the basic steps to obtain the ground state and some low energy excited states of a Hubbard-like Hamiltonian. A more complete discussion of the method can be found in Refs. [17], [18], [19], [22].

The Lanczos procedure starts with an arbitrary state vector $|f_0\rangle$ which has some overlap with the ground state, i.e, $\langle\phi_0|f_0\rangle \neq 0$. Once $|f_0\rangle$ is selected, we define a new vector by applying the Hamiltonian $\mathcal{H}$ to $|f_0\rangle$, and then subtracting the projection over $|f_0\rangle$

$$|f_1\rangle = \mathcal{H}|f_0\rangle - \frac{\langle f_0|H|f_0\rangle}{\langle f_0|f_0\rangle}|f_0\rangle,$$

which satisfies $\langle f_1|f_0\rangle = 0$. The next vector, $|f_2\rangle$, is constructed in such way that it is orthogonal to the previous two:

$$|f_2\rangle = \mathcal{H}|f_1\rangle - \frac{\langle f_1|\mathcal{H}|f_1\rangle}{\langle f_1|f_1\rangle}|f_1\rangle - \frac{\langle f_0|\mathcal{H}|f_1\rangle}{\langle f_0|f_0\rangle}|f_0\rangle. \qquad (2.3)$$

It can be easily checked that $\langle f_2|f_0\rangle = 0$ and $\langle f_2|f_1\rangle = 0$. This procedure is then iterated to generate an orthogonal basis as:

$$|f_{i+1}\rangle = \mathcal{H}|f_i\rangle - a_i|f_i\rangle - b_i^2|f_{i-1}\rangle, \qquad (2.4)$$

where, $i = 0, 1, 2, ...,$ and the coefficients are given by

$$a_i = \frac{\langle f_i|H|f_i\rangle}{\langle f_i|f_i\rangle}, \qquad b_i^2 = \frac{\langle f_i|f_i\rangle}{\langle f_{i-1}|f_{i-1}\rangle}, \tag{2.5}$$

with $b_0 = 0$, $|f_{-1}\rangle = 0$. On this basis, the Hamiltonian $\mathcal{H}$ has a tridiagonal form.

We use a modified Lanczos method to calculate the ground state $|\psi_0\rangle$ [19], in which a 2×2 matrix in the Lanczos basis ($|f_0\rangle$ and $|f_1\rangle$) is constructed and diagonalized at each Lanczos iteration. The eigenvector of the 2×2 matrix with lowest energy is used as the initial state, $|f_0\rangle$, in the next Lanczos iteration. The ground state can be exactly obtained for a sufficiently large number of iterations, i.e., $N_{steps} \to N_H$. In practice, for the Hubbard-like Hamiltonians considered here, the ground state can be accurately obtained for N_{steps} of the order of a few tens to hundreds. The choice of N_{steps} is based on the convergence of the energy of the lowest eigenstate of $\mathcal{H}$. For each Lanczos step, the lowest energy is calculated and compared with the energy of the previous one, i.e, $\delta = \frac{|\epsilon_0(i) - \epsilon_0(i-1)|}{\epsilon_0(i)}$, where $\epsilon_0(i)$ is the lowest energy at Lanczos step i. Here we interrupt the Lanczos procedure whenever $\delta < 10^{-10}$.

The Lanczos method also allows for the calculation of dynamical properties of the system [18], [21]. The spectral function is defined as

$$\mathcal{O}(\omega) = \sum_{i=1}^{N_H} |\langle \psi_i|O|\psi_0\rangle|^2 \delta[\omega - (E_0 - E_i)], \tag{2.6}$$

where O represents some pertubation on the ground state, and $|\psi_i\rangle$ are the eigenvectors of $\mathcal{H}$ with eigenvalues E_n. For example, for $O = c_{\mathbf{k}}$, $\mathcal{O}(\omega)$ is the spectral density function $A(\mathbf{k}, \omega)$. This quantity can be directly measured in angle-resolved photonemission (ARPES) experiments. Here we set $\hbar = 1$.

In order to evaluate Eq. (2.6) numerically we use the Lanczos method to write $\mathcal{H}$ in a tridiagonal form. Instead of starting the Lanczos process with a random vector, we choose the following initial state

$$|f_0\rangle = \frac{O|\psi_0\rangle}{\langle \psi_0|O^\dagger O|\psi_0\rangle}.$$

The Lanczos procedure described above is then used to obtain the eigenstates of $\mathcal{H}$. In terms of the Lanczos basis, $\{|f_i\rangle\}$, the eigenstates of $\mathcal{H}$ are written as

$$|\psi_n\rangle = \sum_m c_m^n |f_m\rangle, \tag{2.7}$$

where the column vector containing the entries $\{c_m^n\}$, with $m = 0, 1, 2, ..., N_{steps}$, is the eigenvector associated whith the eigenvalue E_n, and N_{steps} is the number of iterations considered in the construction of the Lanczos basis. Substituting Eq. (2.7) in Eq. (2.6), we obtain

$$\mathcal{O}(\omega) = \frac{1}{\pi} \sum_n |c_0^n|^2 |\langle\psi_0|O^\dagger O|\psi_0\rangle|^2 \frac{\Delta}{\Delta^2 + (\omega - (E_n - E_0))^2}, \tag{2.8}$$

where the set of numbers $\{c_0^n\}$ represent the first component of each eigenvector obtained when the tridiagonal Hamiltonian matrix is diagonalized [18]. Note that the δ-functions have been replaced by a Lorentzian,

$$\delta(x) = \lim_{\Delta \to \infty} \frac{1}{\pi} \frac{\Delta}{\Delta^2 + x^2}.$$

In practice a finite value is assigned to Δ. Here we defined $\Delta = 2t/N_s$ [23], where t is the hopping matrix element of the HM. To test the convergence of the procedure, we compare the spectral function with a particular Δ, and test by inspection how the results evolve with the number of iterations, N_{steps}; here we consider $N_{steps} = 100$.

2.2 Twist-averaged boundary conditions

One is usually interested in determining the physical properties in the thermodynamic limit, $N_s \to \infty$. However, the use of small clusters may lead to deceptive finite-size effects (FSE). It is therefore important to mitigate these FSE. Here we list three FSE that arise when dealing with an N_s sites cluster with periodic boundary condition (PBC). (i) Only commensurate densities can be accessed, i.e., $n = N_e/N_s$; e.g., for the $N_s = 8$ cluster, $n = 0, 0.125, 0.25, ..., 2$. (ii) Only a relatively small number of **k**-points can be accessed

in the first Brillouin zone (1 BZ). (iii) The degeneracies that appear in the single-particle spectrum of the non-interacting (NI) system ($U = 0$). For example, a NI system with $N_s = 4$ at half-filling, $N_e = 4$, has a degenerate ground-state. In this case, the single-particle states at the Fermi energy are not fully occupied; see the red squares in Fig. 2.2 (a). As a consequence of this open shell effect, the ground state of an interacting system ($U \neq 0$) can have a spurious non-zero value for the total spin S [24]. A possible way to circumvent this is to consider an antiperiodic boundary condition (APBC). It is important to stress that all aforementioned FSE already appear in the NI system. In order to minimize the FSE, here we adopt the method of twist-averaged boundary conditions (TABC) [25], [26], [27], [28]. As shown below, the grand canonical ensemble (GCE) formulation of the TABC method provides the exact ($N_s \to \infty$) single-particle properties of a NI system. And, most importantly, it improves the FSE related to points (i), (ii), and (iii) for the interacting system.
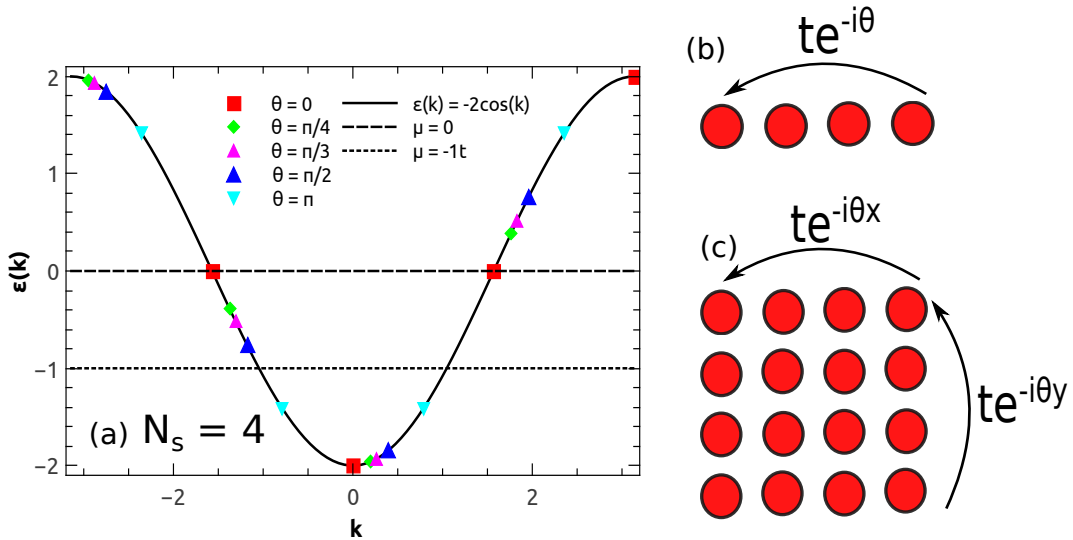
Figure 2.2: (a) The dispersion relation for the 1D HM, $\epsilon = -2t\cos(k)$, is shown as a continuous line, while the points show the results for different TBC for a system with $N_s = 4$. The horizontal lines highlight the chemical potentials $\mu = 0$ and $\mu = -1t$; see text. TBC are introduced through phases θ [for the chain, panel (b)], and θ_x and θ_y [for the square lattice, panel (c)] in the hopping term, see text.

The typical interacting system we consider is the Hubbard model, whose Hamiltonian

can be written as

$$\mathcal{H} = -\sum_{\langle \mathbf{i}, \mathbf{j} \rangle, \sigma} \left(t_{i,j} c^{\dagger}_{\mathbf{i}\sigma} c_{\mathbf{j}\sigma} + t^{*}_{i,j} c^{\dagger}_{\mathbf{j}\sigma} c_{\mathbf{i}\sigma} \right) + U \sum_{\mathbf{i}} \left(n_{\mathbf{i}\uparrow} - \frac{1}{2} \right) \left(n_{\mathbf{i}\downarrow} - \frac{1}{2} \right) - \mu \sum_{\mathbf{i}} (n_{\mathbf{i}\uparrow} + n_{\mathbf{i}\downarrow}).$$

Whenever a fermion hops between two adjacent copies of the cluster, the hopping term picks up a phase, $t_{i,j} = te^{\theta_\alpha}$, where $\alpha = x$ or y are the BC direction; otherwise, $t_{i,j} = t$. Periodic boundary conditions correspond to $\theta_\alpha = 0$, while antiperiodic corresponds to $\theta_\alpha = \pi$, and the general conditions with $\theta_\alpha \neq 0$ and π, correspond to the twisted boundary condition (TBC); see Fig. 2.2 (b) and (c).

An equivalent way to implement a general TBC is to consider that the phase θ_α is uniformly distributed across the system, i.e., $t_{i,j} = te^{\theta_\alpha / L_\alpha}$ [26]. In this way, it is easy to show that a general TBC does not destroy the translational symmetry of the Hamiltonian. However, the inversion symmetry is broken when a general TBC is considered [27], [28].

For a one dimensional system, the quantization of the momentum $\mathbf{k}$-points can be obtained assuming the boundary condition

$$c^{\dagger}_{N_s+1,\sigma} = e^{-i\theta} c^{\dagger}_{1,\sigma}, \qquad c_{N_s+1,\sigma} = e^{i\theta} c_{1,\sigma}. \tag{2.9}$$

Using the momentum representation for the creation and annihilation operators

$$c_{j,\sigma} = \frac{1}{\sqrt{N_s}} \sum_{k} e^{ikj} c_{k,\sigma}, \qquad c^{\dagger}_{j,\sigma} = \frac{1}{\sqrt{N_s}} \sum_{k} e^{-ikj} c^{\dagger}_{k,\sigma},$$

in the relations (2.9), we obtain the k points in terms of the TBC phase, θ,

$$k = \frac{2\pi n + \theta}{L}, \tag{2.10}$$

where $n = 0, 1, 2..., N_s - 1$. For the square ($N_s = 16$) cluster of Fig. 2.1, each dimension has an independent momentum quatization, and

$$k_\alpha = \frac{2\pi n_\alpha + \theta_\alpha}{L}.$$

The definition of the $\mathbf{k}$-points in terms of the TBC phases for the two-dimensional clusters with $N_s = 8$ and $N_s = 10$ is worked out in the Appendix B. We assume that each

component of the TBC is restricted to be within the range:

$$0 \leq \theta_\alpha \leq 2\pi. \tag{2.11}$$

With this choice of range, each momentum state $\mathbf{k}$ occurs precisely once in the 1 BZ, and the exact Fermi surface of a NI system can be recovered [27].

By considering different sets of TBC $\vec{\theta} = (\theta^x, \theta^y)$, it is possible to access different $\mathbf{k}$-points in the 1 BZ, mimicking the dense 1 BZ in the thermodynamic limit $(N_s \to \infty)$. Thus, the quantities of interest can be obtained as averages over different realizations of TBC $\vec{\theta^i} = (\theta^i_x, \theta^i_y)$. The expectation value of an observable $\hat{A}$ within the TABC method is therefore given by

$$\langle A \rangle = \frac{1}{N_r^d} \sum_i \left\langle A(\vec{\theta^i}) \right\rangle, \tag{2.12}$$

where N_r^d is the number of TBC considered in the average, and d is the lattice dimension, $d = 1$ or 2. The set of TBC $\{\vec{\theta^i}\}$ is chosen to be within the range of Eq. (2.11).

First we discuss the application of the TABC to a NI system. Figure 2.2 shows the exact dispersion relation, $\epsilon(k) = -2t\cos(k)$. The calculated single-particle energies of a system with $N_s = 4$ and different TBC θ are presented in different colours. One important aspect of the GCE formulation of the TABC is that it is possible to obtain densities which are not commensurate with the system size, i.e., $n = N_e/N_s$ For example, for $\mu = -1t$, the TABC gives for the particle density

$$n = \frac{1}{N_s} \sum_i \left\langle c^\dagger_{i\uparrow} c_{i\uparrow} + c^\dagger_{i\downarrow} c_{i\downarrow} \right\rangle,$$

the nominal value $n = 12/5$; sectors with $N_e = 2$ and $N_e = 4$ are accessed. In the GCE formulation, the TABC generates a fluctuation in the number of particles, N_e. Thus the particle density n can be tuned, by choosing an appropriate μ. As shown below, this is also true for an interacting system. Following Ref. [27], we call this procedure the twist-averaged grand canonical ensemble (TA-GCE). Furthermore, the inclusion of different TBC eliminates the open shell effects when filling up single-particle states. For

the $N_s = 4$ chain of Fig. 2.2 (a), the choice of a TBC with $\theta \neq 0$ eliminates the open shell effects at half-filling, since states with k and $-k$ are no longer degenerate.

The TA-GCE technique gives the exact results ($N_s \rightarrow \infty$) for single-particle properties of a NI system. This is related to the fact that the eigenstates of a NI system are product of Bloch states $|\mathbf{k}, \sigma\rangle$, i.e., $|\psi\rangle = \prod_i |\mathbf{k_i}, \sigma_i\rangle$. As a consequence, the probability of occupation of a state with momentum $\mathbf{k}$ is given by the Fermi distribution $n(\mathbf{k}) = \left[e^{\beta(\epsilon(\mathbf{k}) - \mu)} + 1 \right]^{-1}$, and the particle density by

$$n(\mu) = \sum_{\mathbf{k}} \frac{1}{\exp\left[\beta(\epsilon(\mathbf{k}) - \mu)\right] + 1}, \tag{2.13}$$

where for a given TBC θ^i, a finite set of $\epsilon(\mathbf{k})$ is considered in the sum. If we consider the TABC, Eq. (2.12), for $N_r \rightarrow \infty$ the set of single particle energies, $\epsilon(\mathbf{k})$, expected in the thermodynamic limit, is recovered, and the expected thermodynamic density, $n(\mu)$ is obtained.

The same argument can be applied to other single-particle quantities. Furthermore, at zero temperature the momentum occupation, $n_\sigma(\mathbf{k}) = \left\langle c^\dagger_{\mathbf{k}\sigma} c_{\mathbf{k}\sigma} \right\rangle$, within the Fermi surface (FS) defined by μ, can be exactly obtained; thus the FS for a NI system can be exactly recovered with the TA-GCE. Based on this argument, only single-particle properties are guaranteed to be exact; other properties, such as correlation functions, may still display FSE, though much less serious than with PBC or APBC.

In the canonical ensemble (CE) formulation of the TABC a fixed particle number is considered, and the TABC generates fluctuations in the chemical potential, μ. In this case, the exact FS cannot be obtained even for a NI system in some cases. For the 2D square lattice considered here just at half-filling ($n = 1$), it is possible to recover the exact FS with the CE TABC. This feature of the TABC method will be used here in the study of the two dimensional extended Hubbard model at half-filling. For other fillings, one must use the GCE formulation in order to obtain the exact ($N_s \rightarrow \infty$) momentum occupation $n(\mathbf{k})$ for a NI system. A discussion about this issue can be found in Ref.[25].

The arguments used in the previous paragraphs do not apply to an interacting system. In this case, the eigenstates of the Hamiltonian cannot be expressed as a product of single-particle Bloch states, so that related quantities can no longer be written as in Eq. (2.13). However, it can be shown that the TABC substantially reduces the FSE occurring in the LD of small clusters: this is done by comparing the LD + TABC results with calculations for larger systems using other methods. The next section is devoted to show some benchmarking resuts for the interacting system.

2.3   Tests of the LD + TABC method

The TABC + LD method was previously used to obtain some properties of the HM [energy, specific heat, momentum occupation $n_\sigma(\mathbf{k})$, and particle density $n(\mu)$] in Refs. [25], [26], [29], [30]. As in this thesis we extend the application of this method to the calculation of other quantities, it is instructive to present some benchmarking for the TABC + LD method results. Results from Determinantal Quantum Monte Carlo (DQMC) for the two-dimensional HM, and the Density Matrix Renormalization Group (DMRG) for the 1D HM [23] will be used for comparison. In this section we present results for the particle density $n(\mu)$ for the 2D HM, the momentum occupation function $n_\sigma(\mathbf{k})$, the spectral density function $A(\mathbf{k}, \omega)$ and the density of states, $N(\omega)$. These results will be explored in Chapters 6, 7 and 8.

Local density as function of μ**:** $n(\mu)$

The qualitative shape of the function $n(\mu)$ can be drawn with the aid of the features of the 2D HM. For $U > 0$ the half-filled HM is a Mott insulator. In this case, the system has a finite charge gap, $\Delta_c \neq 0$, and is incompressible, i.e., $dn(\mu)/d\mu = 0$. As a consequence, the curve $n(\mu)$ displays a Mott plateau around $\mu = 0$. For $\mu > \Delta_c$, i.e. $n(\mu) > 1$, the system is metallic and compressible, i.e., $dn(\mu)/d\mu > 0$.

Figure 2.3 (a) shows $n(\mu)$, for $U = 3t$ and $\mu > 0$; particle-hole symmetry can be
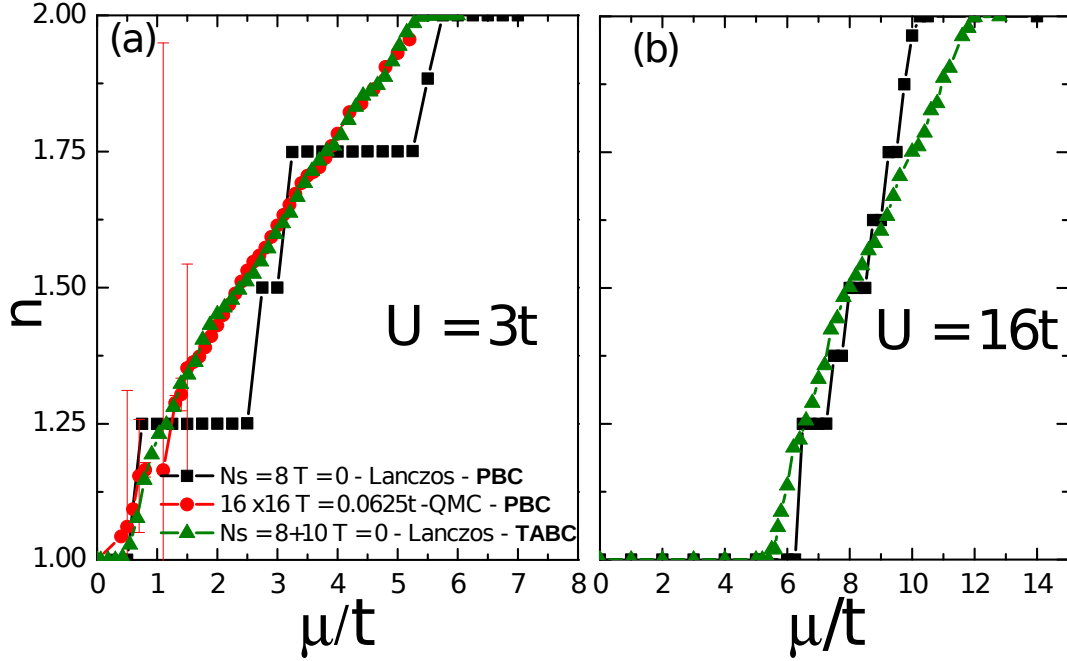
Figure 2.3: Density as a function of the chemical potential μ for the 2D Hubbard model. (a) $U = 3t$. Each curve corresponds to a different method. The curve with black squares corresponds to the $N_s = 8$ cluster with PBC. The red circles to DQMC results for a cluster with $N_s = 16 \times 16$ and PBC; the temperature used in the DQMC simulation is low enough to obtain the ground state properties[7]. The green triangles correspond to an average over results of the $N_s = 8$ and $N_s = 10$ cluster using the TABC method. For each cluster, $N_r = 50 - 100$ realizations of TBC were used. (b) $U = 16t$.

used to obtain the relation, $n(\mu) + n(-\mu) = 2$; see Appendix A. The μ dependence of n for the $N_s = 8$ cluster with PBC (black squares) shows some spurious plateaux at the commensurate densities, $n = N_e/N_s$. Determinantal QMC results for a larger system (16×16) are also shown in Fig. 2.3 (a), the large error bars around $\mu = 0$ being a consequence of the so called sign-problem [7]. A comparison with DQMC results indicates that the plateaux for $\mu \neq 0$ are in fact FSE. With the TABC method (green triangles), $n(\mu)$ is free from the spurious plateaux. Furthermore, one observes a good agreement in the region of μ in which the DQMC results are not affected by the sign problem, and the Mott plateau can be clearly seen. Figure 2.3 (b) shows the same graph for a larger value $U = 16t$. The FSE are less drastic at stronger couplings: the plateaux are narrower for larger U, and as it happens for the $U = 3t$ case, the spurious plateaux are removed

when TABC is considered, and incommensurate densities can be obtained. The DQMC calculation of $n(\mu)$ for larger values of U is hindered by a worsening of the sign-problem. In this sense, the Lanczos + TABC can be seen as a complementary method in this region of parameters. Other local quantities as functions of μ can be obtained using the Lanczos + TABC method; in Chapter 6 we will show results for the double occupancy $D(\mu)$, the local moment $m^2(\mu)$, and the nearest-neighbour spin-spin correlation functions $\langle S_i S_j(\mu) \rangle$.

Momentum occupation function: $n_\sigma(\mathbf{k})$
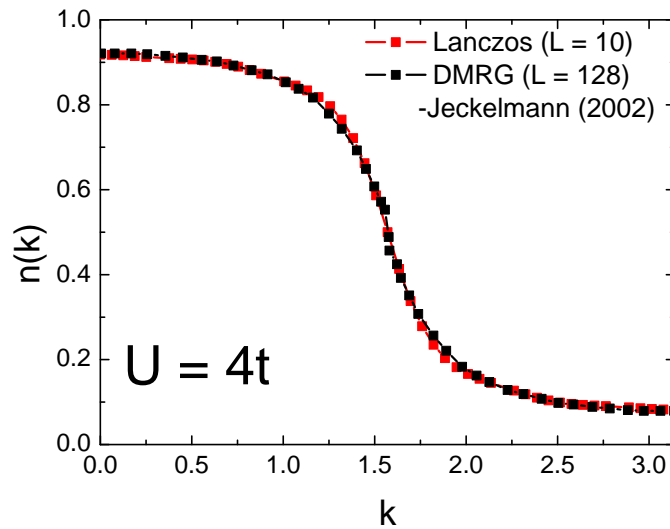
Figure 2.4: Momentum occupation, $n_\sigma(k)$, for the 1D Hubbard model at half-filling, $U = 4t$, $N_s = 10$ and $N_r = 50$ (red points). The black points are DMRG data for $N_s = 128$ and open boundary condition, extracted from Ref. [23]

Let us also discuss some results for the momentum occupation function, $n_\sigma(\mathbf{k})$. This quantity is of particular interest for optical lattice experiments. In Chapter 7, we will show results for $n_\sigma(\mathbf{k})$ for the extended HM at half-filling, and, as it will be shown, $n_\sigma(\mathbf{k})$ can be used to signal some of the quantum phase transitions occurring in this model.

In Fig. 2.4 we show $n_\sigma(\mathbf{k})$ for a one-dimensional HM with $N_s = 10$ for an ensemble of $N_r = 50$ realizations of TBC. We also show, for comparison, results from the DMRG
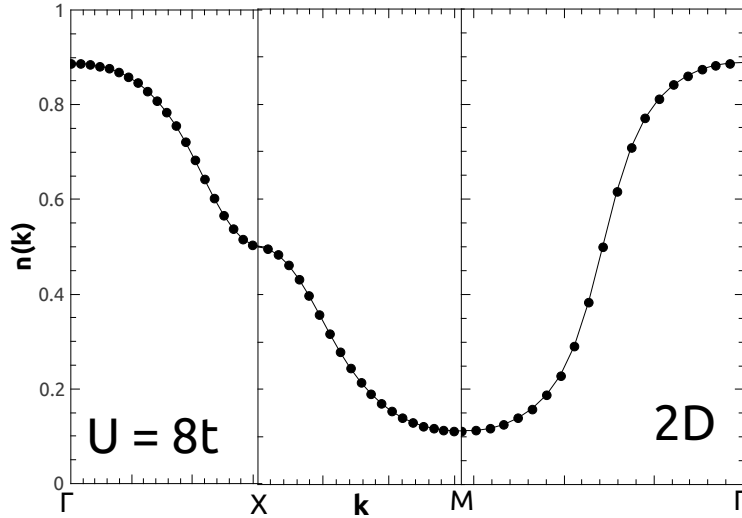
Figure 2.5: Momentum occupation $n_\sigma(\mathbf{k})$ for the 2D Hubbard model at half-filling, $U = 8t$, $N_s = 16$ cluster and $N_r = 18$. $\Gamma = (0,0)$, $X = (\pi, 0)$, and $M = (\pi, \pi)$.

method for a much larger system, $N_s = 120$ [23]. A good agreement between the two methods can be seen to occur. For $n_\sigma(k = 0)$, the relative difference is less then 0.4%. We also show in Fig. 2.5 $n_\sigma(\mathbf{k})$ for the 2D case, with $N_s = 16$ and $N_r = 18$.

Despite the good agreement with the thermodynamic limit at half-filling, we do not find a good agreement for $n \neq 1$. In this case, the ground state properties of the 1D HM in the thermodynamic limit are expected to be those of a Tomonaga-Luttinger liquid, for which $n(k)$ has the characteristic form [31]

$$n(k) \approx n(k_F) - C|k - k_F|^\alpha \operatorname{sign}(k - k_F).$$

The TABC + LD method does not reproduce this result. This issue has already been discussed in Ref. [25]. In the present work we concentrate on $n_\sigma(\mathbf{k})$ at the half-filling.

Single-particle spectral function $A(\mathbf{k}, \omega)$ and density of states $N(\omega)$

Here we show results for the single particle-spectral function, $A(\mathbf{k}, \omega)$, for the one-dimensional HM. The TABC was also employed in order to minimize FSE in the spectral

density function, $A^{\pm}(\mathbf{k}, \omega)$. For a given TBC, $\vec{\theta}_i$, we use the Lanczos method to obtain

$$A^{\pm}(\mathbf{k}, \omega, \vec{\theta}_i) = \sum_n |\langle\psi_n|c^{\pm}_{\mathbf{k},\sigma}|\psi_0\rangle|^2 \delta[\omega \pm (E_0(\vec{\theta}_i) - E_n(\vec{\theta}_i))], \qquad (2.14)$$

where $c^{+}_{\mathbf{k},\sigma}$ and $c^{-}_{\mathbf{k},\sigma}$ stand for $c^{\dagger}_{\mathbf{k},\sigma}$ and $c_{\mathbf{k},\sigma}$, repectively, and the single-particle excitations $c^{\dagger}_{\mathbf{k},\sigma}|\psi_0\rangle$ and $c_{\mathbf{k},\sigma}|\psi_0\rangle$ represent the creation of an electron and a hole with momentum $\mathbf{k}$, respectively. The function $A^{\pm}(\mathbf{k}, \omega)$ measures the spectral weight of adding an electron or a hole with momentum $\mathbf{k}$ and energy ω in the ground state $|\psi_0\rangle$. For a NI system the single-particle excitations correspond to quasiparticles with well defined energies, $\epsilon(\mathbf{k})$, where $\epsilon(\mathbf{k})$ is the dispersion relation. In this case the expected thermodynamic limit, $A^{\pm}(\mathbf{k}, \omega)$, $A^{\pm}(\mathbf{k}, \omega) = \delta(\omega - \epsilon(\mathbf{k}))$, can be recovered when we consider an infinite ensemble of TBC. Figure 2.6 (a) shows $A^{\pm}(k, \omega)$ for the 1D NI system.

For a Fermi liquid $A^{\pm}(\mathbf{k}, \omega) \approx \delta(\omega - \epsilon(\mathbf{k}))$, and the TABC also gives exact results in the thermodynamic limit [27]. Nevertheless, the concept of a quasiparticle with well defined energy and momentum in general does not work for an interacting system. In this case the excitations $c^{\dagger}_{\mathbf{k},\sigma}|\psi_0\rangle$ and $c_{\mathbf{k},\sigma}|\psi_0\rangle$ are not eigenstates of the Hamiltonian and in principle $A^{\pm}(\mathbf{k}, \omega)$ can no longer be written as a delta function. A 1D metalic system, for example, is a Tomonaga-Luttinger liquid for which the low-energy excitations are characterized by spin-charge separation.

In fact, spin-charge separation occurs in the one-dimensional HM: a single electronic excitation (e.g., $c_{k,\sigma}|\psi_0\rangle$) decomposes into two independent excitations carrying either spin (spinon) or charge (holon). The single-particle spectral function $A(k, \omega)$ is a standard probe for this phenomenon. At half-filling, $A(k, \omega)$ has been previously obtained with cluster pertubation theory (CPT) and dDMRG [32], [23]. In Fig. 2.6 (b) we show our results for $A^{-}(k, \omega < 0)$ with $U = 8t$ obtained with the TABC + LD method. The predominant spectral weight occurs for $k/\pi \le 1/2$, and within the energy range $-5t \le \omega - \mu \le -2t$. Due to the finite charge gap at half-filling, the lowest energy spectral weight (in relation to the Fermi level), has a finite energy, $\omega \approx -2t$, and is carried by the
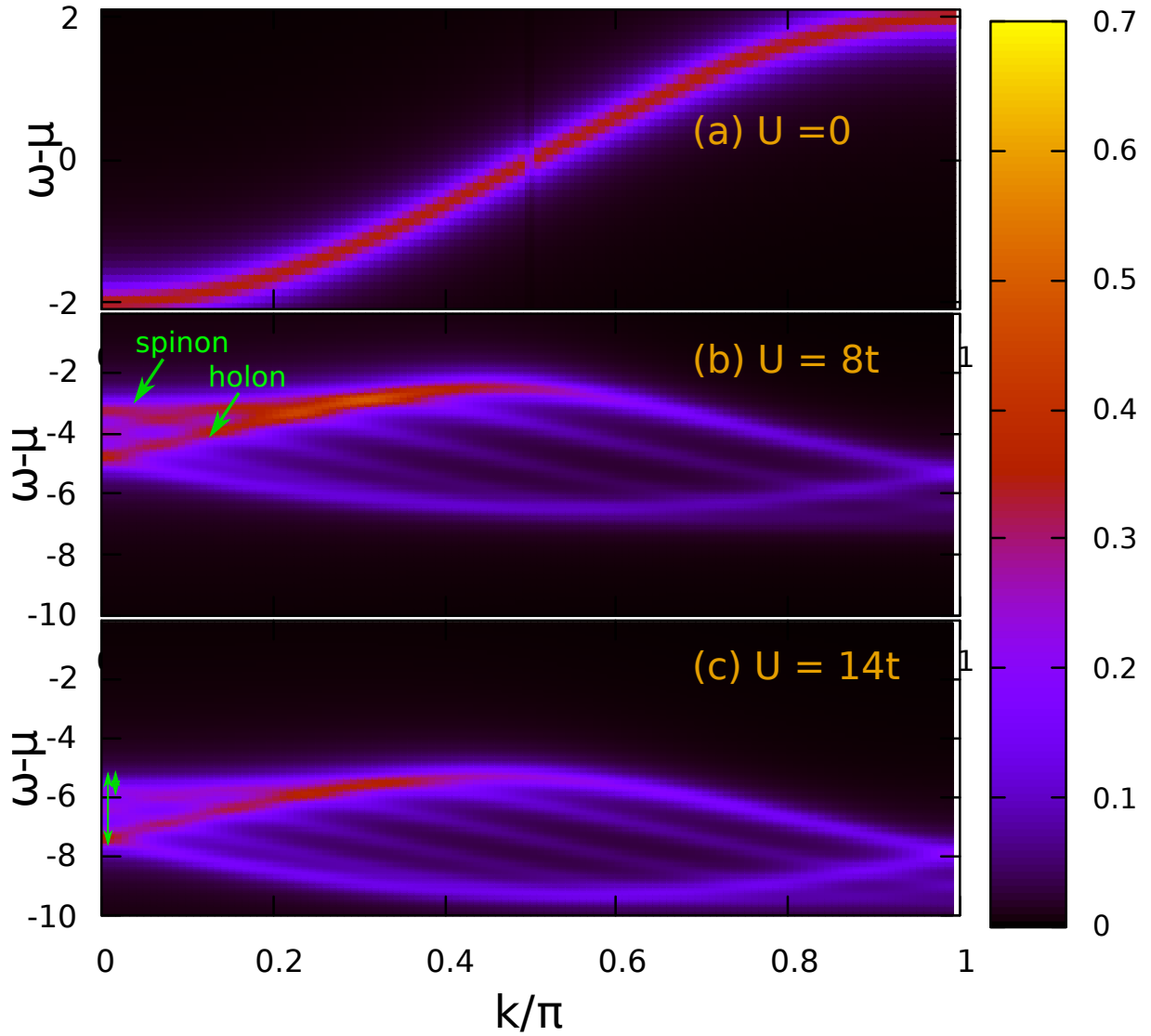
Figure 2.6: Colour plot of the spectral density function $A^-(k, \omega)$ for the 1D HM at half-filling, $N_s = 12$ and $N_r = 20$. The Fermi level is at $\omega - \mu = 0$. In (a) $U = 0$; $A^-(k, \omega) = \delta(\omega + 2t\cos(k))$. (b) $U = 8t$, the arrows indicates the spinon and holon branches, see the text. Despite the small size of the system, spin-charge separation is visible. (c) $U = 14t$, the arrows at $k/\pi = 0$ indicates the spinon and holon bandwidths.

mode $k/\pi = 1/2$. Furthermore, an important result for the 1D HM is the splitting of the spectral weight of $A^-(k, \omega)$ into two predominant branches within the range $0 \leq k \leq \pi/2$ (these branches are marked by arrows in Fig. 2.6 (b)) [32], [33]. A comparison with the exact Bethe ansatz solution of the 1D HM allows one to recognize these branches as spinon and holon bands; see Ref. [23]. In the strong coupling limit ($U \to \infty$), the bandwidth of the spinon and holon excitations are given by the magnetic exchange coupling $W_{spinon} = J \sim 4t^2/U$, and the hopping energy scale, $W_{holon} = 2t$, respectively [31], [34]. Thus the single-particle excitations of the 1D HM are charaterized by these two energy scales $J_{eff} = 4t^2/U$ and $2t$, which is a signature of spin-charge separation [35]. Figure 2.6 (c) shows $A^-(k, \omega)$ for $U = 14t$; the values obtained for the spinon and holon bandwidths are in agreement with the Bethe Ansatz prediction.
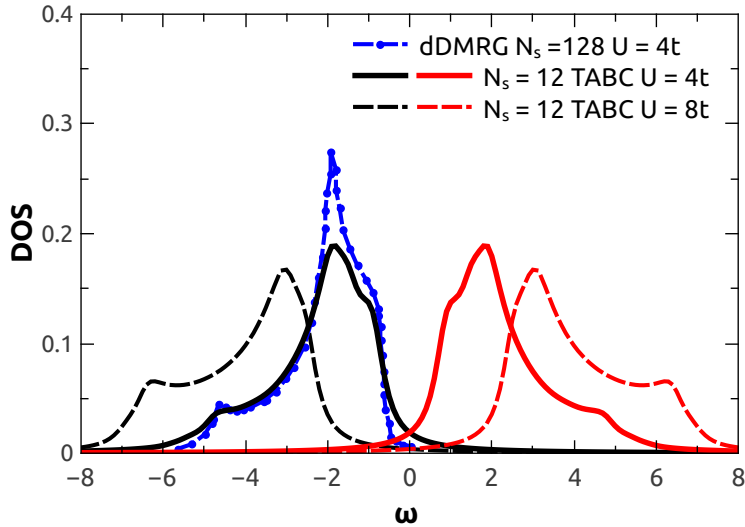
Figure 2.7: DOS of 1D HM at half-filling and $N_s = 12$. For the black curve we considered the TABC method with $N_r = 20$, $U = 4t$. The blue curve correspond to the dDMRG results extracted of Ref. [23] for $N_s = 128$.

The TABC can also be used to minimize FSE in the calculation of the density of states (DOS). In terms of the spectral density function, $A^\pm(k, \omega)$, the TABC expression for the

DOS is given by

$$N^{\pm}(\omega) = \frac{1}{N_r N_s} \sum_i \sum_{\mathbf{k}} A^{\pm}(\mathbf{k}, \omega, \vec{\theta_i}), \tag{2.15}$$

where $N^-(\omega)$ and $N^+(\omega)$ are the density of *occupied* and *unoccupied* states, respectively, and N_r is the number of TBC realizations considered.

In the DOS for the half-filled HM, a charge gap is formed around $\omega - \mu = 0$ (with $\mu = 0$), and the density of occupied and unoccupied states splits into the so-called Lower Hubbard Band (LHB) and Upper Hubbard Band (UHB). Figure 2.7 shows the DOS for $U = 4t$ and $U = 8t$ at half-filling. A good agreement is found when we compare with the results of dDMRG calculations for a chain with $N_s = 120$. For $U = 8t$ the size of the charge gap increases. In Chapter 7 we present the DOS for the extended HM away from half-filling.

Chapter 3

Quantum Monte Carlo

In this Chapter we discuss some basic aspects of the quantum Monte Carlo (QMC) method Stochastic Series Expansion (SSE). The SSE method has become a standard technique for simulating lattice models of quantum spins. The reason for this success is that SSE simulations scale with high efficiency, typically linearly in the number of lattice sites and the inverse temperature, $\mathcal{O}(N\beta)$ [36]. In addition, loop-type updating schemes can be efficiently implemented [37]. Thus, SSE provides exact results for very large systems; for the isotropic Heisenberg model, systems up to $N \approx 10^4$ were considered here. Systems sizes $N \approx 10^4$ achieved in SSE simulations are particularly important in the study of disordered systems, for which a careful study of finite-size effects has to be performed. The SSE method will be used in Chapter 4 to study effetcts of non-magnetic impurities close to a singlet-antiferromagnetic quantum critical point. In Chapter 5 we obtain the phase diagram of the 1/3 depleted lattice at the half-filling, using the Heisenberg model to represent the regime $U \to \infty$.

In this Chapter we describe the basic steps of the implemention of the SSE simulation for the isotropic Heisenberg model [38], [22].

3.1 Stochastic Series Expansion (SSE)

Like any QMC method, the goal of SSE is to construct an importance sampling scheme which leads to the calculation of some observable $\left\langle \hat{A} \right\rangle$. For the moment, let us consider that $\left\langle \hat{A} \right\rangle$ corresponds to the following estimator,

$$\left\langle \hat{A} \right\rangle = \frac{1}{Z} \operatorname{Tr} \left(\hat{A} e^{-\beta \hat{H}} \right) \rightarrow \frac{\sum_X A(X) W(X)}{\sum_X W(X)}, \tag{3.1}$$

where X corresponds to a SSE configuration (to be defined below) and $W(X)$ its weight. In general terms, the SSE scheme can be summarized in three steps. First, a representation of the partition function based on the Taylor expansion of $e^{-\beta \hat{H}}$ is obtained. This will lead to the definition of a SSE configuration X and the weight $W(X)$. Second, with the weight $W(X)$ at hand, the Metropolis algorithm is used to generate a succession of most likely configurations [38]. Some basic update schemes for the isotropic Heisenberg model will be described here. The last step is to calculate the quantities of interest, through Eq. (3.1). For the Heisenberg model we show how to perform the calculation of spin-spin correlation functions and of the AFM order parameter [39]. We also discuss the calculation of the imaginary-time spin-spin correlation function [40].

The starting point of the SSE is to expand the partition function in a Tayler series [36],

$$Z = \operatorname{Tr} \left(e^{-\beta \hat{H}} \right) = \sum_n \sum_\alpha \frac{\beta^n}{n!} \langle \alpha | (-\hat{H})^n | \alpha \rangle. \tag{3.2}$$

where $\{|\alpha\rangle\}$ is a convenient Hilbert basis, for example the S^z eigenbase; $\{|\alpha\rangle\} = \{|S_1^z S_2^z S_3^z ... S_{N_s}^z\rangle$. We next insert the set of complete basis states, $\sum_\alpha |\alpha\rangle\langle\alpha|$ between the n products of $(-H)$.

$$Z = \sum_n^\infty \sum_{\{\alpha_i\}} \frac{\beta^n}{n!} \langle \alpha_0 | (-\hat{H}) | \alpha_1 \rangle \langle \alpha_1 | (-\hat{H}) | \alpha_2 \rangle ... \langle \alpha_{n-1} | (-\hat{H}) | \alpha_n \rangle, \tag{3.3}$$

where the condition $|\alpha_n\rangle = |\alpha_0\rangle$ is necessary to keep the trace nonzero, and $\sum_{\{\alpha_i\}}$ is a sum over all possible configurations of the basis states $\{|\alpha_i\rangle\}$. For the majority of the

cases of interest the aforementioned trace is impossible to be performed exactly. In the SSE method the partition function is obtained with the aid of an importance sampling of the product of the n matrix elements. Here we will discuss the basic steps to implement the SSE method for the isotropic Heisenberg model.

It is important to anticipate that the weight of a given SSE configuration, $W(x)$, is proportional to the product of the n matrix elements. In that sense each individual matrix element $\langle \alpha_{i-1} | (-\hat{H}) | \alpha_i \rangle$ must be positive, in oder to be interpreted as a probability. Some of the matrix elements may be negative, depending on the precise form of H. This is a manifestation of the so called "sign-problem". This problem can be avoided if all the terms of the Hamiltonian have (or can be made to have) a negative sign in front of them. As will be shown below, the Heisenberg model on a bipartite lattice can be written in the "sign-free" form [36]. With this in mind, let us consider that a generic Hamiltonian can be written in the following form,

$$\hat{H} = -\sum_t \sum_b \hat{H}_{t,b}, \tag{3.4}$$

where the index t refers to the type of operator: $t = 1$ is a diagonal operator, and $t = 2$ is a non-diagonal operator in the basis $\{|\alpha_i\rangle\}$; the index b refers to the lattice bonds. Furthermore, the action of $H_{t,b}$ on a basis state is proportional to another basis vector, i.e., $\hat{H}_{t,b}|\alpha_i\rangle = a_{t,p}|\alpha_{i+1}\rangle$, and $a_{t,b} > 0$. Substituting in Eq. (3.3), yields

$$Z = \sum_{n=0}^{\infty} \sum_{\{\alpha_i\}} \sum_{\{S_n\}} \frac{\beta^n}{n!} \prod_{p=1}^{n} \langle \alpha_{p-1} | \hat{H}_{t_p,b_p} | \alpha_p \rangle, \tag{3.5}$$

where $\sum_{\{S_n\}}$ is a sum over all possible combinations of the product of operators for a given Taylor exponent n, and the index p represents the position in the sequence of operators S_n. Let us consider a simple example, $H = -(\hat{H}_A + \hat{H}_B)$. For $n = 2$, the possible combinations are $(-\hat{H})^n = \hat{H}_{A_1}\hat{H}_{A_2} + \hat{H}_{A_1}\hat{H}_{B_2} + \hat{H}_{B_1}\hat{H}_{A_2} + \hat{H}_{B_1}\hat{H}_{B_2}$, so in this case $p = 1$ or 2. A given configuration S_n will be called the "string S_n" [36] and will be represented as

$$[t_1, b_1], [t_2, b_2], ..., [t_n, b_n],$$

In the SSE method, the partition function and the expectation values of interest are obtained using importance sampling in a combined space of the basis states $\{\alpha_i\}$ (Ising spins for the Heisenberg model) and the strings S_n [36]. A given combination of basis states $\{\alpha\}$ and a string of operators S_n represents a SSE configuration, i.e., $(\{\alpha\}, S_n)$. An efficient scheme of local and loop updates of the configurations $(\{\alpha\}, S_n)$ can be estabilished for quantum spin systems [37], [41]. An important aspect of the update scheme is that the statistically relevant exponent of the Taylor series is centred around

$$\langle n \rangle \propto N_s \beta,$$

[see Eq.(3.17)], and assuming $\langle E \rangle \propto N_s$. We can thus define a cutoff $n_{max} = M$, above which any configuration $(\{\alpha\}, S_n)$ gives zero contribution for the partition function. In other words, it is possible to truncate the Taylor expansion in M. Even though this truncation is not necessary, it facilitates the scheme of updates. Then it is possible to work with a fixed Taylor exponent M inserting $M - n$ "fill-in", or unit operators $H_{0,0} = \hat{I}$ into the operator string S_M [36]. These unit operators do not contribute to the partition function. For a given configuration with n non-unit operators, the different ways of selecting the positions of the unit operators in the string of operators is given by the binomial coefficient, $M!/(M-n)!n!$. Then it is necessary to divide the partition function by these values. The truncated partition function is given by

$$Z = \sum_{\{\alpha_i\}} \sum_{\{S_M\}} \frac{\beta^n (M-n)!}{M!} \prod_{p=1}^{M} \langle \alpha_{p-1} | \hat{H}_{t_p,b_p} | \alpha_p \rangle. \tag{3.6}$$

Here $\{S_M\}$ denotes the set of all concatenations of M operators H_{t_p,b_p} and n is the number of nonunit operators in S_M. Finally, we can define the weight of a given SSE configuration $(\{\alpha\}, S_n)$ as

$$W(\{\alpha\}, S_M) = \frac{\beta^n (M-n)!}{M!} \prod_{p=1}^{M} \langle \alpha_{p-1} | \hat{H}_{t_p,b_p} | \alpha_p \rangle. \tag{3.7}$$

Thus the partition function is defined as

$$Z = \sum_{\{\alpha_i\}} \sum_{\{S_M\}} W(\alpha_i, S_M). \tag{3.8}$$

The choice of the cutoff M will be discussed below.

We now discuss the calculation of the weight $W(\{\alpha\}, S_n)$ for the isotropic spin 1/2 Heisenberg model [22], whose Hamiltonian reads,

$$\hat{H} = -J \sum_{<i,j>} \mathbf{S_i} \cdot \mathbf{S_j}, \tag{3.9}$$

where i and j label the sites of a bipartite lattice, and $\langle i, j \rangle$ represent nearest-neighbour sites. The basis states $\{|\alpha\rangle\}$ are the eigenstates of the S^z operators,

$$S_i^z|\alpha\rangle = \pm\frac{1}{2}|\alpha\rangle, \tag{3.10}$$

where i is a lattice site.

In order to calculate Eq. (3.7), $W(\{\alpha\}, S_M)$, we rewrite Eq. (3.9), defining the operators

$$\hat{H}_{1,b} = J\left(\frac{1}{4} - S_{i(b)}^z S_{j(b)}^z\right),$$
$$\hat{H}_{2,b} = \frac{J}{2}\left(S_{i(b)}^+ S_{j(b)}^- + S_{i(b)}^- S_{j(b)}^+\right), \tag{3.11}$$

where $\hat{H}_{1,b}$ and $\hat{H}_{1,2}$ are diagonal and non-diagonal operators, respectively, acting on the bond b connecting sites $i(b)$ and $j(b)$. The Heisenberg Hamiltonian can be cast in the form of Eq. (3.4). A factor 1/4 was added to $\hat{H}_{1,b}$ to simplify the calculation of $W(\alpha, S_M)$, and to guarantee that the diagonal contribution of $\hat{H}$ to the weight $W(\{\alpha\}, S_M)$ is always positive. It is important to mention that the addition of a constant in the Hamiltonian does not alter the physical properties of the system. The operator $\hat{H}_{2,b}$ was multiplied by -1 to guarantee that the non-diagonal contribution of $\hat{H}$ for the weight $W(\{\alpha\}, S_M)$ is always positive. This is possible due to the important sublattice rotation symmetry of the

spin operators on a bipartite lattice. The same symmetry cannot be used in a frustrated lattice, such as triangular and kagome lattices. In these cases, it is not possible to get rid of the infamous sign-problem [38].

We are now in position to obtain the weight of a configuration $(\{\alpha\}, S_M)$ for the isotropic Heisenberg model. The matrix elements of a pair of spins connected by the bond b are given by,

$$\langle\uparrow\uparrow|\hat{H}_{1,b} + \hat{H}_{2,b}|\uparrow\uparrow\rangle = \langle\downarrow\downarrow|\hat{H}_{1,b} + \hat{H}_{2,b}|\downarrow\downarrow\rangle = 0$$

$$\langle\uparrow\downarrow|\hat{H}_{1,b} + \hat{H}_{2,b}|\uparrow\downarrow\rangle = \langle\downarrow\uparrow|\hat{H}_{1,b} + \hat{H}_{2,b}|\downarrow\uparrow\rangle = 1/2$$

$$\langle\uparrow\downarrow|\hat{H}_{1,b} + \hat{H}_{2,b}|\downarrow\uparrow\rangle = \langle\downarrow\uparrow|\hat{H}_{1,b} + \hat{H}_{2,b}|\uparrow\downarrow\rangle = 1/2. \tag{3.12}$$

Then it is straightforward to show that

$$W(\{\alpha\}, S_M) = \frac{\beta^n(M-n)!}{M!}\prod_{p=1}^{M}\langle\alpha_{p-1}|\hat{H}_{t_p,b_p}|\alpha_p\rangle = \left(\frac{\beta}{2}\right)^n\frac{(M-n)!}{M!}, \tag{3.13}$$

where n is the number of nonunity operators in a string of operators S_M.

Having presented how to obtain the the weight of a given configuration, we now turn to the problem of how the different configurations $(\{\alpha\}, S_M)$ are sampled in the SSE scheme. For Heisenberg models, local and loop updates can be efficiently implemented. Here we will not present an exhaustive discussion of all updating schemes for Heisenberg models; we refer to Refs. [37], [41], instead.

One important aspect that must be considered during the sampling of the SSE configurations is that the product of matrix elements,

$$\prod_{p=1}^{M}\langle\alpha_{p-1}|\hat{H}_{t_p,b_p}|\alpha_p\rangle = \langle\alpha_0|(\hat{H}_{t_{p_1},b_{p_1}})|\alpha_1\rangle\langle\alpha_1|(\hat{H}_{t_{p_2},b_{p_2}})|\alpha_2\rangle...\langle\alpha_{M-1}|(\hat{H}_{t_{p_M},b_{p_M}})|\alpha_M\rangle,$$

must be periodic, i.e., $|\alpha_0\rangle = |\alpha_M\rangle$. Otherwise the weight associated with configuration $(\{\alpha\}, S_M)$ is null. Examples of updating schemes that satisfy this periodic condition are [41]:

(i) Diagonal updates: replace a unit operator by a diagonal operator acting on bond b, and vice-versa, i.e. $H_{0,0} \leftrightarrow H_{1,b}$.

(ii) Off-diagonal updates (local or loop): change the operator type, diagonal $\leftrightarrow$ off-diagonal, for two (local) or several (loop) operators.

(iii) Flip spins on state $|\alpha\rangle = |\alpha_0\rangle$ that are not acted by the string of operators on S_n.

Here we focus on the discussion of the diagonal updates. First of all, the update must satisfy detailed balance:

$$P(A \rightarrow B) = min\left(\frac{P(B \rightarrow A)W(B)}{P(A \rightarrow B)W(A)}, 1\right). \tag{3.14}$$

Where $P(A \rightarrow B)$ is the probability of acceptance of a new configuration A, given that the current configuration is B, and $W(A)$ and $W(B)$ are the weights of configurations A and B, respectively.

In update (i) a diagonal operator is inserted ($n \rightarrow n + 1$) or removed ($n \rightarrow n - 1$) from the string of operators S_M, where n is the number of non-unit operators. Using the formula for the weight of a configuration [Eq. (3.13], and detailed balance, we can obtain the probability of (a) switch a unit operator $H_{0,0}$ by a diagonal operator $H_{1,b}$ acting on a random bond b, and (b) switch a diagonal operator $H_{1,b}$ by a unit operator $H_{0,0}$, as

$$(a) \;\; P(n \rightarrow n + 1) = min\left(N_b \frac{\beta}{2(M - n)}, 1\right),$$

$$(b) \;\; P(n \rightarrow n - 1) = min\left(\frac{1}{N_b} \frac{2(M - n)}{\beta}, 1\right), \tag{3.15}$$

where N_b is the number of the bonds on the lattice, and was inserted in the relations to guarantee datailed balance, i.e.,

$$\frac{P(b \rightarrow 0)}{P(0 \rightarrow b)} = N_b.$$

This means that there are N_b ways of selecting a given bond with index b, but only one way of removing an operator.

Then one can use the diagonal update together with the Metropolis algorithm to sample the SSE configurations. The simulation starts with a SSE configuration $(\{\alpha\}, S_M)$, for instance, one in which all the operators of S_M are equal to $H_{0,0}$ and a random spin state $|\alpha\rangle$. During the update, each operator in the string S_M is visited once. Whenever an identity operator $H_{0,0}$ is found, a random bond index b is selected, and the update $H_{0,0} \rightarrow H_{1,b}$ is performed if $P(n \rightarrow n+1) \geq 1$. If $P(n \rightarrow n+1) < 1$ a random number r is generated, and the update is accepted if $r \geq P(n \rightarrow n+1)$; otherwise the update is rejected. Similarly, whenever a diagonal operator $H_{1,b}$ is found, the probability $P(n \rightarrow n-1)$ is used to perform the update, $H_{1,b} \rightarrow H_{0,0}$. During the diagonal updating scheme, the number of non-unit operators n in the string fluctuates. After visiting all operators on the string S_M, one MC diagonal update sweep is concluded.

The diagonal update scheme does not change the off-diagonal operators of the string S_M. Due to the periodic condition, a single off-diagonal operator $H_{2,b}$ cannot be switched by unit or diagonal operator. In this case, the loop update can be used to sample the SSE configurations. In this scheme the types of a set of operators are changed, i.e., $\{H_{a_1,b_1} H_{a_2,b_2}...H_{a_l,b_l} \rightarrow H_{3-a_1,b_1} H_{3-a_2,b_2}...H_{3-a_l,b_l}\}$. The implementation of this updating scheme will not be discussed here; details can be found in Ref. [37]. It is important to mention here that in the loop update the number of non-unit operators in the string S_M, n, is not changed. Finally, in update (iii) the spins that are not acted by any operators of S_M are flipped with a probability $1/2$.

We now turn to the question of determining M. As mentioned before it is possible to define a truncation Taylor exponent M, such that for $n > M$ all the SSE configurations $W(\alpha, S_n)$ contribute with a zero weight to the partition function. The choice of M is made during the thermalization process. It is clearly desirable to choose M as small as possible without compromising the accuracy of the calculation. This can be done by starting the simulation with a small M and continually monitoring the number of unit operators $H_{0,0}$ in the string of operators. If this number becomes smaller than some low

number, M is increased by adding $H_{0,0}$ operators to the string. This process is continued until equilibrium is reached. In practice, the simulation starts with a string with M' unit operators, i.e., $n = 0$. After the first MC sweep, the number of non-unit operators can vary. Then one changes the size of the string M' after each MC sweep, using the following condition: if $M' < n + n/3$, a new $M' = n + n/3$ is chosen. The thermalization process is concluded when M' does not change after a certain number of MC sweeps.

The actual simulation is then carried out with the value of M thus obtained. After the thermalization process, the quantities of interest are obtained. In the next section we describe the calculation of expectation values.

3.2   Expectation values in SSE

Efficient estimators for many static observables within the SSE method were derived by Sandvik et. al. [36], [39]. Here we describe the basic steps to calculate the quantities to be used in Chapter 4 and 5.

As was done for the partition function Z, Eq. (3.6), the thermal average of an operator $\hat{A}$ can be written as a sum of diagonal matrix elements:

$$\left\langle \hat{A} \right\rangle = \frac{1}{Z} \sum_{\alpha} \sum_{\{S_M\}} \beta^n \frac{(M-n)!}{M!} \langle \alpha | \hat{A} \prod_{p=1}^{M} \hat{H}_{t_p,b_p} | \alpha \rangle. \tag{3.16}$$

The estimator of the total energy E can be easily obtained with the aid of the expression $\langle E \rangle = -\left(\partial/\partial\beta\right)\ln Z$. Considering Eq. (3.6) for Z, we obtain

$$\langle E \rangle = -\frac{1}{\beta}\langle n \rangle, \tag{3.17}$$

where $\langle n \rangle$ is the thermal average of the Taylor exponent n. In order to obtain other estimators (e.g., spin-spin correlation function, magnetization, etc), we rewrite Eq. (3.16) in terms of the weight $W(\alpha, S_M)$,

$$\left\langle \hat{A} \right\rangle = \frac{\sum_{\alpha} \sum_{\{S_M\}} A(\alpha, S_M) W(\alpha, S_M)}{\sum_{\alpha} \sum_{\{S_M\}} W(\alpha, S_M)}, \tag{3.18}$$

where

$$A(\alpha, S_M) = \begin{cases} \dfrac{\langle\alpha|\prod_{p=1}^{M}\hat{A}\hat{H}_{t_p,b_p}|\alpha\rangle}{\langle\alpha|\prod_{p=1}^{M}\hat{H}_{t_p,b_p}|\alpha\rangle}, & \text{if} \quad W(\alpha, S_M) \neq 0, \\ 0, & \text{if} \quad W(\alpha, S_M) = 0, \end{cases}$$

and $W(\alpha, S_M)$ is given by Eq. (3.7).

The evaluation of Eq. (3.18) is simplified by the fact that a set of configurations $(\{\alpha(i)\}, S_M(i))$ with equal weight can be obtained using one SSE configuration $(\{\alpha\}, S_M(i))$ with $W(\{\alpha\}, S_M(i)) \neq 0$, i.e.,

$$W(\alpha, S_M) = W[\alpha(i), S_M(i)], \tag{3.19}$$

where $i = 0, 1, ..., M-1$. In order to explain how the states $(\alpha(i), S_M(i))$ are obtained, we follow Ref. [36], and define the binary counterparts H'_{t_p,b_p} to the operator H_{t_p,b_p} of S_M:

$$\langle\alpha'|H'_{t_p,b_p}|\alpha\rangle = \begin{cases} 1, & \text{if} \quad \langle\alpha'|H_{t_p,b_p}|\alpha\rangle \neq 0, \\ 0, & \text{if} \quad \langle\alpha'|H_{t_p,b_p}|\alpha\rangle = 0, \end{cases}$$

i.e., on acting on a basis vector, H'_{t_p,b_p}, either delivers zero or a basis vector. Let us consider a configuration (α, S_M) for which $W(\alpha, S_M) \neq 0$. The definition of the equal weight states $(\alpha(i), S_M(i))$ is motivated by the following relation:

$$\langle\alpha|H_{t_M,b_M}...H_{t_2,b_2}H_{t_1,b_1}|\alpha\rangle = \langle\alpha|H'^{\dagger}_{t_1,b_1}H_{t_1,b_1}H_{t_M,b_M}...H_{t_2,b_2}H_{t_1,b_1}H'_{t_1,b_1}|\alpha\rangle, \tag{3.20}$$

where $H'^{\dagger}_{t_1,b_1}$ is the adjoint of the operator H'_{t_1,b_1}. Equation (3.20) can be cast in the form

$$\langle\alpha|H_{t_M,b_M}...H_{t_2,b_2}H_{t_1,b_1}|\alpha\rangle = \langle\alpha(1)|H_{t_1,b_1}H_{t_M,b_M}...H_{t_2,b_2}|\alpha(1)\rangle, \tag{3.21}$$

where we defined the ith propagated state $|\alpha(i)\rangle$ as

$$|\alpha(i)\rangle = \prod_{p=1}^{i} H'_{t_p,b_p}|\alpha\rangle. \tag{3.22}$$

On the right-hand side of Eq. (3.21), the original sequence of indices on the string S_M was cyclically permuted once, i.e.,

$([t_1, b_1][t_2, b_2][t_3, b_3]...[t_M, b_M]) \rightarrow ([t_2, b_2][t_3, b_3]...[t_M, b_M][t_1, b_1])$; this expression also holds when S_M is cyclically permuted i times, i.e.,

$$\langle \alpha | H_{t_M,b_M}...H_{t_2,b_2} H_{t_1,b_1} | \alpha \rangle = \langle \alpha(i) | H_{t_i,b_i} H_{t_{i-1},b_{i-1}}...H_{t_1,b_1} H_{t_M,b_M}...H_{t_{i+1},b_{i+1}} | \alpha(i) \rangle, \quad (3.23)$$

where $i \geq 2$.

In the configuration $(\alpha(i), S_M(i))$, $S_M(i)$ represents a string obtained by cyclically permuting i times the original string of operators S_M, and $|\alpha(i)\rangle$ is an ith propagated state. It is important to emphasize that although the set of configurations $(\alpha(i), S_M(i))$, $i = 0, 1..., M-1$, gives terms of equal weight, the functions $A(\alpha(i), S_M(i))$ need not to be the same for every i.

In practice, after each MC step a SSE configuration (α, S_M) is chosen, and $\left\langle \hat{A} \right\rangle$ is calculated using the set of equal weight configurations $(\alpha(i), S_M(i))$. Equation (3.18) can be rewritten as

$$\left\langle \hat{A} \right\rangle = \frac{1}{M} \sum_{i=0}^{M-1} A(\alpha(i), S_M(i)). \quad (3.24)$$

If $\hat{A}$ is a diagonal operator in the basis $\{|\alpha\rangle\}$, we have the simple expression

$$\left\langle \hat{A} \right\rangle = \frac{1}{M} \sum_{i=0}^{M-1} A(i),$$

where $A(i) = \langle \alpha(i) | \hat{A} | \alpha(i) \rangle$. After a certain number of MC sweeps, N_{sweep}, the MC averages of the quantities of interest are performed as

$$A = \frac{1}{N_{sweep}} \sum_{m=1}^{N_{sweep}} \left\langle \hat{A} \right\rangle (m).$$

For the Heisenberg model we obtain the z component of the spin correlation function,

$$\langle S_l^z S_m^z \rangle = \frac{1}{M} \sum_{i=0}^{M-1} S_l^z(i) S_m^z(i), \quad (3.25)$$

where l and m are site labels, and $S_l^z(i) = \langle \alpha(i) | \hat{S}_l^z | \alpha(i) \rangle$ corresponds to the expectation value on Ising-like states. Other observables for this model were obtained using the same procedure.

3.2.1 Imaginary time correlation function

In the previous section we described how to calculate static thermodynamic quantities, e.g., spin-spin correlation function and the AFM order parameter. Another quantity of interest is the spin relaxation rate, which, as will be discussed in Section 4.3, is given by

$$\frac{1}{T_1} = \lim_{\omega \to 0} \frac{A^2}{2} S_{i,i}(\omega), \tag{3.26}$$

where A is the hyperfine coupling, and $S_{i,j}(\omega)$ is the Fourier transfomation of the dynamical spin-spin correlation function,

$$S_{i,j}(\omega) = \int_0^\infty \left\langle S_i^z(t) S_j^z(0) \right\rangle,$$

with $S_i^z(t) = e^{it\hat{H}} S_i^z e^{-it\hat{H}}$. Despite the fact that dynamical quantities like $1/T_1$ cannot be obtained directly with QMC methods, it is possible to calculate imaginary-time correlation functions within the framework of SSE [39], [40]. The latter is related to real time quantities by a Laplace transformation. With the imaginary-time spin-spin correlation function being defined by

$$C_{l.m}(\tau) = \left\langle e^{\tau\hat{H}} S_l^z e^{-\tau\hat{H}} S_m^z \right\rangle = \frac{1}{Z} \{ e^{\tau\hat{H}} S_l^z e^{-\tau\hat{H}} S_m^z \}, \tag{3.27}$$

the starting point to obtain an SSE estimator for $C_{l.m}(\tau)$ is to consider a Taylor expansion of $e^{\tau\hat{H}}$. In Ref. [39] an expression for $C_{l,m}(\tau)$ in terms of the propagated states $|\alpha(l)\rangle$ is obtained as

$$\left\langle e^{\tau\hat{H}} S_l^z e^{-\tau\hat{H}} S_m^z \right\rangle = \left\langle \sum_{\Delta l=0}^L \frac{L!}{(L-\Delta l)!\Delta l!} \left(\frac{\tau}{\beta}\right)^{\Delta l} \left(1 - \frac{\tau}{\beta}\right)^{L-\Delta l} c_{l,m}(\Delta l) \right\rangle, \tag{3.28}$$

where the correlator $c_{l,m}(\Delta l)$ is defined as

$$c_{l,m}(\Delta l) = \frac{1}{M} \sum_{l=0}^{M-1} S_l^z(l + \Delta l) S_m^z(l), \tag{3.29}$$

and $S_m^z(l) = \langle \alpha(l)|\hat{S}_m^z|\alpha(l)\rangle$; $|\alpha(l)\rangle$ is the l-propagated state, see Eq. (3.22). In this thesis we obain the correlation function $C_{i,j}(\tau)$ using the method of ref. [40]. The strategy is to calculate the correlator $C_{l,m}(\Delta l)$ "on the fly" while constructing the loop update.

In general, it is difficult to obtain $S_{i,i}(\omega)$ from the QMC simulation, since it requires analytic continuation from Matsubara to real frequencies [42]. Here we used the approximation described in Ref. [43], which relates $1/T_1$ directly with the long imaginary-time behaviour of the spin autocorrelation function

$$\frac{1}{T_1} = \frac{A^2}{\pi^2 T} \langle S_i(\tau = \beta/2)S_i(0)\rangle \,. \tag{3.30}$$

The regime of validity of Eq.(3.30) is discussed in Ref.[43]. In the next Chapter, the SSE method will be used to obtain the spin relaxation rate, $1/T_1$, in the Heisenberg bilayer model.

Chapter 4

Impurities near an antiferromagnetic-singlet quantum critical point

The effects of impurities have been widely investigated in spin-gapped systems [1], [44], [45], [46], [47]. As an example, we mention the Zn subtitution for Cu in the spin-1/2 two-leg ladder system, $Sr(Cu_{1-x}Zn_x)_2O_3$. In the pure case ($x = 0$), this material is characterized by a nonmagnetic ground state with an energy gap in its spin excitation spectra, i.e., a spin gap [48]. Nevertheless, when a small fraction of Zn ($x = 0.01$) is introduced, the magnetic susceptibility increases at low temperatures, indicating the existence of free localized moments in the otherwise spin-gapped system [1]; see Fig. 4.1 (a). The interpretation is that the nonmagnetic impurities break the rung singlets, leaving free spins-1/2 behind. Furthermore, measurements of the NMR spectrum indicate the formation of a staggered magnetization (AF puddles) in the vicinity of the Zn impurities, see Fig. 4.1 (b) [44]. Similar studies were performed in other spin-gapped systems: $CuGeO_3$, $BiCu_2PO_6$, etc [45], [47]. From the theoretical side, impurity-induced effects have been studied using quantum Monte Carlo (QMC) simulations as well [49], [50], [51].

More recently, a similar effect has been observed in heavy-fermion materials in which Cd doping of superconducting $CeCoIn_5$ induces long-range magnetic order [2], [53]. The
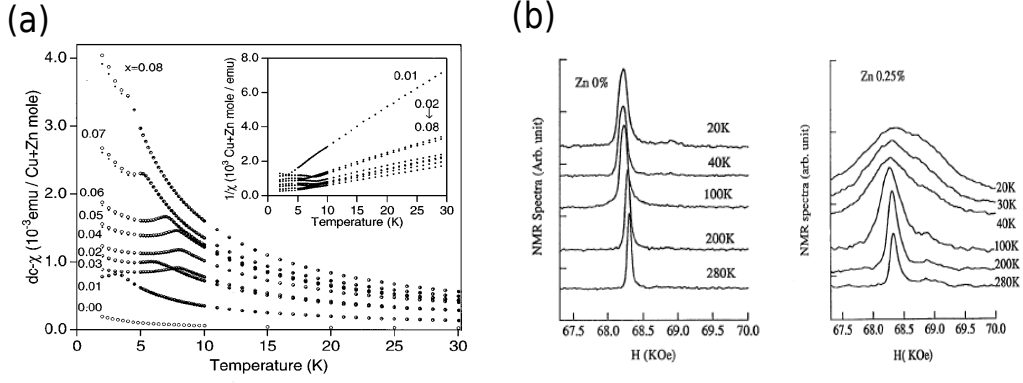
Figure 4.1: (a) Temperature dependence of the dc magnetic susceptibility of $Sr(Cu_{1-x}Zn_x)_2O_3$ [1]. (b) NMR spectra of $Sr(Cu_{1-x}Zn_x)_2O_3$ for $x = 0$ and $x = 0.25$ [44]. The NMR spectrum is a mere histogram of the local fields among all nuclear sites, thus its width reflects the electronic local magnetization [44], [52]. The broadening of the NMR spectrum indicates the formation of a sttagered magnetization around the Zn impurity.

underlying mechanism is believed to be a local reduction of conduction electron-local moment (c-f) hybridization on the Cd sites, suppressing the singlet energy gain, and inducing unscreened localized moments in their immediate vicinity [54]. Figure 4.2 shows some examples of experimental results. The broadening of the NMR spectra linewidth is an indicative of formation of AF puddles around the Cd impurities. Measurements of the spin relaxation rate $1/T_1$ indicate that the regions far from the impurities are not affected by them, and the resulting phase is quite heterogeneous. In addition, the pristine $CeCoIn_5$ is considered a quantum critical system, in the sense that it is in the vicinity of a quantum critical point (QCP) to a AFM phase. Thus the plausible scenario is that in the Cd-doped $CeCoIn_5$, AFM emerges locally in the vicinity of the Cd impurities [53]; as the length of the regions of local AFM order grows and reaches the scale of the distance between impurities, the system can undergo long-range order, see Fig. 4.2 (c)

Motivated by these results, in this work we investigate the effects of impurities near an antiferromagnetic-singlet quantum critical point(QCP). The results were published in Ref. [3], which is reproduced in Appendix D. The main results are highlighted in the body of this Chapter.
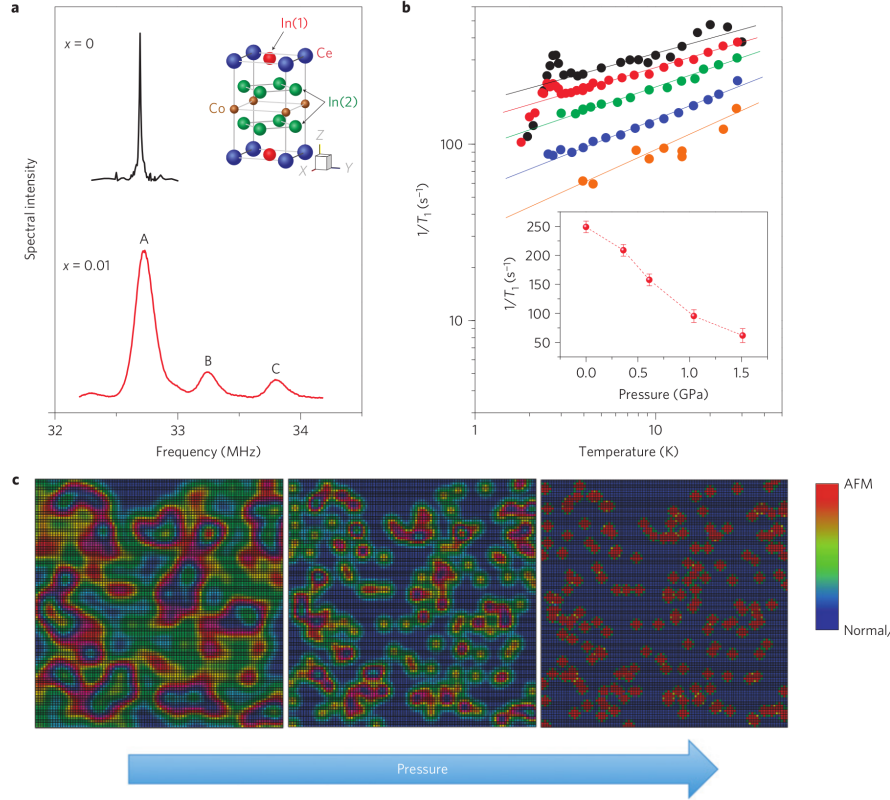
Figure 4.2: (a) NMR spectra of CeCoIn$_5$ and 1% Cd-doped CeCoIn$_5$. The broadening of spectra linewidth indicates the formation of AF puddles around the impurity. (b) Spin relaxation rate $1/T_1$. (c) Schematic illustration of the dependence on pressure of the size of the AFM regions induced around the Cd atoms that replace In in CeCoIn$_5$. The pressure tunes the system away from the quantum critical point. The spatial extent of AFM regions shrinks with pressure. For a higher pressure, the magnetic correlation length becomes shorter than inter-droplet spacing, leading to suppression of the long-ranged antiferromagnetic order [2].

4.1 Heisenberg Bilayer

We consider the spin-1/2 Heisenberg bilayer Hamiltonian [55],

$$H = \sum_{\langle ij \rangle, \alpha} J^\alpha \vec{S}_i^\alpha \cdot \vec{S}_j^\alpha + g \sum_i \vec{S}_i^1 \cdot \vec{S}_i^2, \tag{4.1}$$

where subscripts i, j denote spatial sites on a square lattice and superscripts $\alpha = 1, 2$ label the two layers. With the interplane coupling $g = 0$, the independent planes have antiferromagnetic long-range order (AFM) at $T = 0$ [56]. In this case the spin-spin correlation length, ξ, diverges as $T \to 0$ and the system has gapless spin excitations.

For a large g there is a tendency for neighbouring interlayer spins to form singlets. In this interlayer-singlet-rich phase, both the spin-spin correlation lenght, ξ, and the spin excitation gap are finite at $T = 0$. The Heisenberg bilayer model describes a quantum phase transition between an AFM and a singlet ground state.

The position of the QCP, g_c, where the AFM-singlet transition takes place, was previously estabilished through finite size extrapolations of the the AF order parameter [55], [57]. As a test of our SSE code, we first reproduce these calculations. The square of the order parameter is obtained by summing the spin-spin correlations throughtout the lattice, normalized to the number of spins, N. If these correlations are short ranged (i.e., decaying exponentially), the local contributions to the sum, when divided by N, vanish; by contrast, if the correlations extend over the entire lattice, then the order parameter is nonvanishing. The square of AF order parameter is defined as

$$\langle m^2 \rangle = \left\langle \left(\frac{1}{N} \sum_i (-1)^{x_i + y_i + \alpha} S_i^{\alpha} \right)^2 \right\rangle. \tag{4.2}$$

For finite-sized systems, the correlation lenght, ξ, of spin-spin correlations is limited by the finiteness of the lattice, so the AF structure factor, $\langle m^2 \rangle / N$, saturates above some crossover inverse temperature, β^*. This saturated value is taken as an estimate for $\langle m^2 \rangle$ in the ground state. Figure 4.3 shows the inverse-size dependence of $\langle m^2 \rangle$, obtained for $\beta = 80 > \beta^*$ and different values of g. For $g < 2.52$, the AF order parameter extrapolates to a finite value, which indicates that the ground state has AFM order. On the other hand, for $g \geq 2.52$, $\langle m^2 \rangle$ extrapolates to zero, and the system is in a singlet ground state. We thus obtain $g_c \approx 2.52$, in agreement with Ref. [57].

4.2 Non-magnetic impurities

Our aim here is to discuss the effects of non-magnetic impurities by removing spins in the layer $\alpha = 2$; see Fig. 4.4 (a). In what follows we summarize our findings, while a detailed presentation of the results can be found in Appendix D.
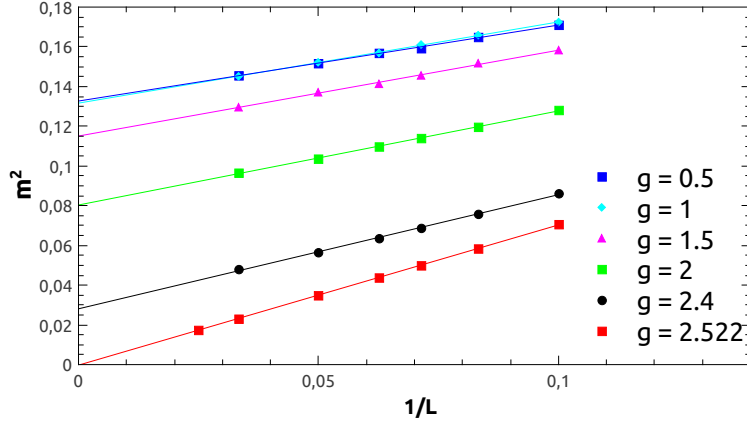
Figure 4.3: Finite-size scaling of the square AF order parameter for the clean Heisenberg bilayer model. L is the linear size of the bilayer; here we considered $L = 10, 12, 14, 16, 20, 30, 40$.

An important result is that this kind of impurities induces AFM order in an otherwise singlet phase, $g > g_c$. A plausible picture for the impurities-induced AFM is as follows [49], [58], [50]. The removal of a single spin from the bilayer system in the singlet phase leaves one spin-1/2 behind, which creates an effective local moment. This is corroborated by the fact that the $T \to 0$ asymptotic impurity susceptibility - defined as the difference between the susceptibility with and without impurity - has a Curie form, $\chi^z_{imp} \to C/T$, with $C = S(S+1)/3$. Furthermore, between two effective local moments located in sites i and j, there exists an effective interaction mediated by spins in an interlayer-singlet state, see Fig. 4.4 (a). The effective exchange interaction oscillates in phase with an amplitude that decays exponentially as

$$J_{eff} \approx (-1)^{-|i-j+1|} \exp(l/\xi), \tag{4.3}$$

where l is the separation between impurities, and ξ is the correlation length for the clean system [50], [51]. Hence the staggered nature with respect to the original lattice is completely preserved, and the effective spins are antiferromagnetically ordered at $T = 0$. In the strong coupling regime ($g/J \gg 1$), the impurities-coupling can be understood with the aid of an l-order pertubation theory; see Fig. 4.4 (b).
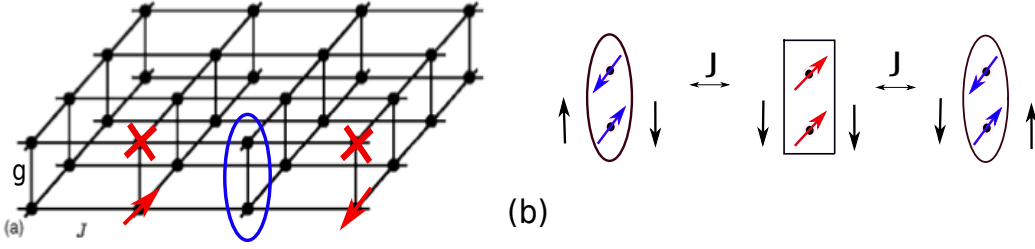
Figure 4.4: (a) The arrangement of spin interactions in the Bilayer: there are two different couplings, J (intraplane) and g (interplane). In addition, we consider that two spins were removed from layer $\alpha = 2$ (two impurities); the effective coupling between two unpaired spins is given by Eq. (4.3). (b) Illustration of the second-order process responsible for the effective coupling between the two unpaired spins of (a), in the limt $g/J \gg 1$. Here two exchange interactions J effective flip the unpaired spins, with a triplet interplane intermediate state. The effective Hamiltonian is $H_{eff} = J_{eff} S_i^1 \cdot S_j^1 + k$, where k is a constant. The effective interaction between two unpaired spins separated by a distance l is given by an l-order process.

In the present work we use SSE to examine the effect of a finite fraction of impurities, p, in the vicinity of the AFM-singlet QCP, $g \approx g_c$. We define the impurity susceptibility, χ_{imp}, as

$$\chi_{\text{imp}} = \left. \frac{d \langle m^2 \rangle}{dp} \right|_{p=0}, \tag{4.4}$$

which measures the response of the system as a small fraction of impurities (e.g., $p = 0.01$) is introduced. Figure 4.5 shows that χ_{imp} has a sharp peak at g_c. The effect of impurities is especially large close to the QCP . Farther away from the the QCP in the AF phase $g < 2$, the impurity susceptibility is negative, which indicates that impurities inhibit AFM.

4.3   Nuclear magnetic ressonance (NMR)

We have also obtained the NMR spin relaxation rate $1/T_1$. Here we explain the derivation of Eq. (3) of Appendix D, which relates $1/T_1$ with the imaginary part of the electronic dynamical susceptibility, $\chi''(\vec{q}, \omega)$. The contents of this section is based on Ref. [59]. For a nuclear spin I_i at site i, the coupling to the electronic spin S_i is given by the hyperfine
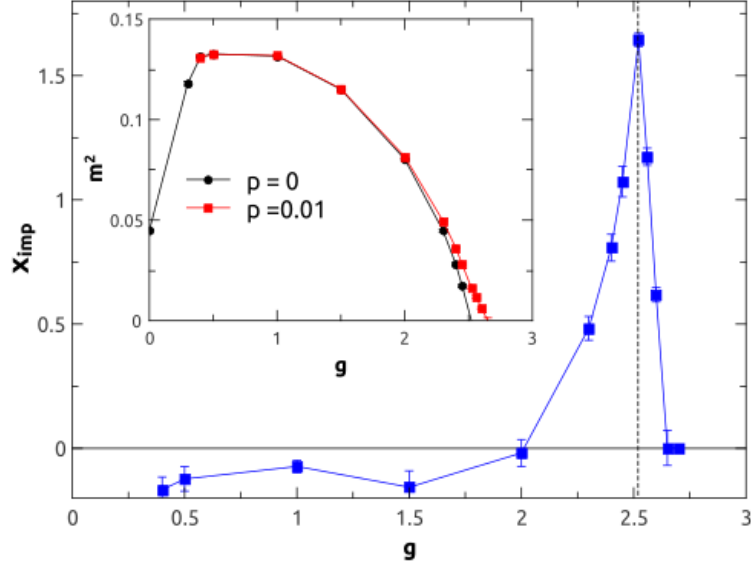
Figure 4.5: The impurity susceptibility, χ_{imp}, as function of g is sharply peaked at g_c (vertical dashed line): impurities induce AF order. Away from g_c, $\chi_{\text{imp}} < 0$: impurities reduce the AF order parameter. Inset: shows the g dependence of $\langle m^2 \rangle$ for $p = 0.01$ (square) and clean system (circles). Both the shift in g_c and the large effect of impurities at the QCP are evident. Data for $\langle m^2 \rangle$ have been extrapolated to $L = \infty$. The inverse temperature $\beta = 80$.

Hamiltonian,

$$\mathcal{H} = \gamma H^z I_i^z + A I_i^z S_i^z + A \frac{1}{2} \left(I_i^+ S_i^- + I_i^- S_i^+ \right), \tag{4.5}$$

where γ is the nuclear gyromagnetic ratio, and A is an isotropic hyperfine coupling, representing a contact interaction. We also include an external magnetic field, H^z, in the Hamiltonian.

The external magnetic field gives rise to a Zeeman splitting, $\delta E = \gamma H^z$, in terms of which the Larmor frequency is given by $\omega_L = \delta E / \hbar$. The hyperfine interaction affects the nuclear spin in two ways: (i) the diagonal term generates a shift in the Larmor frequency, known as Knight shift; (ii) the non-diagonal part of the hyperfine interaction corresponds to a spin-flip exchange between the electronic spin and the nuclear spin. These processes do not shift the resonance frequency, but do affect the dynamics of the nuclei and is responsible for the relaxation process.

The expression for $1/T_1$ can be obtained with the aid of time-dependent pertubation theory. The first two terms of Eq. (4.5) correspond to the non-perturbed Hamiltonian, H_0, and the non-diagonal part is the pertubation, $V(t)$. To first-order pertubation theory, a generic state $|\psi(t)\rangle$ is given by:

$$|\psi(t)\rangle = |\psi(0)\rangle - \frac{i}{\hbar} \int_0^t e^{\frac{-iH_0 t}{\hbar}} V(t) e^{\frac{iH_0 t}{\hbar}} |\psi(0)\rangle dt. \tag{4.6}$$

We assume that at $t = 0$ the nuclear spin is in the excited state, $|i\rangle = |\downarrow\rangle$, of H_0. The transition to the excited state can be caused by a perpendicular magnetic field, but this process will not be described here. At $t > 0$, the transition probability for the ground state, $|f\rangle = |\uparrow\rangle$, is given by,

$$|\langle f|i\rangle|^2 = \frac{A^2}{4\hbar^2} \int_0^t \int_0^{t'} e^{-i\omega_L(t-t')} \langle s_f|S_i^-(t)|s_i\rangle \langle s_i|S_i^+(t')|s_f\rangle dt dt'.$$

Using time translation symmetry,

$$|\langle f|i\rangle|^2 = \frac{A^2}{4\hbar^2} t \int_0^\infty e^{-i\omega_L t} \langle s_f|S_i^-(t) S_i^+(0)|s_f\rangle dt.$$

Finally, the spin relaxation rate $1/T_1 = \frac{d|\langle f|i\rangle|^2}{dt}$, is obtained as

$$\frac{1}{T_1} = \frac{A^2}{4\hbar^2} \int_0^\infty e^{-i\omega_L t} \left\langle S_i^-(t) S_i^+(0) \right\rangle dt. \tag{4.7}$$

For now on we set $\hbar = 1$ and $k_B = 1$.

The dynamical correlation function $\left\langle S_i^-(t) S_i^+(0) \right\rangle$ is described by the Heisenberg bilayer Hamiltonian [Eq. (4.1)]; using the SU(2) symmetry of the Hamiltonian, we have $\left\langle S_i^-(t) S_i^+(0) \right\rangle = 2 \left\langle S_i^z(t) S_i^z(0) \right\rangle$. Equation (3) from Appendix D is then obtained with the aid of fluctuation-dissipation theorem [60],

$$S(\mathbf{q}, \omega_L) = 2\chi''(\mathbf{q}, \omega_L)/(1 - e^{-\beta\omega_L}),$$

where $S(\mathbf{q}, \omega)$ is the Fourier transform of the dynamical correlation function, $\left\langle S_i^z(t) S_j^z(0) \right\rangle$, and $\chi''(\mathbf{q}, \omega)$ is the imaginary part of the dynamical susceptibility [59]. Since the resonance

frequency ω_L is small compared to the electronic spin flucuations J, $1/T_1$ effectively measures $S(q, \omega \rightarrow 0)$). The real-time autocorrelation function, $\langle S_i^z(t) S_i^z(0) \rangle = \text{Tr}(e^{-\beta H} S_i^z(t) S_i^z(0))$, was obtained using the long imaginary-time behaviour of the spin-spin correlation function [43]; further details about this calculation are given in Chapter 3 and in Appendix D.
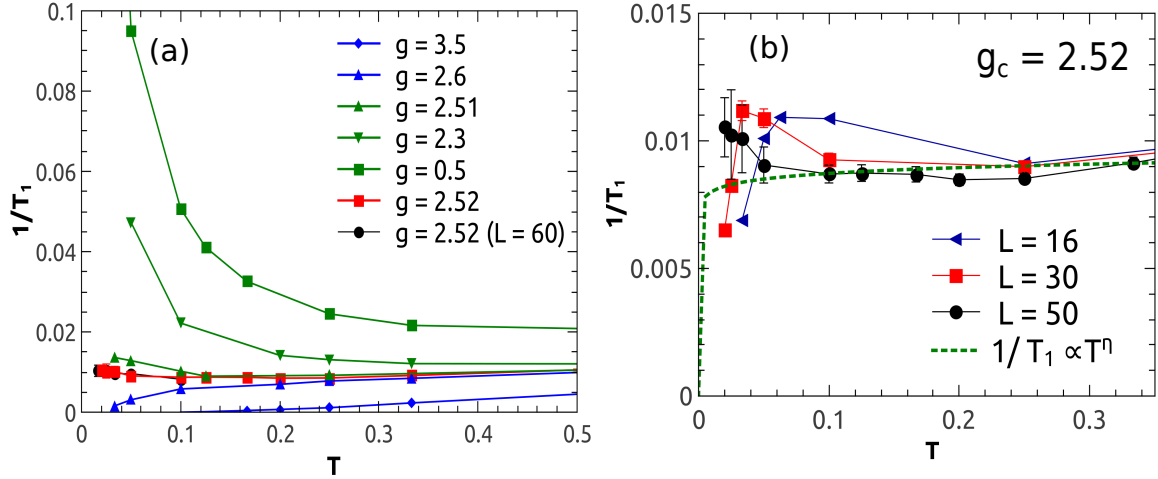
Figure 4.6: (a) Clean system: Spin relaxation rate as a function of T for different values of g. At the critical value, $g_c \approx 2.52$, $1/T_1$ is nearly temperature-independent. Unless otherwise stated, data are for lattices of linear size $L = 50$. (b) Blow up of (a) at $g = g_c$ for different lattice sizes, L.

In Appendix D we show the results for $1/T_1$ for a system with one impurity. Here we discuss the temperature dependence of $1/T_1$ for several values of the interlayer coupling g in the clean Heisenberg bilayer, see Fig. 4.6 (a). In the AF phase ($g < g_c$), $1/T_1$ increases as the temperature is lowered, due to the increase of spin fluctuations. On the other hand, due to the presence of the spin gap, $1/T_1$ goes to zero in the singlet phase ($g > g_c$). At high temperatures (i.e., $0.3J < T < 0.5J$), $1/T_1$ is nearly constant in both regimes [61]. The range of temperatures for which $1/T_1$ is nearly T-independent increases as g approaches the QCP. Exactly at g_c, our data are consistent with this behaviour extending to low temperatures, down to $T \sim 10^{-2} J$. While we cannot test this at high temperatures without going beyond the range of validity of the long imaginary-time approximation

used to obtain $1/T_1$ [43], at low temperatures we are limited by finite-size effects. Indeed, Fig. 4.6 (b) shows $1/T_1$ as a function of T, at $g = g_c$, but for different lattice sizes. The data exhibit some T dependence for $T \lesssim 0.1J$, but these fluctuations are reduced as the lattice size increases. In addition, Ref. [61] establishes that in the critical regime the relaxation rate is described by the nearly T-independent function, $1/T_1 \sim T^\eta$, whith the exponent $\eta = 0.0357$. This power-law is plotted as a dashed line in Fig. 4.6 (b). Our data for $1/T_1$, at g_c and low temperatures, are consistent with a very weak temperature dependence.

Chapter 5

Magnetic order-disorder transitions on a one-third-depleted square lattice

In this work we analyse the magnetic properties of the Hubbard model in the one-third-depleted (1/3-depleted) square lattice of Fig. 5.1. One motivation to investigate this geometry is provided by recent experimental [62] and theoretical [63] studies of the layered nickelates $La_4Ni_3O_8$. In this material, the formal Ni valence of $+1.5$ is separated into Ni^{1+} (spin 1/2) and Ni^{2+} (spin 0), so that spin-1/2 stripes are formed, as in Fig. 5.1. Here we will investigate the magnetic properties formed by such arragement of spin-1/2. To this end, we consider the Hubbard model on the 1/3-depleted square lattice,

$$\mathcal{H} = -t \sum_{\langle ij \rangle \sigma} \left(c_{i\sigma}^\dagger c_{j\sigma} + c_{j\sigma}^\dagger c_{i\sigma} \right) + t' \sum_{\langle\langle ij \rangle\rangle \sigma} \left(c_{i\sigma}^\dagger c_{j\sigma} + c_{j\sigma}^\dagger c_{i\sigma} \right) + U \sum_i \left(n_{i\uparrow} - \frac{1}{2} \right)\left(n_{i\downarrow} - \frac{1}{2} \right)$$

$$(5.1)$$

where t and t' model two types of bonds: ones which are the nearest-neighbours bonds of the original, full square lattice (t), and ones which connect through the diagonal rows of removed sites, and which were next-nearest neighbours of the original lattice (t'); see Fig. 5.1. For $U \to \infty$, the Hubbard Hamiltonian can be mapped into the Heisenberg model using second order pertubation theory in the hopping parameters t and t',

$$\mathcal{H} = J \left[\sum_{\langle ij \rangle} \vec{S}_i \cdot \vec{S}_j + g \sum_{\langle\langle ij \rangle\rangle} \vec{S}_i \cdot \vec{S}_j \right], \qquad (5.2)$$
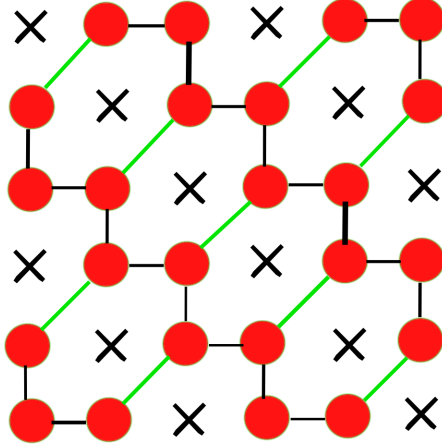
Figure 5.1: The one-third depleted square lattice. A regular array of black crosses is removed, leaving the red site structure. We will assume two types of bonds exist: connections between nn (black)[t or J] and nnn (green) [t' or J'] sites of the original square geometry.

with exchange constants J and gJ on the two types of bonds of Fig. 5.1, such that $t'/t = \sqrt{gJ/J}$. Similarly to the square lattice, this structure remains bipartite, a fact that has consequences to antiferromagnetic (AFM) order without frustration, and also to the abscence of a sign problem in quantum Monte Carlo (QMC) simulations. For $t = t'$, or $J = gJ$, the 1/3-depleted lattice is equivalent to the Honeycomb lattice. In this case, the AFM long-ranged order emerges at half-filling for a finite value of U, $U_c \approx 3.87$ [64], [65], which is in constrast with the regular square lattice, where AFM occurs at infinitesimal values of U at $T = 0$, due to the van Hove singularity and the nesting of the Fermi surface; see Appendix A. Furthermore, in the Heisenberg limit, a finite value is obtained for the AFM order parameter, $m \approx 0.26$ [66].

Here we investigate the onset of long-ranged AFM order on the the half-filled 1/3-depleted lattice considering $t \neq t'$, and $J \neq gJ$, in both the Hubbard and the Heisenberg regimes, respectively. The properties of the Hubbard model were obtained using determinant quantum Monte Carlo (DQMC) method; these calculations were performed in collaboration with the first author of Ref. [4]. The Heisenberg Hamiltonian, Eq. (5.2),

was treated within linear spin wave theory (LSWT); see Appendix C, and the stochastic series expansion (SSE) QMC. In what follows we summarize our findings, while a detailed presentation of the results can be found in Appendix E.

Figure 5.2 (a) shows the AF order parameter (obtained with the aid of finite size scaling) as a function of the coupling g. The order parameter first increases with g, reaching a maximum at the honeycomb limit $g = 1$, and then decreasing. Long-ranged AFM vanishes above a critical g_c; QMC gives $g_c = 1.75 \pm 0.01$, and LSWT greatly overestimates the persistence of LRAFO at large g [4]. We estabilished a phase diagram
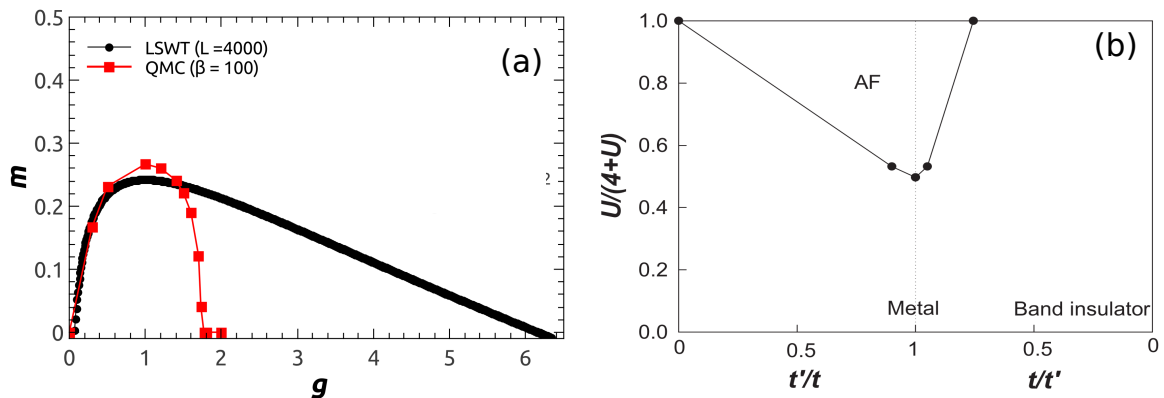
Figure 5.2: (a) AF oder parameter obtained with SSE and LSWT. The SSE results were obtained with the aid of finite size scaling. With LSWT(SSE), long-ranged AFM disappears above $g_c = 6.20 \pm 0.02(1.75 \pm 0.01)$. (b) Phase diagram. The $U \to \infty$ Heisenberg limit is along the top of the figure, $U/(4 + U) = 1$, and is extracted from the data of (a). For $U = 0$, the system is a band insulator for $t/t' > 0.5$, and a semi-metal otherwise.

showing the region in the parameters space $(t'/t, U)$ where the long-ranged AFM phase is present, see Fig. 5.2 (b). The critical interaction $U_c \approx 3.87$ for the isotropic honeycomb lattice, $t = t'$ was shown to increase with anisotropy, $t \neq t'$.

Chapter 6

Fermionic atoms in a two-dimensional optical lattice

One motivation of the experiments with optical lattice is to emulate the Fermionic Hubbard model. The realization of the Mott state in a 3D optical lattice (OL) was the first step in this direction [8], [9].

6.1 Optical Lattice Hubbard Model

We consider the OL Hubbard model (HM):

$$
\mathcal{H} = -\sum_{\langle \mathbf{i},\mathbf{j} \rangle,\sigma} t_{\mathbf{i}\mathbf{j}} \left(c_{\mathbf{i}\sigma}^{\dagger} c_{\mathbf{j}\sigma} + h.c. \right) + U \sum_{\mathbf{i}} (n_{\mathbf{i}\uparrow} - 1/2)(n_{\mathbf{i}\downarrow} - 1/2)
$$
$$
- \sum_{\mathbf{i}} (\mu_0 - V_t r_{\mathbf{i}}^2)(n_{\mathbf{i}\uparrow} + n_{\mathbf{i}\downarrow}), \tag{6.1}
$$

where $\mathbf{i}$ runs over the N_s sites of a square lattice, the spin state is $\sigma = \uparrow$ or $\downarrow$, and $n_{\mathbf{i}\sigma} = c_{\mathbf{i}\sigma}^{\dagger} c_{\mathbf{i}\sigma}$; $t_{\mathbf{i}\mathbf{j}}$ is the hopping integral between sites $\mathbf{i}$ and $\mathbf{j}$, U is the magnitude of the on-site repulsion, μ_0 is the (bare) chemical potential. In addition, we also considered a harmonic trap term, V_t, which measures the trap curvature, and $r_{\mathbf{i}}$ measures the distance of site $\mathbf{i}$ to the center of the trap. The physical meaning of each term of the Hamiltonian is illustrated in Fig. 6.1. An important aspect is that t, U, and V_t can be tuned in the experiments. The lattice depth, V_0, is controlled by the laser intensity, and tunes

the tunneling rate between lattice sites, t. The interaction U between two atoms on the same site corresponds to an s-wave scattering, whose scattering lenght a can be tuned by exploring Feshbach resonances [67]. The harmonic trap curvature V_t is produced either by the optical lattice beams or by an additional magnetic trap [68], [9].
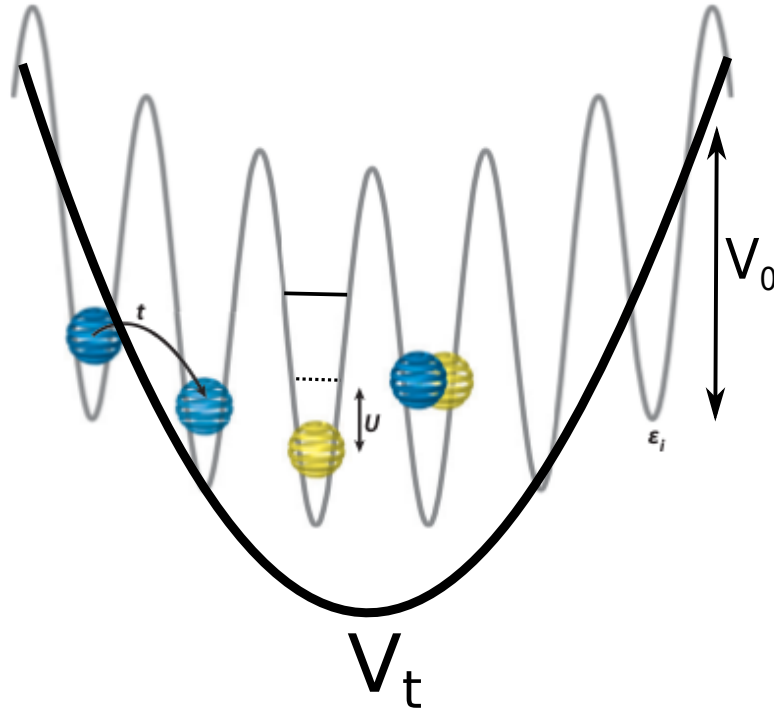
Figure 6.1: Schematic picture for the basic physical ingredients of OL experiments. The circles represent fermionic atoms (e.g., ^{40}K and ^{6}Li). Each color is associated to a different hyperfine state (spin). Tunneling between nearest neighbour sites is controlled by t. The on-site interaction between atoms with different spins, U. V_t is a measure of the trap opening. Due to the presence of the trap, each site has an on-site energy ϵ_i. The depth of each potential well V_0. In the Hubbard regime just the lowest band is accessed; transitions to excited states are unlikely. The figure was extracted from Ref. [68].

An important consequence of the confinement is that different phases can coexixt within the trap. For instance, a Mott region in the center (Mott core) can coexist with a mettallic region in the wings of the trap [8]. Experimentally, the Mott phases can be detected by global measurements, such as the global compressibility, which probes the response of the system to a change in external confinement. Here the harmonic trap is taken care of through the local-density approximation (LDA), and the homogeneous 2D

HM was solved using the TABC method.

6.1.1   Local Density Approximation (LDA)

In the LDA we consider that the value of a specific quantity (e.g., local density, $n(\mathbf{r})$) in a specific position $\mathbf{r}$ of the trap is given by

$$n(r) \rightarrow n_{hom}[\mu(r)], \tag{6.2}$$

where $n_{hom}[\mu]$ is the local density obtained by solving the 2D homogeneous Hubbard model; see Fig. 2.3 in Section 2.3. $\mu(r)$ is given by

$$\mu(r) = \mu_0 - V_t r^2, \tag{6.3}$$

and,

$$r = \sqrt{\frac{\mu_0 - \mu}{V_t}}. \tag{6.4}$$

Furthermore, for a 2D trap the number of particles is given by

$$N = \int_0^\infty n_{hom}(r) d^2 r. \tag{6.5}$$

Considering Eq. (6.4) and by changing the variable $(r \rightarrow \mu)$ in the integral, we obtain

$$N = \frac{\pi}{V_t} \int_{-\infty}^{\mu_0} n_{hom}(\mu) d\mu. \tag{6.6}$$

Within the LDA, the value of μ_0 defines the number of particles within the trap. In the LDA implementation we choose a specific value of N and trap oppening V_t and then obtain μ_0. With μ_0 at hands we are able to obtain the density profile across the trap using Eq. (6.2), for any configuration of N, V_t, and U. It is important to note that within the LDA μ_0 is a function of NV_t. This fact motivates us to define the effective density, $\rho \sim NV_t$ (see below).

In what follows we summarize our findings, while a detailed presentation of the results can be found in Appendix F. Our main result is that the use of experimentally accessible global quantities, such as compressibility and (derivative of) average double occupancy, can be used to map out local phases and phase separation. In a two dimensional OL the Mott phase appears with two shapes: Mott core and Mott ring. We show in Fig. 6.2 a phase diagram highlighting the regions in parameter space in which Mott rings and Mott core are formed. We analysed our results in terms of an effective density $\rho \sim NV_t$ (N
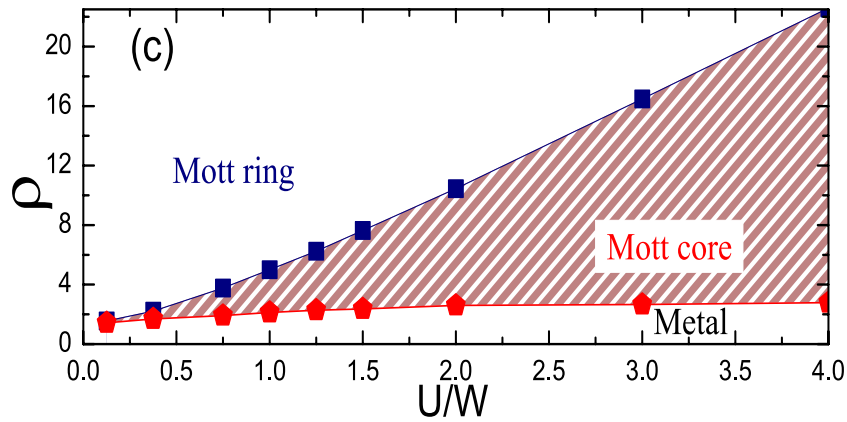
Figure 6.2: Phase diagram in ρ and U/W parameter space. $\rho = NV_t/4t$ is the effective atomic density, and $W = 8t$ is the bandwidth. 'Metal" designates a phase in which the whole trap is in a metallic state. The red and blue lines are $\rho_c(U/W)$ and $\rho_c(U/W)$, respectively, see text

is the number of atoms in the atomic cloud). One important result, is that as the trap narrows, a Mott core forms at some value of the effective density, ρ_c, which, upon further narrowing, becomes a Mott ring at ρ_m, see Fig. 6.2. Furthermore, the fraction of atoms in a Mott state displays a maximum at the ring-core transition, ρ_m. We believe the results presented in this work should be important for the experimental control of the Mott state in a two-dimensional OL.

Before closing this Chapter, it is worth mentioning here two important advances in OL experiments which occured after the conclusion of our work (2015): (i) The possibility of detecting and controlling fermionic optical lattice systems at the level of single sites and single particles in two-dimensional OL [69], [70]. We show in Fig. 6.3 a single-
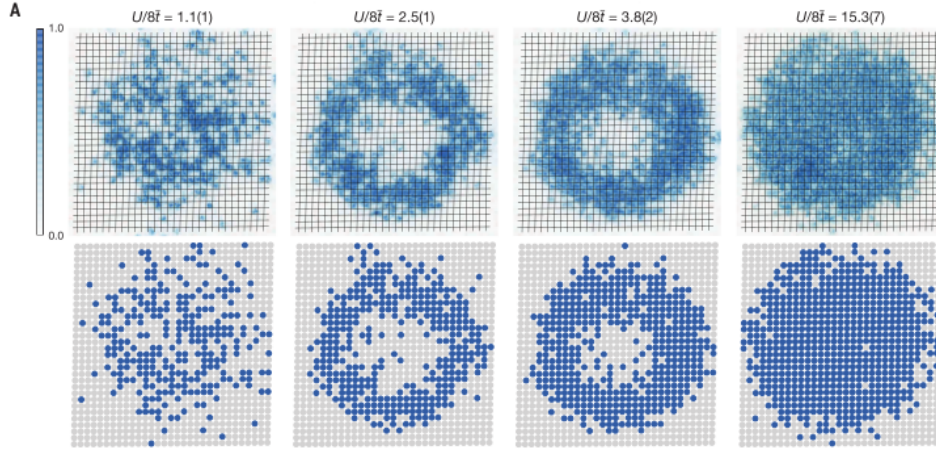
Figure 6.3: Site-resolved images of Mott ring and Mott core in a two-dimensional OL [69]. Bright points correspond to the flourescence image of singly occupied sites. The occupation of every site is determined as unity for single particle of either spin and zero for the case of an empty sites or doubly occupied site. The images of the atoms in the square-lattice are shown for varying interactions U/W; where $W = 8\bar{t}$ is the bandwidth. For the weakest interactions ($U/W = 1.1(1)$) it is observer a purely mettalic state. For intermediate interactions ($U/W = 2.5(1)$ and $U/W = 3.8(2)$) a Mott ring structure is observed, where mettalic, Mott insulator, and band insulator core phases coexist. Finally, for the strongest interactions ($U/W = 15.3(7)$) a large Mott core is observed.

site resolution image of the formation of Mott ring and Mott cores regions as the on-site interaction is increased. This result is in line with those obtained in our work [16]. (ii) The second advance was the observation of antiferromagnetic correlations [71]. It is already possible to achieve temperatures at which the AFM correlation length is larger than the OL size [72], which can be considered a long-ranged AFM state. Current experiments are trying to analyse the properties of the system near half-filling, aiming to answer open questions about the doped HM, such as the presence or not of a superconducting ground state.

Chapter 7

Metal-insulator transitions in the extended Hubbard model

The metal-insulator (MIT) transitions induced by doping with holes a Mott insulator (Mott transition) has attracted a significant amount of interest in recent years. One of the main reasons for the continuing interest is the emergence of high temperature super-conductivity upon doping an insulating Néel state in cuprate materials [18]. The Hubbard Model is considered to be the simplest model that accounts for the Mott transition, in the sense that just the on-site electron-electron repulsion U is needed. In this case, the undoped phase at half-filling is characterized by gapless spin and gapped charge excitations. One important aspect of the Mott transition described by the HM is that doping induces a redistribution of spectral weight in the density of states (DOS), and low energy states are created at the Fermi level [73],[74],[20], [75]. An important result obtained for the HM is that this low energy spectral weight *per spin* at the Fermi level, W_{FL}, satisfies the inequality $W_{FL} \geq \delta_h$ [73], where $\delta_h = 1 - N_e/N_s$ is the hole concentration (a simple explanation for this result will be given below). For comparison, one should note that within a rigid band description of a band insulator, doping simply causes a shift in the chemical potential, with the occupation of one particle per spin channel, leading to $W_{FL} = \delta_h/2$.

On the other hand, the inclusion of a nearest-neighbour interaction V leads to the

Extended Hubbard Model (EHM); V is known to induce fundamental changes in the ground state properties of the system, whose phase diagram of the one dimension has been intensively studied both at quarter and half-filling [76], [77], [78], [79], [80]. At half-filling, the ground state displays two insulating phases: (i) a spin density wave (SDW) with gapless spin and gapped charge excitations, and (ii) a charge density wave (CDW) with both spin and charge gapped excitations; see the phase diagram in Fig. 7.1 (a). A bond-order wave (BOW) also appears in a narrow region of the phase diagram between the SDW-CDW transition. The BOW phase is characterized by alternating strengths of the kinetic-energy on the bonds of the chain [79], [81]; this phase will not be explored here. By contrast, at quarter filling the ground state displays a MIT induced by U or V [76], [80]. The insulating phase exhibits a long-range-ordered CDW, but, unlike the half-filled case, the CDW phase has gapless spin excitations; see the phase diagram in Fig. 7.1 (b).
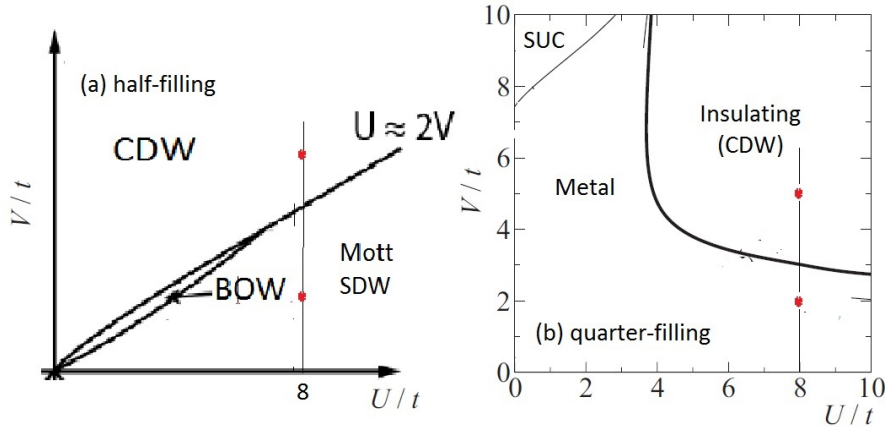
Figure 7.1: Schematic phase diagram of the one-dimensional extended Hubbard model at (a) half-filling and (b) quarter-filling. Red points mark the regions of the phase diagram which will be explored in the present work. In panel (b), a phase displaying dominant superconducting fluctuations (SUC) is shown for completeness [76] but will not be explored here.

The 1D EHM is believed to be a minimal model for some quasi-one-dimensional Mott insulators, such as the cuprate compounds $SrCuO_2$ and Sr_2CuO_3. In this sense, the

renewed interest in the 1D EHM was motivated by the experimental observation of the phenomenon of spin-charge separation through angle-resolved photon emission (ARPES) in $SrCuO_2$. In these experiments it was found that the low energy electronic excitations split into holon and spinon bands; the bandwidth of the former scales with the electronic hopping energy, t, while the bandwidth of the latter scales with the magnetic exchange coupling, J [35], [82]. From the theoretical side, the spectral properties of the 1D EHM has been investigated at half-filling [83], where evidence of spin-charge separation was found in the SDW phase, but not in the CDW phase [84]. As one dopes away from half-filling, the 1D EHM undergoes two density-driven MIT's [75], [79]: (a) one from a Mott SDW to a metal; and (b) one from a CDW to a metal. For the latter it was argued that, differently from the Mott transition, the spectral weight induced upon doping may follow $W_{FL} \approx \delta_h/2$, and that the MIT is well described by a rigid-band picture [85]; however, no attempt to provide a quantitative prediction for the low-energy spectral weight transfer, W_{FL}, has been advanced.

In order to bridge this gap, here we study the spectral properties of the 1D EHM. We focus on two main issues: (1) At half-filling we revisit the issue of spin-charge separation, and obtain the momentum occupation function for different values of V; see Section 7.2. (2) Away from half-filling we characterized the MIT's by analysing the evolution of the DOS with doping between quarter and half-filling; see the red points in Fig. 7.1 and Section 7.3. But first, in Section 7.1, we describe the EHM and some ground state properties at quarter and half-filling, and we also show the quantities considered here. In Section 7.4 we present our conclusions.

7.1   Model and Methods

The Hamiltonian of the Extended Hubbard Model (EHM) is given by

$$\mathcal{H} = - \sum_{\langle i,j \rangle, \sigma} t_{i,j} \left(c_{i\sigma}^{\dagger} c_{j\sigma} + h.c. \right) + U \sum_i \left(n_{i\uparrow} - \frac{1}{2} \right) \left(n_{i\downarrow} - \frac{1}{2} \right)$$
$$+ \frac{V}{2} \sum_{\langle i,j \rangle} \left(n_i - 1 \right) \left(n_j - 1 \right) - \mu \sum_i n_i, \tag{7.1}$$

where i runs over the N_s sites of the chain, the spin state is $\sigma = \uparrow, \downarrow$, $n_{\mathbf{i}\sigma} = c_{\mathbf{i}\sigma}^{\dagger} c_{\mathbf{i}\sigma}$, and $n_{\mathbf{i}} = n_{\mathbf{i}\uparrow} + n_{\mathbf{i}\downarrow}$; $t_{i,j}$ is the hopping integral between nearest-neighbour sites i and j, U and V are the strengths of the on-site and nearest-neighbour interactions, respectively, and μ is the chemical potential. Here we consider repulsive interactions, $U \geq 0$ and $V \geq 0$. The EHM Hamiltonian written as in Eq. (7.1) is manifestly particle-hole symmetric. We use the Lanczos method for chains up to $N_s = 12$ with twisted boundary conditions (TBC), in the sense that whenever a fermion hops between two adjacent copies of the chain, the hopping term picks up a phase, $t_{i,j} = e^{i\phi}$; otherwise $t_{i,j} = t$

Here we focus on the two insulating phases described by the 1D EHM at half-filling: (i) a Mott insulator with a spin-density-wave (SDW), and (ii) a charge density wave (CDW). One can qualitatively characterize these phases in the strong coupling limit, $V, U \gg t$. In this regime, the boundary between CDW-SDW is given by $U = 2V$.

- For $U > 2V$, doubly occupied sites are avoided and the ground state is dominated by a SDW configuration:

$$|\psi_0\rangle \approx \frac{1}{\sqrt{2}} \left(| \uparrow_1, \downarrow_2, \uparrow_3, ..., \uparrow_{L-1}, \downarrow_L \rangle - | \downarrow_1, \uparrow_2, \downarrow_3, ..., \downarrow_{L-1}, \uparrow_L \rangle \right). \tag{7.2}$$

The average occupation of each site is equal to one. To second order perturbation theory there is an effective AF interaction between spins given by $J_{eff} = 4t^2/(U-V)$. In 1D, due to quantum fluctuations no true long-ranged AFM phase is formed. In this case the SDW phase is characterized by a power-law decay of the spin-spin

correlations:

$$C_{spin}(r) = \left\langle S_i^z S_{i+r}^z \right\rangle, \tag{7.3}$$

where $S_i^z = (n_{i,\uparrow} - n_{i,\downarrow})$ is the spin operator.

- On the other hand, for $2V > U$, configurations with singly occupied sites are avoided due to the Coulomb repulsion V, and the ground state is dominated by a CDW configuration:

$$|\psi_0\rangle \approx \frac{1}{\sqrt{2}} \left(|\uparrow\downarrow_1, 0_2, \uparrow\downarrow_3, ..., \uparrow\downarrow_{L-1}, 0_L\rangle + |0_1, \uparrow\downarrow_2, 0_3, ..., 0_{L-1}, \uparrow\downarrow_L\rangle \right). \tag{7.4}$$

Doubly occupied sites alternate with empty sites. In this case, a discrete Ising symmetry is broken, and a true CDW long-range ordered is formed at $T = 0$ in 1D [77]. The CDW phase is characterized by a long-ranged charge-charge correlation function:

$$C_{charge}(r) = \langle n_i n_{i+r} \rangle - \langle n_i \rangle^2. \tag{7.5}$$

Away from the strong coupling regime the position of the CDW-SDW transition was obtained for different values of U. For $U = 8t$, $V_c = 4.14t$ [77], [84]. Furthermore, there is a consensus that for $U < U_m \approx 5$ a BOW phase arises in a narrow region between the CDW-SDW transitions [79], [81], [77].

At quarter filling, for $U \to \infty$ the EHM is equivalent to a half-filled spinless fermion model which, upon increasing V from zero, undergoes a MIT to a CDW insulator at $V = 2t$ [80].

- In the regime $V, U \gg t$, doubly occupied sites and configurations with parallel spins electrons are avoided due to the Coulomb repulsion, and the ground state is dominated by a CDW configuration:

$$\begin{aligned} |\psi_0\rangle \approx \frac{1}{2} \ &\left(|\uparrow_1, 0_2, \downarrow_3, 0_4, ..., \downarrow_{L-1}, 0_L\rangle - |\downarrow_1, 0_2, \uparrow_3, 0_4, ..., \uparrow_{L-1}, 0_L\rangle \right. \\ + \ &\left. |0_1, \uparrow_2, 0_3, \downarrow_4, ..., 0_{L-1}, \downarrow_L\rangle - |0_1, \downarrow_2, 0_3, \uparrow_4, ..., 0_{L-1}, \uparrow_L\rangle \right). \end{aligned} \tag{7.6}$$

In this case, singly occupied sites alternate with empty sites.

Here we investigate the spectral properties of the EHM between quarter and half-filling. The quantity of interest here is the single particle spectral function:

$$A^-(k, \omega < 0, \phi_i) = \sum_n |\langle \psi_n | c_{k,\sigma} | \psi_0 \rangle|^2 \delta[\omega - (E_0(\phi_i) - E_n(\phi_i))],$$

$$A^+(k, \omega > 0, \phi_i) = \sum_n |\langle \psi_n | c_{k,\sigma}^\dagger | \psi_0 \rangle|^2 \delta[\omega + (E_0(\phi_i) - E_n(\phi_i))] \quad (7.7)$$

where $|\psi_0\rangle$ and $|\psi_n\rangle$ respectively denote the ground state with energy E_0 and the excited state with energy E_n, $c_{k,\sigma}^\dagger$ creates a particle with momentum k and spin σ, and ϕ_i is the specified TBC. In ARPES experiments, high energy photons knock electrons out of the material, and their energy and momentum are measured; the quantity $A^-(k, \omega)$ is proportional to the measured intensity obtained in these experiments [86]. On the other hand, $A^+(k, \omega)$ is measured in inverse photonemission experiments (IPES) [86]. The single-particle spectral functions, $A^-(k, \omega)$ and $A^+(k, \omega)$, probe photonemission (PES) and inverse photonemission (IPES) processes [18], [20].

We also obtain the momentum occupation function

$$n_\sigma(k) = \int_{-\infty}^{\mu} A(k, \omega, \phi_i) d\omega, \quad (7.8)$$

and the density of states (DOS),

$$N^\pm(\omega) = \frac{1}{N_s N_r} \sum_{k,i} A^\pm(k, \omega, \phi_i). \quad (7.9)$$

The DOS is calculated performing an average over $N_r = 30 - 100$ realizations of TBC, ϕ_i. $N^-(\omega)$ and $N^+(\omega)$ represent the density of unoccupied (PES) and occupied (IPES) states, respectively.

7.2 Half-filling

The single-particle spectral function $A^-(k, \omega)$ of the the 1d EHM at half-filling has been investigated previously using DMRG [83] and a variational cluster pertubation theory approach [84]. Here we revisit these results using the Lanczos method with a set of
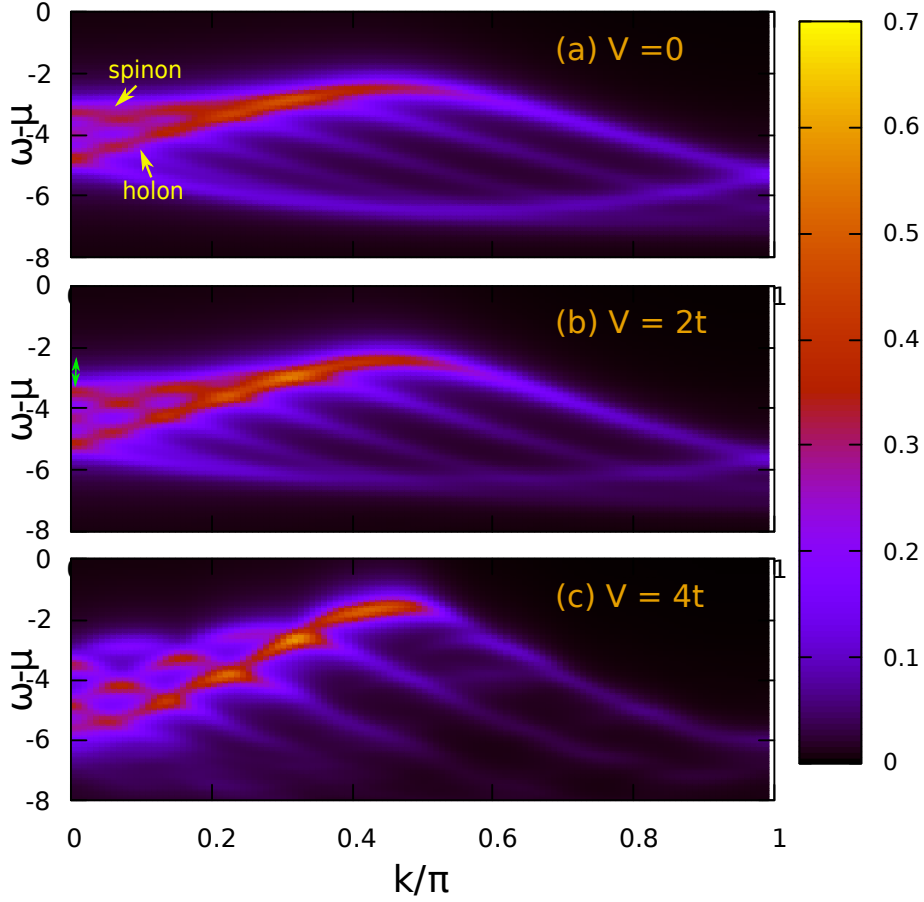
Figure 7.2: Color plot of the single-particle spectral function $A(k,\omega)$ at half-filling for $U = 8t$. We considered a chain with $N_s = 12$ sites and $N_r = 20$ realizations of TBC. The ground state is in the SDW phase. $V < V_c = 4.14t$ [77]. (a) HM ($V = 0$); the arrows indicates the spinon and holon branches. (b) $V = 2t$; the green arrow at $k = 0$ indicates the width of the spinon band. (c) $V = 4t$.

$N_r = 20$ realizations of TBC. We also investigate the behaviour with V of the momentum occupation function, $n_\sigma(k)$, which has not been previously discussed, and present results of the DOS.

The PES $A^-(k,\omega)$ is a standard probe for spin-charge separation in low dimensional systems [35], [82]: it corresponds to the decomposition of a single electronic excitation (e.g., $c_{k,\sigma}|\psi_0\rangle$) into two independent excitations carrying either spin (spinon) or charge (holon). The color plot of $A^-(k,\omega)$ for the 1D EHM obtained with the Lanczos method for different values of V is shown in Fig. 7.2; the Fermi level is at $\omega - \mu = 0$. Let us

first discuss the results for the 1D HM, Fig. 7.2 (a). The predominant spectral weight occurs for $k/\pi \leq 1/2$, and within the energy range $-5t \leq \omega - \mu \leq -2t$. Due to the finite charge gap at half-filling, the lowest energy spectral weight (in relation to the Fermi level), has a finite energy, $\omega \approx -2t$, and is carried by the mode $k/\pi = 1/2$. Furthemore, an important result of the 1D HM is the splitting of the spectral weight of $A^-(k, \omega)$ into two predominant branches, whithin the range $0 \leq k \leq \pi/2$ (these branches are marked by arrows in Fig. 7.2 (a)) [32], [33]. A comparision with the exact Bethe ansatz solution of the 1D HM allows one to recognize these branches as spinon and holon bands; see Ref. [23]. In Fig. 7.2 (a), the bandwidth of spinon and holon bands can be obtained at $k = 0$, $\omega_{spinon} - 2t$ and $\omega_{holon} - 2t$; the former scales with the effective exchange, $J_{eff} = 4t^2/U$, while the latter scales with the hopping energy, $2t$ [34]. Thus the single-particle excitations of the 1D HM are charaterized by these two energy scales $J_{eff} = 4t^2/U$ and $2t$, which is a signature of spin-charge separation [35]. In order to get an intuitive idea of the spin-charge separation in the 1D HM, we illustrate in Fig. 7.3 the propagation of a single hole in a SDW background.

An examination of Fig. 7.2 (b) indicates that for $V = 2t$, $A^-(k, \omega)$ exhibits the same qualitative behaviour as for the HM, namely the signature of spin-charge separation [84]. In this case, the bandwidth of spinon excitations is expected to be of the order of the effective exchange coupling $J_{eff} = 4t^2/(U - V)$ in the strong coupling regime $(U > 2V \gg t)$. The arrow at $k = 0$ in Fig. 7.2 (b) indicates the bandwidth of spinon excitations. We also analyse $A^-(k, \omega)$ for $V = 4t$ in Fig. 7.2 (c). Due to the proximity to the CDW-SDW transition, the FSE are more dramatic in this case; as a consequence, we observe discontinuities in $A^-(k, \omega)$. Nonetheless, one can still see the reminiscent splitting of the low energy spectral weight, which is a signature of spin-charge separation. Thus, as in Ref. [84], we conclude that spin-charge separation is present up to the transition point, V_c.

Now we consider a range of parameters such that the system is in the CDW phase;
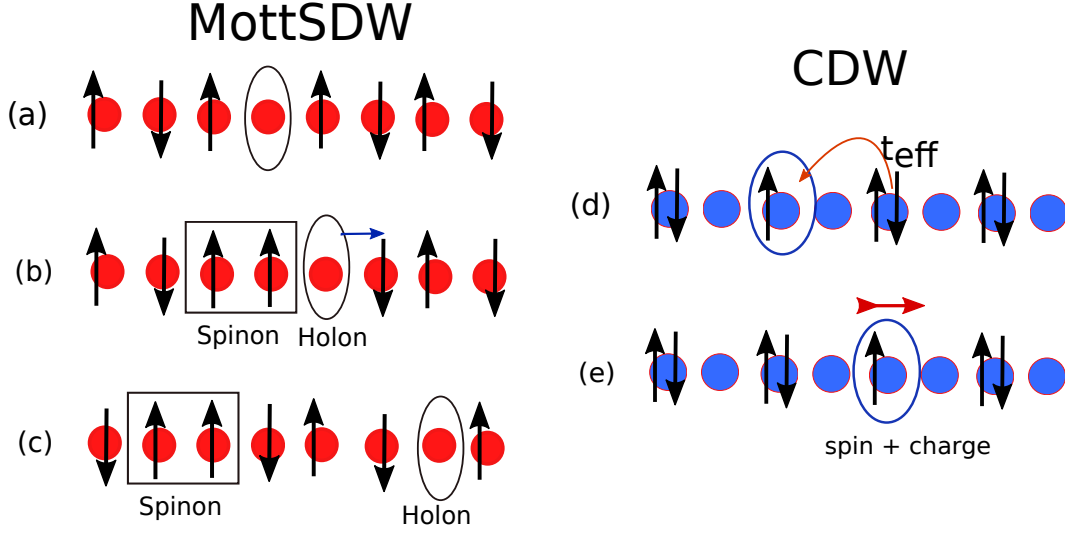
Figure 7.3: (a), (b) and (c) Schematic picture of hole propagation in the SDW background. A hole is created in the half-filled 1D HM. In (a) the hole is surrounded by two up spins. In (b) the hole propagates and a domain wall is formed. Now the hole is surrounded by one up and one down spin . In (c) the original configuration, a hole surrounded by two up spins has split into a hole surrounded by antiferromagnetically aligned spins ('holon') and a domain-wall like configuration, two adjacent up spins, which contain an excess spin $1/2$ with respect to the initial antiferromagnet ('spinon'). (d) and (e) Hole propagation in the CDW background. Hole propagates through second neighbour sites and carries spin and charge degrees of freedom, see text. No spin-charge separation takes place in this case.

see Figs. 7.4. The behaviour of $A^-(k,\omega)$ is qualitatively different from the one found for the SDW phase. In this case, the charge gap also opens at $k = \pi/2$. Nevertheless, the low energy spectral weight of $A^-(k,\omega)$ is characterized by a single band, and no signature of spin-charge separation is observed [84]. Comparing Figs. 7.4 (a), (b), and (c) we see that the effect of increasing V is to decrease the width of the the low-energy band, and to spread out the spectral weight for modes with $k > \pi/2$. Furthermore, the higher energy spectral weight is suppressed with V.

In order to gain insight into the nature of the low-energy excitations in the CDW phase we consider second order perturbation theory for a system with a single hole. Treating the hopping term of Eq. (7.1) as a pertubation, we obtain the following effective Hamiltonian
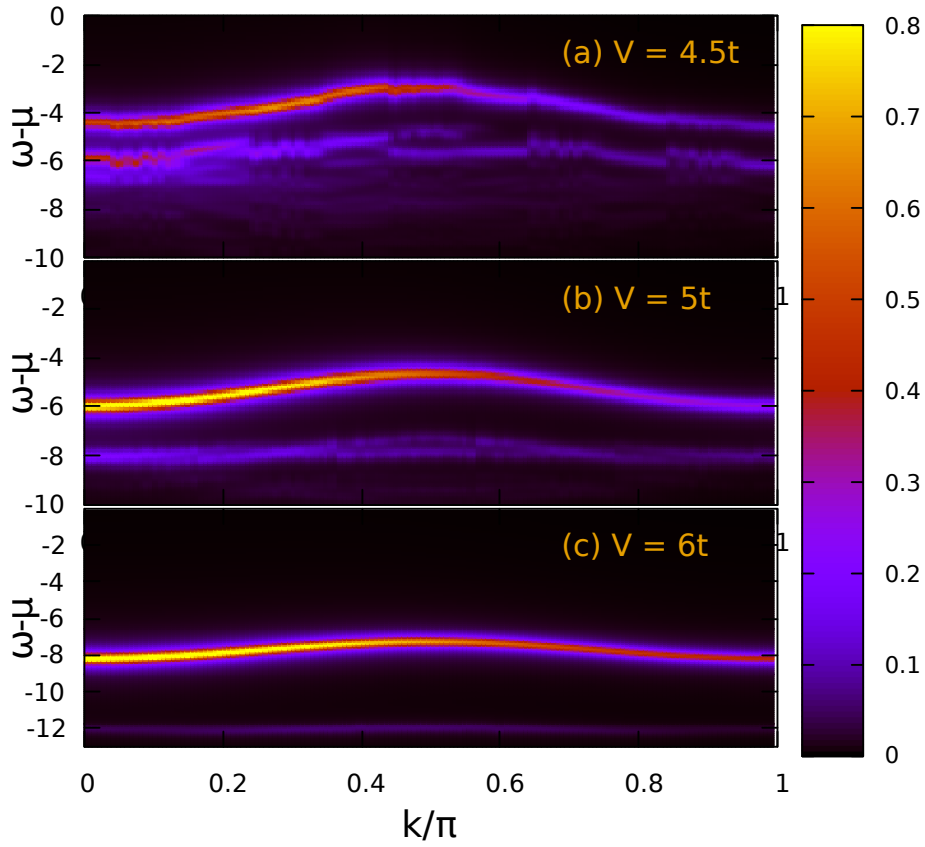
Figure 7.4: Same parameters of Fig. 7.2 The ground state is in the CDW phase. $V > V_c = 4.14t$ [77]. (a) $V = 4.5t$, (b) $V = 5t$; (c) $V = 6t$.

up to second order

$$\mathcal{H}_{eff} = E_0^{(0)} + t_{eff} \sum_{i,\sigma} c_{i,\sigma}^\dagger c_{i+2,\sigma}, \tag{7.10}$$

where i runs over the N_s sites of the chains, $E_0^{(0)}$ is the zeroth order energy of the system, and $t_{eff} = t^2/(2V - U)$. This Hamiltonian describes hopping between second-neighbour sites; thus the dispersion relation of a single hole is given by

$$\epsilon^{hole}(k) = - \left(\frac{\Delta_c}{2} + 2t_{eff} \cos(2k) \right), \tag{7.11}$$

where $\Delta_c = 4V - U$ is the charge gap obtained in the atomic limit ($t = 0$). The low energy spectral weight of $A^-(k,\omega)$ shown in Fig. 7.4 (c) ($V = 6t$) is well described by this dispersion relation [85]. In Figs. 7.4 (b) and (c), both the charge gap and the bandwidth of the low energy spectral weight of $A^-(k,\omega)$ are overestimated by Eq. (7.11), which indicates that the system deviates from the strong coupling regime as V appoaches V_c. Nevertheless, even in these cases the low energy spectral weight of $A^-(k,\omega)$ is described by a single holon band, and no signature of spin-charge separation is observed. Figures 7.3 (d) and (e) give an intuitive picture for the PES lowest energy excitations in the CDW phase: an electron hops between second neighbour sites through a second order process, and, in effect, a hole moves carrying both charge and spin degrees of freedom.

Now let us discuss the momentum occupation function, $n_\sigma(k)$, in the 1d EHM. It is worth pointing out that the function $n_\sigma(k)$ is equal to the total spectral weight of the mode with momentum k; see Eq. (7.8). In Figs. 7.5 (a) and (b) we show $n_\sigma(k)$ for $U = 4t$ and $U = 8t$, respectively, and for different values of V. At $k = k_F = \pi/2$, due to the particle-hole symmetry relation $n_\sigma(k) = 1 - n_\sigma(k + \pi)$, $n_\sigma(k) = 1/2$ for all cases considered. For $k \neq k_F$, we note that $n_\sigma(k)$ is a nonmonotonic function of V. For $k < \pi/2$, $n_\sigma(k)$ increases with V in the SDW phase ($V < V_c$), while it decreases with V in the CDW phase ($V > V_c$). This result can be related to the behaviour of $A^-(k,\omega)$ shown in Figs. 7.2 and 7.4. In the SDW phase ($V = 0$ and $V = 2t$), due to the spin-charge separation
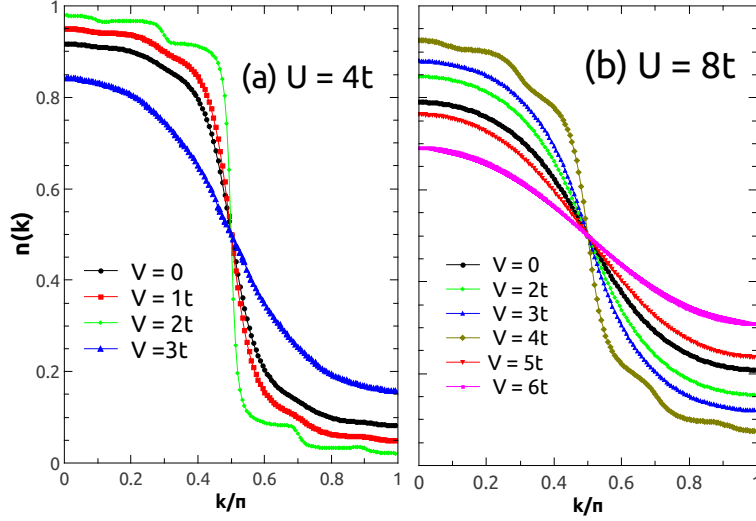
Figure 7.5: Momentum occupation function $n(k)$ for the 1d EHM. We considered a chain with $N_s = 12$ sites and $N_r = 20$ realizations of TBC. (a) $U = 4t$ (b) U = 8t, and different values of V.

the predominant spectral weight occurs for $k \leq \pi/2$. On the other hand, in the CDW phase ($V = 5t$ and $V = 6t$) the spectral weight spreads out to modes with $k > \pi/2$.

The nonmonoticity of $n_\sigma(k)$ with V is well illustrated by the graph of $n_\sigma(k = 0)$ as a function of V; see Fig. 7.6. The first-neighbour spin and charge correlation functions are C_{spin} and C_{charge}, respectively. For $U = 8t$, DMRG results indicate that there is a first order SDW-CDW transition at $V_c = 4.14t$ [77]. The transition is signalled in Fig. 7.6 (b) by an abrupt change in C_{spin} and C_{charge} at $V = 4.1$. The peak of $n_\sigma(k)$ coincides with the critical V_c. We conclude that $n_\sigma(k)$ can be used to pinpoint the first order SDW-CDW quantum phase transition. For $U = 4t$ there is consensus in the literature that there are two continous transitions in a narrow region of the $U - V$ phase diagram around $V \approx U/2$; SDW to BOW and BOW to CDW. For $U = 4t$, the system is in the BOW phase in the range $1.877t \leq V \leq 2.164t$ [81]. Figure 7.6 (a) shows that the behaviour of $n_\sigma(k)$ with V for $U = 4t$ resembles the one found for $U = 8t$: $n_\sigma(k)$ increases up to $V \approx 2.1$ and then starts to decrease with V as the system enters the CDW phase. Our result indicates that the peak of $n_\sigma(k = 0)$ is associated to the transition to the CDW phase. We have found
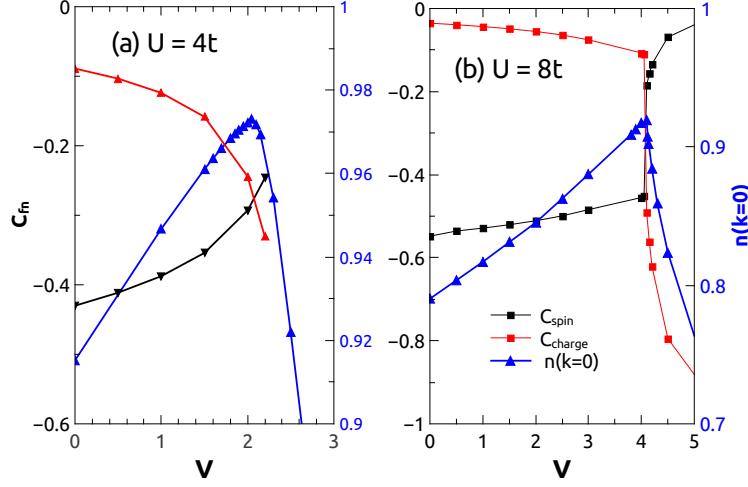
Figure 7.6: *Right axis*: First neighbour spin and charge correlation, C_{fn}^{spin} and C_{fn}^{charge}, respectively. *Left axis*: $n_\sigma(k = 0)$ as function of V. In this graph we considered $N_s = 12$. (a) $U = 4t$ (b) $U = 8t$ and differents values of V. For $U = 4t$ and $U = 8t$, $V_c = 2.15t$ and $V_c = 4.14$, respectively [77].

no signature for the SDW-BOW transition for $V \sim 1.8$. It is important to mention that, in order to investigate the BOW phase, larger systems are necessary; so DMRG studies of $n_\sigma(k)$ close to V_c are necessary to settle this issue for $U = 4t$.

We close this section showing the graph of the DOS for the 1D EHM with $U = 8t$ and $V = 2t$, and $U = 8t$ and $V = 5t$; see Fig. 7.7. In the SDW phase, the DOS splits into the so called upper Hubbard band and lower Hubbard band. Here we use the nomenclature lower band (LB) and upper band (UB). As in the SDW phase, for $U = 8t$ and $V = 5t$, a charge gap opens up and the DOS splits into LB and UB. In the next section we discuss the doping effect in the DOS.

7.3   Doped system

In this section we investigate the evolution of the DOS upon doping with holes away from half-filling. We define the fraction of hole doping as $\delta_h = 1 - N_e/N_s$. Here we focus on the two set of parameters ($U = 8t$, $V = 2t$) and ($U = 8t$, $V = 5t$), for which two kinds of Metal-inslutator transitions (MIT) are induced: (i) the Mott transition, and (b) CDW-
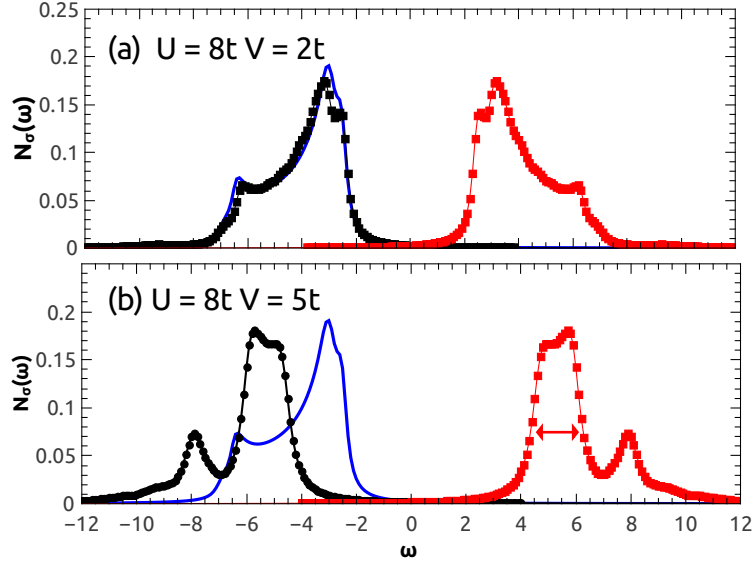
Figure 7.7: Density of occupied (black curve) and unoccupied (red curve) states for the half-filled 1D EHM obtained by integrating the single particle spectral function $A^-(k, \omega)$ shown in Fig. 7.2 (b) and Fig. 7.4 (b), respectively; see Eq. (7.9). (a) $U = 8t$ and $V = 2t$ (SDW phase); and (b) $U = 8t$ and $V = 5t$ (CDW phase). The CDW bandwidth is given by $\mathcal{W} \approx 4t_{eff} = 4t^2/(2V - U)$ (marked by the double arrow). For comparison we also show the DOS of the HM with $U = 8t$ (blue curve).

Metal transtion. Furthermore, a MIT takes place as one approaches the quarter-filling by increasing δ_h for $U = 8t$ and $V = 5t$ [80].

We can get a qualitative idea of the evolution of the DOS upon doping by analysing the EHM in the atomic limit ($t = 0$) in Eq. (7.1). The arguments presented here are inspired on Refs. [73], [85], [87]. First, we consider that the ground state is in the SDW phase, $U > 2V \gg t$; see Fig 7.8. At half-filling there are N occupied states in the LB, associated to singly occupied sites, and N unoccupied states in the UB, associated to doubly occupied sites; see Fig 7.8 (A1). These states are separated by an energy gap, $\Delta_c = U$. Let us now consider a hole-doped system, see Fig. 7.8 (B1). There are now $N - 1$ occupied states in the LB, and $N - 1$ unoccupied states in the UB. This leaves two states on the site with a missing electron; these two states lie at the Fermi level. Hence, the amount of low-energy spectral weight *per spin* induced by doping the half-filled SDW
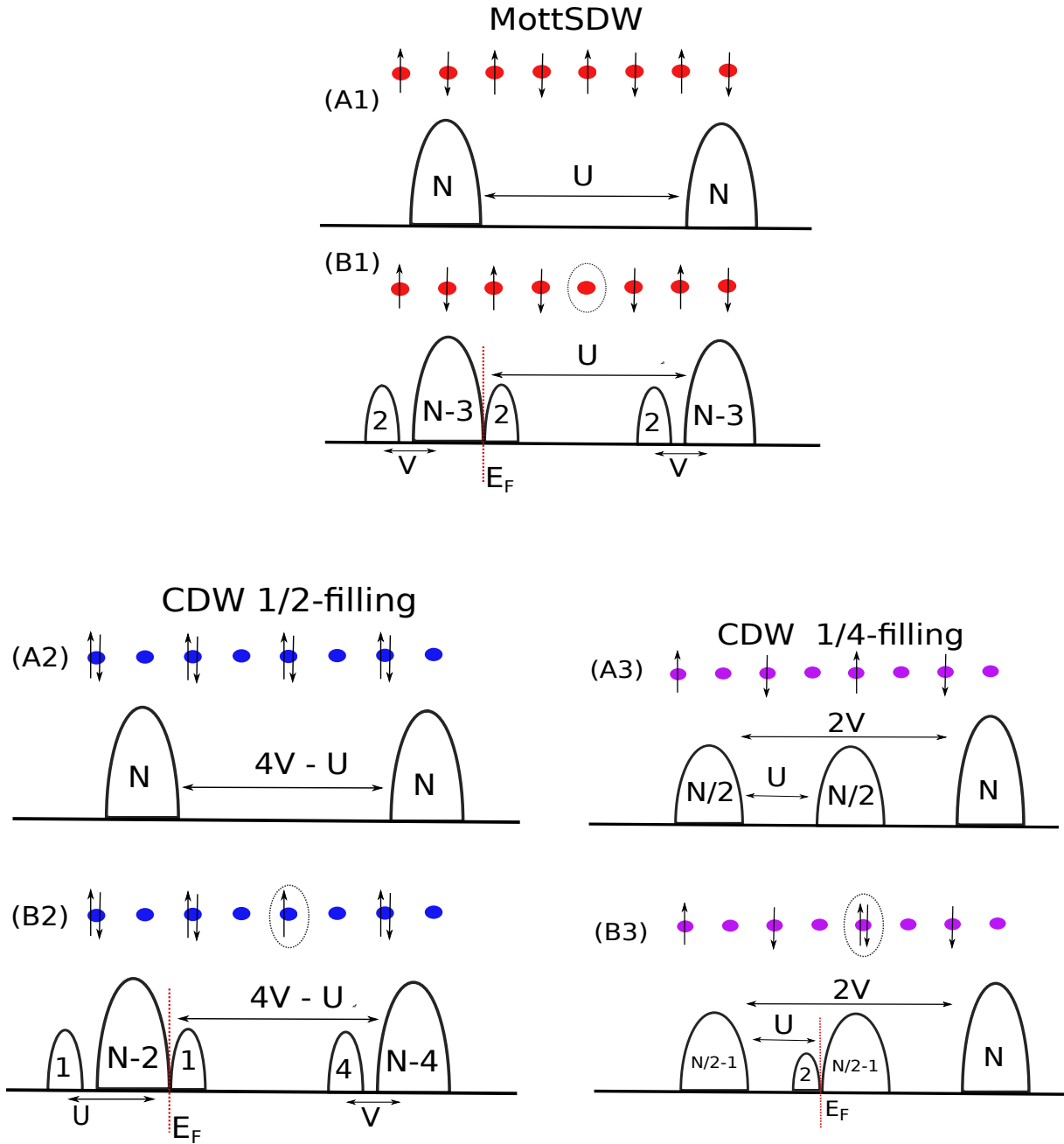
Figure 7.8: Spectral weight redistribution with doping in the atomic limit of the EHM($t = 0$). For $t = 0$ the bands are infinitely narrow; they have been broadened here strictly for effect. The Fermi level is marked by the red vertical line, or is in the midle of the gap. (A1) Half-filling in the MottSDW phase, and (B1) one hole doped system. (A2) Half-filling in the CDW phase, and (B2) one hole doped system. (A3) Quarter-filling in the CDW-phase, and (B3) one electron doped system; see text for explanation.

phase is given by $W_{FL} = \delta_h$. This argument shows that the effect of doping is to remove spectral weight from both the UB and LB and to create additional states at the Fermi level [20], [73], [75]. It is worth mentioning that this is in contrast to the rigid band description of a band insulator, in which case doping simply causes a shift in the chemical potential, with the occupation of one particle per spin channel, or $W_{FL} = \delta_h/2$.

Let us now consider the ground state in the CDW phase, i.e., $2V > U \gg t$ [85]. At half-filling there are N occuppied states associated with doubly occupied sites, and N unoccupied states associated with empty sites: a charge gap $\Delta_c = 4V - U$ opens up between the UB and the LB; see Fig. 7.8 (A2). The removal of one electron from half-filling leaves one site singly occupied. This state lies at the Fermi level. Thus, in the CDW phase, the amount of low energy spectral weight per spin is given by $W_{FL} = \delta_h/2$, which is in contrast with the Mott transition, for which a spectral weight $W_{FL} = \delta_h$ appears at the top of the LB. In this case, the states of the UB are not transferred to the Fermi level as in the Mott transition; see Fig. 7.8 (B2). Finally, we show in Figs. 7.8 (A3) and (B3) the DOS as the system approaches quarter filling. If we disregard the states separated by the LB by $2V$, the spectral weight redistribution with doping is equivalent to that for the HM [85]. Upon adding one electron to the system, two occupied states are created at the Fermi level; in this case, the low energy spectral weight induced by doping is given by $W_{FL} = \delta_h$.

We now discuss the results for the DOS obtained with the Lanczos + TABC method for $t \neq 0$. Figure 7.9 shows $N^-(\omega)$ (black curve) and $N^+(\omega)$ (red curve) versus $\omega - \mu$ in the SDW phase ($U = 8t$ and $V = 2t$) and for different values of δ_h; the Fermi level is at $\omega = 0$. The evolution of the DOS with doping in the SDW phase exhibits the same qualitative behaviour as for the HM [20], [73], [75]. At half-filling [Fig. 7.9 (a)] the Mott gap forms at the Fermi level and the DOS splits into a LB and an UB. Comparing Figs. 7.9 (a) and (b) we see that the effects of doping are to shift the upper edge of the LB to $\omega = 0$, and to create low energy states above the Fermi level. Further doping increases

Figure 7.9: $N^-(\omega)$ (black curve) and $N^+(\omega)$ (red curve) for $U = 8t$ and $V = 2t$ for different values of δ_h. $N_s = 8$ chain in the grand canonical ensemble. The density of holes is defined as $\delta_h = 1 - \langle n \rangle$, where $\langle n \rangle$ is the averaged particle density obtained with $N_r = 50$ realizations of TBC.

the amount of spectral weight transferred from the UB to just above the Fermi level; see Fig. 7.9 (c). It is important to note that the low energy states are created within the undoped gap; these states are called in-gap states [20], [75].

Figure 7.10 shows the evolution of $N^-(\omega)$ and $N^+(\omega)$ with doping in the CDW phase $(U = 8t, V = 5t)$. At half-filling a charge gap opens up at the Fermi level and the DOS splits into a LB and an UB; see Fig. 7.10 (a). Doping yields the DOS depicted in Figs. 7.10 (b) and (c). As it occurs for the Mott transition, doping induces a MIT and low energy unoccupied states are created at the Fermi level. These states are separated by an energy gap from the higher energy states of the UB, and further increase in doping pushes the UB states to lower energies. Below we investigate how these UB states are transferred to the Fermi level upon doping.

In order to quantify the amount of spectral weight per spin transferred to the Fermi
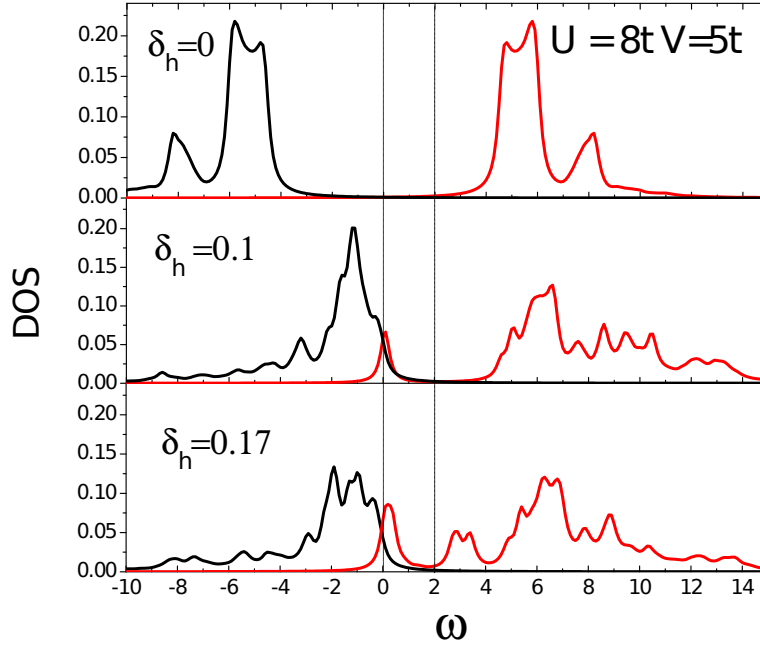
Figure 7.10: $N^-(\omega)$ (black curve) and $N^+(\omega)$ (red curve) for $U = 8t$ and $V = 5t$ for different values of δ_h. Chain with $N_s = 8$ in the grand canonical ensemble. The density of holes is defined as $\delta_h = 1 - \langle n \rangle$, where $\langle n \rangle$ is the averaged particle density obtained with $N_r = 50$ realizations of TBC.

level we define

$$W_{FL} = \int_0^\Gamma d\omega DOS(\omega), \tag{7.12}$$

where Γ is a cutoff defined by the bandwidth of low energy states, while $\omega = 0$ is the position of the Fermi level. As it can be seen in Figs. 7.9 and 7.10, the band of low-energy states created upon doping is separated by an energy gap from the UB; in these cases we define by inspection $\Gamma = 3t$ and $\Gamma = 2t$, respectively. The total spectral weight W_{FL} may be seen as the effective number of degrees of freedom in the low-energy regime, responsible for the low-energy physics [87]. The total spectral weight of $N_\sigma^-(\omega)$ is given by the number of particles with spin σ, $W_{LB} = (1 - \delta_h)/2$; and using the sum rule for the DOS, $\int_{-\infty}^\infty d\omega [N^+(\omega) + N^-(\omega)] = 1$, we define the spectral weight of the UB as $W_{UB} = 1 - W_{LB} - W_{FL}$. At half-filling, $W_{LB} = W_{UB} = 1/2$. Upon doping, W_{UB} represents the spectral weight that remains in the UB.

Figure 7.11 shows $W_{FL}(\delta_h)$ and $W_{UB}(\delta_h)$ for different values of V in the Mott transi-
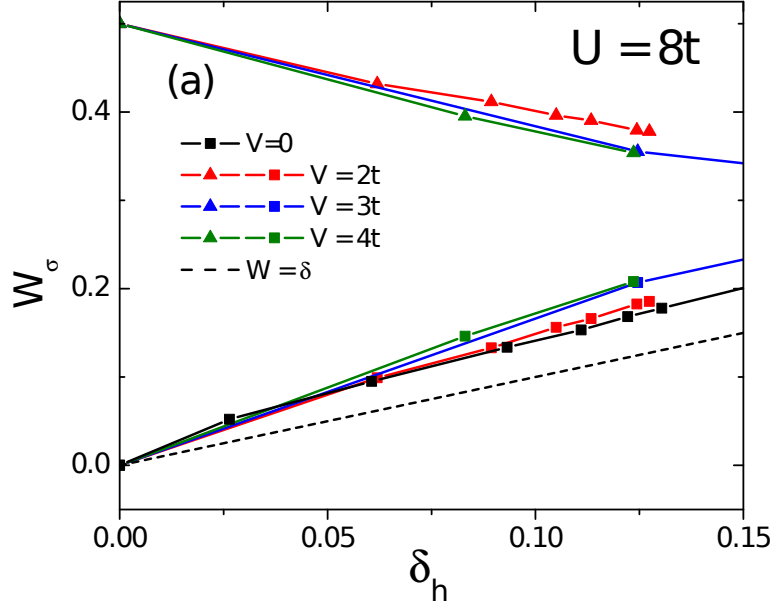
Figure 7.11: Low-energy spectral weight at the Fermi level, W_{FL} (squares), and spectral weight of the UB, W_{UB} (triangles), as a function of hole doping, δ_h, for $U = 8t$ and different values of $V < V_c \approx 4.1$. W_{FL} and W_{UB} were obtained from the DOS graphs, see text and Fig. 7.9.

tion. The behaviour of $W_{FL}(\delta_h)$ and $W_{UB}(\delta_h)$ is qualitatively the same as the one found for the HM [73], [74], [75]. For $\delta_h > 0$, spectral weight from both the LB and UB is transferred to the Fermi level, i.e., $W_{UH}(\delta_h)$ decreases with $\delta_h > 0$, and as a consequence, $W_{FL}(\delta_h) > \delta_h$. Furthermore, as one increases V, $W_{FL}(\delta_h)$ slightly increases, as it can be seen in Fig. 7.11. This is consistent with the result obtained for the HM that the lower-energy states bandwidth is given by the spin effective exchange $O(J)$ for $U = 8t$ [33].

We further examine the effect of doping on each individual k mode by investigating the single-particle spectral function for $U = 8t$ and $V = 2t$. Figures 7.13 (a) and (b) show $A(k, \omega)$ for $\delta_h = 0$ and $\delta_h = 0.17$, respectively. As already discussed in the previous section, at half-filling the spectral weight is predominant for modes $k < \pi/2$, and the stronger peak of $A(k, \omega)$ splits in spinon and holon branches, as it can be seen for modes $k/\pi < 0.2$. Comparing Figs. 7.13 (a) and (b), we see that doping creates a band of low energy states that extends from $k \approx 0.4\pi$ to $k = \pi$. This result is qualitatively the same
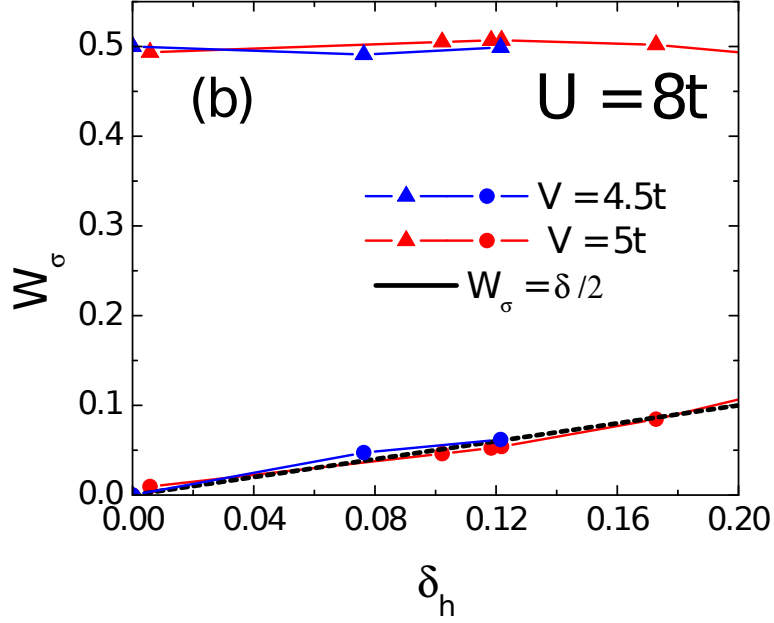
Figure 7.12: Low-energy spectral weight at the Fermi level, W_{FL} (circles), and spectral weight of the UB, W_{UB} (triangles), as a function of hole doping, δ_h, for $U = 8t$ and different values of $V > V_c \approx 4.1$. W_{FL} and W_{UB} were obtained from the DOS graphs, see text and Fig. 7.10.

as the one obtained for the HM in Ref [33].

On the other hand, the redistribution of spectral weight in the CDW-Metal transition shows a qualitatively different behaviour from the one obtained for the Mott transition. The behaviour of $W_{FL}(\delta_h)$ and $W_{UB}(\delta_h)$ with δ_h in the CDW-Metal for $V = 4.5t$ and $V = 5t$ is shown in Fig. 7.12. The spectral weight of the UB is not transferred to the Fermi level, i.e., $W_{UB}(\delta_h)$ does not change with δ_h and is equal to $W_{FL}(\delta_h) = 1/2$. As it can be seen in Fig. 7.10, the effect of a small doping in the DOS is to push the higher energy states of the UB to lower energies, but, differently from the Mott transition, these states are not directly transferred to the Fermi level for a tiny δ_h; here we considered densities up to $\delta_h = 0.17$. Furthermore, our results indicate that $W_{FL}(\delta_h)$ follows the same behaviour as the one obtained in the atomic limit, $W_{FL}(\delta_h) = \delta_h/2$. Further increase in doping pushes the high energy states, and the UB collapses with the states at the Fermi level. Thus, the definition of the low energy spectral weight $W_{FL}(\delta_h)$ becomes meaningless
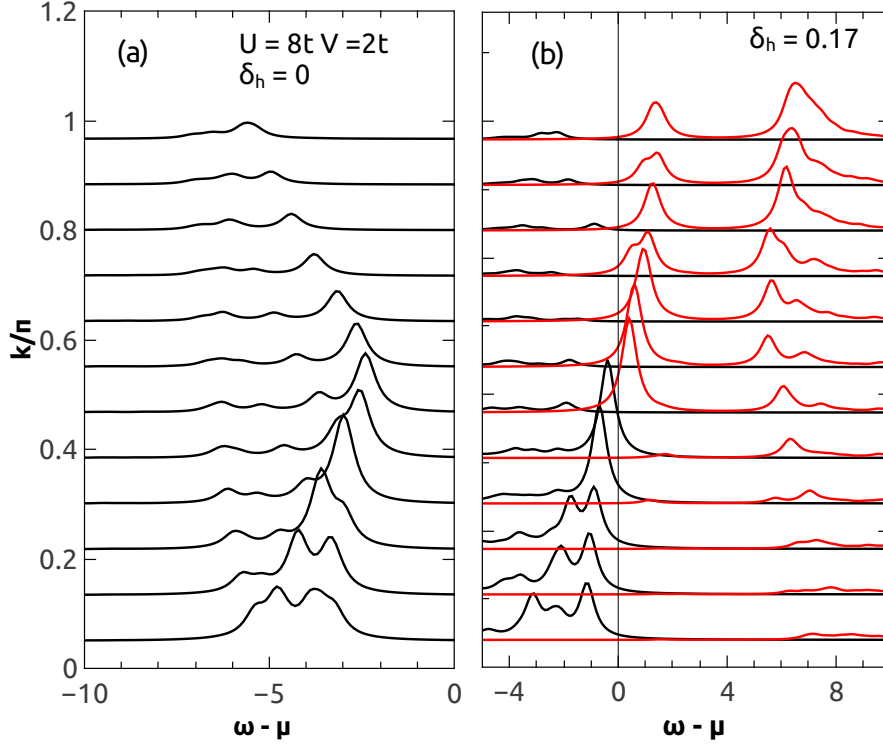
Figure 7.13: Single particle spectral function $A^-(k,\omega)$ (black curve) and $A^+(k,\omega)$ (red curve) for $U = 8t$ and $V = 2t$. $N_s = 12$ and two TBC were used, $\phi = 0.6\pi$ and $\phi = 1.6\pi$. (a) Half-filling, $\delta_h = 0$, (b) $\delta_h = 0.17$.

when the gap fills up upon increasing δ_h. We conclude that for tiny dopings the low energy spectral weight may follow $W_{FL}(\delta_h) \approx \delta_h/2$.

Next let us investigate the filling dependence of the single particle spectral function for $U = 8t$ and $V = 5t$; see Figs. 7.14 (a) and (b). Figures 7.14 (a) and (b) show $A(k,\omega)$ for $\delta_h = 0$ and $\delta_h = 0.17$, respectively. Comparing Figs. 7.14 (a) and (b), we see that the low energy spectral weight appearing just above the Fermi level is carried by k modes centred around $k = \pi/2$, and, in contrast to the Mott transition, no low energy spectral weight appears for modes around $k = \pi$. Furthermore, the single-particle dipersion at half-filling remains basically unchanged. This result indicates that for small doping, $\delta_h = 0.17$, the spectral weight of the UB is not transferred to the Fermi level. Thus the low energy states of the DOS can be described by an *almost* rigid band-picture.

As δ_h increases, a second doping-driven MIT occurs at quarter filling [80]. At this
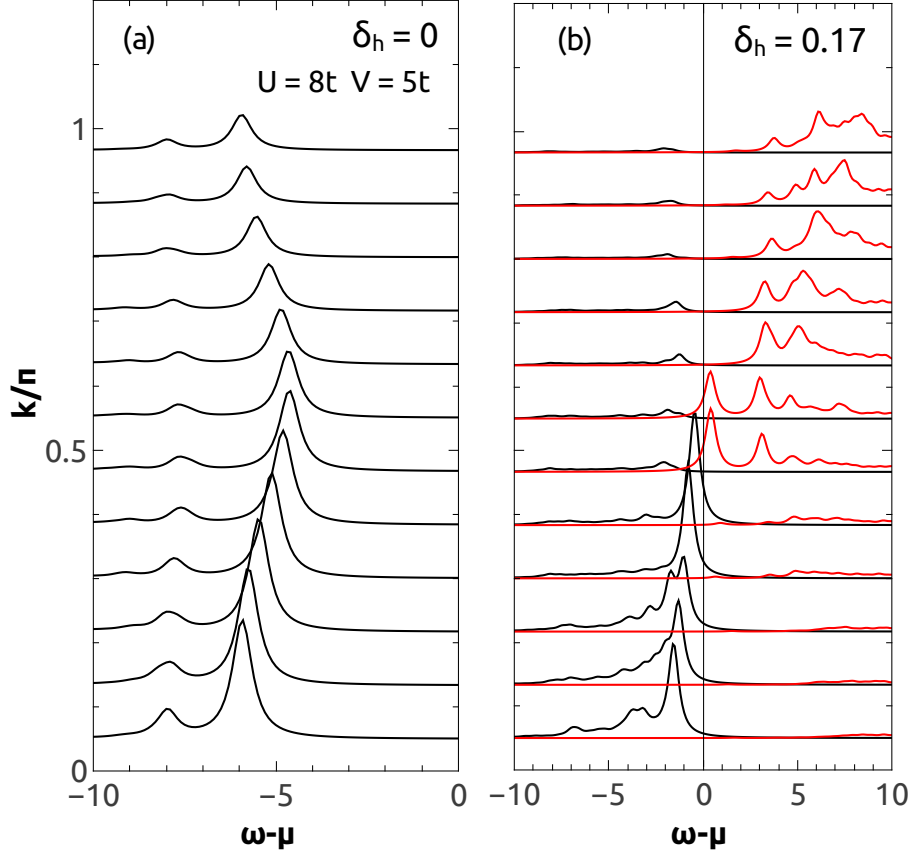
Figure 7.14: Single particle spectral function $A^-(k,\omega)$ (black curve) and $A^+(k,\omega)$ (red curve) for $U = 8t$ and $V = 5t$. $N_s = 12$ and two TBC were used, $\phi = 0.6\pi$ and $\phi = 1.6\pi$. (a) Half-filling, $\delta_h = 0$, (b) $\delta_h = 0.17$.

filling the system is also a CDW. Figure 7.15 shows the DOS for $U = 8t$ and $V = 5t$ and different densities $\langle n \rangle$. Here it is worth defining the electron doping concentration as $\delta_e = \langle n \rangle - 0.5$, so that δ_e increases from the bottom to the top of Fig. 7.15. For $\delta_e = 0$, a charge gap opens up at the Fermi level; see Fig. 7.15 (a). Increasing δ_e generates occupied states below the Fermi level, and a MIT takes place. We quantified the amount of low energy spectral weight lying below the Fermi level, $W_{FL}(\delta_e)$, by calculating Eq. (7.12) in the energy interval within the two vertical lines of Fig. 7.15. Figure 7.16 shows $W_{FL}(\delta_e)$ as a function of δ_e for $U = 8t$ and $V = 5t$. We found that $W_{FL}(\delta_e) > \delta_e$. It is important to mention that at half-filling the effect of electron doping is equal to hole doping due to
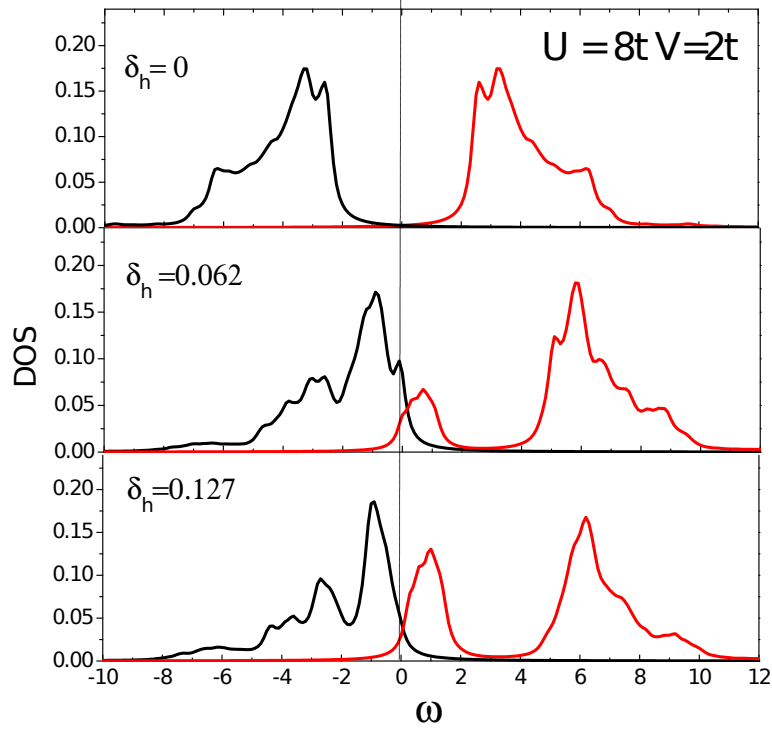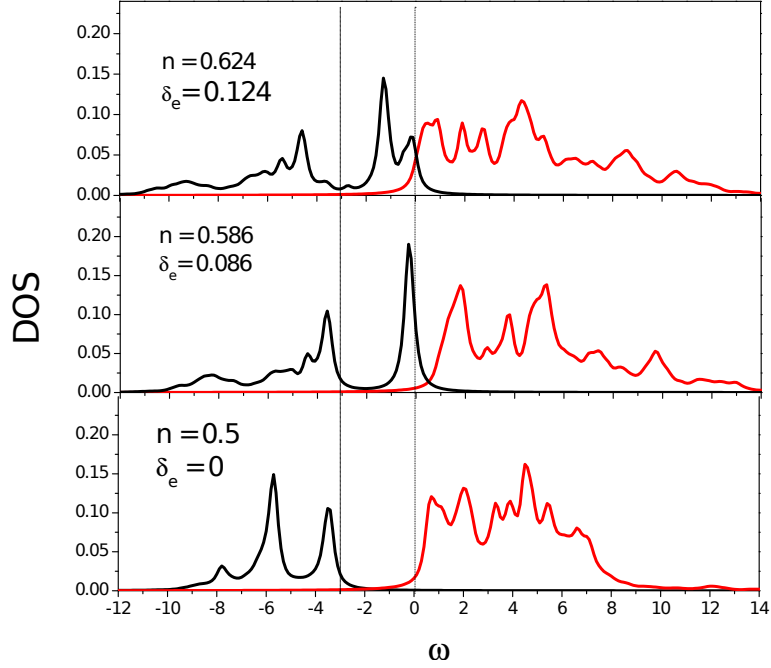
Figure 7.15: $N^-(\omega)$ (black curve) and $N^+(\omega)$ (red curve) for $U = 8t$ and $V = 5t$ for different values of δ_e. Chain with $N_s = 8$ in the grand canonical ensemble. The density of electrons is defined as $\delta_e = \langle n \rangle - 0.5$, where $\langle n \rangle$ is the averaged particle density obtained with $N_r = 50$ realizations of TBC.

particle-hole symmetry, and consequently $W_{FL}(\delta_h) = W_{FL}(\delta_e)$. Thus at quarter-filling, despite the system being on a CDW state, the low energy SW $W_{FL}(\delta_e)$ induced by electron doping follows the same behaviour as the one found for the Mott transition.

7.4 Conclusions

We have investigated the spectral properties of the 1d EHM using the Lanczos method with TABC. At half-filling, $A(k,\omega)$ splits into spinon and holon branches, which is a signature of spin-charge separation of the low energy single-particle excitations [84]. On the other hand, no signature of spin-charge separation was observed in the CDW phase. In this case, we found that the low-energy spectral weight of $A(k,\omega)$ can be described by Eq. (7.11), corresponding to the energy of a single hole in the strong-coupling limit. We have also obtained the momentum distribution function $n_\sigma(k)$, which has not been
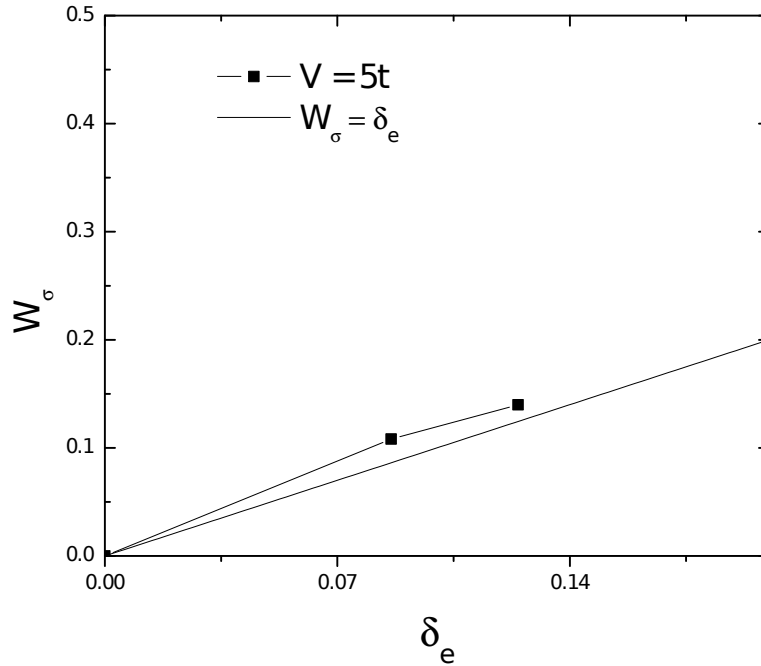
Figure 7.16: Spectral weight W_{FL} and W_{UB} as a function of electron doping, δ_e, for $U = 8t$ and $V = 5t$. W_{FL} and W_{UB} were obtained from the DOS graphs, see text and Fig. 7.15.

explored before for the EHM. One important result is that the momentum occupation of a mode k provides a signature for the transition to the CDW phase. More specifically, for $k < \pi/2$, $n_\sigma(k)$ is a nonmonotonic function of V, displaying a peak at the transition to the CDW phase.

Away from half-filling, we characterized the Mott and CDW-Metal transitions by investigating the evolution of the DOS upon doping. We also quantified the low-energy spectral weight created at the Fermi level, W_{FL}. In the Mott transition, as is already known for the HM [73],[75], spectral weight from both the LB and UB is transferred to the Fermi level, and $W_{FL}(\delta_h) > \delta_h$. For a given doping fraction, δ_h, W_{FL} slightly increases with V.

The evolution of the DOS with doping in the CDW-Metal transition is qualitatively different from the Mott transition. In this case, the spectral weight from the UB is pushed into lower energies upon doping, but is not transferred to the Fermi level for a tiny amount of doping. For $U = 8t$ and $V = 5t$ we have established that the low energy spectral weight

at the Fermi level follows $W_{FL}(\delta_h) \approx \delta_h/2$, up to $\delta_h < 0.17$. Furthermore, the behaviour of the spectral function away from half-filling indicates that for small dopings the system is well described by a rigid band. Finally, doping the insulating quarter-filled CDW system with electrons leads to a low-energy spectral weight $W_{FL}(\delta_e) > \delta_e$, as it occurs for the Mott transition.

Chapter 8

Dipolar Extended Hubbard Model

As mentioned before in the Chapter 6, optical lattice (OL) experiments have been used as a platform to emulate the Hubbard model. One important achievement in this direction was the realization of an antiferromagnetic (AFM) state [71], [72]. Another advancing direction with ultracold systems deals with atoms or molecules possessing a dipole moment [88]. A quantum degenerate Fermi gas of dipolar magnetic atoms (e.g., ^{161}Dy and ^{167}Er) has already been realized [89], [90]. The anisotropic and long-range character of the dipole-dipole interaction opens up the possibility of studying novel phases of matter [11]. In this sense, trapped dipolar atoms in an OL can realize extended Hubbard models, in which not just on-site, but next nearest-neighbour interactions are taken into account [12].

The inclusion of nearest-neighbour interaction V in the extended Hubbard model (EHM) can give rise, for instance, to a checkerboard charge density wave (CDW) ground-state [91], [92]. At half-filling the EHM describes a CDW-AFM transition by increasing V. Here we consider a case of current interest in the context of OL's, namely that of a ultra-cold dipolar atoms. The dipolar EHM incorporates both the long-range and anisotropic characters of the dipole-dipole interactions. This model has been recently explored by different techniques at half-filling for both spinless [93], [94], [95], [96] and spin-1/2 particles [97], [98]. In Ref. [97] the functional renormalization group technique was used to explore the phase diagram of the dEHM in the weak coupling regime. However, experiments are

usually carried out in the opposite regime, i.e., when the interaction is larger than the kinetic energy, so that a strong-coupling description is more appropriate. Furthermore, it was shown that away from half-filling the dEHM exhibits CDW phases with charge arrangements different from the EHM [99].

Antiferromagnetic and CDW phases can be experimentally probed by measuring spin and charge correlation functions with a quantum gas microscope. Experimental results can then be directly compared with numerical simulations for the Hubbard model [71]. On the other hand, an important experimental tool to probe phase transitions in OL experiments is given by time-of-flight measurements, which provide information about the momentum occupation function [100].

Here we use the Lanczos method to explore the ground state phase diagram of the dEHM at half-filling. In order to investigate the competition between AFM and CDW phases, we obtain the spin and charge correlation functions, and also examine the momentum occupation function, $n_\sigma(\mathbf{k})$, across the phase transitions described by the dEHM. This Chapter is organized as follows: In Section 7.1 we present the model and the quantities of interest. Section 7.2 revisits the EHM. In Section 7.3 we obtain the properties of the dEHM in the atomic limit ($t = 0$). In Section 7.4 we obtain the phase diagram of the dEHM. Section 7.5 deals with the behaviour of $n_\sigma(\mathbf{k})$, while in Section 7.6 we present our conclusions.

8.1   Model and Methods

We consider the dipolar Extended Hubbard Model (dEHM) for a two-component (pseudo-spin-1/2) dipolar Fermi gas in a square OL at half-filling [99], [97]. The two pseudospin states can be two hyperfine states of the dipolar atoms, and the dEHM Hamiltonian is
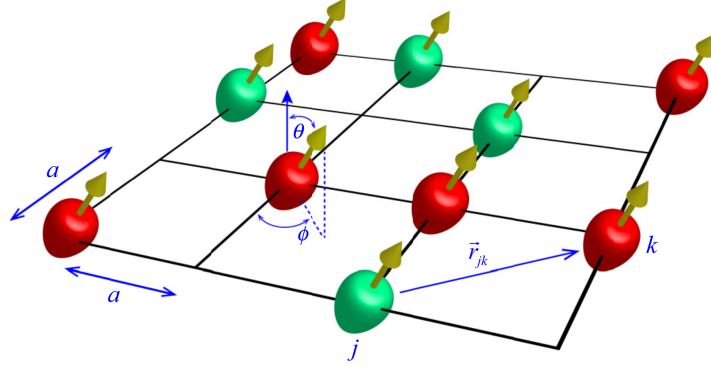
Figure 8.1: Dipolar fermions in a square optical lattice. The circles represent fermionic atoms. Each color is associated to a different hyperfine state (spins up and down). The orientation of the dipoles is given by the spherical angles θ and ϕ. The figure was extracted from Ref. [99].

given by

$$
\mathcal{H} = - \sum_{\langle i,j \rangle, \sigma} t_{i,j} \left(c_{i\sigma}^{\dagger} c_{j\sigma} + h.c. \right) + U \sum_{i} \left(n_{i\uparrow} - \frac{1}{2} \right) \left(n_{i\downarrow} - \frac{1}{2} \right)
$$
$$
+ \sum_{i,j} \frac{V_{i,j}}{2} \left(n_i - 1 \right) \left(n_j - 1 \right), \tag{8.1}
$$

where i runs over the N_s sites of the 2D clusters of Fig. 2.1, the spin state is $\sigma =\uparrow, \downarrow$, $n_{\mathbf{i}\sigma} = c_{\mathbf{i}\sigma}^{\dagger} c_{\mathbf{i}\sigma}$, and $n_{\mathbf{i}} = n_{\mathbf{i}\uparrow} + n_{\mathbf{i}\downarrow}$; $t_{i,j}$ is the hopping integral between nearest-neighbour sites i and j, U is the strength of the on-site interaction, and $V_{i,j}$ is the dipole interaction

$$
V_{i,j} = \frac{V}{r_{i,j}^3} \left[1 - 3(\hat{r}_{i,j} \cdot \hat{d})^2 \right], \tag{8.2}
$$

where $\mathbf{r_{i,j}} = \mathbf{r}_i - \mathbf{r}_j$ is the vector connecting sites i and j, and the vector $\mathbf{d} = d\hat{d}$ represents the magnetic dipole moment. We assume that all the dipoles are parallel, with $\hat{d} = (1, \theta, \phi)$ [99], [93], [97]. where the angles θ and ϕ are controlled by an external magnetic field [12]; see Fig. 8.1. The dEHM Hamiltonian written as in Eq. (8.1) is manifestly particle-hole
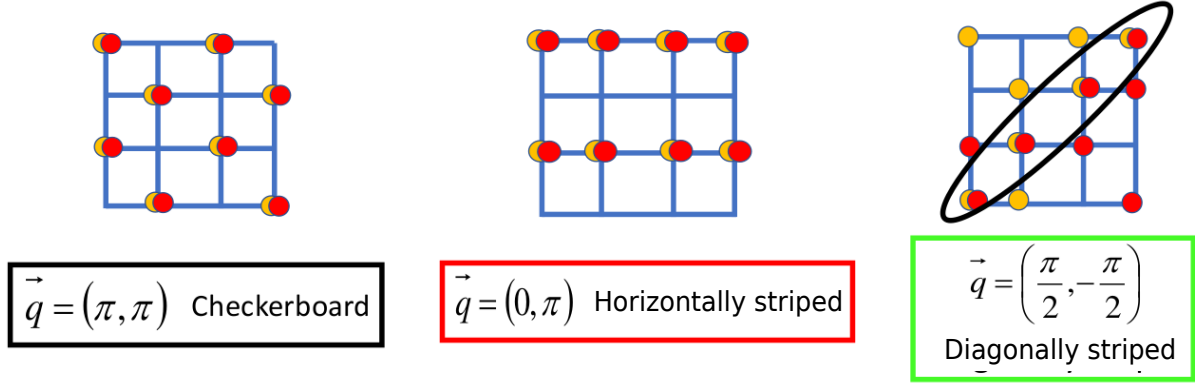
Figure 8.2: Cartoon showing the charge arrangement corresponding to wave vectors (a) $\mathbf{q} = (\pi, \pi)$, $\mathbf{q} = (0, \pi)$, and (c) $\mathbf{q} = (\pi/2, -\pi/2)$. The red and the yellow circles represent spins up and down.

symmetric. We consider that $V_{i,j}$ extends up to second nearest-neighbour sites,

$$V_x = V[1 - 3(\sin\theta\cos\phi)^2]$$

$$V_y = V[1 - 3(\sin\theta\sin\phi)^2]$$

$$V_{d1} = \frac{V}{2^{3/2}}\{1 - \frac{3}{2}[\sin\theta(\cos\phi + \sin\phi)]^2\}$$

$$V_{d2} = \frac{V}{2^{3/2}}\{1 - \frac{3}{2}[\sin\theta(\cos\phi - \sin\phi)]^2\} \tag{8.3}$$

where (V_x, V_y) and (V_{d2}, V_{d2}) are first and second neighbour interactions, respectively. This cutoff for $V_{i,j}$ is introduced due to the relatively small size of the 2D cluster, but one expects that the main features of the dipolar interaction, namely anisotropy and the possibility of attractive interactions, are already present. We use the Lanczos method for the 2D clusters of Fig. 2.1 with PBC. In addition, in order to obtain $n_\sigma(\mathbf{k})$ we also consider twisted boundary conditions (TBC), in the sense that whenever a fermion hops between two adjacent copies of the 2D clusters, the hopping term picks up a phase, $t_{i,j} = e^{i\phi}$; otherwise $t_{i,j} = t$.

We want to probe the onset of magnetic and charge order. To this end, we calculate the spin-spin correlation function

$$C_{spin}(\mathbf{r}) = \langle S_0^z S_\mathbf{r}^z \rangle, \tag{8.4}$$

where $S_i^z = (n_{i,\uparrow} - n_{i,\downarrow})$ is the spin operator, and $\mathbf{r}$ is the position vector, and the charge-charge correlation function

$$C_{charge}(\mathbf{r}) = \langle n_0 n_{\mathbf{r}} \rangle. \tag{8.5}$$

Furthermore, we collect the contributions to the spin-spin and charge-charge correlation functions from different sites, and calculate the spin and charge structure factors

$$SF_{spin}(\mathbf{q}) = \sum_{\mathbf{r}} e^{-i\mathbf{q}\cdot\mathbf{r}} C_{spin}(\mathbf{r}),$$
$$SF_{charge}(\mathbf{q}) = \sum_{\mathbf{r}} e^{-i\mathbf{q}\cdot\mathbf{r}} \left[C_{charge}(\mathbf{r}) - \langle n_0 \rangle \langle n_{\mathbf{r}} \rangle \right], \tag{8.6}$$

where $\mathbf{q}$ is the wave vector. $SF_{spin}(\mathbf{q})$ and $SF_{charge}(\mathbf{q})$ peak at values of $\mathbf{q}$ corresponding to the dominant magnetic and charge arrangements, respectively. For the two-dimensional Hubbard model at half-filling, the peak of $SF_{spin}(\mathbf{q})$ located at $\mathbf{q} = (\pi, \pi)$ signals anti-ferromagnetic (AFM) order in the ground state [5], [6]. Here we investigate the onset of AFM and of different charge orderings for the dEHM at half-filling; see Fig. 8.2.

An important experimental tool for experiments with optical lattices is the time-of-flight measurements [100], which is used to obtain information about the momentum occupation function

$$n_\sigma(\mathbf{k}) = \left\langle c_{\mathbf{k}\sigma}^\dagger c_{\mathbf{k}\sigma} \right\rangle. \tag{8.7}$$

We also obtain this quantity, and investigate its evolution throughout different $\mathbf{k}$-points in the first Brillouin zone in terms of the anisotropic dipolar interaction $V_{i,j}$.

8.2 Extended Hubbard Model (EHM)

First, we consider the usual extended Hubbard Model (EHM), i.e, $V_x = V_y = V$ and $V_{d1} = V_{d2} = 0$. In 2D, and at half-filling, the EHM has been previously studied in Refs. [91], [92], [85], [84]. For $U = 8t$, this system undergoes a first-order quantum phase transition between an AFM and a checkerboard CDW (cbCDW) for $V = 2.023t$ [84]. As a test of our code, we first reproduce these calculations. Figures 8.3 shows the
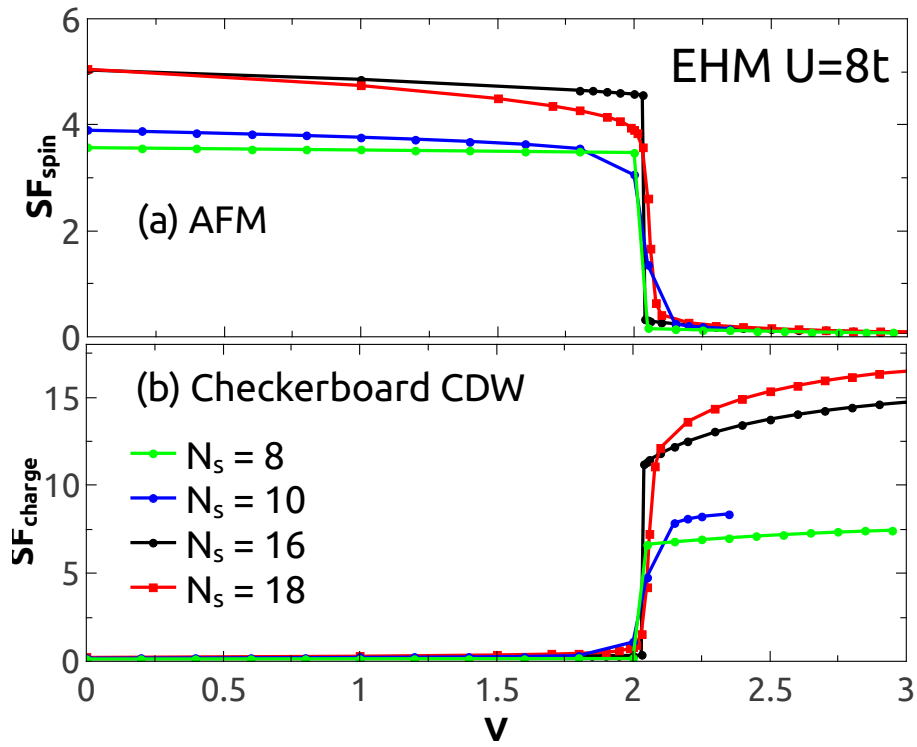
Figure 8.3: Structure factor as a function of V for the standard EHM. We considered the clusters with $N_s = 8, 10, 16, 18$ sites of Fig. 2.1. In (a) we consider the spin SF with $\mathbf{q} = (\pi, \pi)$ and (b) the charge SF with $\mathbf{q} = (\pi, \pi)$, which correspond to the checkerboard CDW.
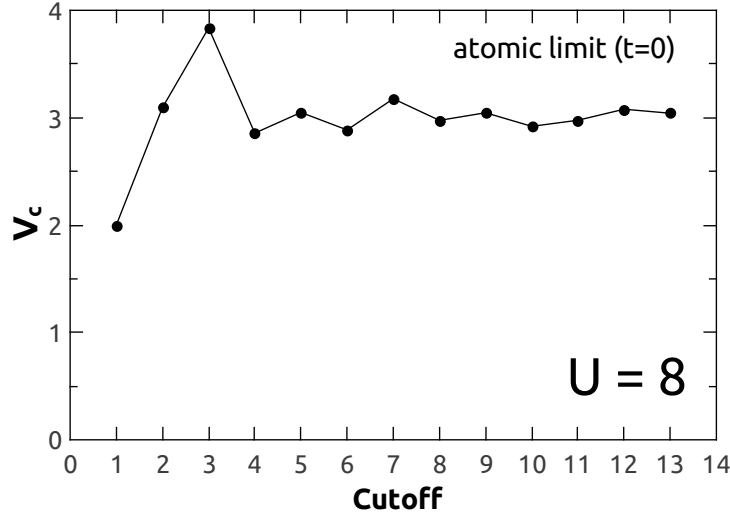
Figure 8.4: AFM-CDW critical V for $U = 8$ in the atomic limit $t = 0$ as function of the *cutoff* introduced in the interaction $V_{i,j}$ for the isotropic case, $\theta = 0$. Cutoff = 1, 2, ... means that the interaction is up to first-, second-, ..., further-neighbours.

V dependence of the spin and charge structure factors (SF's) for different cluster sizes with periodic boundary conditions; both cases correspond to $\mathbf{q} = (\pi, \pi)$. SF_{spin} is almost constant for $V < 2$ and has an abrupt change at $V \approx 2.05$. Comparing the results for different sizes we note that SF_{spin} increases with N_s for $N_s = 8, 10, 16$, which is indicative of AFM long-range order. For all clusters considered, SF_{spin} has an abrupt drop at $V \approx 2.05$, where the AFM correlations are suppressed. On the other hand, SF_{charge} has an abrupt increase from zero at $V \approx 2.05$, and the value of SF_{charge} for a given V increases with N_s, indicating long-range CDW order.

8.3 Limiting case: Atomic limit(t=0)

The AFM-CDW transition can be understood by a strong coupling argument ($U, V \gg t$). To zeroth order perturbation theory, we assume the atomic limit ($t = 0$), so the total energy of the system can be easily computed. For a Mott insulating state, i.e., one particle

per site, each particle interacts with four nearest-neighbours, and the total energy is

$$E_0^{Mott} = 2VN_s + C,$$

where C is a constant, while in a checkerboard CDW state there are $N_s/2$ doubly occupied sites, and the total energy is

$$E_0^{cbCDW} = \frac{UN_s}{2} + C,$$

The nearest-neighbour interaction V increases the energy of the Mott state, in such way that if $V > U/4$, the cbCDW state becomes the ground state. It is important to mention that for $U = 8$, the critical V that we obtain in Fig. 8.3 ($V_c = 2.05t$) is well described by the atomic limit. For the Mott state ($V < U/4$), the effective Hamiltonian obtained up to second order pertubation theory is given by the isotropic Heisenberg model, $\mathcal{H} = J_{eff} \sum_{\langle i,j \rangle} S_i \cdot S_j$, with $J_{eff} = 4t^2/(U - V)$, which has an AFM ground state.

We investigate the long-range aspect of the dipolar interaction by obtaining V_c in the atomic limit for $\theta = 0$ in Eq. (8.2); in this case the dipolar interaction is isotropic. Fig. 8.4 shows V_c as function of the cutoff considered for $V_{i,j}$. Introducing a cutoff up to first-neighbour (cutoff= 1), we obtain the result discussed in the last paragraph, $V_c = 2$, while for second-neighbour (cutoff= 2), V_c increases to $V_c = 3.09$. The physical reason for this increase is that interactions along the diagonal increase the energy of the cbCDW state. As the cutoff increases beyond second-neighbour, V_c oscillates with the cutoff, but quickly tends to a finite saturated value. The reason for the oscillation of V_c is that for some distances the interaction increases the energy of the cbCDW state, while for others this does not happen. Furthermore, we note that for cutoff= 13 V_c is just 1% different from the critical V found for the cutoff= 2.

Let us now explore the anisotropic character of the dipolar interaction in the atomic limit. Setting $\phi = 0$ and $\theta = \pi/2$ in Eq. (8.3) yields an anisotropic interaction: $V_y = V$, $V_x = -2V$, and $V_{d1} = V_{d2} = -V/\sqrt{2}$. For $V \gg U$, the atractive interaction in the **x** direction favours the formation of a horizontally-striped CDW (hCDW); see Fig. 8.2
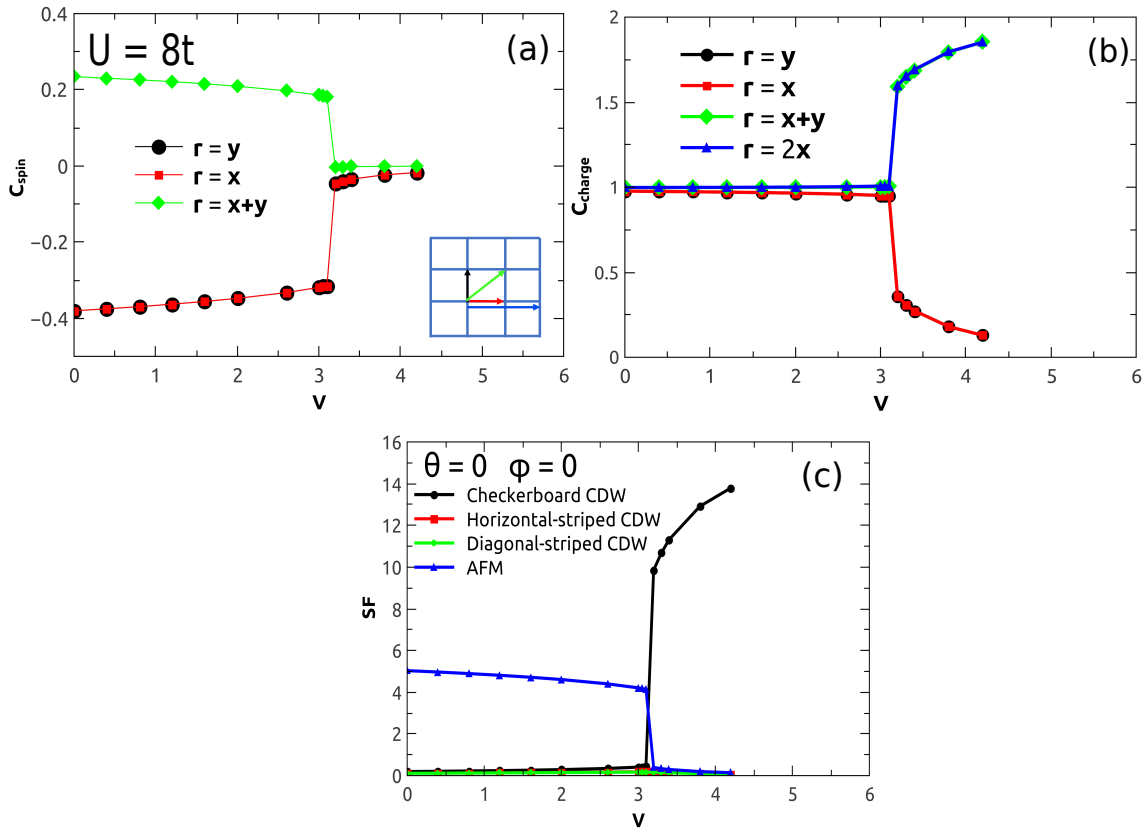
Figure 8.5: V dependence of correlation functions for $U = 8t$ and $\theta = 0$. Panels (a) and (b) show $C_{spin}(\mathbf{r})$ and $C_{charge}(\mathbf{r})$, respectively, for different distances $\mathbf{r}$. Panel (c) shows the spin SF with $\mathbf{q} = (\pi, \pi)$ and the charge SF with $\mathbf{q} = (\pi, \pi)$ (checkerboard), $\mathbf{q} = (0, \pi)$ (horizontal-striped), and $\mathbf{q} = (\pi/2, -\pi/2)$ (diagonal-striped).

(b). The hCDW state competes with the Mott state and the cbCDW for $U \sim V$ and intermediate values of θ. We then obtain the energies of these states in the atomic limit. Setting $\phi = 0$ in Eq. (8.3), it is straightforward to show that

$$E_0^{Mott}(\theta) = N_s V \left[\left(\frac{4 + \sqrt{2}}{2} \right) - 3 \left(\frac{4 + \sqrt{2}}{4} \right) \sin^2(\theta) \right] + C,$$

$$E_0^{cbCDW}(\theta) = N_s \left[\frac{U}{2} + \frac{V}{\sqrt{2}} \left(1 - \frac{3}{2} \sin^2(\theta) \right) \right] + C,$$

$$E_0^{hCDW}(\theta) = N_s \left[\frac{U}{2} + V \left(1 - 3 \sin^2(\theta) \right) \right] + C, \tag{8.8}$$

where C is a constant. In the $V \gg U$ regime, the energy of the Mott state is the largest one, and the phases cbCDW and hCDW compete as θ varies from 0 to $\pi/2$. Comparing E_0^{cbCDW} and E_0^{hCDW} we establish that the cbCDW-hCDW transiton takes place at $\theta^* \approx 0.4$ for $V \gtrsim 4$. In the next section we compare the boundaries between the AFM, cbCDW and hCDW phases defined by Eqs. (8.8) with the Lanczos results for the dEHM.

8.4 Dipolar EHM

In this section we show the Lanczos results for the dEHM for $U = 8t$ obtained for the $N_s = 16$ sites cluster with periodic boundary condition (PBC). First, we consider the isotropic case, i.e., $\theta = 0$. Figures 8.5 (a) and (b) show the spin and charge correlation functions, C_{spin} and C_{charge}, respectively, for different distances $\mathbf{r}$. For $V \lesssim 3.1t$, the first and second-neighbour C_{spin} have negative and positive values, respectively, and in both cases $C_{charge}(\mathbf{r}) \approx 1$, which is characteristic of a Mott insulating state with AFM correlations. For $V \gtrsim 3.1t$, spin correlations are suppressed, and the first-neighbour $C_{charge}(\mathbf{r})$ decreases with V, while the second one increases and tends to the saturated value, $C_{charge}(\mathbf{r}) = 2$. This charge correlation arrangement corresponds to a checkerboard CDW (cbCDW). Figure 8.5 (c) shows SF_{AFM} and SF_{CDW}, with different wave vectors $\mathbf{q}$. Similarly to what we obtain for the EHM, an abrupt change of SF_{AFM} and SF_{CDW}
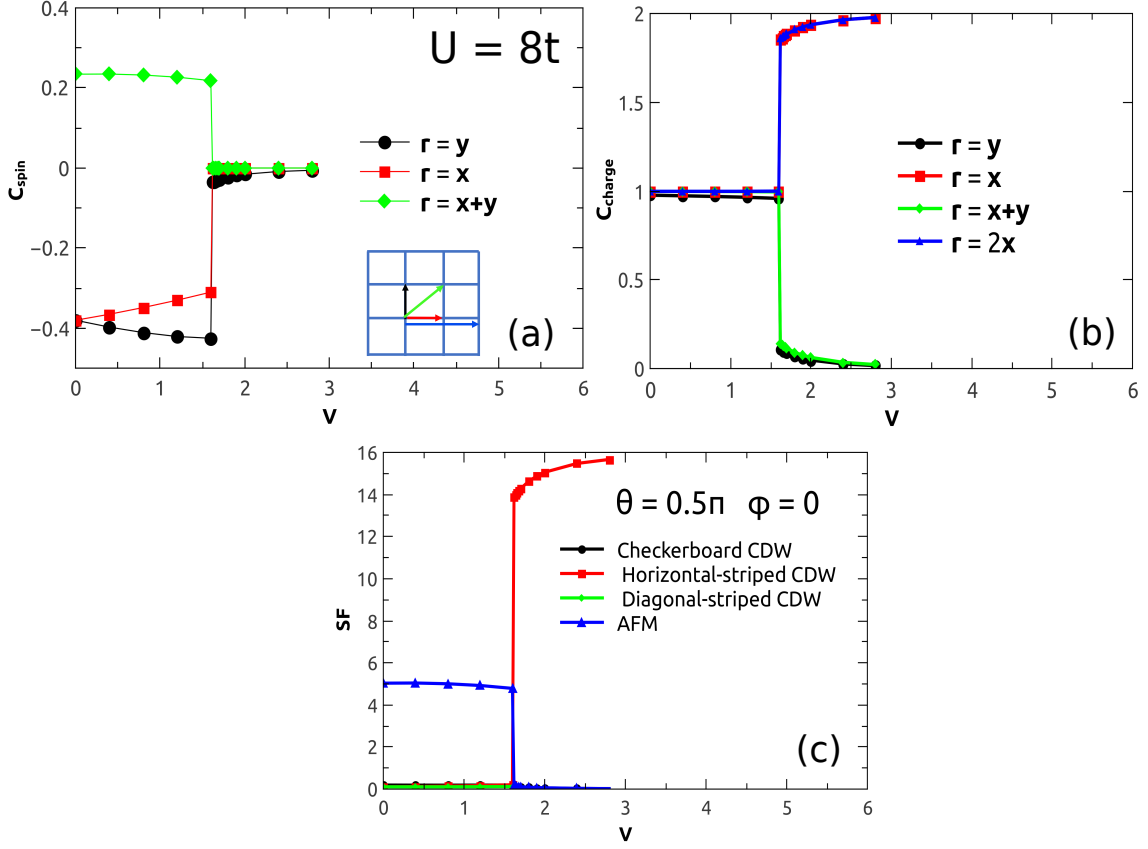
Figure 8.6: V dependence of correlation functions for $U = 8t$, $\theta = 0.5\pi$ and $\phi = 0$. Panels (a) and (b) show $C_{spin}(\mathbf{r})$ and $C_{charge}(\mathbf{r})$, respectively, for different distances $\mathbf{r}$. Panel (c) shows the spin SF with $\mathbf{q} = (\pi, \pi)$ and charge SF with $\mathbf{q} = (\pi, \pi)$ (checkerboard), $\mathbf{q} = (0, \pi)$ (horizontal-striped), and $\mathbf{q} = (\pi/2, -\pi/2)$ (diagonal-striped).

allows us to identify an AFM-cbCDW transition at $V_c \approx 3.1t$. We note that the addition of second-neighbour interactions, V_{d1} and V_{d2}, increases the value of V_c, in comparison with the one found for the EHM, as expected from the atomic limit prediction.

We now consider the dipole direction to be parallel to the plane of the lattice, i.e., $\theta = \pi/2$, which leads to an anisotropic interation; see Eq. (8.3). In Figs. 8.6 (a) and (b) we show C_{spin} and C_{charge} for $\phi = 0$. For $V \lesssim 1.6t$, anisotropic AFM spin correlations are formed between first- and second-neighbour sites, with $C_{spin}(\mathbf{x}) \neq C_{spin}(\mathbf{y})$. On the other hand, for $V \gtrsim 1.6t$, the charge correlations for $\mathbf{r} = \mathbf{y}$ and $\mathbf{r} = \mathbf{x} + \mathbf{y}$ are suppressed, while the ones for $\mathbf{r} = \mathbf{x}$ and $\mathbf{r} = 2\mathbf{x}$ increase with V and tend to the saturated value,
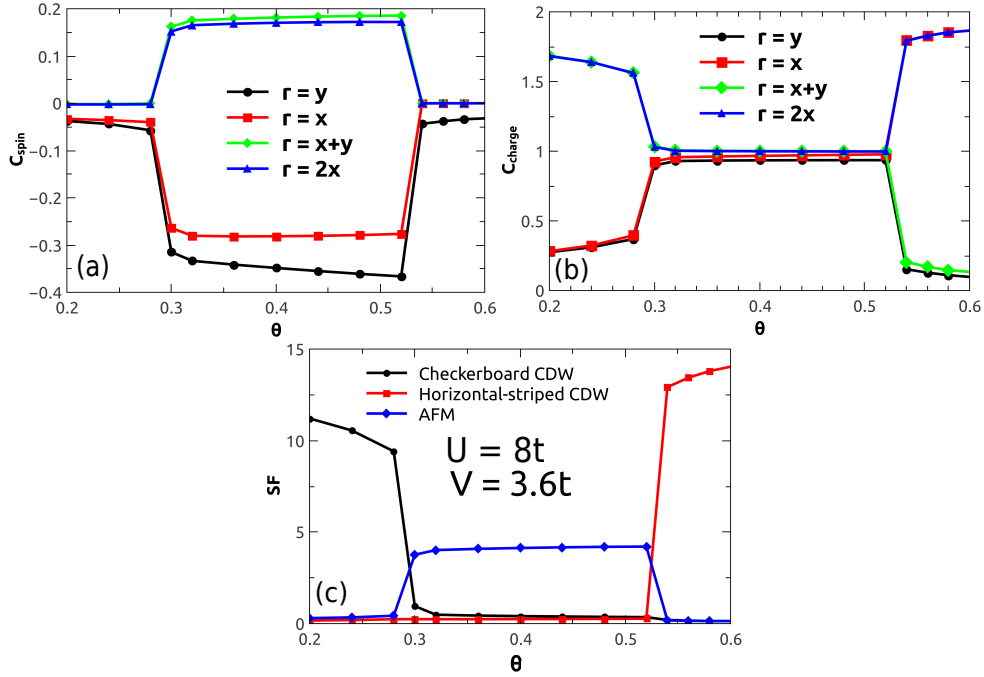
Figure 8.7: θ dependence of correlation functions for $U = 8t$, $V = 3.6t$ and $\phi = 0$. Panels (a) and (b) show $C_{spin}(\mathbf{r})$ and $C_{charge}(\mathbf{r})$, respectively, for different distances $\mathbf{r}$. Panel (c) shows the spin SF with $\mathbf{q} = (\pi, \pi)$ and charge SF with $\mathbf{q} = (\pi, \pi)$ (checkerboard), $\mathbf{q} = (0, \pi)$ (horizontally striped).

$C_{charge}(\mathbf{r}) = 2$. This charge correlation arrangement corresponds to a hCDW. The AFM-hCDW transition occurs at $V_c \approx 1.6t$, as it can be seen from the graph of the spin and charge SF as functions of V; see Fig. 8.6 (c).

As discussed above, the anisotropic dipolar interaction can induce different CDW phases when the non local interactions are large enough to suppress AFM correlations. We now discuss the transitions induced by varying the dipole direction θ. In Figs. 8.7 we show the θ dependence of C_{spin} and C_{charge} for $\phi = 0$ and $V = 3.6t$. For intermediate values of θ, $0.3 \lesssim \theta \lesssim 0.55$, a Mott insulating phase with $C_{charge} \approx 1$ and AFM spin correlations is formed; see Figs. 8.7 (a) and (b). For other values of θ the AFM correlations are suppressed, and cbCDW and hCDW charge correlations are formed for $\theta \lesssim 0.3$ and $\theta \gtrsim 0.55$, respectively. As V increases, the intermediate range of θ in which AFM correlations are dominant shrinks, and is completely suppressed for a V larger than some V^*. As
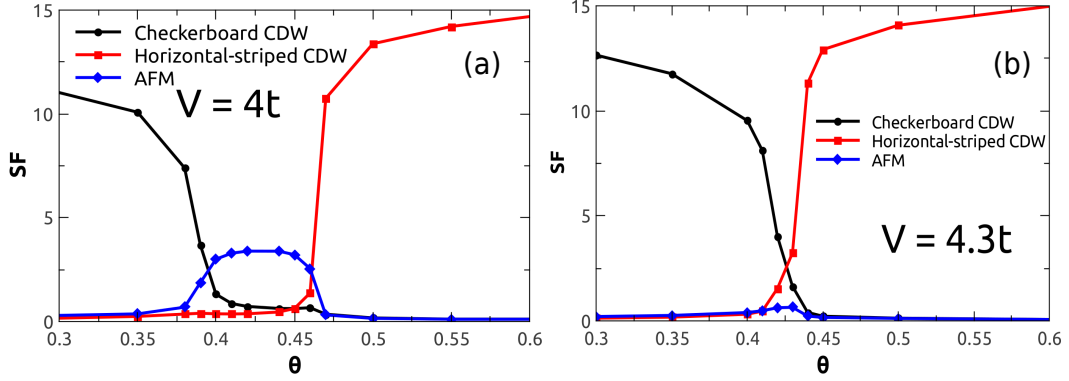
Figure 8.8: θ dependence of spin and charge SF with $\mathbf{q} = (\pi, \pi)$ (checkerboard) and $\mathbf{q} = (0, \pi)$ (horizontally striped) for $U = 8t$, $\phi = 0$, and (a) $V = 4t$, (b) $V = 4.3t$

discussed in the previous section, in the atomic limit, $V^* \approx 4t$, and the cbCDW-dCDW transition takes place at $\theta^* = 0.4$. Nevertheless, for $U = 8t$, it is still possible to see an intermediate AFM phase for $V = 4t$, see Fig. 8.8 (a). On the other hand, for $V = 4.3t$ no intermediate AFM phase is observed as θ varies, see Fig. 8.8 (b).

We obtain the spin and charge SF for different values of V and θ, from which we draw a phase diagram in the space of parameters V and θ, for $\phi = 0$; see Fig. 8.9. It is important to mention that due to the relatively small system sizes we cannot ascertain the onset of long-rang order for both AFM and CDW phases. Nevertheless, we can establish which correlations, AFM or CDW, and which CDW arrangement dominates (within error bars) for a given value of V and θ. Hence a more precise statement is that the phase diagram of Fig. 8.9 shows the regions of the space of parameters, V and θ, where AFM or CDW (checkerboard or h-striped) correlations dominate. The points in Fig. 8.9 are extracted from the graphs of the spin and charge SF as function of V. The error bars describe the uncertainties in the values of V_c; see Fig. 8.10. In addition , we also present the atomic limit prediction for the boundaries between AFM, cbCDW and hCDW phases. As it can be seen, the phase diagram for $U = 8t$ can be qualitatively explained by the atomic limit results. However, for $\theta = 0.42$ the cbCDW phase dominates for an intermediate range of V; see Fig. 8.10 (c). This indicates that the vertical cbCDW-dCDW boundary
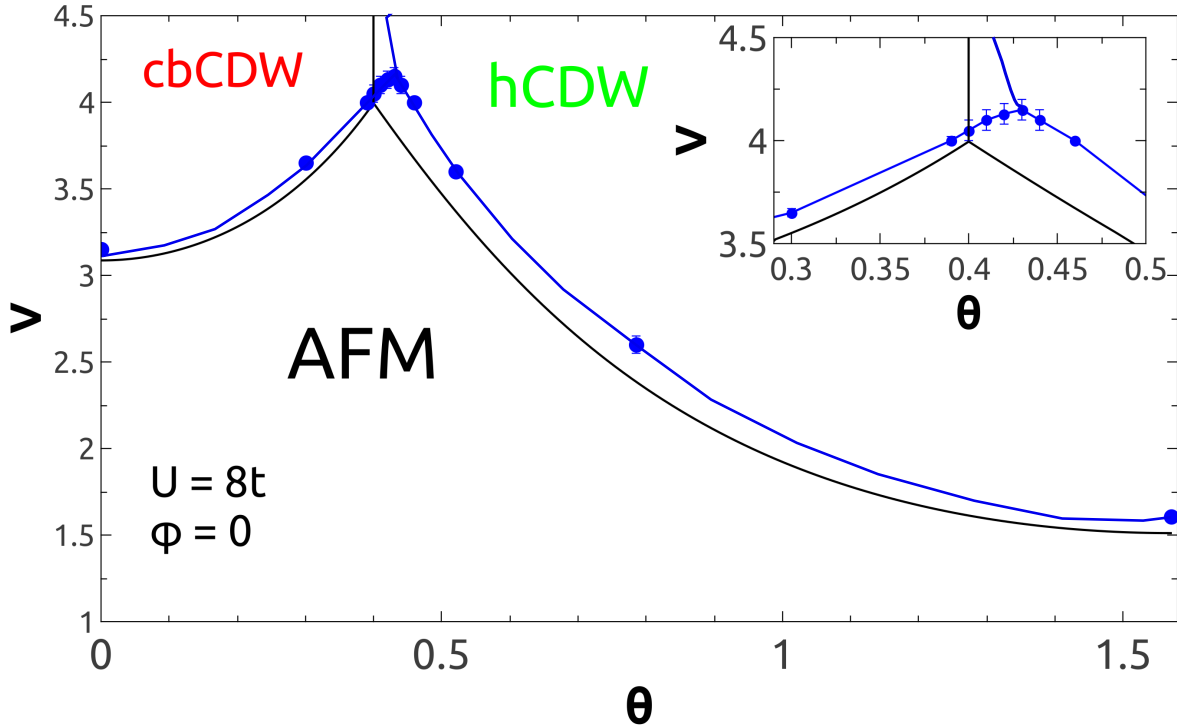
Figure 8.9: Phase diagram showing the regions in the space of parameters V and θ dominated by AFM, cbCDW, and hCDW correlations. The continuous line is the atomic limit ($t = 0$) result for the boundaries between the AFM, cbCDW and hCDW phases. The points are estimations for the critical V_c and were extracted from the graphs of the the spin and charge SF as function of V, see Fig. 8.10.

at $\theta \approx 0.4$ might have an inclination for $U = 8t$; see inset of Fig. 8.9. Summing up, an interesting result we have obtained is that by varying θ, one can induce different AFM-CDW transitions.
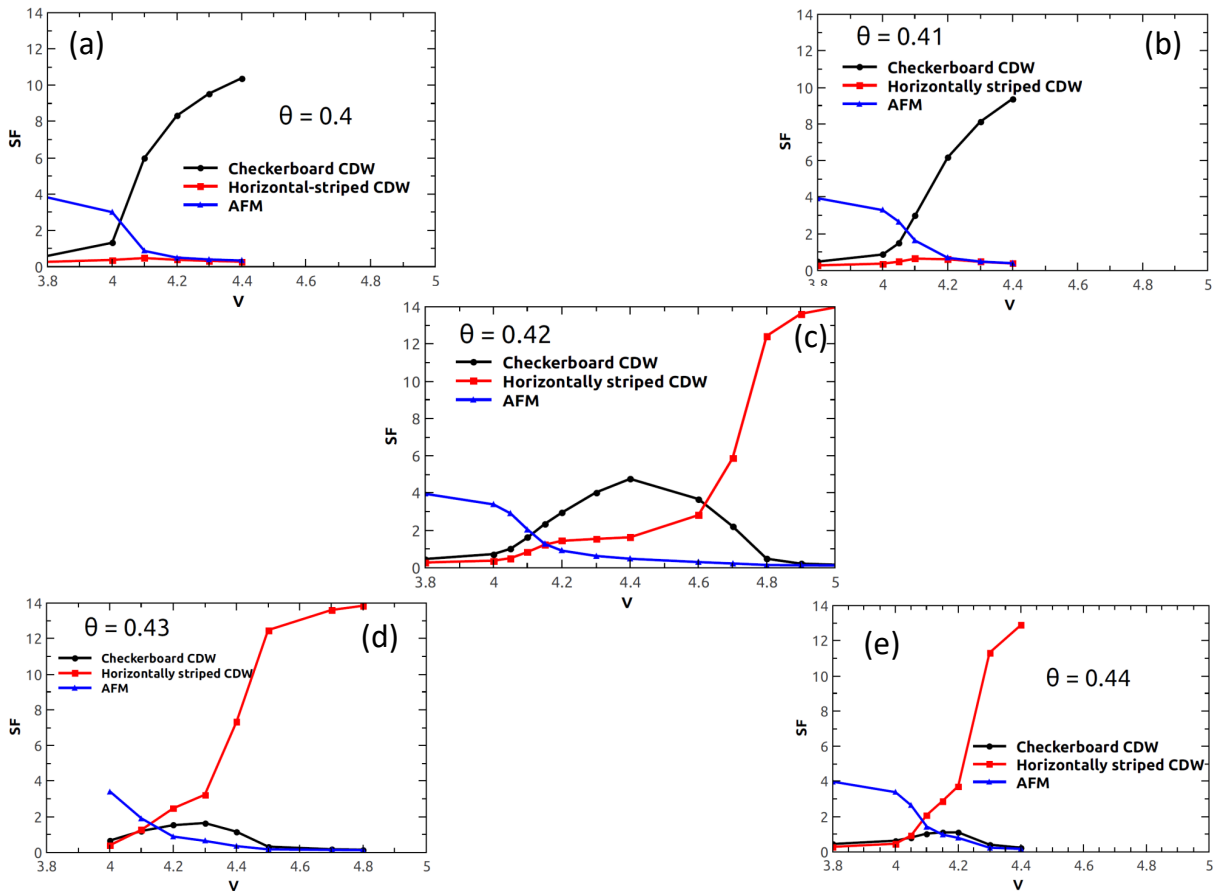
Figure 8.10: V dependence of spin and charge SF for $U = 8t$ and $\phi = 0$ and (a) $\theta = 0.4$, (b) $\theta = 0.41$, (c) $\theta = 0.42$, and (d) $\theta = 0.43$, and (e) $\theta = 0.44$.

8.5 Momentum distribution function

In this section we show results for the momentum occupation function, $n_\sigma(\mathbf{k})$. Our aim here is to investigate the behaviour of $n_\sigma(\mathbf{k})$ for different $\mathbf{k}$-points within the 1BZ in terms of the non local interaction, $V_{i,j}$. Here we consider the $N_s = 16$ sites cluster with different twisted boundary conditions.

First, it is worth discussing the effects of the particle-hole (ph) symmetry of Eq. (8.1) in $n_\sigma(\mathbf{k})$. The ph transformation

$$c_{i\sigma} = (-1)^i \tilde{c}_{i\sigma}^\dagger$$

$$c_{i\sigma}^\dagger = (-1)^i \tilde{c}_{i\sigma}, \tag{8.9}$$

where $\tilde{c}_{i\sigma}^\dagger$ and $\tilde{c}_{i\sigma}$ are fermionic creation and destruction operators, is expressed in $\mathbf{k}$-momentum space as

$$c_{\mathbf{k},\sigma} = \tilde{c}_{\mathbf{k}+\vec{\pi},\sigma}^\dagger$$

$$c_{\mathbf{k}\sigma}^\dagger = \tilde{c}_{\mathbf{k}+\vec{\pi},\sigma},$$

where $\vec{\pi} = (\pi, \pi)$. It is then straightforward to obtain the ph transformation of $n_\sigma(\mathbf{k})$

$$n_\sigma(\mathbf{k}) = \left\langle c_{\mathbf{k}\sigma}^\dagger c_{\mathbf{k}\sigma} \right\rangle \rightarrow \left\langle \tilde{c}_{\mathbf{k}+\vec{\pi},\sigma} \tilde{c}_{\mathbf{k}+\vec{\pi},\sigma}^\dagger \right\rangle = 1 - \left\langle \tilde{c}_{\mathbf{k}+\vec{\pi},\sigma}^\dagger \tilde{c}_{\mathbf{k}+\vec{\pi},\sigma} \right\rangle, \tag{8.10}$$

or,

$$n_\sigma(\mathbf{k}) + \tilde{n}_\sigma(\mathbf{k} + \vec{\pi}) = 1, \tag{8.11}$$

where $\rightarrow$ stands for ph transformation, and $\tilde{n}_\sigma(\mathbf{k}) = \left\langle \tilde{c}_{\mathbf{k},\sigma}^\dagger \tilde{c}_{\mathbf{k},\sigma} \right\rangle$. The fact that the dEHM Hamiltonian is invariant under the ph transformation leads to $n_\sigma(\mathbf{k} + \vec{\pi}) = \tilde{n}_\sigma(\mathbf{k} + \vec{\pi})$. Hence the momentum occupation function at half-filling satisfies the following relation

$$n_\sigma(\mathbf{k}) + n_\sigma(\mathbf{k} + \vec{\pi}) = 1. \tag{8.12}$$

A consequence of the aforementioned relation is that if

$$n_\sigma(\mathbf{k}) = n_\sigma(\mathbf{k} + \vec{\pi}), \tag{8.13}$$
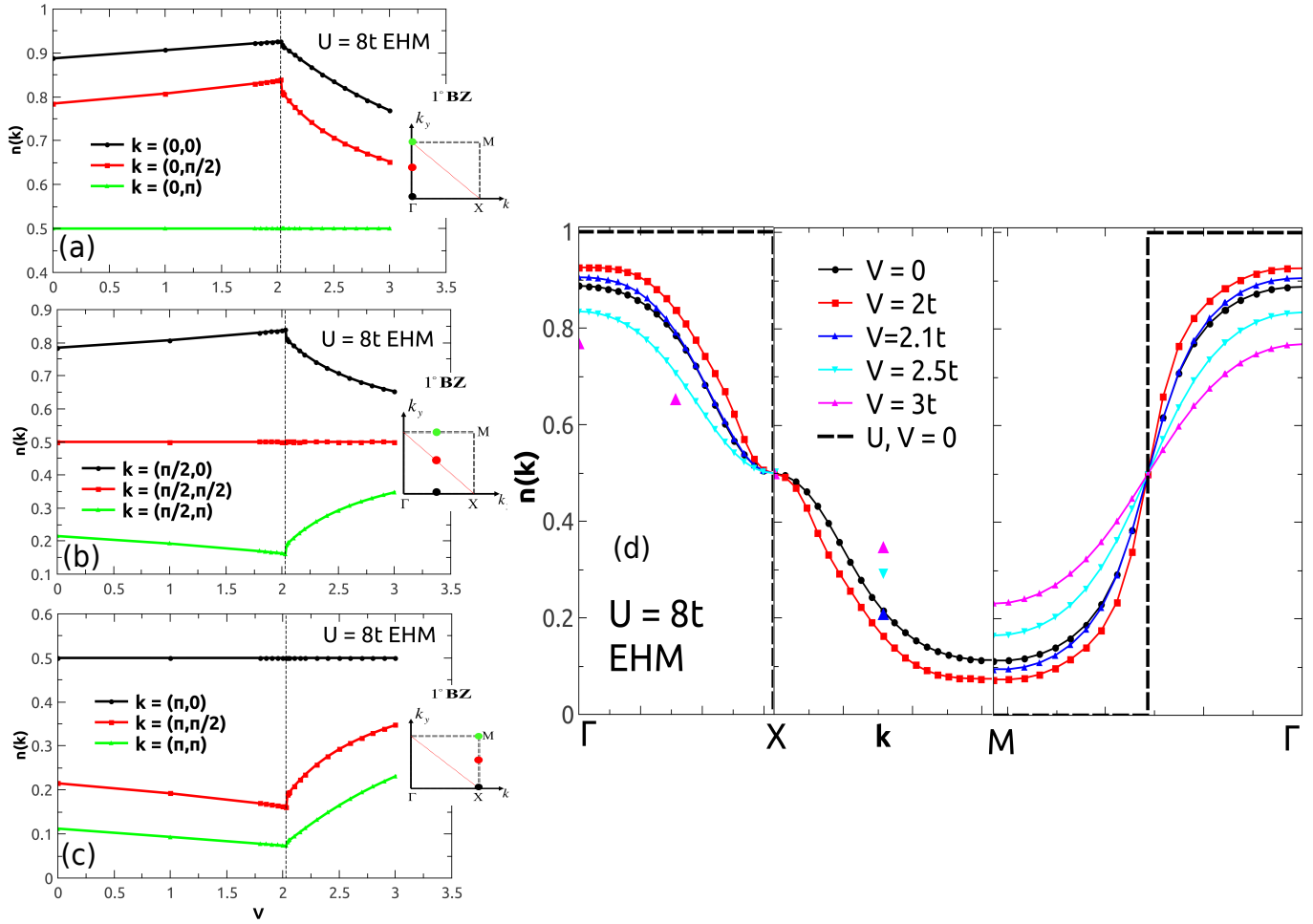
Figure 8.11: Momentum distribution for the EHM with $U = 8t$. Panels (a), (b) and (c) show $n_\sigma(\mathbf{k})$ as a function of V for different $\mathbf{k}$-points. A portion of the 1BZ is illustrated in the inset of the panels with the points $\Gamma = (0,0)$, $X = (\pi, 0)$, and $M = (\pi, \pi)$. The red line marks the Fermi surface of the NI system. Panel (d) is shows $n_\sigma(\mathbf{k})$ across three paths of the 1BZ, the black dashed line corresponds to results for the non-interacting case.

due to other symmetries of the Hamiltonian, then $n_\sigma(\mathbf{k}) = 1/2$, for any value of U and V. For example, the translational and time reversal symmetries lead to the following relations

$$n_\sigma(\mathbf{k}) = n_\sigma(\mathbf{k} \pm 2\vec{\pi})$$

$$n_\sigma(\mathbf{k}) = n_\sigma(-\mathbf{k}),$$

respectively. Using these relations, it is then straightforward to show that $n_\sigma[\mathbf{k} = (\pi/2, \pi, 2)] = n_\sigma(\mathbf{k} + \vec{\pi})$. Thus, $n_\sigma(\pi/2, \pi/2) = 1/2$.

For the non-interacting (NI) system, $\mathbf{k}$ is a good quantum number, so that at $T = 0$

$$n_\sigma(\mathbf{k}) = \begin{cases} 1, & \text{if} \quad |\mathbf{k}| < |\mathbf{k_F}|, \\ 0, & \text{if} \quad |\mathbf{k}| > |\mathbf{k_F}|. \end{cases}$$

For the interacting system, $\mathbf{k}$ is no longer a good quantum number, and the occupation $n_\sigma(|\mathbf{k}| > |\mathbf{k_F}|) \neq 0$. The function $n_\sigma(\mathbf{k})$ has been previously studied for the HM [25], [101]. Below we show that for some $\mathbf{k}$-points within the 1BZ, $n_\sigma(\mathbf{k})$ can be used to signal the AFM-CDW transition in the dEHM.

Figures 8.11 (a), (b) and (c) show $n_\sigma(\mathbf{k})$ for the EHM as a function of V for $U = 8t$ and for different $\mathbf{k}$-points within the 1BZ. For $\mathbf{k} = (\pi/2, \pi/2)$, $n_\sigma = 1/2$ for any value of V, as was discussed above; see Fig. 8.11 (b). The fact that the interaction is isotropic also guarantees that Eq. (8.13) holds for $\mathbf{k} = (0, \pi)$ and $(\pi, 0)$, which yields $n_\sigma = 1/2$; see Figs. 8.11 (a) and (c). For the other $\mathbf{k}$-points shown, $n_\sigma(\mathbf{k})$ provides a signature for the AFM-cbCDW transition, $V_c = 2.05t$. In Fig. 8.11 (a), for instance, $n_\sigma(\mathbf{k})$ has a peak at $V_c = 2.05t$ for $\mathbf{k} = (0, 0)$ and $(0, \pi/2)$. Furthermore, using Eq. (8.12), we see that at $V_c = 2.05t$, the peak of n_σ at $\mathbf{k} = (0, 0)$ becomes a minimum at $\mathbf{k} = (\pi, , \pi)$; see Fig. 8.11 (c). In addition, Fig. 8.11 (d) shows the momentum distribution function across three paths of the 1BZ for different values of V. The evolution of $n_\sigma(\mathbf{k})$ as V increases can then be traced as follows: for $\mathbf{k} < \mathbf{k_F}$, $n_\sigma(\mathbf{k})$ increases with V in the AFM phase up to the AFM-CDW transition, and then decreases in the CDW phase; for $\mathbf{k} > \mathbf{k_F}$, $n_\sigma(\mathbf{k})$ exhibits
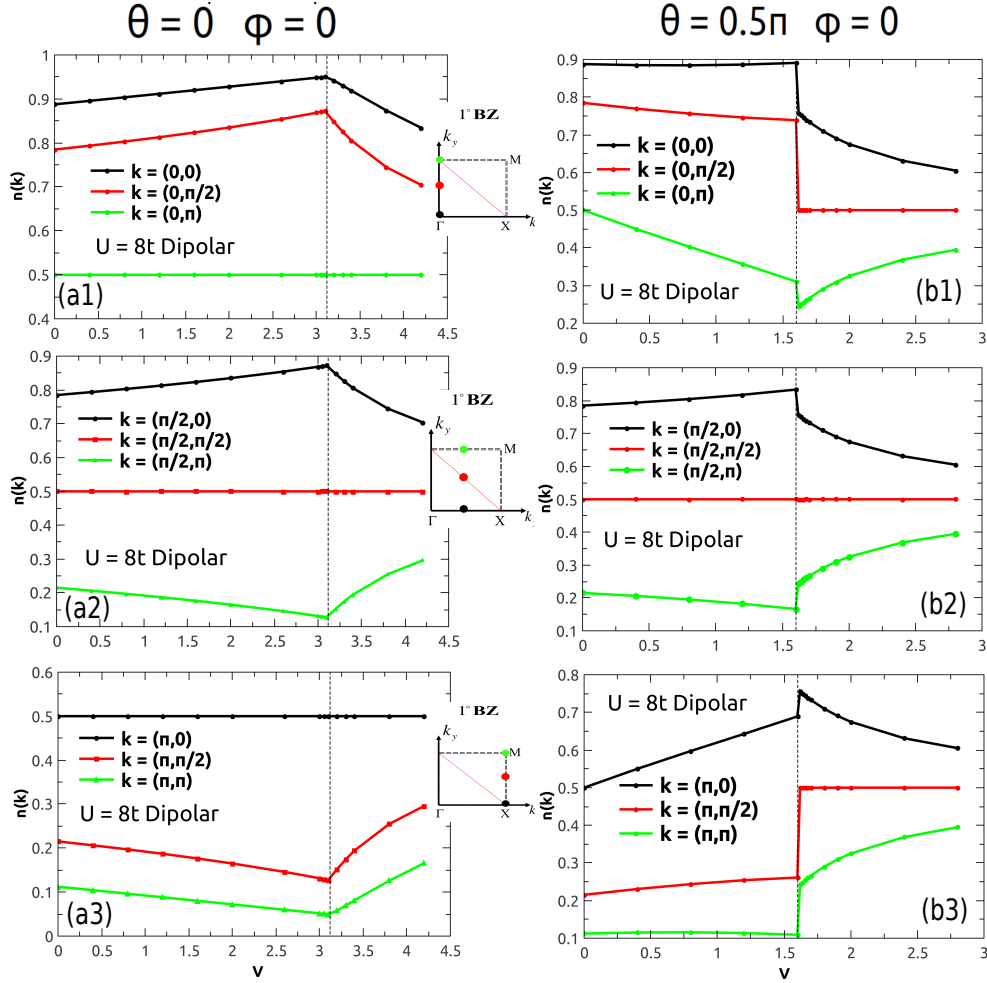
Figure 8.12: Results of the dEHM. In all panels is shown $n_\sigma(\mathbf{k})$ as a function of V for different $\mathbf{k}$-points and $U = 8t$. In (a1), (a2) and (a3) $\theta = 0$, and (b1), (b2) and (b3) $\theta = \pi/2$ and $\phi = 0$.

the opposite trend, i.e., it decreases with V in the AFM phase up to the AFM-CDW transition, and then increases in the CDW phase.

We now consider the dipolar interaction. Figures. 8.12 (a) show $n_\sigma(\mathbf{k})$ as function of V for $\theta = 0$ (isotropic interaction). The results resemble the ones found for the EHM, i.e., $n_\sigma(\mathbf{k})$ for $\mathbf{k} < \mathbf{k_F}$ (or $\mathbf{k} > \mathbf{k_F}$) provides a signature for the AFM-cbCDW transition at $V_c \approx 3.1t$. In adition $n_\sigma(\mathbf{k}) = 1/2$ for any V for $\mathbf{k} = (0,\pi)$, $(\pi,0)$ and $(\pi/2,\pi/2)$. On the other hand, Fig. 8.12 (b) shows $n_\sigma(\mathbf{k})$ as a function of V for $\theta = \pi/2$ and $\phi = 0$ (which leads to an anisotropic interaction with $V_x \neq V_y$). Differently from the isotropic

case, $n_\sigma[\mathbf{k} = (0, \pi)]$ and $n_\sigma[\mathbf{k} = (\pi, 0)]$ are not V-independent. Due to the breakdown of lattice rotation symmetry, Eq. (8.13) does not hold for these $\mathbf{k}$-points. Thus the presence of an anisotropic interaction induces fundamental modifications in the occupation of the modes $\mathbf{k} = (0, \pm\pi)$ and $\mathbf{k} = (\pm\pi, 0)$. Furthemore, for the other $\mathbf{k}$ modes, n_σ still provides a signature for the AFM-dCDW transition at $V_c \approx 1.6t$.

8.6   Conclusions

In this work we used the Lanczos method to study the dEHM at half-filling. The anisotropic character of the dipolar interaction induces different kinds of CDW phases: cbCDW and hCDW. These phases compete with the AFM phase when the non local interaction V varies. For $\phi = 0$ we have proposed a phase diagram in the space of parameters V and θ. One interesting result is that the competition between the cbCDW and the hCDW phase broadens the region in the phase diagram in which the AFM correlations dominate. Futhermore the variation of θ can induce different AFM-CDW transitons, such as the cbCDW-AFM-hCDW one.

We have also ivestigated the momentum occupation function for different $\mathbf{k}$ points within the 1BZ. For some $\mathbf{k}$-points, n_σ signals the AFM-CDW transitions induced by varying V. In addition, due to the particle-hole symmetry, $n_\sigma(\mathbf{k})$ is an interaction-independent function for a set of points when an isotropic interaction is considered, but not in the presence of anisotropy.

Chapter 9

Conclusions

In the first two works presented in this thesis (Chapter 4 and 5) we used the quantum Monte Carlo method stochastic series expansion (SSE) and linear spin-wave theory to study localized spin systems described by Heisenberg-like models.

In Chapter 4, we examined the effects of impurities in the proximity of an antiferromagnetic-singlet quantum citical point. Using QMC simulations we have shown that the impurity susceptibility, defined as the response of the AF order parameter to the removal of a small number of spins, exhibits a sharp peak at the QCP so that low disorder concentrations readily lead to long-range order. The critical concentration p_c for randomness to induce long-range AF order in the singlet phase, at moderate β, is well described by $\xi\sqrt{p_c} \sim 0.4$, where ξ is the spin-correlation length at $g > g_c$. Furthermore we also have obtained the spin relaxation rate $1/T_1$. In the clean system, we verified that $1/T_1$ is nearly temperature independent at the QCP, and have also shown that it has an abrupt increase on an impurity site, which provides a clear signature of the QCP.

In Chapter 5, we have investigated the magnetic ordering of the Heisenberg model on a one-third-depleted lattice. We used spin-wave theory and SSE QMC to determine the range of the ratio $g = J'/J$ in which an AFM phase exists at $T = 0$. We have established that an AFM-singlet quantum phase transition occurs for $g_c = 1.75 \pm 0.01$, and that AFM order persists to very small J'/J as a consequence of the fact that extended one-dimensional chains are still present when $J' = 0$. The itinerant limit described by the

Hubbard model was also examined; the determinantal QMC simulations used to study the HM was performed by the first author of Ref.[4]. The critical interaction strength $U_c \sim 3.87$ for $t' = t$(honeycomb limit), in which the semimetal-AFM takes place, was shown to increase with the anisotropy $t' \neq t$, where t'/t is the ratio of the hoppings of the two bonds.

The other line of problems that we explored here (Chapater 6 and 8) was motivated by ultracold atoms in optical lattice (OL) experiments. In these works we used the LD + TABC method to study ground state properties of Hubbard-like models.

In Chapter 6, we considered the two-dimensional OL Hubbard model. We show that fermionic atoms trapped in 2D OL display several interesting features when analyzed in terms of an effective density, $\rho \approx NV_t$ (N is the number of atoms in the cloud, and V_t is the trap opening). As the trap narrows, a Mott core forms at some ρ_c, which, upon further narrowing, becomes a Mott ring at ρ_m. The fraction of atoms in a Mott state displays a maximum at ρ_m, so that the number of atoms in a Mott state does not grow with U/W beyond the ring-core transition. A phase diagram for the boundaries $\rho_m(U/W)$ and $\rho_c(U/W)$ was proposed, which should be useful in the experimental control of the geometry of the Mott state. These special densities can be experimentally identified through the global compressibility and the double occupancy.

We have also obtained the single-particle spectral function, $A(\mathbf{k}, \omega)$, for the one-dimensional EHM using the TABC + LD method in Chapter 7. At half-filling we revisited the issue of spin-charge separation in both the spin density wave (SDW) and charge density wave (CDW) insulating phases. As previously shown in the literature, we show that no spin-charge separation takes place in the CDW phase. We also studied the evolution of the density of states (DOS) upon doping in both the Mott and CDW-metal transitions by quantifying the spectral weight induced at the Fermi level, W_{FL}. The evolution of DOS with doping is qualitatively different for the two transitions. While for the Mott transition, $W_{FL} > \delta$, in the CDW-metal, $W_{FL} \approx \delta/2$, and the behaviour of $A(\mathbf{k}, \omega)$ is well

described by a rigid band picture. In contrast, doping the insulating quarter-filled CDW system with electrons leads to $W_{FL} > \delta$, as it occurs for the Mott transition.

In Chapter 8, we considered the two-dimensional dipolar Extended Hubbard model (dEHM) at half-filling. The study of this model has been motivated by recent experiments with dipolar atoms in OL. Contrary to the half-filled 2D homogeneous HM, which has been intensively explored in the literature, the dEHM in the regime of parameters explored here has not been discussed before. For this reason, we just focused on the homogeneous properties of dEHM, and did not consider any trapping potential. We have shown that the anisotropic character of the dipolar interactions can give rise to different CDW phases. These phases compete with the AFM phase as the non local interaction V varies. In addition, the variation of the dipolar interaction, induced by changing the direction of the dipoles, leads to different AFM-CDW transitions. We have also shown that the momentum occupation function provides a signature for the AFM-CDW transition as a function of V.

Appendix A

Hubbard model

The Hubbard model (HM) offers one of the simplest ways to understand how the interactions between electrons can give rise to Mott insulating, magnetic, and superconducting phases in a solid. It was proposed in the early 1960's and was initially applied to understand the behaviour of the transition metal monoxides (FeO, NiO, CoO) compounds which are antiferromagnetic Mott insulators, yet had been predicted to be metalic by methods that do not consider the effects of strong correlations [102]. More recently, the HM has been intensively studied in the context of optical lattices experiments, as discussed on this thesis.

The HM Hamiltonian is

$$
\mathcal{H} = - t \sum_{\langle \mathbf{i},\mathbf{j} \rangle, \sigma} \left(c_{\mathbf{i}\sigma}^{\dagger} c_{\mathbf{j}\sigma} + h.c. \right) + U \sum_{\mathbf{i}} \left(n_{\mathbf{i}\uparrow} - \frac{1}{2} \right) \left(n_{\mathbf{i}\downarrow} - \frac{1}{2} \right)
$$
$$
- \mu \sum_{\mathbf{i}} (n_{\mathbf{i}\uparrow} + n_{\mathbf{i}\downarrow}), \tag{A.1}
$$

where the first term is the hopping term, the second one is the interaction energy (it has been written in the particle-hole symmetric form; see below), and the final term is the chemical potential which controls the filling.

The purpuse of this Appendix is to present some properties of HM in the two extremes, $U = 0$ and $U \to \infty$, and to discuss the particle-hole symmetry. We only include topics which are relevant to this thesis and, therefore, many interesting aspects of the HM have

been omitted.

A.1 Particle-hole symmetry

The Hubbard Hamiltonian has a particle-hole (ph) symmetry which allows us to relate its properties for different set of parameters. We consider the ph transformation by introducing the new fermionic operators, $\tilde{c}_{i\sigma}^\dagger$ and $\tilde{c}_{i\sigma}$, which exchange the role of creation and destruction:

$$c_{\mathbf{i}\sigma} = (-1)^{\mathbf{i}}\tilde{c}_{\mathbf{i}\sigma}^\dagger$$
$$c_{\mathbf{i}\sigma}^\dagger = (-1)^{\mathbf{i}}\tilde{c}_{\mathbf{i}\sigma}. \tag{A.2}$$

The ph transformation for the number operator is

$$n_{\mathbf{i}\sigma} = 1 - \tilde{n}_{\mathbf{i}\sigma},$$

where $\tilde{n}_{\mathbf{i}\sigma} = \tilde{c}_{\mathbf{i}\sigma}^\dagger \tilde{c}_{\mathbf{i}\sigma}$.

Let us now consider what happens to the Hamiltonian under the ph transformation. Here we consider a bipartite lattice, i.e., a lattice that can be divided into two sublattices A and B in such a way that a site in A has all its neighbours in B and vice-versa. As examples of bipartite lattices, we mention the square and the honeycomb lattices.

The hopping term transforms as

$$c_{\mathbf{i}\sigma}^\dagger c_{\mathbf{j}\sigma} = (-1)^{\mathbf{i}+\mathbf{j}}\tilde{c}_{\mathbf{i}\sigma}\tilde{c}_{\mathbf{j}\sigma}^\dagger = \tilde{c}_{\mathbf{j}\sigma}^\dagger \tilde{c}_{\mathbf{i}\sigma},$$

where $(-1)^{\mathbf{i}+\mathbf{j}} = (-1)$ for a bipartite lattice. It is then straightforward to show that, under the ph transformations, the HM is

$$\mathcal{H} = -t\sum_{\langle \mathbf{i},\mathbf{j}\rangle,\sigma} \left(\tilde{c}_{\mathbf{i}\sigma}^\dagger \tilde{c}_{\mathbf{j}\sigma} + h.c. \right) + U\sum_{\mathbf{i}} \left(\tilde{n}_{\mathbf{i}\uparrow} - \frac{1}{2} \right) \left(\tilde{n}_{\mathbf{i}\downarrow} - \frac{1}{2} \right)$$
$$+ \mu\sum_{\mathbf{i}} (\tilde{n}_{\mathbf{i}\uparrow} + \tilde{n}_{\mathbf{i}\downarrow}) + C, \tag{A.3}$$

where C is a constant. Thus the HM with a given μ maps into the HM with the sign of the chemical potential reversed, and that for $\mu = 0$, the HM is invariant. In fact this implies that the whole phase diagram of the HM on a bipartite lattice is symmetric about half-filling, as we discuss below.

The ph transformation of the particle density operator for a given μ leads to

$$\langle n_{\mathbf{i}\uparrow} + n_{\mathbf{i}\downarrow} \rangle = 2 - \langle \tilde{n}_{\mathbf{i}\uparrow} + \tilde{n}_{\mathbf{i}\downarrow} \rangle .$$

Thus we obtain

$$n(\mu) + n(-\mu) = 2. \tag{A.4}$$

Where we use the fact that $\tilde{n}(\mu) = n(-\mu)$. Equation (A.4) alow us to conclude that for $\mu = 0$ the system is at half-filling; moreover at this filling the HM is invariant under the ph transformation.

It is worth to mentioning here that the extended Hubbard models considered in Chapters 7 and 8 is also ph symmetric at the half-filling.

A.2   The noninteracting limit $(U = 0)$

In the absence of of interactions $(U = 0)$, it is convenient to transform operators to momentum space by defining

$$c_{\mathbf{j}\sigma} = \frac{1}{\sqrt{N_s}} \sum_{\mathbf{k}} e^{i\mathbf{kj}} c_{\mathbf{k}\sigma}. \tag{A.5}$$

The non-interacting (NI) HM is diagonal in terms of these operators

$$H = \sum_{\mathbf{k}\sigma} (\epsilon(\mathbf{k}) - \mu) c_{\mathbf{k}\sigma}^{\dagger} c_{\mathbf{k}\sigma}, \tag{A.6}$$

where $\epsilon(\mathbf{k})$ is the dispersion relation. For a square lattice

$$\epsilon(\mathbf{k}) = -2t(\cos{(k_x)} + \cos{(k_y)}). \tag{A.7}$$

Figure A.1 (a) shows the Fermi surface for different fillings. In the half-filled case $(\mu = 0)$, the fact that $\epsilon(\mathbf{k}_F) = \epsilon(\mathbf{k}_F + \vec{\pi})$ means that there is a perfect nesting at the Fermi surface;
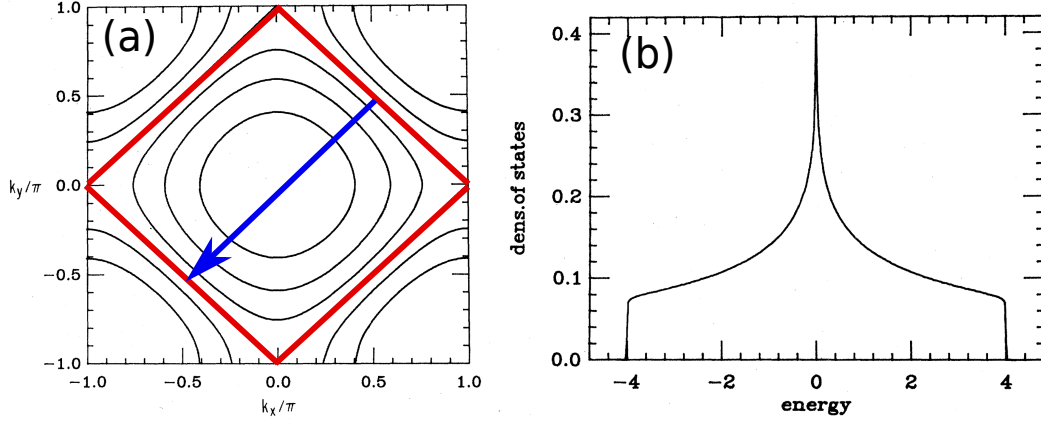
Figure A.1: (a) Fermi surface for the two-dimensional square lattice. Band fillings are $n = 0.25, 0.5, ..., 1.5$ starting from the inner surface. The Fermi surface of half-filled case is marked by a full red line. Note that it is nested; the blue arrow representes the AFM wave vector $\vec{\pi} = (\pi, \pi)$. (b) Density of states for the 2D square-lattice. The van Hove singularity at the origin is logarithmic. Both Figs. (a) and (b) were extracted from Ref. [103].

the nesting vector is $\vec{\pi} = (\pi, \pi)$. Furthermore, at this filling, the density of states (DOS) exhibits a van Hove singularity [103], see Fig. A.1 (b).

The nesting, the van Hove singularity and the particle-hole symmetry at half-filling have important consequences for the magnetic properties of the interacting system. In order to see these consequences, let us consider the $\mathbf{q}$-dependent magnetic susceptibility within the random-phase approximation (RPA) [104]

$$\chi(\mathbf{q}) = \frac{2\chi_0(\mathbf{q})}{1 - U\chi_0(\mathbf{q})}, \tag{A.8}$$

where $\chi_0(\mathbf{q})$ is the $\mathbf{q}$-dependent zero frequency susceptibility for the non-interacting case

$$\chi_0(\mathbf{q}) = -\frac{1}{N} \sum_{\mathbf{k}} \frac{f(\epsilon(\mathbf{q} + \mathbf{k})) - f(\epsilon(\mathbf{k}))}{\epsilon(\mathbf{q} + \mathbf{k}) - \epsilon(\mathbf{k})}, \tag{A.9}$$

$f(\epsilon)$ is the Fermi distribution function. $\chi_0(\mathbf{q})$ peak at values of $\mathbf{q}$ corresponding to the dominant magnetic arrangement. For the square lattice, $\mathbf{q} = (0, 0)$ and $\mathbf{q} = (\pi, \pi)$ correspond to ferromagnetic and antiferromagnetic (AFM) arrangements, respectively. Furthermore, the condition $U\chi_0(\mathbf{q}) > 1$, is the condition for a magnetic instability, and

the critical value of the interaction strength in which the magnetic transition takes place correponds to [105]

$$U = 1/\chi_0(\mathbf{q}).$$

For ph symmetric systems, the dispersion relation has the special property [104]

$$\epsilon(\mathbf{k} + \mathbf{Q}) = -\epsilon(\mathbf{k}), \tag{A.10}$$

where $\mathbf{Q}$ is the AFM wave vector defined by the bipartite structure of the lattice. For the square lattice $\mathbf{Q} = (\pi, \pi)$. Using the relation (A.10), we can write Eq. (A.9) as

$$\chi_0(\mathbf{Q}) = -\int \frac{N(\epsilon)f(\epsilon)}{\epsilon}d\epsilon, \tag{A.11}$$

where $N(\epsilon)$ is the density of states. For the half-filled square lattice, due to the van Hove singularity at the Fermi level, $\chi_0(\mathbf{Q})$ has a log-squared singularity at the AFM wave vector [103]. Hence RPA predicts that the critical value for the AFM transition is $U_c = 0$. Furthermore, at half-filling, the AFM mean-field solution has a finite gap, and the ground state corresponds to an insulating AFM for $U > 0$ [103].

Before closing this section, we use the same RPA arguments for the honeycomb lattice. In this case, the half-filled NI system is a semi-metal and the DOS is

$$N(\epsilon) \sim |\epsilon|,$$

i.e., it vanishes at the Fermi level. Hence, differently from the square lattice case, $\chi_0(\mathbf{Q})$ does not diverge, and RPA predicts that the transition to an insulating AFM state occurs for a finite value of U [105]. Quantum Monte Carlo simulations obtain $U_c \sim 3.87$ [64], [65], as discussed on Chapter 5.

A.3   Strong coupling limit $(U \to \infty)$

In this section, we consider that the system is at half-filling (i.e., $\mu = 0$) and $U \to \infty$. In this regime it is appropriate to use perturbation theory, where we assume that the
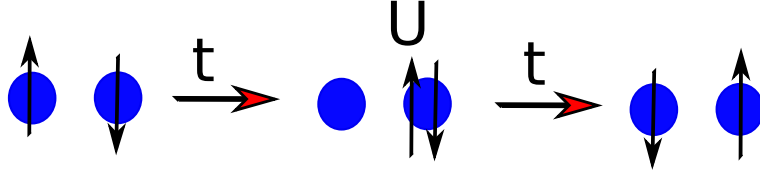
Figure A.2: Cartoon illustrating an example of the virtual hopping responsible for the superexchange interaction. In this case, two spins are exchanged through an intermediated doubly-occupied state.

interacting term of Eq. (A.1) is the non-perturbed part H_0, and the hopping one is the pertubation V. To zeroth order, we assume the atomic limit ($t = 0$). In this case, the ground state corresponds to configurations with just singly occupied sites, as for example

$$|\psi_0^n\rangle = |\uparrow_1, \downarrow_2, \uparrow_3, ..., \uparrow_{L-1}, \downarrow_L\rangle_{n=1}, |\downarrow_1, \downarrow_2, \downarrow_3, ..., \downarrow_{L-1}, \uparrow_L\rangle_{n=2}, ... \quad (A.12)$$

It is important to note that all configurations with just singly occupied sites have the same ground state energy, E_0. Thus the ground state is 2^{N_s}-fold degenerate (i.e., $n = 1, 2, ..., 2^{N_s}$), where N_s is the number of sites.

Let us now consider degenerate pertubation theory up to second order. Denoting by E_0 the ground state of the interacting term, H_0, and by E_m the other eigenenergies, $H_0|m\rangle = E_m|m\rangle$ for $E_m \neq E_0$. For two vectors $|\psi_0^i\rangle$ and $|\psi_0^j\rangle$, and up to second oder in V,

$$\langle\psi_0^i|H_{eff}|\psi_0^j\rangle = E_0 + \langle\psi_0^i|V|\psi_0^j\rangle + \sum_{|m\rangle \neq |\psi_0\rangle} \frac{\langle\psi_0^i|V|m\rangle\langle m|V|\psi_0^j\rangle}{E_0 - E_m}. \quad (A.13)$$

Thus, the degenerate pertubation theory leads to an effective Hamiltonian H_{eff}; which acts only in the degenerate subspace of H_0, and describes the relevant degrees of freedom in the regime that $U \to \infty$.

For the case discussed here, the charges are frozen in the sites, and the relevant degrees of freedom are the spins of the particles. In this case, the term responsible for the first-order corrections is null, while the second-order virtual hoppings generate a superexchange

interaction between the spins, see Fig. A.2; and the effective Hamiltonian is

$$H_{eff} = J \sum_{\langle i,j \rangle} \mathbf{S_i} \cdot \mathbf{S_j}, \tag{A.14}$$

whith $J = 4t^2/U$. For both the square and honeycomb lattices, QMC simulations obtain an AFM ground state for the aforementioned Hamiltonian [56], [106].

Appendix B

Twisted boundary conditions in tilted clusters

In this Appendix we discuss how twisted boundary conditions are implemented on the tilted clusters of Fig. B.1. In terms of the creation and destruction operators, an arbitrary boundary condition is given by the following relation,

$$c^{\dagger}_{\mathbf{r}',\sigma} = e^{-i\theta_l} c^{\dagger}_{\mathbf{r},\sigma},$$

$$c_{\mathbf{r}',\sigma} = e^{i\theta_l} c_{\mathbf{r},\sigma} \tag{B.1}$$

where $\mathbf{r}$ e $\mathbf{r}'$ are two sites connected by the translation vector (equivalent sites),

$$\mathbf{R} = n_1 \mathbf{L_1} + n_2 \mathbf{L_2}.$$

Here n_1 and n_2 are integers, and $\mathbf{L_1}$ and $\mathbf{L_2}$ are the vectors describing the periodicity of the cluster; see Fig. B.1. The twisted boundary conditions (TBC) θ_1 and θ_2 are considered in both $\mathbf{L_1}$ and $\mathbf{L_2}$ directions.

In $\mathbf{k}$-momentum space, the creation and destruction operators are given by,

$$c^{\dagger}_{\mathbf{r},\sigma} = \frac{1}{\sqrt{N}} \sum_{\mathbf{k}} e^{-i\mathbf{k}\mathbf{r}} c^{\dagger}_{\mathbf{k},\sigma},$$

$$c_{\mathbf{r},\sigma} = \frac{1}{\sqrt{N}} \sum_{\mathbf{k}} e^{i\mathbf{k}\mathbf{r}} c_{\mathbf{k},\sigma}. \tag{B.2}$$
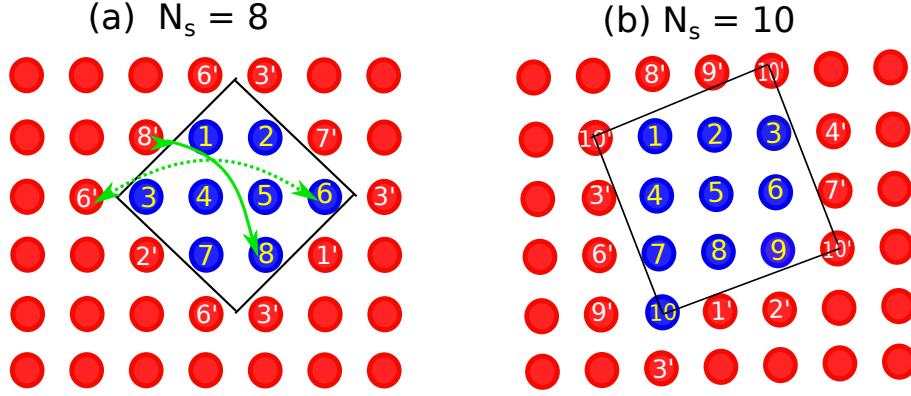
Figure B.1: Tilted two dimensional clusters. The square lattice can be generated by suitable translations of the clusters; $\mathbf{R} = n_1\mathbf{L_1} + n_2\mathbf{L_2}$, where n_1 and n_2 are integers. Here $\mathbf{L_1}$ and $\mathbf{L_2}$ are the vectors of peiodicity of the cluster. (a) For $N_s = 8$ cluster, $\mathbf{L_1} = (-2, 2)$ and $\mathbf{L_2} = (2, 2)$, and (b) for $N_s = 10$ $\mathbf{L_1} = (-1, 3)$ and $\mathbf{L_2} = (3, 1)$. The TBC is considered both in the $\mathbf{L_1}$ direction and in the $\mathbf{L_2}$ direction, θ_1 and θ_2, respectively. In order to guarantee translation symmetry one must consider the extra TBC $\theta_{(1,2)}$, see text.

Using the twisted boundary condition, Eq. (B.1), we can estabilish the conditions for quantization of $\mathbf{k}$-points,

$$\mathbf{k} \cdot (\mathbf{r'} - \mathbf{r}) = 2\pi n + \theta_l. \tag{B.3}$$

It is important to mention that Eq. (B.3) must be satisfied in order to guarantee translational symmetry.

In order to satisfy Eq. (B.3), we must consider the following boundary conditions for the $N_s = 8$ cluster,

$$c^\dagger_{8',\sigma} = e^{-i\theta_1} c^\dagger_{8,\sigma} \tag{B.4}$$

$$c^\dagger_{7',\sigma} = e^{-i\theta_2} c^\dagger_{7,\sigma} \tag{B.5}$$

$$c^\dagger_{6',\sigma} = e^{-i\theta_{(1,2)}} c^\dagger_{6,\sigma}, \tag{B.6}$$

where TBC θ_1 is considered between the sites connected by $\mathbf{L_1}$ (e.g., sites 8 and 8′ in Fig. B.1 (a)); θ_2 is considered between the sites connected by $\mathbf{L_2}$; and the extra TBC $\theta_{(1,2)}$ is considered between the sites connected by $\bar{\mathbf{R}} = -\mathbf{L_1} + \mathbf{L_2}$; see Fig. B.1 (a). Conditions

(B.4) and (B.5) lead to the quantization of $\mathbf{k}$-points in the $\mathbf{L_1}$ and $\mathbf{L_2}$ directions,

$$k_1 = \frac{2\pi m_1 + \theta_1}{L}$$
$$k_2 = \frac{2\pi m_2 + \theta_2}{L}. \tag{B.7}$$

Here $L = 2\sqrt{2}$ is the linear size of the tilted cluster, and m_1 and m_2 are integers; we consider $\mathbf{k} = k_1(\mathbf{L_1}/L_1) + k_2(\mathbf{L_2}/L_2)$. Furthemore, the extra conditon (B.6) leads to

$$k_2 - k_1 = \frac{2\pi m_{(1,2)} + \theta_{(1,2)}}{L} \tag{B.8}$$

Taking (B.7) into (B.8) yields

$$\theta_2 - \theta_1 - \theta_{(1,2)} = 2\pi(m_{(1,2)} + m_1 - m_2) = 2\pi\bar{m}, \tag{B.9}$$

where $\bar{m}$ is an integer number. Thus, in order to satisfy Eq. (B.3), one must consider the following constraint between the TBC θ_1, θ_2 and $\theta_{(1,2)}$,

$$\theta_{(1,2)} = \theta_2 - \theta_1 - 2\pi\bar{m}. \tag{B.10}$$

The BC for the $N_s = 10$ cluster is given by,

$$c^\dagger_{1',\sigma} = e^{-i\theta_1} c^\dagger_{1,\sigma} \tag{B.11}$$

$$c^\dagger_{7',\sigma} = e^{-i\theta_2} c^\dagger_{7,\sigma} \tag{B.12}$$

$$c^\dagger_{6',\sigma} = e^{-i\theta_{(1,2)}} c^\dagger_{6,\sigma} \tag{B.13}$$

where the TBC θ_1 is considered between the sites connected by $\mathbf{L_1}$; θ_2 is considered between the sites connected by $\mathbf{L_2}$; and the extra TBC $\theta_{(1,2)}$ is considered between the sites connected by $\bar{\mathbf{R}} = \mathbf{L_1} + \mathbf{L_2}$; see Fig. B.1 (b), Similarly to the discussion for the $N_s = 8$ cluster, Eq. (B.3) leads to the following constraint between the TBC θ_1, θ_2 and $\theta_{(1,2)}$,

$$\theta_{(1,2)} = \theta_1 + \theta_2 - 2\pi\bar{m}. \tag{B.14}$$

Appendix C

Linear spin-wave theory

In this Appendix we present the Linear Spin Wave Theory (LSWT) used to calculate the sttagared magnetization of the 1/3-depleted lattice on Chapter 5; for comparison we also show the results for the magnetization of the anisotropic square lattice, i.e., $J_x \neq J_y$. The Heisenberg Hamiltonian for a bipartite system with $N_A = N_B$ (N_α is the number of sites on sublattice α) is

$$\mathcal{H} = \sum_{\mathbf{i} \in A, \delta} J(\delta) S_{\mathbf{i}}^A S_{\mathbf{i}+\delta}^B, \tag{C.1}$$

where $\mathbf{i}$ runs over the sites of subsystem A, and $\mathbf{i} + \delta$ are the nearest-neighbour sites of site $\mathbf{i}$. For the 1/3 depleted lattice

$$\delta_1 = a(1,0), \quad \delta_2 = a(0,1), \quad \delta_3 = a(-1,-1), \tag{C.2}$$

where a is the lattice parameter, we set $a = 1$, and $J(1) = J(2) = J$, $J(3) = J'$.

C.1 Linear spin wave theory (LSWT)

The spin operators can be expressed in terms of bosonic operators as introduced by Holstein-Primakoff (HP) [107]. The HP operators are defined with respect to a given direction, here we consider the $\mathbf{z}$ direction:

$$S_i^z = S - a_i^\dagger a_i, \quad S_i^+ = \sqrt{2} f(a_i^\dagger a_i) a_i, \quad S_i^- = \sqrt{2} a_i^\dagger f(a_i^\dagger a_i),$$

and,

$$f(a_i^\dagger a_i) = \sqrt{1 - \frac{a_i^\dagger a_i}{2S}}$$

The function $f(a_i^\dagger a_i)$ can be expanded in powers of $1/S$. In the linear approximation, we set $f(a_i^\dagger a_i) = 1$. In this case, we are able to obtain a noninteracting "spin wave" Hamiltonian. This approximation describes small fluctuations around the broken symmetry phase of the Heisenberg model [107], Eq. (C.1).

For a bipartite system we choose two set of HP operators. Ones in sublattice A in the **z** direction $(A \to (a_i^\dagger, a_i))$; and ones in the sublattice B in the $-$**z** direction $(B \to (b_i^\dagger, b_i))$. This arrangement represents an AFM classical state. The rotated spins on subsystem B is defined as:

$$S_j^{z\prime} = -S_j^z, \quad S_j^{-\prime} = S_j^+, \quad S_j^{+\prime} = S_j^-,$$

where $j \in B$. Eqquation (C.1) can then be written as

$$\mathcal{H} = \sum_{\mathbf{i} \epsilon A, \delta} J(\delta)(-S^2 + S(a_\mathbf{i}^\dagger a_\mathbf{i} + b_{\mathbf{i}+\delta}^\dagger b_{\mathbf{i}+\delta}) + S(a_\mathbf{i} b_{\mathbf{i}+\delta} + a_\mathbf{i}^\dagger b_{\mathbf{i}+\delta}^\dagger)),$$

and considering the Fourier transformation of the HP operators,

$$a_\mathbf{i} = \frac{1}{\sqrt{N_A}} \sum_\mathbf{k} e^{i\mathbf{k}\mathbf{r}_i} a_\mathbf{k},$$

$$b_\mathbf{i} = \frac{1}{\sqrt{N_B}} \sum_\mathbf{k} e^{i\mathbf{k}\mathbf{r}_i} b_\mathbf{k}, \tag{C.3}$$

where **k**'s are the wave vectors, the Heisenberg Hamiltonian is

$$\mathcal{H} = -NS^2 J^\star + S \sum_{\mathbf{k},\delta} J(\delta)(a_\mathbf{k}^\dagger a_\mathbf{k} + b_{-\mathbf{k}}^\dagger b_{-\mathbf{k}}) + S \sum_\mathbf{k} (\gamma(\mathbf{k}) a_\mathbf{k} b_{-\mathbf{k}} + \gamma^\dagger(\mathbf{k}) a_\mathbf{k}^\dagger b_{-\mathbf{k}}^\dagger), \tag{C.4}$$

where $J^\star = \sum_\delta J(\delta)$ and $\gamma(\mathbf{k}) = \sum_\delta J(\delta) e^{-i\mathbf{k}\mathbf{r}_\delta}$.

This Hamiltonian can be diagonalized with the aid of the Bogoliubov transformation

$$\alpha_\mathbf{k} = u_\mathbf{k} \, a_\mathbf{k} + v_\mathbf{k} \, b_{-\mathbf{k}}^\dagger, \qquad \beta_\mathbf{k} = v_\mathbf{k} \, a_\mathbf{k}^\dagger + v_\mathbf{k} \, b_{-\mathbf{k}}.$$

where $\alpha_{\mathbf{k}}$ and $\beta_{\mathbf{k}}$ satisfy the canonical bosonic commutation relations when $|u_{\mathbf{k}}|^2 - |v_{\mathbf{k}}|^2 = 1$. Using the inverse transformation

$$a_{\mathbf{k}} = u_{\mathbf{k}}^* \, \alpha_{\mathbf{k}} - v_{\mathbf{k}} \, \beta_{\mathbf{k}}^\dagger, \qquad b_{-\mathbf{k}} = u_{\mathbf{k}}^* \, \beta_{\mathbf{k}} - v_{\mathbf{k}} \, \alpha_{\mathbf{k}}^\dagger,$$

in Eq. (C.4), we obtain

$$\mathcal{H} = -NS^2 J^\star + S \sum_{\mathbf{k}} [J^\star(|u_{\mathbf{k}}|^2 + |v_{\mathbf{k}}|^2) - \gamma(\mathbf{k})u_{\mathbf{k}}^* v_{\mathbf{k}} - \gamma^\dagger(\mathbf{k})v_{\mathbf{k}}^* u_{\mathbf{k}}]$$

$$+ [J^\star(|u_{\mathbf{k}}|^2 + |v_{\mathbf{k}}|^2) - \gamma(\mathbf{k})u_{\mathbf{k}}^* v_{\mathbf{k}} - \gamma^\dagger(\mathbf{k})v_{\mathbf{k}}^* u_{\mathbf{k}}](\alpha_{\mathbf{k}}^\dagger \alpha_{\mathbf{k}} + \beta_{\mathbf{k}}^\dagger \beta_{\mathbf{k}}) +$$

$$(2J^\star u_{\mathbf{k}}^* v_{\mathbf{k}}^* - \gamma(\mathbf{k})u_{\mathbf{k}}^* u_{\mathbf{k}}^* - \gamma^\dagger(\mathbf{k})v_{\mathbf{k}}^* v_{\mathbf{k}}^*)\alpha_{\mathbf{k}} \beta_{\mathbf{k}} +$$

$$(2J^\star u_{\mathbf{k}} v_{\mathbf{k}} - \gamma(\mathbf{k})v_{\mathbf{k}} v_{\mathbf{k}} - \gamma^\dagger(\mathbf{k})u_{\mathbf{k}} u_{\mathbf{k}})\alpha_{\mathbf{k}}^\dagger \beta_{\mathbf{k}}^\dagger.$$

Considering that the coefficients of $\alpha_{\mathbf{k}}^\dagger \beta_{\mathbf{k}}^\dagger$ and $\alpha_{\mathbf{k}} \beta_{\mathbf{k}}$ are zero, we finally obtain the noninteracting "spin wave" Hamiltonian

$$\mathcal{H} = -NS^2 J^\star + S \sum_{\mathbf{k}} (\omega(J^\star, \mathbf{k}) - J^\star) + S \sum_{\mathbf{k}} \omega(J^\star, \mathbf{k})(\alpha_{\mathbf{k}}^\dagger \alpha_{\mathbf{k}} + \beta_{\mathbf{k}}^\dagger \beta_{\mathbf{k}}), \qquad (C.5)$$

where,

$$\omega(J^\star, \mathbf{k}) = J^\star \sqrt{1 - \frac{|\gamma(\mathbf{k})|^2}{J^{\star 2}}}, \qquad (C.6)$$

C.1.1 Staggered magnetization

The staggered magnetization is given by

$$m_s = \frac{1}{N} \left(\sum_{i \epsilon A} \langle S_i^z \rangle - \sum_{i \epsilon B} \langle S_i^z \rangle \right) = S - \frac{1}{N} \sum_{\mathbf{k}} \left\langle a_{\mathbf{k}}^\dagger a_{\mathbf{k}} + b_{\mathbf{k}}^\dagger b_{\mathbf{k}} \right\rangle \qquad (C.7)$$

Writing the above expression in terms of the Bogoliubov operators, we obtain

$$m_s = S + \frac{1}{2} - \frac{1}{N} \sum_{\mathbf{k}} (n_{\mathbf{k}} + 1) \left(\frac{1}{\sqrt{1 - \frac{|\gamma(\mathbf{k})|^2}{J^{\star 2}}}} \right), \qquad (C.8)$$

where $n_{\mathbf{k}} = \left\langle \alpha_{\mathbf{k}}^\dagger \alpha_{\mathbf{k}} + \beta_{\mathbf{k}}^\dagger \beta_{\mathbf{k}} \right\rangle = \frac{1}{e^{\omega(\mathbf{k})/k_B T} - 1}$. The vectors $\mathbf{k}$ are obtained by imposing periodic boundary condtion (PBC) in a finite system. We now show m_s for the anisotropic square lattice and 1/3 depleted lattice.

Square Lattice

For the anisotropic square lattice (J_x, J_y)

$$\gamma(\mathbf{k}) = 2\left(J_x cos(k_x) + J_y cos(k_y)\right),$$

where, $k_i = \frac{2\pi n_i}{L_i}$, with $i = x$ or y, and $n_i = 0, 1, 2, ..., L - 1$; $2L$ is the linear size of the square lattice.

Figure C.1 shows the zero temperature sttagered magnetization m_s as function of $g = J_y/J_x$. For $g = 0$, the system is a bunch of 1d chains and there is no AFM order $m_s = 0$ at $T = 0$. A interesting prediction of LSWT is that a finite "small" coupling $g^* \approx 0.033$ is required in order for AFM order appears [108]. However, more accurate calculations of the anisotropic model shows that $g^* = 0$ [109].
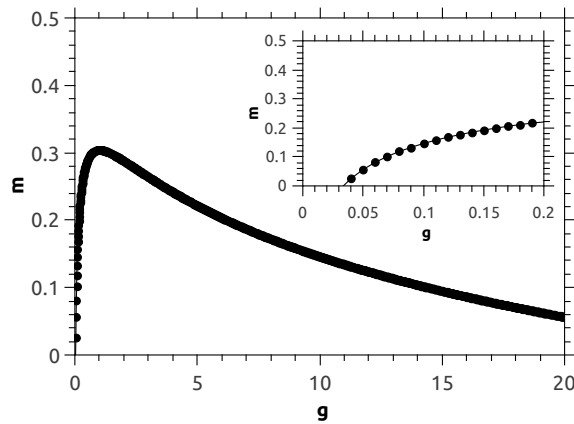
Figure C.1: Staggered magnetization of the anitropic square lattice in the LSWT. g dependence of m_s. The inset shows a blow up for $g \sim 0$.

1/3 depleted lattice

For the 1/3-depleted lattice we choose the real space basis

$$\mathbf{a_1} = (2, -1), \quad \mathbf{a_2} = (1, 1).$$

and the reciprocal space basis,

$$\mathbf{b_1} = \frac{1}{3}(1,-1), \quad \mathbf{a_2} = \frac{1}{3}(1,2).$$

Thus,

$$\gamma(\mathbf{k}) = J\left[e^{-i\left(\frac{k_x+k_y}{3}\right)} + e^{-i\left(\frac{k_x-2k_y}{3}\right)}\right] + J'e^{i\left(\frac{2k_x-k_y}{3}\right)},$$

where, $k_i = \frac{2\pi n_i}{L_i}$, with $n_i = 0,1,2,...,L_i-1$, and L_i is the linear size in the $\mathbf{a_i}$ direction.

Figure 5.2 (a) of Chapater 5 shows the zero temperature sttagered magnetization m_s as function of $g = J'/J$ obtained in the LSWT and quantum Monte Carlo simulations. For $g = 1$, the 1/3-depleted lattice is equivalent to the honeycomb lattice. We obtained the same values of Ref. [66] for m_s, $m_s(\text{QMC}) = 0.26$ and $m_s(\text{LSWT}) = 0.24$. For $g = 0$, the 1/3 lattice is a bunch of "zig-zag" chains and, as it happens in the anisotropic square lattice, there is no AFM order, $m_s = 0$. In this case, LSWT also predicts that a finite coupling is required in order for AFM order appears, $g^* = 0.065 \pm 0.005$. Furthermore, this model describes a quantum phase transition between a AFM and a singlet phase (formed between two "zig-zag" chains) at $g = g_c$. We obtain that $g_c(\text{LSWT}) = 6.2 \pm 0.02$ and $g_c(\text{QMC}) = 1.75 \pm 0.01$.

Appendix D

Impurities near an antiferromagnetic-singlet quantum critical point

Impurities near an antiferromagnetic-singlet quantum critical point

T. Mendes-Santos,[1,2] N. C. Costa,[1] G. Batrouni,[3,4,5] N. Curro,[2] R. R. dos Santos,[1] T. Paiva,[1] and R. T. Scalettar[2]

[1]*Instituto de Física, Universidade Federal do Rio de Janeiro, Caixa Postal 68.528, 21941-972 Rio de Janeiro Rio de Janeiro, Brazil*
[2]*Department of Physics, University of California, Davis, California 95616, USA*
[3]*Université Côte d'Azur, INLN, CNRS, France*
[4]*MajuLab, CNRS-UNS-NUS-NTU International Joint Research Unit UMI 3654, Singapore*
[5]*Centre for Quantum Technologies, National University of Singapore, 2 Science Drive 3, Singapore 117542*
(Received 6 July 2016; revised manuscript received 27 January 2017; published 15 February 2017)

Heavy-fermion systems and other strongly correlated electron materials often exhibit a competition between antiferromagnetic (AF) and singlet ground states. Using exact quantum Monte Carlo simulations, we examine the effect of impurities in the vicinity of such an AF-singlet quantum critical point (QCP), through an appropriately defined "impurity susceptibility" χ_{imp}. Our key finding is a connection within a single calculational framework between AF domains induced on the singlet side of the transition and the behavior of the nuclear magnetic resonance (NMR) relaxation rate $1/T_1$. We show that local NMR measurements provide a diagnostic for the location of the QCP, which agrees remarkably well with the vanishing of the AF order parameter and large values of χ_{imp}.

I. INTRODUCTION

In materials, such as the cuprate superconductors, mobile impurities introduced, e.g., via the replacement of La by Sr, are known to destroy antiferromagnetic (AF) order very rapidly [1,2]. Long-range spin correlations are somewhat more robust to static scatterers, e.g., via Zn substitution for Cu in the same materials [3–5]. This competition of AF and chemical doping is a central feature of many other strongly correlated systems, including Li doping in nickel oxides [6,7], spin chains [8], and ladders [9] and has been explored by quantum Monte Carlo (QMC) approaches in single band fermion models [10] and their strong-coupling spin limits [11].

Materials with multiple fermionic bands or localized spins in multichain or multilayer geometries offer an additional richness to the effect of impurities on AF since even in the clean limit they can exhibit a quantum critical point (QCP) separating AF and singlet phases. Although impurities reduce AF deep in the ordered phase, nearer to the QCP, they can increase AF and even, beginning in the quantum disordered phase, *induce* AF by breaking singlets [8,9]. This has recently been explored in heavy-fermion materials where Cd doping of superconducting CeCoIn$_5$ induces long-range magnetic order [12]. The underlying mechanism is believed to be a local reduction of conduction electron-local moment (c-f) hybridization on the Cd sites, suppressing the singlet energy gain. The experimental observation that the NMR spectra linewidths broaden with Cd substitution indicates that Cd impurities induce AF puddles around them. The size of these AF regions shrinks with pressure, which increases this hybridization towards its value in the absence of disorder, ultimately yielding a revival of superconductivity (SC). However, as indicated by NMR relaxation rate $1/T_1$ measurements, the resulting phase is quite heterogeneous [13] not unlike the stripe and nematic orders which coexist with superconductivity in the cuprates. Prior theoretical work examined domains within a mean-field theory of competing AF and SC orders [13].

A useful initial route to a better understanding of the mechanisms of the evolution of the NMR relaxation rate $1/T_1$

is to single out the contributions from the spin degrees of freedom. This is the approach we follow here in which two antiferromagnetically coupled layers give rise to a competition between an interlayer-singlet-rich and an AF phase. By allowing dilution in the second layer, thus breaking interlayer singlets, one mimics the reduction of c-f hybridization. In addition, from a pragmatic perspective, accessible system sizes for QMC simulations of itinerant fermion systems are not sufficiently large to encompass multiple impurities and carefully study finite-size effects. However, it is known that many of the qualitative features of itinerant AF models, such as the Hubbard Hamiltonian, are reflected in their spin counterparts [14,15], notably the successful modeling of the Knight-shift anomaly, certain aspects of which can be captured either with descriptions in terms of localized spins [16] or itinerant electrons [17]. This paper reports QMC simulations of a disordered bilayer Heisenberg Hamiltonian, characterizing its physics within an exact treatment of quantum many-body fluctuations. Key findings are as follows: (i) An appropriately defined impurity susceptibility captures both the inhibition of AF order deep in the ordered phase and its sharp enhancement near the QCP; (ii) quantitative determination of the AF regions induced by impurities and the criterion for their coalescence into a state with long-range order at experimentally relevant temperature scales; (iii) verification of the suggestion that $1/T_1$ is very weakly temperature dependent at the QCP in the clean system. We also establish that the local value of $1/T_1$ at an impurity site increases abruptly at the QCP and resembles the behavior of the clean system "far away" from the impurity.

QMC, in combination with analytic scaling arguments, has previously been used to study the loss of magnetic order and multicritical points in bilayers where the dilution at a given site discards simultaneously the spins in *both* layers [18]. Interesting topological considerations arise from the removal of a *single* spin from a bilayer system in the singlet phase since an unpaired spin-1/2 object is left behind [19]. QMC has been used to study the spin texture produced by a single impurity [20] as well as the onset of AF order in lattices of dimerized chains [21].

II. MODEL AND METHODS

We consider the spin-1/2 AF Heisenberg bilayer Hamiltonian,

$$H = \sum_{\langle ij \rangle, \alpha} J^\alpha \vec{S}_i^\alpha \cdot \vec{S}_j^\alpha + g \sum_i \vec{S}_i^1 \cdot \vec{S}_i^2, \qquad (1)$$

where subscripts i, j denote spatial sites on a square lattice and superscripts $\alpha = 1, 2$ label the two layers. We study the case when the intraplane exchange constants $J^\alpha = J$ are the same, and we choose $J = 1$ to set the energy scale. g is the interlayer exchange.

The Heisenberg bilayer model considered here describes the competition between AF order and singlet formation, such as in the Kondo effect. The spin-1/2 Heisenberg Hamiltonian has been studied widely as a model of quantum magnetism, in particular, as the AF parent compounds of the cuprate superconductors. In that context, the establishment, via QMC simulations, that long-range order (LRO) occurs in the ground state of the Heisenberg model on a square lattice, i.e., $g = 0$ in Eq. (1) [22] was followed by the demonstration that LRO is also present at $T = 0$ in the half-filled fermion Hubbard Hamiltonian [23,24], emphasizing similarities between the two models, in the insulating phase of the latter.

In the absence of disorder, the AF-singlet transition has been located to high accuracy through finite-size extrapolation of the AF order parameter. The square of the order parameter sums the spin-spin correlations throughout the lattice, normalized to the lattice volume N. If those correlations are short ranged (e.g., decaying exponentially), the local contributions to the sum, when divided by N, vanish. If the correlations extend over the entire lattice, then the order parameter is nonvanishing. In practice, in QMC simulations, careful finite-size scaling is essential to demonstrate LRO. See also Eq. (1) and Fig. (S1) of the Supplemental Material for further discussions [25]. Our focus here will be on the nature of these correlations in the neighborhood of an impurity,

$$\langle m^2 \rangle = \left\langle \left(\frac{1}{N} \sum_i (-1)^{x_i + y_i + \alpha} S_i^\alpha \right)^2 \right\rangle. \qquad (2)$$

For the symmetric case [26,27] $J^1 = J^2$, the critical interlayer exchange is $g_c = 2.5220$. For the "Kondo-like" lattice where one of the intralayer J's is zero, $g_c = 1.3888$.

As in Ref. [26], we use the stochastic series expansion (SSE) method to obtain $\langle m^2 \rangle$. SSE samples terms in a power expansion of $e^{-\beta \hat{H}}$ in the partition function using operator loop (cluster) updates to perform the sampling efficiently [28]. Here we consider bilayer systems with $N = 2 \times L \times L$ and L up to 100 sites.

We also evaluate the NMR relaxation rate, given by the low-frequency limit of the dynamic susceptibility,

$$\frac{1}{T_1} = T \lim_{\omega \to 0} \sum_q A^2 \frac{\chi''(q, \omega)}{\omega}, \qquad (3)$$

where A is the hyperfine coupling and T is the temperature. We obtain $1/T_1$ using the long imaginary-time behavior of the
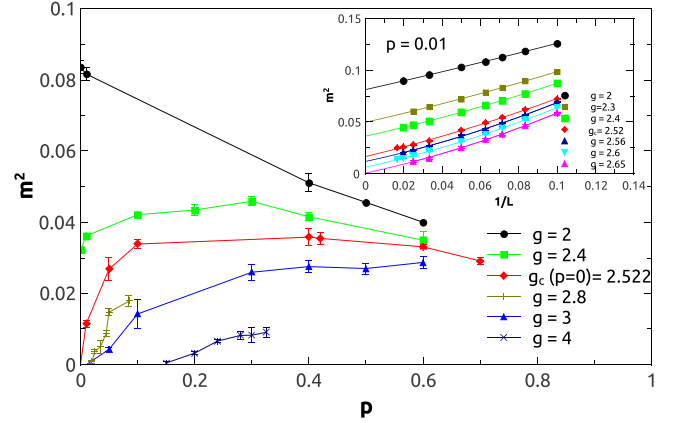
FIG. 1. The square of the staggered magnetization $\langle m^2 \rangle$ as a function of the impurity concentration p for different g's. In the AF phase with $g = 2 < g_c(p = 0) = 2.522$, impurities reduce the order. The effect of impurities near the QCP and in the singlet phase is discussed in the text. The inset: Finite-size scaling of $\langle m^2 \rangle$ for $p = 0.01$. The position of the QCP is increased to $g_c(p = 0.01) = 2.65$. Data were averaged over 120 disorder realizations. The inverse temperature is $\beta = 80$.

spin-spin correlation function,

$$\frac{1}{T_1} = \frac{A^2}{\pi^2 T} \langle S_i(\tau = \beta/2) S_i(\tau = 0) \rangle; \qquad (4)$$

the regime of validity of Eq. (4) is discussed in Ref. [29].

III. AF DOMAINS AND IMPURITY SUSCEPTIBILITY

For a given lattice size L and one disorder realization (i.e., random removal of a fraction p of the spins on layer $\alpha = 2$), we perform the simulations to obtain the quantities of interest; these are then averaged over about 120 disorder realizations. The inset of Fig. 1 shows an example of the size dependence of the AF order parameter thus calculated for a given impurity concentration and different values of g: The intercepts with the vertical axes provide the extrapolated ($L \to \infty$) values for the given p appearing in the main body of the figure. As expected, impurities decrease $\langle m^2 \rangle$ deep within the AF phase ($g = 2$) where they act to reduce the average coordination number of the lattice and hence the tendency to order. Closer to the QCP, a different behavior emerges. Impurities begin to inhibit singlet formation by leaving unpaired moments on their partner sites. The AF order parameter, which had been disrupted by singlet formation, therefore increases with p for $g \lesssim g_c$ and does so especially sharply at $g = g_c$. For $g > g_c$, sufficiently large p can induce AF order, even though these larger interplanar couplings would result in singlet formation in the pure case. The appearance of a finite p_c for $g > g_c$ is discussed further below.

The effect of impurities on the AF order parameter can be characterized by an impurity susceptibility,

$$\chi_{\text{imp}} = \frac{d \langle m^2 \rangle}{dp} \bigg|_{p=0}, \qquad (5)$$

which, as shown in Fig. 2, has a sharp peak at g_c. The effect of impurities is especially large close to the QCP
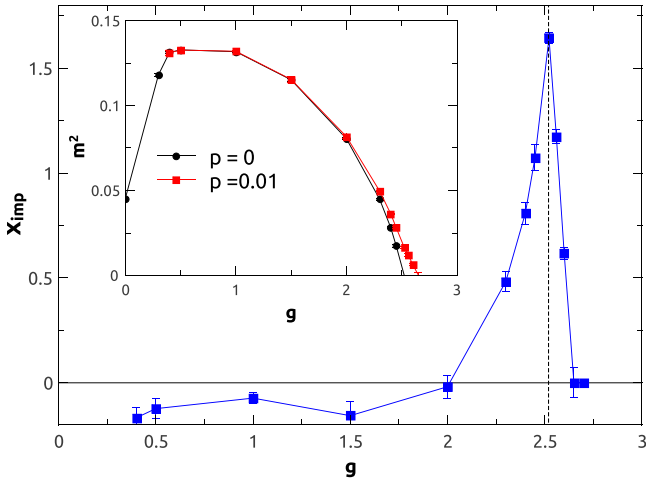
FIG. 2. The impurity susceptibility χ_{imp} is sharply peaked at g_c (vertical dashed line): Impurities induce AF order. Away from g_c, $\chi_{\mathrm{imp}} < 0$: Impurities reduce the AF order parameter. The inset shows the g dependence of $\langle m^2 \rangle$ for $p = 0.01$ (squares) and the clean system (circles); these data were used to obtain χ_{imp}. Both the shift in g_c and the large effect of impurities at the QCP are evident. Data for $\langle m^2 \rangle$ result from extrapolations to $L = \infty$. The inverse temperature is $\beta = 80$.

FIG. 3. (a) Correlation length ξ as a function of g. Data are shown around a single impurity (square) and for the clean system (circles). (b) $\xi \sqrt{p_c}$ is roughly constant, consistent with a picture where AF order occurs when the mean impurity separation $\langle l \rangle$ is proportional to ξ. Data for inverse temperatures $\beta = 40, 80$ were compared to ensure convergence to the ground state. L up to 100 was used to calculate ξ. (c) The AF order parameter at fixed $\beta = 80$ exhibits a sharp crossover indicating the position of the enhanced range of AF order created by the spin-1/2 impurities.

where the system in delicately poised between two phases. Farther away from the QCP in the AF phase $g \lesssim 2$, the impurity susceptibility is negative as in the two-dimensional (2D) Heisenberg model with site dilution [30].

For $g > g_c$, impurities induce AF order in an otherwise singlet phase [31]. We estimate the critical impurity concentration as follows: Prior to the establishment of order, the coupling between two regions centered at sites i and j will oscillate in phase with an amplitude which decays exponentially [32–34] $J_{\mathrm{eff}} \approx J(-1)^{-|i-j+1|} \exp(-\langle l \rangle / \xi)$. Here $\langle l \rangle$ is the mean impurity separation, and ξ is the correlation length in the clean system. For 2D, $\langle l \rangle = 1/\sqrt{p}$. Assuming that the AF order will set in when the average distance between the impurities is on the same scale as ξ yields $\xi \sqrt{p_c} \approx 1$. For a dilute system, we compute ξ by embedding a single impurity in the lattice and evaluating the decay of the spin-spin correlation in its vicinity; see the Supplemental Material [25]. Figure 3(a) shows the resulting ξ, and panel (b) validates the picture that the critical concentration of impurities to induce AF order occurs when $\langle l \rangle = 1/\sqrt{p} \propto \xi$.

There are several subtleties to this argument. At $T = 0$, an exponentially small interaction between impurities can induce order [35]. (This occurs despite the fact that some impurity pairs, which are sufficiently close spatially, lock into singlets [36].) This suggests $p_c = 0$ throughout the singlet phase—an arbitrarily small number of impurities will order despite the rapid decay of their coupling. The effect of these very small couplings is, however, seen only at extremely low T, a fact that is reflected in SSE simulations [35] by the need to study inverse temperatures $\beta \sim 10^4$–10^5 (except very close to the QCP where ξ diverges). In contrast, β which is two to three orders of magnitude smaller is sufficient to reach the ground state on lattices of $L \sim 60$ studied here.

The ordering temperatures in Cd-doped CeCoIn$_5$ are about 2–5 K, and the c-f coupling is reported to be around 49 meV so that $T_c \sim 10^{-2} J$. Thus a more refined interpretation of Fig. 3(b) is that, although AF likely exists at infinitesimal p_c strictly at $T = 0$, panel (b) gives the effective critical impurity concentration to induce AF in the singlet phase at experimental temperature scales [37]. Figure 3(c) shows the position of this sharp crossover in the AF order parameter.

IV. UNIVERSAL BEHAVIOR OF THE NMR RELAXATION RATE

The NMR spin-relaxation rate $1/T_1$ provides an experimental window into doped heavy-fermion materials. Secondary spectral peaks and broadening of the main line implicate the presence of inhomogeneous environments [13]. Here we provide a quantitative description of the effect of impurities on $1/T_1$ and demonstrate that these provide a crisp signature at the QCP.

The main panel of Fig. 4(a) shows the evolution of $1/T_1$ with interlayer coupling at different fixed temperatures for the clean case: It follows the same trend as the AF order parameter $\langle m^2 \rangle$, i.e., it initially rises as the two planes are coupled, has a maximum for $g \approx 0.5$, and then decreases to small values at the QCP. The inset of Fig. 4(a) emphasizes the common crossing point at $g_c \sim 2.52$, which is indicative of a very weak T dependence of $1/T_1$ as the QCP is approached. Indeed, this behavior is consistent with early predictions [38] of universality in clean two-dimensional quantum antiferromagnets, according to which $1/T_1 \sim T^\eta$ with $\eta \approx 0.0375$ [39] and in the Kondo lattice model [40]; more on this in the Supplemental Material [25].
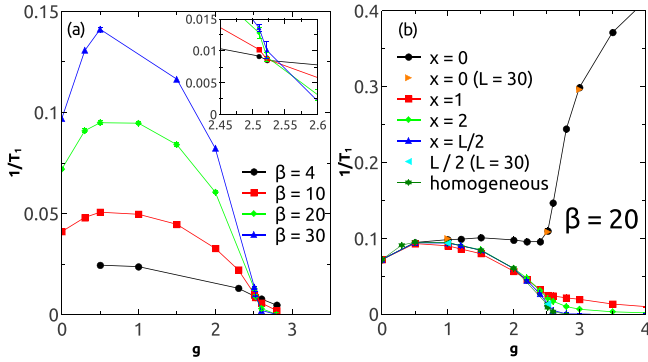
FIG. 4. (a) $1/T_1$ as a function of g for different values of β. The linear size is $L = 50, 60$. The inset: blowup of the crossing point. $g < g_c$, $g = g_c$, and $g > g_c$. (b) g dependence of $1/T_1$ for a system with a single removed spin. $x = 0, 1, 2, L/2$ are different horizontal distances from the impurity. See the text. For the impurity system the linear lattice size is $L = 20, 30$.

The behavior of $1/T_1$ in the presence of disorder is shown in Fig. 4(b). We consider the simplest case of a single spin removed from one layer and compute the relaxation rate of spins in the pure layer as a function of distance x on a horizontal line from the removed site. $x = 0$ corresponds to the removed spin's immediate partner, whereas $x = 1, 2$ are near and next-nearest neighbors and finally at $x = L/2$, far away from the impurity. For $x = 0$ the partner shows a sharp QCP signature. Above $g = g_c$ when all the other spins are locked in singlets, the free spin-1/2 left behind by spin removal has a greatly enhanced $1/T_1$. Meanwhile, the relaxation rate is small for all other sites. For $g = 0$ the spins on the undiluted plane are decoupled from the second layer and hence share a common value of $1/T_1$ regardless of impurities. Figure 4(b) indicates this independent plane behavior extends out to $g \lesssim g_c$ for $x \geqslant 1$. The curve for $x = 0$ breaks away for $g \geqslant 1$ and has a sharp increase at the QCP. Comparison with the results for the clean system shows that $1/T_1$ on the farthest spin is unaffected by the impurity as observed experimentally [37].
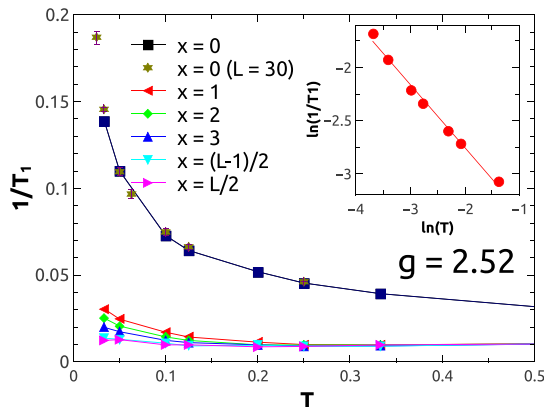
FIG. 5. T dependence of $1/T_1$ for separations x from the impurity. See the text. The inset: determination of the η' exponent. Linear lattices sizes were $L = 20, 30$, somewhat smaller than in previous figures because of the necessity to compute the imaginary time-dependent correlation functions.
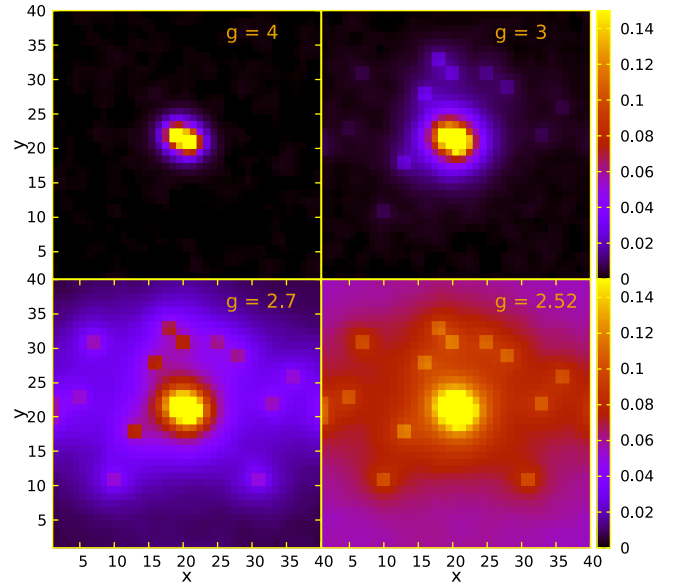
FIG. 6. AF correlation $C(\mathbf{r})$ of the spin at an impurity site with the other spins in the layer $\alpha = 1$. $g = 4$, 3, 2.7, and 2.52. See the text.

We conclude by computing the T dependence of $1/T_1$ at the QCP $g = 2.52$ for this same collection of sites. As emphasized by Fig. 5, $1/T_1$ is weakly temperature dependent away from the impurity site. For the spin left behind at $x = 0$, $1/T_1$ increases substantially as T is lowered and can be described by a power law (the inset). Sachdev *et al.* have argued [19] that the imaginary-time autocorrelation function of an impurity at the QCP scales as $S_i(\tau)S_i(0) \sim \tau^{\eta'}$, implying, through Eq. (4), that $1/T_1 \sim T^{(\eta'-1)}$. Here we obtain $\eta' = 0.41 \pm 0.03$, in agreement with Ref. [20].

Finally, we study correlations between AF puddles believed to form around Cd sites. Figure 6 shows the AF correlation function $C(\mathbf{r}) = (-1)^{\vec{r}} \langle S_{\mathbf{i}}^{1,z} S_{\mathbf{i+r}}^{1,z} \rangle$, around an impurity site $\mathbf{i}$, at the center of the lattice. For $g = 4$ only spins in the close vicinity of an impurity at the lattice center are correlated with it. When $g = 3$ other impurity locations become evident. Correlations start to become substantial over the whole lattice at $g \sim 2.7$. For an impurity density $p = 0.01$ (16 impurities on a 40×40 lattice), enhanced spin-correlation values $g_c = 2.52$ (bottom right panel) are consistent with the establishment of a nonzero order parameter value of $m^2 \sim 0.02$ in Fig. 1.

V. CONCLUSIONS AND OUTLOOK

Exploration of randomness and dilution effects on magnetic and superconducting order is crucial to understanding disordered strongly interacting quantum systems, such as heavy fermions and cuprates. Impurities reduce order but also nucleate ordered domains which, when sufficiently proximate, coalesce to create long-range order [41–43]. We brought together exact QMC calculations of the effect of impurities on spin correlations/domains and the NMR relaxation rate as a system is tuned through a QCP.

Our key conclusions are as follows: (i) The impurity susceptibility, defined as the response of the AF order parameter

to the removal of a small number of spins, exhibits a sharp peak at the QCP so that low disorder concentrations readily lead to long-range order; (ii) the critical concentration p_c for randomness to induce long-range AF order in the singlet phase, at moderate β, is well described by $\xi \sqrt{p_c} \sim 0.4$, where ξ is the spin-correlation length at $g > g_c$; and (iii) verification that the NMR relaxation rate is nearly temperature independent at the QCP and that an abrupt increase in the local value of $1/T_1$ on an impurity site provides a clear signature of the QCP.

Our paper focused on localized Heisenberg spins. Analogous studies dealing with itinerant electrons, such as the periodic Anderson model, are underway [44]. In that case, an impurity is modeled by a site with reduced c-f hybridization $V^* < V$, and similar to our case, it becomes increasingly effective at inducing AF correlations as the AFM-singlet transition is approached.

[1] H. Takagi, T. Ido, S. Ishibashi, M. Uota, S. Uchida, and Y. Tokura, Superconductor-to-nonsuperconductor transition in $(La_{1-x}Sr_x)_2CuO_4$ as investigated by transport and magnetic measurements, Phys. Rev. B **40**, 2254 (1989).

[2] S. Uchida, T. Ido, H. Takagi, T. Arima, Y. Tokura, and S. Tajima, Optical spectra of $La_{2-x}Sr_xCuO_4$: Effect of carrier doping on the electronic structure of the CuO_2 plane, Phys. Rev. B **43**, 7942 (1991).

[3] G. Xiao, M. Z. Cieplak, A. Gavrin, F. H. Streitz, A. Bakhshai, and C. L. Chien, High-Temperature Superconductivity in Tetragonal Perovskite Structures: Is Oxygen-Vacancy Order Important?, Phys. Rev. Lett. **60**, 1446 (1988).

[4] B. Keimer, A. Aharony, A. Auerbach, R. J. Birgeneau, A. Cassanho, Y. Endoh, R. W. Erwin, M. A. Kastner, and G. Shirane, Néel transition and sublattice magnetization of pure and doped La_2CuO_4, Phys. Rev. B **45**, 7430 (1992).

[5] A. V. Mahajan, H. Alloul, G. Collin, and J. F. Marucco, ^{89}NMR Probe of Zn Induced Local Moments in $YBa_2(Cu_{1-y}Zn_y)_3O_{6+x}$, Phys. Rev. Lett. **72**, 3100 (1994).

[6] T. Ido, K. Magoshi, H. Eisaki, and S. Uchida, Optical study of the $La_{2-x}Sr_xNiO_4$ system: Effect of hole doping on the electronic structure of the NiO_2 plane, Phys. Rev. B **44**, 12094(R) (1991).

[7] F. Reinert, P. Steiner, S. Hüfner, H. Schmitt, J. Fink, M. Knupfer, P. Sandl, and E. Bertel, Electron and hole doping in NiO, Z. Phys. B: Condens. Matter **97**, 83 (1995).

[8] M. C. Martin, M. Hase, K. Hirota, G. Shirane, Y. Sasago, N. Koide, and K. Uchinokura, Spin-Peierls and antiferromagnetic phases in $Cu_{1-x}Zn_xGeO_3$: A neutron-scattering study, Phys. Rev. B **56**, 3173 (1997).

[9] M. Azuma, Y. Fujishiro, M. Takano, M. Nohara, and H. Takagi, Switching of the gapped singlet spin-liquid state to an antiferromagnetically ordered state in $Sr(Cu_{1-x}Zn_x)_2O_3$, Phys. Rev. B **55**, R8658 (1997).

[10] M. Ulmke, P. J. H. Denteneer, V. Janis, R. T. Scalettar, A. Singh, D. Vollhardt, and G. T. Zimanyi, Disorder and impurities in Hubbard antiferromagnets, Adv. Solid State Phys. **38**, 369 (1999).

[11] K. H. Hoglund and A. W. Sandvik, Impurity effects at finite temperature in the two-dimensional $S = 1/2$ Heisenberg antiferromagnet, Phys. Rev. B **70**, 024406 (2004).

[12] L. D. Pham, T. Park, S. Maquilon, J. D. Thompson, and Z. Fisk, Reversible Tuning of the Heavy-Fermion Ground State in $CeCoIn_5$, Phys. Rev. Lett. **97**, 056404 (2006).

[13] S. Seo, X. Lu, J.-X. Zhu, R. R. Urbano, N. Curro, E. D. Bauer, V. A. Sidorov, L. D. Pham, T. Park, Z. Fisk, and J. D. Thompson, Disorder in quantum critical superconductors, Nat. Phys. **10**, 120 (2014).

[14] In fact, bilayer Hubbard and Heisenberg models can even track each other semiquantitatively. For example, the Hubbard QCP $(t_\perp/t)_c \sim 1.6$ is rather close to that obtained from the Heisenberg limit $(J_\perp/J)_c = 2.522$ assuming $J = 4t^2/U$. See R. T. Scalettar, J. W. Cannon, D. J. Scalapino, and R. L. Sugar, Magnetic and pairing correlations in coupled Hubbard planes, Phys. Rev. B **50**, 13419 (1994).

[15] K. Held, C. Huscroft, R. T. Scalettar, and A. K. McMahan, Similarities Between the Hubbard and Periodic Anderson Models at Finite Temperatures, Phys. Rev. Lett. **85**, 373 (2000).

[16] K. R. Shirer, A. C. Shockley, A. P. Dioguardi, J. Crocker, C. H. Lin, N. apRoberts-Warren, D. M. Nisson, P. Klavins, J. C. Cooley, Y.-f. Yang, and N. J. Curro, Long range order and two-fluid behavior in heavy electron materials, Proc. Natl. Acad. Sci. USA **109**, 18249 (2012).

[17] M. Jiang, N. J. Curro, and R. T. Scalettar, Universal knight shift anomaly in the periodic Anderson model, Phys. Rev. B **90**, 241109 (2014).

[18] A. W. Sandvik, Multicritical Point in a Diluted Bilayer Heisenberg Quantum Antiferromagnet, Phys. Rev. Lett. **89**, 177201 (2002).

[19] S. Sachdev, C. Buragohain, and M. Vojta, Quantum impurity in a nearly-critical two dimensional antiferromagnet, Science **286**, 2479 (1999).

[20] K. H. Höglund, A. W. Sandvik, and S. Sachdev, Impurity Induced Spin Texture in Quantum Critical 2D Antiferromagnets, Phys. Rev. Lett. **98**, 087203 (2007).

[21] C. Yasuda, S. Todo, M. Matsumoto, and H. Takayama, Site-dilution-induced antiferromagnetic long-range order in a two-dimensional spin-gapped Heisenberg antiferromagnet, Phys. Rev. B **64**, 092405 (2001).

[22] J. D. Reger and A. P. Young, Monte Carlo simulations of the spin-1/2 Heisenberg antiferromagnet on a square lattice, Phys. Rev. B **37**, 5978(R) (1988).

[23] J. E. Hirsch and S. Tang, Antiferromagnetism in the Two-Dimensional Hubbard Model, Phys. Rev. Lett. **62**, 591 (1989).

[24] S. R. White, D. J. Scalapino, R. L. Sugar, E. Y. Loh, J. E. Gubernatis, and R. T. Scalettar, Numerical study of the two-dimensional Hubbard model, Phys. Rev. B **40**, 506 (1989).

[25] See Supplemental Material at http://link.aps.org/supplemental/10.1103/PhysRevB.95.054419 for further discussions.

[26] A. W. Sandvik and D. J. Scalapino, Order-disorder transition in a two-layer quantum antiferromagnet, Phys. Rev. Lett. **72**, 2777 (1994).

[27] L. Wang, K. S. D. Beach, and A. W. Sandvik, High-precision finite-size scaling analysis of the quantum critical point of $S = 1/2$ Heisenberg antiferromagnetic bilayers, Phys. Rev. B **73**, 014421 (2006).

[28] O. F. Syljuasen and A. W. Sandvik, Quantum Monte Carlo with directed loops, Phys. Rev. E **66**, 046701 (2002).

[29] M. Randeria, N. Trivedi, A. Moreo, and R. T. Scalettar, Pairing and Spin Gap in the Normal State of Short Coherence Length Superconductors, Phys. Rev. Lett. **69**, 2001 (1992).

[30] A. W. Sandvik, Classical percolation transition in the diluted two-dimensional $S = 1/2$ Heisenberg antiferromagnet, Phys. Rev. B **66**, 024418 (2002).

[31] A. W. Sandvik, E. Dagotto, and D. J. Scalapino, Nonmagnetic impurities in spin-gapped and gapless Heisenberg antiferromagnets, Phys. Rev. B **56**, 11701 (1997).

[32] M. Sigrist and A. Furusaki, Low-temperature properties of the randomly depleted Heisenberg ladder, J. Phys. Soc. Jpn. **65**, 2385 (1996)

[33] S. Wessel, B. Normand, M. Sigrist, and S. Haas, Order by Disorder from Nonmagnetic Impurities in a Two-Dimensional Quantum Spin Liquid, Phys. Rev. Lett. **86**, 1086 (2001).

[34] J. Bobroff, N. Laflorencie, L. K. Alexander, A. V. Mahajan, B. Koteswararao, and P. Mendels, Impurity-Induced Magnetic Order in Low-Dimensional Spin-Gapped Materials, Phys. Rev. Lett. **103**, 047201 (2009).

[35] N. Laflorencie, D. Poilblanc, and A. W. Sandvik, Magnetic ordering in a doped frustrated spin-Peierls system, Phys. Rev. B **69**, 212412 (2004).

[36] T. Roscilde, Field-induced quantum-disordered phases in $S = 1/2$ weakly coupled dimer systems with site dilution, Phys. Rev. B **74**, 144418 (2006).

[37] R. R. Urbano *et al.*, Interacting Antiferromagnetism Droplets in Quantum Critical CeCoIn$_5$, Phys. Rev. Lett. **99**, 146402 (2007).

[38] A. V. Chubukov and S. Sachdev, Universal Magnetic Properties of La$_{2-\delta}$Sr$_\delta$CuO$_4$ at Intermediate Temperatures, Phys. Rev. Lett. **71**, 169 (1993).

[39] M. Campostrini *et al.*, Critical exponents and equation of state of the three-dimensional Heisenberg universality class, Phys. Rev. B **65**, 144520 (2002).

[40] Q. Si, S. Rabello, K. Ingersent, and J. L. Smith, Locally critical quantum phase transitions in strongly correlated metals, Nature (London) **413**, 804 (2001).

[41] A. J. Millis, D. K. Morr, and J. Schmalian, Local Defect in Metallic Quantum Critical Systems, Phys. Rev. Lett. **87**, 167202 (2001).

[42] J.-X. Zhu, I. Martin, and A. R. Bishop, Spin and Charge Order Around Vortices and Impurities in High-T_c Superconductors, Phys. Rev. Lett. **89**, 067003 (2002).

[43] B. M. Andersen, P. J. Hirschfeld, A. P. Kampf, and M. Schmid, Disorder-Induced Static Antiferromagnetism in Cuprate Superconductors, Phys. Rev. Lett. **99**, 147002 (2007).

[44] A. Benali, Z. Bai, N. J. Curro, and R. T. Scalettar, Impurity-induced antiferromagnetic domains in the periodic Anderson model, Phys. Rev. B **94**, 085132 (2016).

Appendix E

Magnetic order-disorder transitions on a one-third-depleted square lattice

Magnetic order-disorder transitions on a one-third-depleted square lattice

H.-M. Guo,[1,2] T. Mendes-Santos,[2,3] W. E. Pickett,[2] and R. T. Scalettar[2]

[1]*Department of Physics, Beihang University, Beijing 100191, China*
[2]*Physics Department, University of California, Davis, California 95616, USA*
[3]*Instituto de Fisica, Universidade Federal do Rio de Janeiro Cx.P. 68.528, 21941-972 Rio de Janeiro RJ, Brazil*

Quantum Monte Carlo simulations are used to study the magnetic and transport properties of the Hubbard model, and its strong coupling Heisenberg limit, on a one-third-depleted square lattice. This is the geometry occupied, after charge ordering, by the spin-$\frac{1}{2}$ Ni^{1+} atoms in a single layer of the nickelate materials $La_4Ni_3O_8$ and (predicted) $La_3Ni_2O_6$. Our model is also a description of strained graphene, where a honeycomb lattice has bond strengths which are inequivalent. For the Heisenberg case, we determine the location of the quantum critical point (QCP) where there is an onset of long range antiferromagnetic order (LRAFO), and the magnitude of the order parameter, and then compare with results of spin wave theory. An ordered phase also exists when electrons are itinerant. In this case, the growth in the antiferromagnetic structure factor coincides with the transition from band insulator to metal in the absence of interactions.

I. INTRODUCTION

Over the last several decades, quantum Monte Carlo (QMC) methods have been widely used to investigate magnetic, charge, and pairing correlations in the Hubbard Hamiltonian on a square lattice [1–7]. A central issue has been the intimate interplay between these different types of order, most fundamentally the possibility that magnetic correlations give rise to d-wave superconductivity. The occurrence of inhomogeneous (stripe) charge distributions upon doping the half-filled lattice, where antiferromagnetism (AF) survives in regions of low hole concentration but is suppressed on stripes of high concentration, has also been shown to have profound implications for pairing [8].

In more recent studies, the effect of depletion of the square lattice has also been investigated. In this case, a regular removal of sites can be regarded as an extreme limit of the spontaneous formation of charge and spin patterns in which the degrees of freedom on certain sites are completely eliminated. Further types of transitions were then shown to occur within these geometries. Two prominent examples are the Lieb lattice [9], where 1/4 of the sites are removed, giving rise to a flat electronic band and ferromagnetism, and the 1/5-depleted lattice [10–15], where spin liquid phases compete with magnetic order. This latter geometry is realized by the vanadium atom locations in CaV_4O_9, and also by some members of the iron-pnictide family [16,17]. A crucial feature of this situation is the occurrence of two separate types of bonds, and hence of exchange or hopping energies, in the depleted structure.

Depleted lattices can also be formed starting from other, nonsquare, lattices. For example, the Kagomé lattice arises from removing one fourth of the sites of a triangular lattice. Like the Lieb lattice, the Kagomé structure has a flat band. However, because it is not bipartite, the band does not lie between the dispersing ones.

In this paper we investigate the magnetic and charge patterns within the 1/3-depleted square lattice of Fig. 1, which is formed by the red sites remaining after the removal of the black sites, which form stripes along one diagonal. The bonds between red sites are of two sorts: ones which were the near-neighbor bonds of the original, full square lattice, and ones which connect through the diagonal rows of removed sites, and which were next near neighbors of the original lattice. This distinction will be modeled, in the following sections, by allowing for different energy scales on the two types of bonds. Notice that this lattice structure remains bipartite, a fact which has implications for AF order without frustration and also for the absence of a sign problem in QMC simulations.

Figure 1 is equivalent to a strained version of the honeycomb geometry realized in graphene. "Artificial graphene" lattices can be achieved by nanopatterning [18], by molecule-by-molecule assembly [19], or by trapping ultracold atoms on optical lattices. They offer the possibility of tunable bond strengths, for example through application of strain, and have recently been discussed as a means for further investigation of Dirac particles and their associated correlated and topological phases [20]. Graphene with a "Kekulé distortion" [19,21,22] involves the appearance of two distinct bond hoppings, albeit in a pattern different from that of Fig. 1.

A second motivation for investigating the geometry of Fig. 1, which more directly connects with the notion of "depletion" and which also fundamentally involves magnetic order, is provided by recent experimental [23] and theoretical [24] studies of the layered nickelates $La_4Ni_3O_8$ and $La_3Ni_2O_6$. In these materials, the formal Ni valences of $+1.33$ and $+1.5$ are separated into charge ordered Ni^{1+} (spin $\frac{1}{2}$) and Ni^{2+} (spin 0), so that spin-$\frac{1}{2}$ stripes are formed at $45°$ relative to the Ni-O bonds, as in Fig. 1 for $La_4Ni_3O_8$. This charge ordering is accompanied by structural distortions and the opening of a gap. The Ni^{1+} atoms form an AF arrangement in analogy with the magnetism of the CuO_2 planes of the cuprate superconductors. Here we will investigate AF correlations associated with this geometry. Other layered nickelate materials [25–28] have also been investigated with quantum simulations, especially within the classical spin-fermion method [29].

II. STRONG COUPLING (HEISENBERG) LIMIT

We first consider the case of localized spin-1/2 moments on the 1/3-depleted lattice with
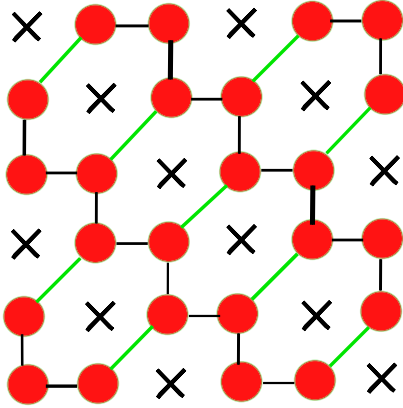
FIG. 1. The one-third-depleted square lattice. A regular diagonal stripe array of black crosses is removed, leaving the red site structure. We will assume two types of bonds exist corresponding to connections between NN (black) and NNN (green) sites of the original square geometry. (See text.)

FIG. 2. Finite size scaling of the square of the AF order parameter m^2 for the spin-1/2 Heisenberg model. For a ratio $g > 1.75 = g_c$ of exchange couplings, a transition to a disordered spin liquid state occurs. LRAFO persists to small values of the interchain exchange. Data were obtained with the SSE algorithm.

Hamiltonian

$$H = J \left[\sum_{\langle ij \rangle} \vec{S}_i \cdot \vec{S}_j + g \sum_{\langle\langle ij \rangle\rangle} \vec{S}_i \cdot \vec{S}_j \right], \qquad (1)$$

with exchange constants J and gJ on the two types of bonds of Fig. 1.

This model can be treated within linear spin wave theory (LSWT) by replacing the spin operators by bosonic ones via the Holstein-Primakoff (HP) transformation, and then invoking the linear approximation describing small fluctuations around the broken symmetry phase. The resulting noninteracting Hamiltonian can be diagonalized in momentum space and through a Bogliubov rotation. The spin wave spectrum is

$$\omega(J^*, k) = J^* \sqrt{1 - \frac{|\gamma(\vec{k})|^2}{J^{*2}}}, \qquad (2)$$

where

$$\gamma(\vec{k}) = \sum_\delta J(\delta) e^{-i\vec{k}\cdot\vec{r}_\delta} = J[e^{-i[(\vec{k}\cdot\vec{a}_1)+(\vec{k}\cdot\vec{a}_2)]/3} + e^{i[(\vec{k}\cdot\vec{a}_1)-2(\vec{k}\cdot\vec{a}_2)]/3}]$$

$$g J e^{i[2(\vec{k}\cdot\vec{a}_1)-(\vec{k}\cdot\vec{a}_2)]/3}, \qquad (3)$$

with lattice vectors $\vec{a}_1 = 2\hat{x} - \hat{y}$ and $\vec{a}_2 = \hat{x} + \hat{y}$. Here $J^* = \sum_\delta J(\delta)$ is the sum of exchange constants over near-neighbor sites. The AFM staggered order parameter

$$m_s = \frac{1}{N} \left(\sum_{i \in A} \langle S_i^z \rangle - \sum_{i \in B} \langle S_i^z \rangle \right) \qquad (4)$$

is obtained in the LSWT, writing $\langle S_i^z \rangle$ in terms of HP operators. At $T = 0$ we obtain

$$m_s = S + \frac{1}{2} - \frac{1}{N} \sum_{\vec{k}} \left(1 - \frac{|\gamma(\vec{k})|^2}{J^{*2}} \right), \qquad (5)$$

where S is the spin.

We can also treat the Hamiltonian more accurately on lattices of finite size using the stochastic series expansion

(SSE) quantum Monte Carlo method [30,31]. SSE samples terms in the power expansion of $e^{-\beta\hat{H}}$ in the partition function. Operator loop (cluster) updates perform the sampling efficiently [30,32]. The square of the staggered magnetization $\langle m_s^2 \rangle$ can be evaluated to high precision, and extrapolated to the thermodynamic limit.

Figure 2 shows the results of SSE simulations for different values of the bond anisotropy g and inverse linear system size $1/L$. The order parameter first increases with g, reaching a maximum at the honeycomb limit $g = 1$, and finally begins to decrease. LRAFO vanishes above $g_c = 1.75 \pm 0.01$. The extrapolated order parameter from SSE (Fig. 2) and from LSWT [Eq. (5)] is given in Fig. 3. LSWT greatly overestimates the persistence of LRAFO at large g. It also predicts a quantum phase transition at small, but nonzero, $g_c = 0.065 \pm 0.005$. Similar to the case of a square lattice with anisotropic exchange [33–35], a zero g_c is expected here though a small nonzero value is obtained in our calculations due to finite size effect.
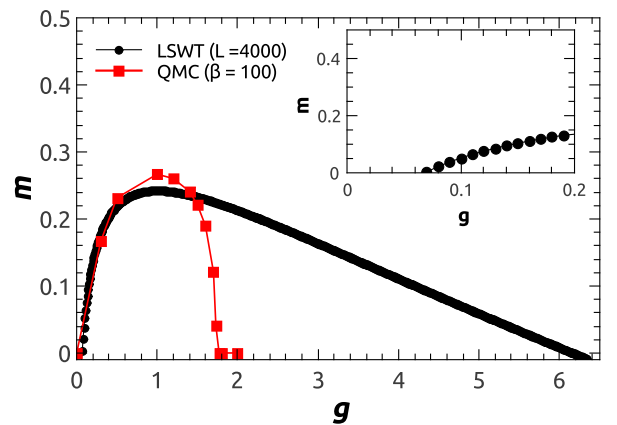
FIG. 3. Extrapolated values of the SSE results for the AF order parameter from Fig. 2 and the results of LSWT analysis, Eq. (5). With LSWT (SSE), LRAFO disappears above $g_c = 6.20 \pm 0.02$ (1.75 ± 0.01). The QMC data are shown in the Supplemental Material [32].

We emphasize the contrast of these results with those of the Heisenberg model on 1/5-depleted lattice [12] appropriate to modeling CaV$_4$O$_9$ where the lower $g_c = 0.60 \pm 0.05$. The difference, as for the case of the anisotropic square lattice, is that for the 1/5-depleted case the building blocks are small clusters (either dimers or four site plaquettes) in both the g small and g large limits. In the present case, two site clusters are formed for large g, but the small g limit still has extended one-dimesnional (1D) structures. These give rise to LRAFO even for small g.

III. ITINERANT LIMIT

We next consider itinerant electrons, a single band Hubbard Hamiltonian on the same 1/3-depleted lattice,

$$H = -t \sum_{\langle ij \rangle \sigma} (c_{i\sigma}^\dagger c_{j\sigma} + c_{j\sigma}^\dagger c_{i\sigma}) - t' \sum_{\langle\langle ij \rangle\rangle \sigma} (c_{i\sigma}^\dagger c_{j\sigma} + c_{j\sigma}^\dagger c_{i\sigma})$$
$$+ U \sum_i \left(n_{i\uparrow} - \frac{1}{2}\right)\left(n_{i\downarrow} - \frac{1}{2}\right). \quad (6)$$

The hoppings along and between the one-dimensional chains are t and t', respectively. The properties of this model are solved using the determinant QMC method [32,36]. In this method the partition function is expressed as a path integral. The discretization of inverse temperature β enables the isolation of the quartic interaction terms which are decoupled via a Hubbard-Stratonovich (HS) transformation. The resulting quadratic fermionic trace is done analytically, and the HS field is then sampled stochastically. Because the scaling is cubic in the lattice size N we study systems only up to $N = 2 \times 12 \times 12$ sites in contrast to the spin models described in the previous section where SSE scales linearly in N and systems up to $N = 1600$ (or more) are accessible. Equation (6) is written in particle-hole symmetric form so that the lattice is half-filled $\rho = \langle n_{i\uparrow} + n_{i\downarrow}\rangle = 1$ for all lattice sites i and any values of t', U, and temperature T. At this electron density, simulations are possible down to low T without encountering the fermion sign problem [37].

In the noninteracting limit of Eq. (6) we have two bands with dispersion,

$$E(\vec{k}) = \pm \{[t + t \cos(\vec{k} \cdot \vec{a}_2) + t' \cos(\vec{k} \cdot \vec{a}_1)]^2$$
$$+ [t \sin(\vec{k} \cdot \vec{a}_2) + t' \sin(\vec{k} \cdot \vec{a}_1)]^2\}^{1/2}. \quad (7)$$

Here the noninteracting band width w is kept fixed, $w = 4t + 2t' = 6$, as t'/t varies, setting the the energy scale $w = 6$ throughout the paper. As illustrated in Fig. 4(a), the band gap Δ vanishes for $t'/t < 2$. These bands touch at two Dirac points for $t'/t = \frac{1}{2}$ in Fig. 4(b). Figure 4(c) shows the band insulating case $t/t' = 0.25$.

To characterize the magnetic properties of Eq. (6) we measure the AF structure factor

$$S_{AF} = \frac{1}{N} \sum_{l,j} (-1)^l \langle \vec{S}_j \cdot \vec{S}_{l+j}\rangle, \quad (8)$$

where the factor $(-1)^l = +1$ (-1) if site l is on the same (different) sublattice of the bipartite structure of Fig. 1.

The spin correlation in the singlet phase falls off exponentially with separation l and S_{AF} is independent of lattice size.
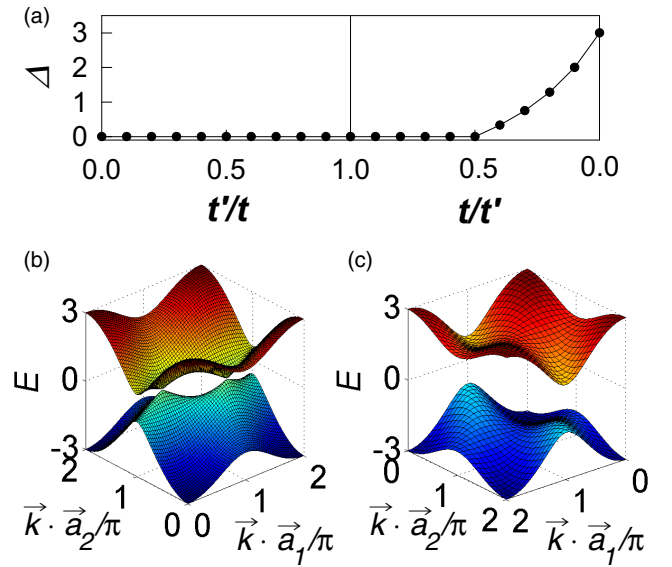
FIG. 4. (a) Band gap Δ as a function of the ratio of hopping. Δ vanishes for $t'/t < 2$. The noninteracting limit is a band insulator ($\Delta > 0$) for $t'/t > 2$. (b) Semimetallic band structure at $t'/t = 0.5$. (c) Insulating band structure at $t/t' = 0.25$.

If LRAFO is present, $S_{AF} \propto N$, since spin correlations remain nonzero out to all distances on a finite lattice.

Figure 5 shows S_{AF} on an $N = 8 \times 8$ lattice for different U as a function of t/t'. It is known that LRAFO exists at the symmetric honeycomb lattice point $t = t'$ only when U is sufficiently large [38–41], with the most accurate value [42] of the critical point $U_c = 3.869 \pm 0.013$. The data of Fig. 5 are suggestive of this result, with S_{AF} being essentially independent of the value of t/t' for $U = 1,2,3$, and becoming both larger and sensitive to the anisotropy for $U \geqslant 4$.
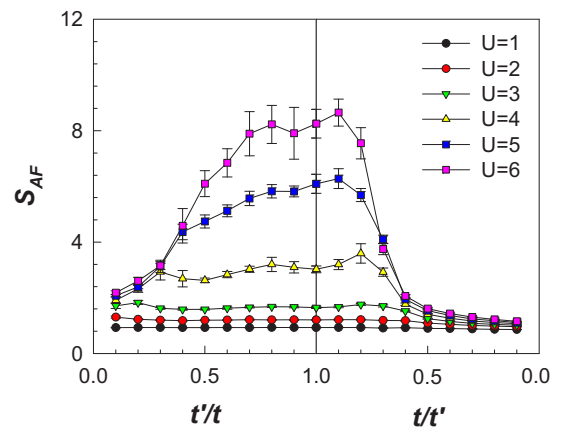
FIG. 5. The AF structure factor S_{AF} is shown as a function of hopping anisotropy for different U. The linear lattice size $L = 8$ so that the number of sites $N = 128$. (There are 64 unit cells each with two sites.) The inverse temperature discretization $\Delta\tau = \beta/L = 1/2U$ except for $U = 1$ where $\Delta\tau = 1/4$. Data were acquired from 25 simulations of 1000 equilibration and 4000 measurement sweeps for each t'/t. The QMC data is shown in the Supplemental Material [32].
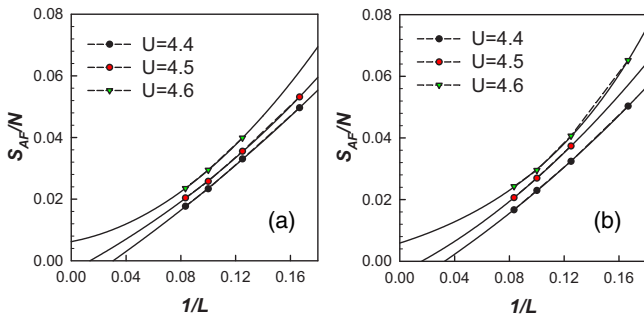
FIG. 6. Finite size scaling of the AF structure factor S_{AF} for $t/t' = 0.95$ (a) and $t'/t = 0.90$ (b). In both cases $U_c > 4.5$ is well above the critical interaction strength $U_c = 3.869$ for isotropic hopping [42].

Finite size scaling can be used to analyze quantitatively the possibility of LRAFO. Such data are shown in Fig. 6. We find that hopping anisotropy increases U_c, in agreement with our results for the g dependence of the order parameter in the strong coupling Heisenberg model (Fig. 3) which falls off to either side of $g = 1$.

A second diagnostic of magnetic order is the near-neighbor spin correlation between adjacent pairs of sites. This can be evaluated for both intra- and interchain bonds, and measures the formation of singlet correlations m_t and $m_{t'}$, respectively, on the associated bonds. Figure 7 shows m_t and $m_{t'}$ for different values of U. For the Heisenberg limit, $U \to \infty$, we use $J \sim t^2/U$ to convert $g = J'/J$ to $\sqrt{t'/t}$. In the strong coupling limit $\langle S_i \cdot S_j \rangle = -\frac{3}{4}$ for a singlet. Here in the Hubbard model, the finite value of the on-site repulsion $U < \infty$ allows for charge fluctuations which reduce the magnitude of the singlet correlator. The quantities m_t and $m_{t'}$ have opposite trends in the two regimes $t' < t$ and $t < t'$ of Fig. 7. When $t/t' < 1$, m_t is suppressed, and $m_{t'}$ increases and saturates with decreasing t/t'. This supports the physical scenario in which singlets are
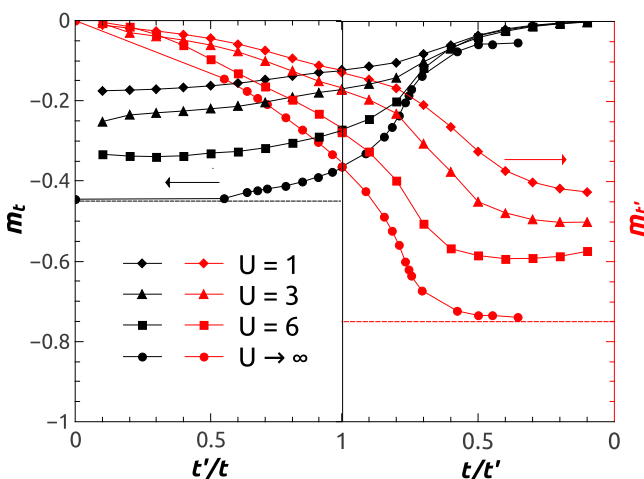
FIG. 7. Near-neighbor (singlet) spin correlation function across intra- and interchain bonds m_t and $m_{t'}$, respectively. $\langle S_i \cdot S_j \rangle$ is large and independent of t'/t for $t'/t \gtrsim 2$. This value matches the point at which a nonzero gap Δ opens in the spectrum, Fig. 4(a). The limiting value at $t' = 0$ ($t = 0$) is 0.4515 [42] (0.75). The QMC data are shown in the Supplemental Material [32].
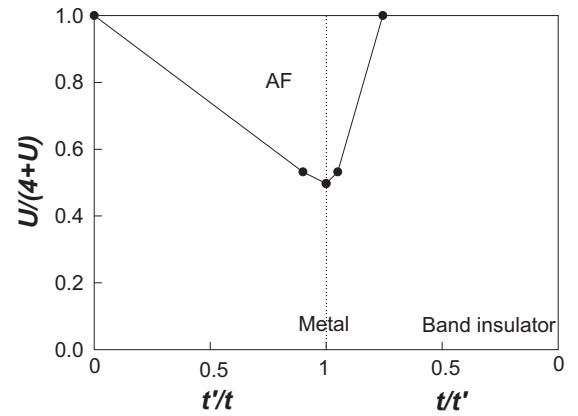
FIG. 8. Phase diagram. The $U = \infty$ Heisenberg limit is along the top of the figure, $U/(4 + U) = 1$, and is extracted from the data of Fig. 3. The critical interaction strength diverges even prior to entry into the band insulator phase at $t/t' = 0.5$.

formed between the stronger t' bonds. On the other hand, if $t'/t < 1$, $m_{t'}$ is diminished. m_t approaches the short range AF correlations of the 1D chains [43], without the formation of singlets on the t bonds. Thus although at first glance Fig. 5 indicates similar, reduced values for S_{AF} for both small t'/t and for small t/t', the singlet correlator of Fig. 7 suggests these are rather distinct limits: full singlets form at $t/t' \to 0$ but not $t'/t \to 0$. It is interesting to note that the crossing of the two NN spin correlators is always at $t = t'$ regardless of U. This is in contrary to what was found in the 1/5-depleted square lattice [15]. The reason is that for the lattice considered here we get a honeycomb lattice at $t = t'$ where all bonds are equivalent. However in the 1/5-depleted case, the bonds remain inequivalent at $t = t'$, so to get the spin correlations the same we need to shift t away from t'.

The evaluation of these magnetic correlations allows us to sketch the phase diagram in the plane of hopping anisotropy and interaction strength shown in Fig. 8. The fact that $g_c = 1.75$ in the Heisenberg limit is less than the anisotropy required to open a nonzero gap Δ in the noninteracting band structure suggests that the destruction of LRAFO involves more than the simple RPA-like criterion of the vanishing of the density of states at the Fermi level. That is, the competing possibility of singlet formation also plays a role in the absence of LRAFO.

IV. CONCLUSION

In this paper we have investigated magnetic ordering on a two-dimensional lattice formed by the regular removal of one third of the sites from a square lattice. We analyzed the strong coupling, Heisenberg limit using spin-wave theory and QMC (SSE), and determined the range of the ratio J'/J on the two types of bonds in which an ordered AF phase exists at $T = 0$. Unlike the one-fifth-depleted lattice, which breaks into small clusters in both the $J = 0$ and $J' = 0$ limits, we have shown that AF order persists to very small J'/J as a consequence of the fact that extended one-dimensional chains are still present when $J' = 0$.

We also used DQMC to study the single band Hubbard Hamiltonian on this lattice. The singlet correlator was found

to grow rapidly for $t'/t \sim 1.5$, coinciding with a loss of AF order and the approach to the band insulator at $t'/t > 2$ in the noninteracting limit. The critical interaction strength $U_c \sim 3.87$ for $t = t'$ was shown to increase with inhomogeneity $t' \neq t$. The effect of *random* removal of sites on AF order has been studied in both itinerant and localized models [44–48].

The one-third-depleted geometry that we investigated has recently been shown to be realized as a result of charge stripe ordering in the nickelates [23,24], so our simulations speak to the conditions for AF order in those materials. The relative strengths of first and second neighbor exchange couplings for nickelates has not yet been addressed. Another key feature is the presence of multiple NiO_2 layers and the surprising nature of charge equivalence between the layers [23,24]. We cannot immediately address this phenomenon, since in our treatment charge ordering is put in *a priori* through our consideration of

a one-third-depleted lattice and, in addition, our restriction to a single layer model.

A more approximate method than DQMC, which considers itinerant electrons interacting with classical spins [49,50], can be employed to treat multiple bands. It may be used to explore the *spontaneous* formation of charge ordering, and we leave the details of this to future study.

[1] S. R. White, D. J. Scalapino, R. L. Sugar, E. Y. Loh, Jr., J. E. Gubernatis, and R. T. Scalettar, Numerical study of the two-dimensional Hubbard model with repulsive Coulomb interaction, Phys. Rev. B **40**, 506 (1989).

[2] D. J. Scalapino, Does the Hubbard model have the right stuff? in *Proceedings of the International School of Physics*, edited by R. A. Broglia and J. R. Schrieffer (North-Holland, New York, 1994), and references cited therein.

[3] Y. M. Vilk and A.-M. S. Tremblay, Non-perturbative many-body approach to the Hubbard model and single-particle pseudogap, J. Phys. I **7**, 1309 (1997).

[4] S. Zhang, J. Carlson, and J. E. Gubernatis, Pairing Correlations in the Two-Dimensional Hubbard Model, Phys. Rev. Lett. **78**, 4486 (1997).

[5] Th. Maier, M. Jarrell, Th. Pruschke, and J. Keller, *d*-Wave Superconductivity in the Hubbard Model, Phys. Rev. Lett. **85**, 1524 (2000).

[6] M. Capone and G. Kotliar, Cellular-dynamical mean-field theory of the competition between antiferromagnetism and *d*-wave superconductivity in the two-dimensional Hubbard model, J. Magn. Magn. Mater. **310**, 529 (2007).

[7] E. Gull, M. Ferrero, O. Parcollet, A. Georges, and A. J. Millis, Momentum space anisotropy and pseudogaps: A comparative cluster dynamical mean field analysis of the doping-driven metal-insulator transition in the two dimensional Hubbard model, Phys. Rev. B **82**, 155101 (2010).

[8] E. Berg, E. Fradkin, S. A. Kivelson, and J. M. Tranquada, Striped superconductors: How spin, charge and superconducting orders intertwine in the cuprates, New J. Phys. **11**, 115004 (2009).

[9] E. H. Lieb, Two Theorems on the Hubbard Model, Phys. Rev. Lett. **62**, 1201 (1989).

[10] N. Katoh and M. Imada, Spin gap in 2-dimensional Heisenberg-model for CaV_4O_9, J. Phys. Soc. Jpn. **64**, 4105 (1995).

[11] K. Ueda, H. Kontani, M. Sigrist, and P. A. Lee, Plaquette Resonating-Valence-Bond Ground State of CaV_4O_9, Phys. Rev. Lett. **76**, 1932 (1996).

[12] M. Troyer, H. Kontani, and K. Ueda, Phase Diagram of Depleted Heisenberg Model for CaV_4O_9, Phys. Rev. Lett. **76**, 3822 (1996).

[13] M. P. Gelfand, W. Zheng, R. R. P. Singh, J. Oitmaa, and C. J. Hamer, Convergent Expansions for Properties of the Heisenberg Model for CaV_4O_9, Phys. Rev. Lett. **77**, 2794 (1996).

[14] W. E. Pickett, Impact of Structure on Magnetic Coupling in CaV_4O_9, Phys. Rev. Lett. **79**, 1746 (1997).

[15] E. Khatami, R. R. P. Singh, W. E. Pickett, and R. Scalettar, Magnetic Correlations and Pairing in the 1/5-depleted Square Lattice Hubbard Model, Phys. Rev. Lett. **113**, 106402 (2014).

[16] B. Wei, H. Qing-Zhen, C. Gen-Fu, M. A. Green, W. Du-Ming, H. Jun-Bao, and Q. Yi-Ming, A novel large moment antiferromagnetic order in $K_{0.8}Fe_{1.6}Se_2$ superconductor, Chin. Phys. Lett. **28**, 086104 (2011).

[17] F. Ye, S. Chi, W. Bao, X. F. Wang, J. J. Ying, X. H. Chen, H. D. Wang, C. H. Dong, and M. Fang, Common Crystalline and Magnetic Structure of Superconducting $A_2Fe_4Se_5$ (A = K, Rb, Cs, Tl) Single Crystals Measured Using Neutron Diffraction, Phys. Rev. Lett. **107**, 137003 (2011).

[18] C. H. Park and S. G. Louie, Making massless Dirac fermions from a patterned two-dimensional electron gas, Nano Lett. **9**, 1793 (2009).

[19] K. K. Gomes, W. Mar, W. Ko, F. Guinea, and H. C. Manoharan, Designer Dirac fermions and topological phases in molecular graphene, Nature (London) **483**, 306 (2012).

[20] M. Polini, F. Guinea, M. Lewenstein, H. C. Manoharan, and V. Pellegrini, Artificial honeycomb lattices for electrons, atoms and photons, Nat. Nanotechnol. **8**, 625 (2013).

[21] C.-Y. Hou, C. Chamon, and C. Mudry, Electron Fractionalization in Two-Dimensional Graphene-like Structures, Phys. Rev. Lett. **98**, 186809 (2007).

[22] B. Roy and I. F. Herbut, Unconventional superconductivity on honeycomb lattice: Theory of Kekulé order parameter, Phys. Rev. B **82**, 035429 (2010).

[23] J. Zhang, Y.-S. Chen, D. Phelan, H. Zheng, M. R. Norman, and J. F. Mitchell, Stacked charge stripes in the quasi-2D trilayer nickelate $La_4Ni_3O_8$, Proc. Natl. Acad. Sci. USA **113**, 8945 (2016).

[24] A. S. Botana, V. Pardo, W. E. Pickett, and M. R. Norman, Charge ordering in Ni^{1+}/Ni^{2+} nickelates: $La_4Ni_3O_8$ and $La_3Ni_2O_6$, Phys. Rev. B **94**, 081105(R) (2016).

[25] J. M. Tranquada, D. J. Buttrey, V. Sachan, and J. E. Lorenzo, Simultaneous Ordering of Holes and Spins in $La_2NiO_{4.125}$, Phys. Rev. Lett. **73**, 1003 (1994).

[26] V. Sachan, D. J. Buttrey, J. M. Tranquada, J. E. Lorenzo, and G. Shirane, Charge and spin ordering in $La_{2-x}Sr_xNiO_{4.00}$

with $x = 0.135$ and 0.20, Phys. Rev. B **51**, 12742 (1995).

[27] H. Yoshizawa, T. Kakeshita, R. Kajimoto, T. Tanabe, T. Katsufuji, and Y. Tokura, Stripe order at low temperatures in La$_{2-x}$Sr$_x$NiO$_4$ with $0.289 \leqslant x \leqslant 0.5$, Phys. Rev. B **61**, R854(R) (2000).

[28] R. Kajimoto, K. Ishizaka, H. Yoshizawa, and Y. Tokura, Spontaneous rearrangement of the checkerboard charge order to stripe order in La$_{1.5}$Sr$_{0.5}$NiO$_4$, Phys. Rev. B **67**, 014511 (2003).

[29] T. Hotta and E. Dagotto, Orbital Ordering, New Phases, and Stripe Formation in Doped Layered Nickelates, Phys. Rev. Lett. **92**, 227201 (2004).

[30] O. F. Syljuasen and A. W. Sandvik, Quantum Monte Carlo with directed loops, Phys. Rev. E **66**, 046701 (2002).

[31] A. W. Sandvik and D. J. Scalapino, Order-Disorder Transition in a Two-Layer Quantum Antiferromagnet, Phys. Rev. Lett. **72**, 2777 (1994).

[32] See Supplemental Material at http://link.aps.org/supplemental/10.1103/PhysRevB.95.045131 for 1: Discussion on the statistical and systematic errors for the SSE and DQMC methods. 2: Validation of DQMC code in the limited cases. 3: Tables of all data in the paper. 4: A plot of energy and NN spin correlator vs g to go along with the Heisenberg model data for the magnetic order parameter in Fig. 3. 5: A plot of energy and double occupancy vs t'/t (and t/t') to go along with the Hubbard model data of Figs. 5 and 7 showing the magnetic structure factor and NN spin correlators.

[33] I. Affleck, M. P. Gelfand, and R. R. P. Singh, A plane of weakly coupled Heisenberg chains: Theoretical arguments and numerical calculations, J. Phys. Math. Gen. **27**, 7313 (1994).

[34] T. Sakai and M. Takahashi, The ground state of quasi-one-dimensional Heisenberg antiferromagnets, J. Phys. Soc. Jpn. **58**, 3131 (1989).

[35] A. W. Sandvik, Multichain Mean-Field Theory of Quasi-One-Dimensional Quantum Spin Systems, Phys. Rev. Lett. **83**, 3069 (1999).

[36] R. Blankenbecler, R. L. Sugar, and D. J. Scalapino, Monte Carlo calculations of coupled boson-fermion systems. I, Phys. Rev. D **24**, 2278 (1981).

[37] E. Y. Loh, J. E. Gubernatis, R. T. Scalettar, S. R. White, D. J. Scalapino, and R. L. Sugar, The sign problem in the numerical simulation of many electron systems, Phys. Rev. B **41**, 9301 (1990).

[38] T. Paiva, R. T. Scalettar, W. Zheng, R. R. P. Singh, and J. Oitmaa, Ground-state and finite-temperature signatures of quantum phase transitions in the half-filled Hubbard model on a honeycomb lattice, Phys. Rev. B **72**, 085123 (2005).

[39] Z. Meng, T. Lang, S. Wessel, F. Assaad, and A. Muramatsu, Quantum spin liquid emerging in two-dimensional correlated Dirac fermions, Nature (London) **464**, 847 (2010).

[40] M. Hohenadler, Z. Y. Meng, T. C. Lang, S. Wessel, A. Muramatsu, and F. F. Assaad, Quantum phase transitions in the Kane-Mele-Hubbard model, Phys. Rev. B **85**, 115132 (2012).

[41] D. Zheng, G.-M. Zhang, and C. Wu, Particle-hole symmetry and interaction effects in the Kane-Mele-Hubbard model, Phys. Rev. B **84**, 205121 (2011).

[42] S. Sorella, Y. Otsuka, and S. Yunoki, Absence of a spin liquid phase in the Hubbard model on the honeycomb lattice, Sci. Rep. **2**, 992 (2012).

[43] J. C. Bonner and M. E. Fisher, Linear magnetic chains with anisotropic coupling, Phys. Rev. **135**, A640 (1964).

[44] M. Ulmke, P. J. H. Denteneer, V. Janis, R. T. Scalettar, A. Singh, D. Vollhardt, and G. T. Zimanyi, Disorder and impurities in Hubbard antiferromagnets, Adv. Solid State Phys. **38**, 369 (1999).

[45] K. H. Hoglund and A. W. Sandvik, Impurity effects at finite temperature in the two-dimensional $S = 1/2$ Heisenberg antiferromagnet, Phys. Rev. B **70**, 024406 (2004).

[46] M. Sigrist and A. Furusaki, Low-temperature properties of the randomly depleted Heisenberg ladder, J. Phys. Soc. Jpn. **65**, 2385 (1996).

[47] S. Wessel, B. Normand, M. Sigrist, and S. Haas, Order by Disorder from Nonmagnetic Impurities in a Two-Dimensional Quantum Spin Liquid, Phys. Rev. Lett. **86**, 1086 (2001).

[48] J. Bobroff, N. Laflorencie, L. K. Alexander, A. V. Mahajan, B. Koteswararao, and P. Mendels, Impurity-Induced Magnetic Order in Low-Dimensional Spin-Gapped Materials, Phys. Rev. Lett. **103**, 047201 (2009).

[49] C. Sen, G. Alvarez, H. Aliaga, and E. Dagotto, Colossal magnetoresistance observed in Monte Carlo simulations of the one- and two-orbital models for manganites, Phys. Rev. B **73**, 224441 (2006).

[50] C. Sen, G. Alvarez, and E. Dagotto, First Order Colossal Magnetoresistance Transitions in the Two-Orbital Model for Manganites, Phys. Rev. Lett. **105**, 097203 (2010).

Appendix F

Size and shape of Mott regions for fermionic atoms in a two-dimensional optical lattice

Size and shape of Mott regions for fermionic atoms in a two-dimensional optical lattice

Tiago Mendes-Santos, Thereza Paiva, and Raimundo R. dos Santos

Instituto de Física, Universidade Federal do Rio de Janeiro, Caixa Postal 68528, 21941-972 Rio de Janeiro, RJ, Brazil

We investigate the harmonic-trap control of the size and shape of Mott regions in the Fermi-Hubbard model on a square optical lattice. The use of Lanczos diagonalization on clusters with twisted boundary conditions, followed by an average over 50–80 samples, drastically reduces finite-size effects in some ground-state properties; calculations in the grand-canonical ensemble together with a local-density approximation allow us to simulate the radial density distribution. We have found that as the trap closes, the atomic cloud goes from a metallic state to a Mott core and to a Mott ring; the coverage of Mott atoms reaches a maximum at the core-ring transition. A "phase diagram" in terms of an effective density and of the on-site repulsion is proposed as a guide to maximize the Mott coverage. We also predict that the usual experimentally accessible quantities, the global compressibility and the average double occupancy (rather, its density derivative), display detectable signatures of the core-ring transition. Some spin-correlation functions are also calculated and predict the existence Néel-like ordering within Mott cores and rings.

I. INTRODUCTION

Ultracold atoms in optical lattices have emerged as an invaluable tool in the study of strongly correlated fermions [1–3]. The range of applications has broadened, shedding light on the problems of coherence and entanglement [2]; also, imaging has become an important asset [4] in the study of dynamics of quantum phase transitions [5]. Ultracold atoms in optical lattices also may act as quantum simulators, in the sense that experiments can extract information on many-body models which have so far eluded many theoretical approaches [3]. For instance, the compressibility of ^{40}K atoms in an optical lattice has been measured as a function of both trap compression and on-site repulsion [6]: as the trap is deepened or the repulsion between atoms is increased, first a Mott "shell" develops within an overall metallic phase, followed by the emergence of a Mott core; the appearance of these Mott regions is in line with theoretical predictions for a trapped Hubbard model [7–10]. The controlled appearance of Mott regions represents an important step towards the experimental observation of antiferromagnetism in fermionic atomic clouds [11]; as such it could also help elucidate its role as a precursor to the superconducting state in cuprates [3], especially in relation to the the two-dimensional CuO_2 planes. In this respect, one must be able to characterize the size and form of the Mott region for the trap parameters at hand. Here we focus on aspects of the latter issue for the case of a square optical lattice; this choice of lattice is motivated both by the possibility of singling out some special features brought about by the van Hove singularity and by the use of an unbiased calculational method (see below). Our main result is that the use of experimentally accessible *global* quantities, such as compressibility and (derivative of) average double occupancy, can be used to map out *local* phases and phase separation; accordingly, we have established a "phase diagram" describing the boundaries between the Mott ring and core in terms of trap depth, fermion repulsion, and the number of particles.

II. MODEL AND METHODOLOGY

The fermionic atoms are described by a repulsive Hubbard model with a position-dependent chemical potential (due to a parabolic confining potential), namely,

$$\mathcal{H} = - \sum_{\langle \mathbf{i},\mathbf{j}\rangle,\sigma} t_{\mathbf{ij}}(c_{\mathbf{i}\sigma}^{\dagger} c_{\mathbf{j}\sigma}) + U \sum_{\mathbf{i}}(n_{\mathbf{i}\uparrow} - \tfrac{1}{2})(n_{\mathbf{i}\downarrow} - \tfrac{1}{2})$$
$$- \sum_{\mathbf{i}} \left(\mu_0 - V_t r_{\mathbf{i}}^2\right)(n_{\mathbf{i}\uparrow} + n_{\mathbf{i}\downarrow}), \tag{1}$$

where $\mathbf{i}$ runs over the N_s sites of the lattice, the spin state is $\sigma = \uparrow$ or $\downarrow$, and $n_{\mathbf{i}\sigma} = c_{\mathbf{i}\sigma}^{\dagger} c_{\mathbf{i}\sigma}$; $t_{\mathbf{ij}}$ is the hopping integral (or tunneling rate) between sites $\mathbf{i}$ and $\mathbf{j}$, U is the magnitude of the on-site repulsion, μ_0 is the (bare) chemical potential, V_t measures the trap curvature, and $r_{\mathbf{i}}$ measures the distance of site $\mathbf{i}$ to the center of the trap.

We first consider the homogeneous Hamiltonian (i.e., $V_t = 0$) on the clusters of Fig. 1(a). Whenever a fermion hops between two adjacent copies of the cluster [or, equivalently, reenters through an opposite edge of the same cluster, as in Fig. 1(b)], the hopping term picks up a phase, $t_{\mathbf{ij}} = te^{i\varphi_{\mathbf{ij}}}$; otherwise, $t_{\mathbf{ij}} = t$ (the bandwidth $W = 8t$ sets the energy scale). Periodic boundary conditions (PBC) correspond to $\varphi_{\mathbf{ij}} = 0, \forall \mathbf{i},\mathbf{j}$, and antiperiodic ones correspond to $\varphi_{\mathbf{ij}} = \pi, \forall \mathbf{i},\mathbf{j}$. Different sets of pairs $\boldsymbol{\varphi} \equiv (\varphi_x, \varphi_y)$ yield different allowed $\mathbf{k}$ points, and finite-size effects are minimized by considering an ensemble of *random* sets $\boldsymbol{\varphi}^{(\ell)}, \ell = 1,\ldots,M$; for each $\boldsymbol{\varphi}^{(\ell)}$, we calculate the quantities of interest (see below) and average over the M realizations [12–16]. In so doing, the number of allowed $\mathbf{k}$ points increases, mimicking the dense ($N_s \to \infty$) Brillouin zone (BZ). Clusters of up to ten sites are amenable to Lanczos diagonalizations, and Fig. 2(a) compares three different results for the fermion density as a function of the chemical potential. Lanczos diagonalization with PBC displays spurious *plateaus* ("closed-shell" effects [17]), which are wiped out with averaged boundary conditions (ABC). ABC also improve considerably the agreement with quantum Monte Carlo (QMC) results on much larger lattices, with the advantage of being free from the "minus-sign problem" at low temperatures [17,18], signaled in Fig. 2(a) by the large error bars for $\mu/t \lesssim 2$; the corruption of QMC worsens in the more interesting regime, $U > W$.
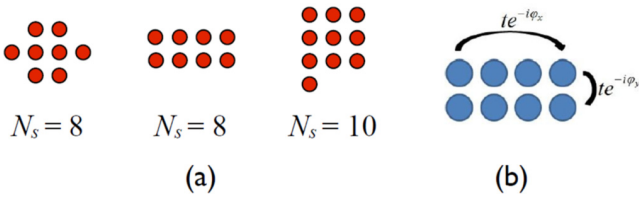
FIG. 1. (Color online) (a) Square-lattice clusters; (b) "twisted" boundary conditions introduced through phases φ_x and φ_y in the hopping term (see text).

III. RESULTS AND DISCUSSIONS

The harmonic trap is taken care of through the local-density approximation (LDA): we assume the fermion density at a distance r from the trap center is given by the uniform density at the value $\mu = \mu_0 - V_t r^2$, with μ_0 determined by fixing $N = 2\pi \int_0^\infty n(r) r \, dr = (\pi/V_t) \int_{-\infty}^{\mu_0} d\mu \, n(\mu)$, with $n(\mu)$ being the fermion density. LDA is known to provide a good description of density profiles but can fail for spectral properties [7,19,20]. Our results were obtained for $N \sim 10^3$ atoms and typically between 50 and 80 samples of BC, which also include the different clusters of Fig. 1. Although we limit our study to ground-state properties, the results are relevant to actual experiments: In the temperature scale $k_B T \lesssim t$, already accessible to experiments, the entropy is associated with the spin, not "charge," degrees of freedom; therefore, the density and compressibility (see below) do not vary appreciably with temperature in this regime [20].

Figure 2(b) shows typical radial distributions of atoms for different trap openings. For shallow traps the cloud spreads out, minimizing repulsion, thus favoring a single metallic phase with average site occupancy less than 1. As the trap narrows, phase separation sets in: the atoms confined around the trap center form an incompressible core with singly occupied sites over a radius of approximately 15 optical lattice sites; the atoms surrounding this Mott core are in a metallic state. Further trap narrowing leads to the formation of an insulating Mott ring, surrounded by metallic phases; with increasing V_t, the
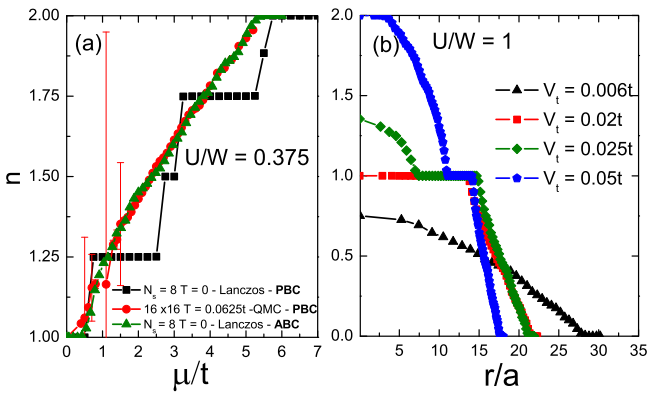

FIG. 2. (Color online) (a) Fermion density vs chemical potential using different methods: Lanczos diagonalization with PBC and ABC and QMC. The spurious plateaus with PBC are removed when ABC are used. (b) Radial distribution for $N = 10^3$ atoms for different trap depths V_t.
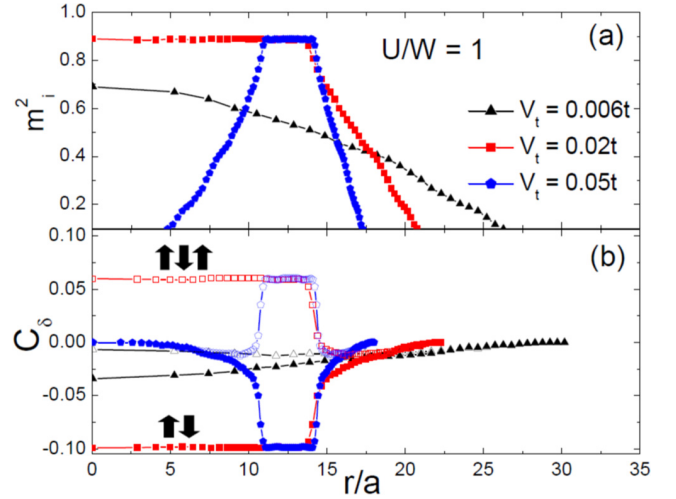

FIG. 3. (Color online) (a) Local-moment radial distribution. (b) First-neighbor (solid symbols) and second-neighbor (open symbols) spin-correlation functions, calculated at different positions; arrows illustrate the magnetic arrangements.

metallic core eventually becomes a "band-insulating" center (site occupancy of two fermions per site, within a radius of only a few lattice sites). We will see below that for fixed V_t, the evolution of Mott phases with increasing U is reversed: metallic to ring to core.

The magnetic properties of the cloud are influenced by the phase separation. For a homogeneous system, the local moment in the ground state, $m_{\mathbf{i}}^2 \equiv \langle [n_{\mathbf{i}\uparrow} - n_{\mathbf{i}\downarrow}]^2 \rangle$, is maximum at the Mott insulating density [21]. Figure 3(a) shows the radial local-moment distribution for the optical lattice: the nearly saturated plateaus (for $V_t/t = 0.02$ and 0.05) occur exactly at the half-filled sites, as depicted in Fig. 2(b); this provides further evidence that these rings and cores are, indeed, Mott regions. We have also examined the spin-spin correlation function, $C_\delta = \langle S_{\mathbf{i}}^z S_{\mathbf{i}+\delta}^z \rangle$, where $\delta = a\hat{\mathbf{x}}$ or $a\hat{\mathbf{y}}$ for nearest neighbors and $\delta = a\hat{\mathbf{x}} + a\hat{\mathbf{y}}$ for next-nearest neighbors; a is the lattice spacing. Figure 3(b) shows C_δ for the same trap openings discussed in Fig. 3(a). Within both Mott regions (ring and core), the local moments are strongly correlated, that is, both nearest- and next-nearest-neighbor correlations are saturated in a Néel-like arrangement; by contrast, the correlations are suppressed outside the Mott regions. For the wide trap, the correlations are much weaker, showing no saturation throughout the trap. Therefore, in order to probe a Néel state, experimenters have at their disposal not just Mott cores but Mott rings as well.

Figure 4(a) shows the number of atoms in the Mott state N_M as a function of the trap depth V_t/t for a fixed on-site repulsion U/W and for different total numbers of trapped atoms. Two thresholds are clearly identified: the one at smaller V_t/t signals the first appearance of a Mott region (the core), while the one at larger V_t/t marks the maximum number of Mott atoms; the latter also coincides with the changeover between core and ring geometries. As the number of atoms increases, the Mott regions appear at wider traps, but the two thresholds approach each other.
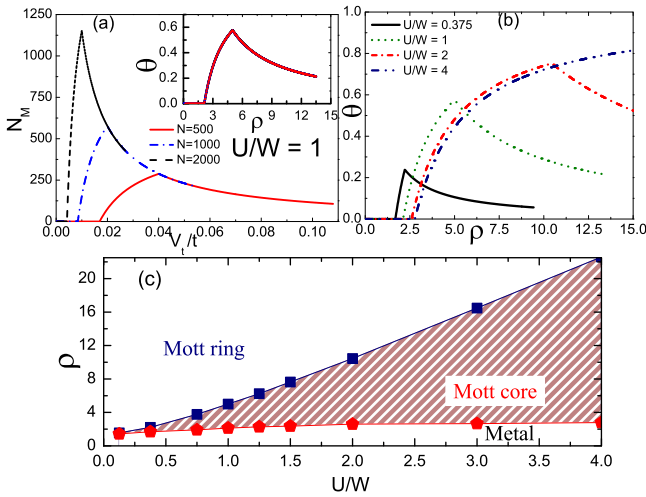
FIG. 4. (Color online) (a) Number of atoms in a Mott state N_M vs trap depth for different numbers of atoms in the cloud N. The inset shows the fraction of atoms in a Mott state, $\theta \equiv N_M/N$, in terms of the scaled density, which tracks V_t/t (see text). (b) Mott fraction θ as a function of the scaled density for several values of U. (c) Phase diagram: the bottom and top curves respectively show ρ_c and ρ_m (see text).

The trap brings about another length scale, $\zeta \equiv \sqrt{4t/V_t}$ [19,22], the effective trap size. We then plot the fraction of Mott atoms, $\theta \equiv N_M/N$, in terms of an effective atomic density, $\rho = N/\zeta^2$: the data collapse into a single curve [inset of Fig. 4(a)]. This perfect universal behavior (for a given U/W) can be shown to be an artifact of the LDA; nonetheless, the overall trend of Fig. 4(b), which shows the evolution of the Mott coverage with U/W, can certainly be used as a guide to optimize the area of the Mott regions in actual experiments. We note that the lowest threshold density ρ_c increases quite slowly with U/W. By contrast, ρ_m, the density at which the Mott atomic fraction peaks (above which the Mott region is a ring), displays a significant increase with U/W; likewise, Fig. 4(b) shows that the peak width also increases monotonically with U/W. In three-dimensional optical lattices, values of $U/W \lesssim 7$ have been tuned for ^{40}K [6,23], as well as values of $\lesssim 3$ for ^{6}Li [11,20]; Fig. 4(b) indicates that with values of $U/W \sim 4$ on two-dimensional optical lattices, one can expect to find at least 50% of the atoms in a Mott state for a wide range of effective densities.

These results are summarized in the phase diagram in Fig. 4(c): both ρ_c and ρ_m are shown as functions of the repulsion U/W, thus highlighting the regions in parameter space in which Mott rings and Mott cores are formed. The diagram shows that U (tuned by, e.g., a magnetic field probing the Feshbach resonance) controls the range of effective densities in which Mott cores are found: larger values of U/W allow more flexibility in the choice of trap openings and number of atoms in the cloud. It also sets limits (through ρ_m) beyond which one can select Mott rings instead: the larger the values of U/W are, the tighter the traps have to be in order to generate rings.

The experimental probes used in Ref. [6] to detect the presence of Mott phases in the trapped cloud are the global
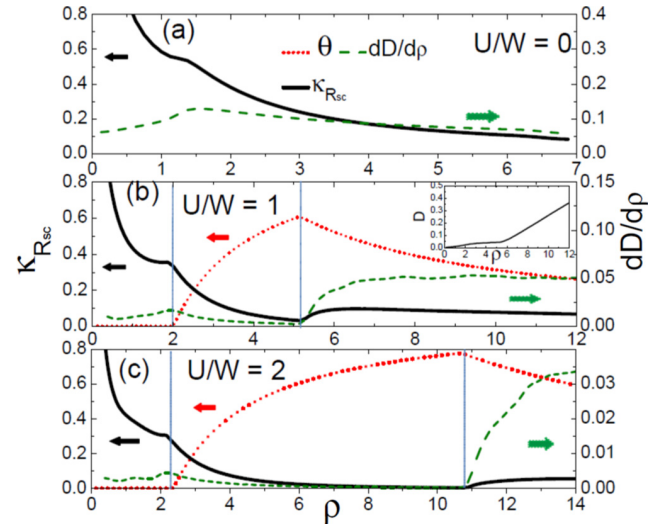

FIG. 5. (Color online) Global compressibility (solid black line; left axis), derivative of double occupancy (dashed green line; right axis), and Mott coverage (dotted red line; left axis) as functions of the effective density. Each panel is for a fixed value of U/W; data for the compressibility are scaled by $\sqrt{2N}$ for clarity. The inset in (b) is the double occupancy, whose derivative is plotted in the main panels. For $U/W \neq 0$, the light blue vertical lines guide the eyes to signatures of ρ_c and ρ_m.

compressibility, defined as

$$\kappa_{R_{sc}} \equiv -\frac{1}{R_{sc}^2}\frac{dR_{sc}}{d\rho}, \quad R_{sc} = \sqrt{\frac{\langle R^2 \rangle}{N_\sigma}}, \qquad (2)$$

where $\sqrt{\langle R^2 \rangle}$ is the mean-square average cloud size and $N_\sigma = N/2$ for an unpolarized gas, and the global double occupancy

$$D = \frac{1}{N}\int d^2r\, d_{\uparrow\downarrow}(r)\, n(r), \quad d_{\uparrow\downarrow} = \langle n_\uparrow n_\downarrow \rangle. \qquad (3)$$

As we now discuss, these quantities can be used to distinguish between the core and rings. For completeness, we mention that other definitions of compressibility, local and global, have been adapted to the context of trapped atoms [19,20,22,24,25], but they have not been used to map shapes and sizes of the Mott regions.

Figure 5 shows our results for these probes; data for $\theta(\rho)$ from Fig. 4(b) have also been included for comparison. For $U = 0$ [Fig. 5(a)], $\kappa_{R_{sc}}(\rho)$ shows a hump when the chemical potential crosses the van Hove singularity; for the square lattice this occurs when sites near the trap center are singly occupied ($n = 1$), while for the simple cubic lattice our calculations (not shown) indicate that this occurs at the edge of the singularity, corresponding to the occupation $n \sim 0.4$. For $U \neq 0$, the hump in $\kappa_{R_{sc}}(\rho)$ persists but is now followed by a drop; interestingly, a similar hump appears in one instance of the corresponding experimental data for the three-dimensional optical lattice [6], but as far as we know, a systematic analysis has not been carried out. A comparison with the plots of $\theta(\rho)$ correlates this drop with ρ_c: the second derivative of R_{sc} appears to be discontinuous at ρ_c. Further, this drop is interrupted at some larger effective density, which is now associated with ρ_m, beyond which $\kappa_{R_{sc}}(\rho)$ goes through a
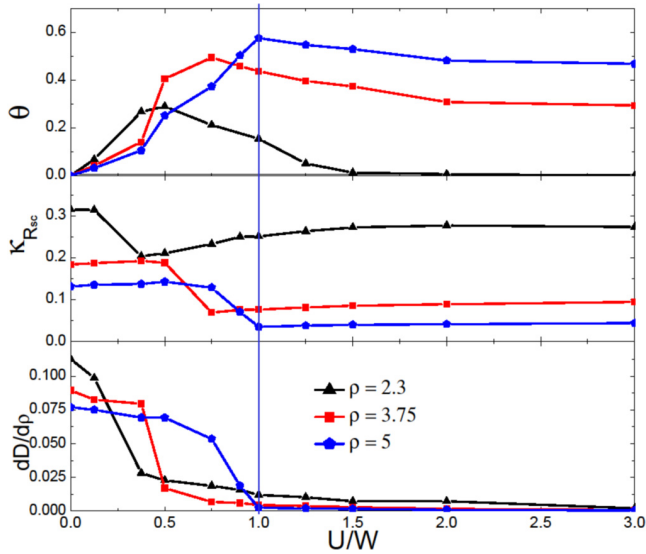
FIG. 6. (Color online) (top) Mott coverage, (middle) global compressibility, and (bottom) D' as a function of U/W for different ρ. The vertical line across the panels locates the critical value of U/W for the formation of a Mott core when $\rho = 5$ (see text).

ρ_c and ρ_m, as a result of a large fraction of atoms being in Mott states. Therefore, the use of D' allows one to resolve these critical effective densities.

It is also instructive to discuss the behavior with U/W for three fixed effective densities, as shown in Fig. 6. For $\rho = 5$, the ring-core "transition" occurs at $(U/W)_c = 1$, the value at which a vertical line is drawn: θ is peaked, and both $\kappa_{R_{sc}}$ and D' abruptly change their slopes. As ρ decreases, so does $(U/W)_c$, but for sufficiently small ρ (e.g., $\rho = 2.3$ in Fig. 6), the Mott core cannot withstand strong repulsion and becomes metallic. Again, the signature of the ring-core transition can also be sought in the U/W dependence of these global quantities.

IV. CONCLUSIONS

In summary, fermionic atoms trapped in a two-dimensional optical lattice display several interesting features when analyzed in terms of an effective density, $\rho \propto N V_t$ (N is the number of atoms in the cloud, and V_t is the trap opening). As the trap narrows, a Mott core forms at some ρ_c, which, upon further narrowing, becomes a Mott ring at ρ_m. The fraction of atoms in a Mott state $\theta(\rho)$ displays a maximum at ρ_m, so that the number of atoms in a Mott state does not grow with U/W beyond the ring-core transition. A phase diagram for the boundaries $\rho_m(U/W)$ and $\rho_c(U/W)$ was proposed, which should be useful in the experimental control of the geometry of the Mott state. These special densities can be experimentally identified through the global compressibility and the double occupancy D (actually, $\partial D/\partial \rho$). Finally, we note that the density of states leaves detectable traces on measurable quantities. This could pave the way for studies of trapped fermionic atoms in two dimensions addressing two long standing issues related to the Hubbard model: the Fermi-liquid nature (marginal or otherwise [26,27]) of the ground state and the evolution from a Mott insulator to superconductor, as in the cuprates.

local maximum. The latter rise was clearly visible in the experimental data for ultracold ^{40}K atoms [6] and was actually used to signal the appearance of a Mott region in three dimensions; unfortunately, cores or "shells" could not be systematically resolved by those data, which have also been somewhat smoothed by the low, but finite, temperatures.

The inset in Fig. 5(b) shows the average double occupancy $D(\rho)$ rising slowly from zero for wide traps and sharply beyond ρ_m: the decrease in the Mott coverage beyond this trap depth (for fixed N) allows double occupancy to set in between the trap center and the Mott ring [see Fig. 2(b)]. However, a distinctive signature of ρ_c cannot be unambiguously identified in the $D(\rho)$ plots. By contrast, the panels for $U/W \neq 0$ in Fig. 5 show that $D' \equiv \partial D/\partial \rho$ does display a local maximum at ρ_c and a sudden rise at ρ_m. These signatures are more distinctive for larger values of U/W, when D' goes to zero between

[1] B. DeMarco and D. S. Jin, Science **285**, 1703 (1999).

[2] I. Bloch, Nature (London) **453**, 1016 (2008).

[3] T. Esslinger, Annu. Rev. Condens. Matter Phys. **1**, 129 (2010).

[4] J. F. Sherson, C. Weitenberg, M. Endres, M. Cheneau, I. Bloch, and S. Kuhr, Nature (London) **467**, 68 (2010).

[5] J. Simon, W. S. Bakr, R. Ma, M. Eric Tai, P. M. Preiss, and M. Greiner, Nature (London) **472**, 307 (2011).

[6] U. Schneider, L. Hackermüller, S. Will, T. Best, I. Bloch, T. A. Costi, R. W. Helmes, D. Rasch, and A. Rosch, Science **322**, 1520 (2008).

[7] R. W. Helmes, T. A. Costi, and A. Rosch, Phys. Rev. Lett. **100**, 056403 (2008).

[8] S. Fuchs, E. Gull, L. Pollet, E. Burovski, E. Kozik, T. Pruschke, and M. Troyer, Phys. Rev. Lett. **106**, 030401 (2011).

[9] T. Paiva, Y. L. Loh, M. Randeria, R. T. Scalettar, and N. Trivedi, Phys. Rev. Lett. **107**, 086401 (2011).

[10] S. Chiesa, C. N. Varney, M. Rigol, and R. T. Scalettar, Phys. Rev. Lett. **106**, 035301 (2011).

[11] R. A. Hart, P. M. Duarte, T.-L. Yang, X. Liu, T. Paiva, E. Khatami, R. T. Scalettar, N. Trivedi, D. A. Huse, and R. G. Hulet, Nature (2015), doi:10.1038/nature14223.

[12] E. Y. Loh, Jr. and D. K. Campbell, Synth. Met. **27**, A499 (1988).

[13] J. Tinka Gammel, D. K. Campbell, and E. Y. Loh, Jr., Synth. Met. **57**, 4437 (1993).

[14] C. Gros, Phys. Rev. B **53**, 6865 (1996).

[15] C. Lin, F. H. Zong, and D. M. Ceperley, Phys. Rev. E **64**, 016702 (2001).

[16] S. Chiesa, P. B. Chakraborty, W. E. Pickett, and R. T. Scalettar, Phys. Rev. Lett. **101**, 086401 (2008).

[17] R. Mondaini, K. Bouadim, T. Paiva, and R. R. dos Santos, Phys. Rev. B **85**, 125127 (2012).

[18] R. R. dos Santos, Braz. J. Phys. **33**, 36 (2003).

[19] M. Rigol and A. Muramatsu, Phys. Rev. A **69**, 053612 (2004).

[20] P. M. Duarte, R. A. Hart, T.-L. Yang, X. Liu, T. Paiva, E. Khatami, R. T. Scalettar, N. Trivedi, and R. G. Hulet, Phys. Rev. Lett. **114**, 070403 (2015).

[21] T. Paiva and R. R. dos Santos, Phys. Rev. B **58**, 9607 (1998).

[22] M. Rigol, A. Muramatsu, G. G. Batrouni, and R. T. Scalettar, Phys. Rev. Lett. **91**, 130403 (2003).

[23] R. Jordens, N. Strohmaier, K. Gunter, H. Moritz, and T. Esslinger, Nature (London) **455**, 204 (2008).

[24] V. W. Scarola, L. Pollet, J. Oitmaa, and M. Troyer, Phys. Rev. Lett. **102**, 135302 (2009).

[25] S. Taie, R. Yamazaki, S. Sugawa, and Y. Takahashi, Nat. Phys. **8**, 825 (2012).

[26] Y. Kakehashi and P. Fulde, Phys. Rev. Lett. **94**, 156401 (2005).

[27] G. Benfatto, A. Giuliani, and V. Mastropietro, Ann. Henri Poincare **7**, 809 (2006).

Bibliography

[1] M. Azuma, Y. Fujishiro, M. Takano, M. Nohara, and H. Takagi, "Switching of the gapped singlet spin-liquid state to an antiferromagnetically ordered state in $sr(cu_{1-x}zn_x)_2o_3$," *Phys. Rev. B*, vol. 55, pp. R8658–R8661, Apr 1997. 1, 37, 38

[2] S. Seo, X. Lu, J.-X. Zhu, R. R. Urbano, N. Curro, E. D. Bauer, V. a. Sidorov, L. D. Pham, T. Park, Z. Fisk, and J. D. Thompson, "Disorder in quantum critical superconductors," *Nature Physics*, vol. 9, no. 12, pp. 1–6, 2013. 1, 37, 39

[3] T. Mendes-Santos, N. Costa, G. Batrouni, N. Curro, R. dos Santos, T. Paiva, and R. Scalettar, "Impurities near an antiferromagnetic-singlet quantum critical point," *Phys. Rev. B*, vol. 95, p. 054419, 2017. 2, 38

[4] H. Guo, T. Mendes-Santos, W. Pickett, and R. Scalettar, "Magnetic order-disorder transitions on a one-third-depleted square lattice," *Phys. Rev. B*, vol. 95, p. 045131, 2017. 2, 48, 49, 101

[5] J. E. Hirsch and S. Tang, "Antiferromagnetism in the two-dimensional hubbard model," *Phys. Rev. Lett.*, vol. 62, pp. 591–594, Jan 1989. 3, 84

[6] S. WHITE, D. SCALAPINO, R. SUGAR, E. LOH, J. GUBERNATIS, SCALET-TAR, and RT, "A numerical study of the two–dimensional hubbard model with repulsive coulomb interaction," *Physical Review B*, vol. 40, p. 506, 1989. 3, 84

[7] R. R. D. Santos, "Introduction to quantum Monte Carlo simulations for fermionic systems," *Brazilian Journal of Physics*, vol. 33, no. 1, pp. 36–54, 2003. 3, 17

[8] R. Jördens, K. J. Günter, H. Moritz, T. Esslinger, J. Meineke, J.-P. Brantut, D. Stadler, and T. Müller, "A Mott insulator of fermionic atoms in an optical lattice," *Nature*, vol. 455, no. September, p. 204, 2008. 4, 50, 51

[9] U. Schneider, L. Hackermüller, S. Will, T. Best, I. Bloch, T. Costi, R. Helmes, D. Rasch, and A. Rosch, "Metallic and insulating phases of repulsively interacting fermions in a 3d optical lattice," *Science*, vol. 322, no. 5907, pp. 1520–1525, 2008. 4, 50, 51

[10] A. Mazurenko, C. S. Chiu, G. Ji, M. F. Parsons, M. Kanász-nagy, R. Schmidt, F. Grusdt, E. Demler, D. Greif, and M. Greiner, "A cold-atom Fermi–Hubbard antiferromagnet," *Nature Publishing Group*, vol. 545, no. 7655, pp. 462–466, 2017. 4

[11] M. A. Baranov, M. Dalmonte, G. Pupillo, and P. Zoller, "Condensed matter theory of dipolar quantum gases," *Chemical Reviews*, vol. 112, no. 9, pp. 5012–5061, 2012. 4, 80

[12] S. Baier, M. J. Mark, D. Petter, K. Aikawa, L. Chomaz, Z. Cai, M. Baranov, P. Zoller, and F. Ferlaino, "Extended bose-hubbard models with ultracold magnetic atoms," *Science*, vol. 352, no. 6282, pp. 201–205, 2016. 4, 80, 82

[13] T. Paiva, Y. L. Loh, M. Randeria, R. T. Scalettar, and N. Trivedi, "Fermions in 3d optical lattices: Cooling protocol to obtain antiferromagnetism," *Physical review letters*, vol. 107, no. 8, p. 086401, 2011. 4

[14] S. Fuchs, E. Gull, L. Pollet, E. Burovski, E. Kozik, T. Pruschke, and M. Troyer, "Thermodynamics of the 3d hubbard model on approaching the néel transition," *Phys. Rev. Lett.*, vol. 106, p. 030401, Jan 2011. 4

[15] R. W. Helmes, T. A. Costi, and A. Rosch, "Mott transition of fermionic atoms in a three-dimensional optical trap," *Phys. Rev. Lett.*, vol. 100, p. 056403, Feb 2008. 4

[16] T. Mendes-Santos, T. Paiva, and R. R. Dos Santos, "Size and shape of mott regions for fermionic atoms in a two-dimensional optical lattice," *Phys. Rev. A*, vol. 91, no. 2, p. 023632, 2015. 4, 54

[17] H. Q. Lin and J. E. Gubernatis, "Exact diagonalization methord for quantum systems," 1993. 7, 8, 9

[18] E. Dagotto, "Correlated electrons in high-temperature superconductors," *Reviews of Modern Physics*, vol. 66, no. 3, p. 763, 1994. 7, 9, 10, 11, 55, 60

[19] E. R. Gagliano, E. Dagotto, A. Moreo, and F. C. Alcaraz, "Correlation functions of the antiferromagnetic Heisenberg model using a modified Lanczos method," *Phys. Rev. B*, vol. 34, no. 3, p. 1677, 1986. 7, 9, 10

[20] E. Dagotto, A. Moreo, F. Ortolani, J. Riera, and D. J. Scalapino, "Density of states of doped Hubbard clusters," *Physical Review Letters*, vol. 67, no. 14, p. 1918, 1991. 7, 55, 60, 70, 71

[21] E. Gagliano and C. Balseiro, "Dynamical Properties of Quantum Many-Body Systems at Zero Temperature," *Phys. Rev. Lett.*, vol. 59, no. 26, p. 2999, 1987. 7, 10

[22] A. W. Sandvik, "Computational studies of quantum spin systems," *AIP Conference Proceedings*, vol. 1297, no. 2010, pp. 135–338, 2010. 9, 24, 28

[23] E. Jeckelmann and H. Benthien, "Computational Many-Particle Physics," vol. 739, pp. 621–635, 2008. 11, 16, 18, 19, 20, 22, 62

[24] T. Paiva and R. R. Dos Santos, "Magnetism in one-dimensional Hubbard superlattices," *Phys. Rev. B*, vol. 62, no. 11, p. 7007, 2000. 12

[25] C. Gros, "The boundary condition integration technique : results for the Hubbard model in 1D and 2D," *Z. Phys. B - Condensed Matter*, vol. 86, p. 359, 1992. 12, 15, 16, 19, 97

[26] C. Gros, "Control of the finite-size corrections in exact diagonalization studies," *Phys. Rev. B*, vol. 53, no. 11, p. 6865, 1996. 12, 13, 16

[27] C. Lin, F. H. Zong, and D. M. Ceperley, "Twist-averaged boundary conditions in continuum quantum Monte Carlo algorithms.," *Phys. Rev. E*, vol. 64, p. 016702, 2001. 12, 13, 14, 20

[28] K. Zawadzki, I. D'Amico, and L. N. Oliveira, "Symmetries and boundary conditions with a twist," *Brazilian Journal of Physics*, vol. 47, no. 5, pp. 488–511, 2017. 12, 13

[29] N. Paris, A. Baldwin, and R. T. Scalettar, "Mott and band-insulator transitions in the binary-alloy Hubbard model: Exact diagonalization and determinant quantum Monte Carlo simulations," *Phys. Rev. B*, vol. 75, no. 16, p. 165113, 2007. 16

[30] S. Chiesa, P. B. Chakraborty, W. E. Pickett, and R. T. Scalettar, "Disorder-induced stabilization of the pseudogap in strongly correlated systems," *Physical Review Letters*, vol. 101, no. 8, p. 086401, 2008. 16

[31] H. J. Schulz, G. Cuniberti, and P. Pieri, "Fermi liquids and luttinger liquids," *arXiv:cond-mat/9807366*, 1998. 19, 22

[32] D. Senechal, D. Perez, and M. Pioro-Ladrire, "Spectral Weight of the Hubbard Model through Cluster Perturbation Theory," *Physical Review Letters*, vol. 84, no. 3, p. 522, 2000. 20, 22, 62

[33] M. Kohno, "Spectral properties near the Mott transition in the one-dimensional Hubbard model," *Physical Review Letters*, vol. 105, no. 10, p. 106402, 2010. 22, 62, 73, 74

[34] R. G. Pereira, K. Penc, S. R. White, P. D. Sacramento, and J. M. P. Carmelo, "Charge dynamics in half-filled Hubbard chains with finite on-site interaction," *Phys. Rev. B*, vol. 85, no. 16, p. 165132, 2012. 22, 62

[35] C. Kim, A. Y. Matsuura, Z.-X. Shen, N. Motoyama, H. Eisaki, S. Uchida, T. Tohyama, and S. Maekawa, "Observation of spin-charge separation in one-dimensional srcuo$_2$," *Phys. Rev. Lett.*, vol. 77, pp. 4054–4057, Nov 1996. 22, 57, 61, 62

[36] A. W. Sandvik and J. Kurkijärvi, "Quantum monte carlo simulation method for spin systems," *Phys. Rev. B*, vol. 43, pp. 5950–5961, Mar 1991. 24, 25, 26, 27, 32, 33

[37] A. W. Sandvik, "Stochastic series expansion method with operator-loop update," *Physical Review B*, vol. 59, no. 22, pp. R14157–R14160, 1999. 24, 27, 29, 31

[38] R. G. Melko, "Stochastic series expansion quantum Monte Carlo," *Strongly Correlated Systems: Numerical Methods*, pp. 185–206, 2013. 24, 25, 29

[39] A. Sandvik, "A generalization of handscomb's quantum monte carlo scheme-application to the 1d hubbard model," *Journal of Physics A: Mathematical and General*, vol. 25, no. 13, p. 3667, 1992. 25, 32, 35

[40] A. Dorneich and M. Troyer, "Accessing the dynamics of large many-particle systems using the stochastic series expansion.," *Physical review. E*, vol. 64, p. 066701, 2001. 25, 35, 36

[41] O. F. Syljuasen and A. W. Sandvik, "Quantum Monte Carlo with directed loops," *Physical Review E*, vol. 66, no. 4, p. 046701, 2002. 27, 29

[42] J. E. Gubernatis, M. Jarrell, R. N. Silver, and D. S. Sivia, "Quantum Monte Carlo simulations and maximum entropy: Dynamics from imaginary-time data," *Physical Review B*, vol. 44, no. 12, pp. 6011–6029, 1991. 36

[43] M. Randeria, N. Trivedi, A. Moreo, and R. T. Scalettar, "Pairing and spin gap in the normal state of short coherence length superconductors," *Physical Review Letters*, vol. 69, no. 13, pp. 2001–2004, 1992. 36, 45, 46

[44] N. Fujiwara, H. Yasuoka, Y. Fujishiro, M. Azuma, and M. Takano, "Nmr study of zn doping effect in spin ladder system srcu$_2O_3$," *Phys. Rev. Lett.*, vol. 80, pp. 604–607, Jan 1998. 37, 38

[45] M. Martin, M. Hase, K. Hirota, G. Shirane, Y. Sasago, N. Koide, and K. Uchinokura, "Spin-Peierls and antiferromagnetic phases in Cu1-xZnxGeO3: A neutron-scattering study," *Physical Review B*, vol. 56, no. 6, p. 3173, 1997. 37

[46] M. Julien, T. Feher, M. Horvatic, C. Berthier, on Bakharev, P. Segransan, G. Collin, and J. Marucco, "63Cu NMR evidence for enhanced antiferromagnetic correlations around Zn impurities in YBa2Cu3O6.7," *Physical review letters*, vol. 84, no. 15, p. 3422, 2000. 37

[47] J. Bobroff, N. Laflorencie, L. K. Alexander, A. V. Mahajan, B. Koteswararao, and P. Mendels, "Impurity-induced magnetic order in low-dimensional spin-gapped materials," *Physical Review Letters*, vol. 103, no. 4, p. 047201, 2009. 37

[48] M. Azuma, Z. Hiroi, M. Takano, K. Ishida, and Y. Kitaoka, "Observation of a spin gap in SrCu2O3 comprising spin- Quasi-1D two-leg ladders," *Physical Review Letters*, vol. 73, no. 25, pp. 3463–3466, 1994. 37

[49] A. W. Sandvik, E. Dagotto, and D. J. Scalapino, "Nonmagnetic impurities in spin-gapped and gapless Heisenberg antiferromagnets," *Physical Review B (Condensed Matter)*, vol. 56, no. 18, p. 71425, 1997. 37, 41

[50] N. Laflorencie, D. Poilblanc, and A. W. Sandvik, "Magnetic ordering in a doped frustrated spin-Peierls system," *Physical Review B*, vol. 69, no. 21, p. 212412, 2004. 37, 41

[51] S. Wessel, B. Normand, M. Sigrist, and S. Haas, "Order by disorder from nonmagnetic impurities in a two-dimensional quantum spin liquid," *Physical Review Letters*, vol. 86, no. 6, pp. 1086–1089, 2001. 37, 41

[52] J. Bobroff, H. Alloul, Y. Yoshinari, A. Keren, P. Mendels, N. Blanchard, G. Collin, and J.-F. Marucco, "Using ni substitution and ^{17}o nmr to probe the susceptibility $\chi^{'}(q)$ in cuprates," *Phys. Rev. Lett.*, vol. 79, pp. 2117–2120, Sep 1997. 38

[53] R. R. Urbano, B. L. Young, N. J. Curro, J. D. Thompson, L. D. Pham, and Z. Fisk, "Interacting antiferromagnetic droplets in quantum critical CeCoIn5," *Physical Review Letters*, vol. 99, no. 14, p. 146402, 2007. 37, 38

[54] H. Sakai, F. Ronning, J. X. Zhu, N. Wakeham, H. Yasuoka, Y. Tokunaga, S. Kambe, E. D. Bauer, and J. D. Thompson, "Microscopic investigation of electronic inhomogeneity induced by substitutions in a quantum critical metal CeCoIn5," *Physical Review B*, vol. 92, no. 12, p. 121105, 2015. 38

[55] A. W. Sandvik and D. J. Scalapino, "Order-disorder transition in a two-layer quantum antiferromagnet," *Physical Review Letters*, vol. 72, no. 17, pp. 2777–2780, 1994. 39, 40

[56] J. D. Reger and A. P. Young, "Monte Carlo simulations of the spin-(1/2 Heisenberg antiferromagnet on a square lattice," *Physical Review B*, vol. 37, no. 10, pp. 5978–5981, 1988. 39, 109

[57] L. Wang, K. S. Beach, and A. W. Sandvik, "High-precision finite-size scaling analysis of the quantum-critical point of S=1 2 Heisenberg antiferromagnetic bilayers," *Physical Review B*, vol. 73, no. 1, p. 014431, 2006. 40

[58] C. Yasuda, S. Todo, M. Matsumoto, and H. Takayama, "Site-dilution-induced antiferromagnetic long-range order in a two-dimensional spin-gapped Heisenberg antiferromagnet," *Physical Review B*, vol. 64, p. 092405, 2001. 41

[59] N. J. Curro, "Nuclear magnetic resonance in the heavy fermion superconductors," *Reports on Progress in Physics*, vol. 72, no. 2, p. 51, 2008. 42, 44

[60] P. Coleman, "Introduction to many-body physics," 2015. 44

[61] A. V. Chubukov and S. Sachdev, "Universal magnetic properties of $la_{2-\delta}sr_\delta cuo_4$ at intermediate temperatures," *Phys. Rev. Lett.*, vol. 71, pp. 169–172, Jul 1993. 45, 46

[62] J. Zhang, Y.-S. Chen, D. Phelan, H. Zheng, M. R. Norman, and J. F. Mitchell, "Stacked charge stripes in the quasi-2D trilayer nickelate La $_4$ Ni $_3$ O $_8$," *Proceedings of the National Academy of Sciences*, vol. 113, no. 32, pp. 8945–8950, 2016. 47

[63] A. S. Botana, V. Pardo, W. E. Pickett, and M. R. Norman, "Charge ordering in ni^{1+}/ni^{2+} nickelates: $la_4ni_3o_8$ and $la_3ni_2o_6$," *Phys. Rev. B*, vol. 94, p. 081105, Aug 2016. 47

[64] T. Paiva, R. T. Scalettar, W. Zheng, R. R. P. Singh, and J. Oitmaa, "Ground-state and finite-temperature signatures of quantum phase transitions in the half-filled hubbard model on a honeycomb lattice," *Phys. Rev. B*, vol. 72, p. 085123, Aug 2005. 48, 107

[65] S. Sorella, Y. Otsuka, and S. Yunoki, "Absence of a spin liquid phase in the Hubbard model on the honeycomb lattice.," *Scientific reports*, vol. 2, p. 992, 2012. 48, 107

[66] E. V. Castro and N. M. R. Peres, "Site dilution of quantum spins in the honeycomb and square lattices," *Physica B: Condensed Matter*, vol. 378-380, no. SPEC. ISS., pp. 137–138, 2006. 48, 117

[67] S. Inouye, M. R. Andrews, J. Stenger, H.-J. Miesner, D. M. Stamper-Kurn, and W. Ketterle, "Observation of Feshbach resonances in a Bose-Einstein condensate," *Nature*, vol. 392, no. 6672, pp. 151–154, 1998. 51

[68] T. Esslinger, "Fermi-Hubbard Physics with Atoms in an Optical Lattice," *Annual Reviews of Condensed Matter Physics*, vol. 1, pp. 129–152, 2010. 51

[69] D. Greif, M. F. Parsons, A. Mazurenko, C. S. Chiu, S. Blatt, F. Huber, G. Ji, and M. Greiner, "Site-resolved imaging of a fermionic Mott insulator," *Science*, vol. 351, no. 6276, pp. 953–957, 2016. 53, 54

[70] M. F. Parsons, A. Mazurenko, C. S. Chiu, G. Ji, D. Greif, and M. Greiner, "Site-resolved measurement of the spin-correlation function in the fermi-hubbard model," *Science*, vol. 353, no. 6305, pp. 1253–1256, 2016. 53

[71] R. A. Hart, P. M. Duarte, T.-L. Yang, X. Liu, T. Paiva, E. Khatami, R. T. Scalettar, N. Trivedi, D. A. Huse, and R. G. Hulet, "Observation of antiferromagnetic correlations in the Hubbard model with ultracold atoms," *Nature*, vol. 519, no. 7542, pp. 211–214, 2015. 54, 80, 81

[72] B. Mukherjee, Z. Yan, P. B. Patel, Z. Hadzibabic, T. Yefsah, J. Struck, and M. W. Zwierlein, "Homogeneous Atomic Fermi Gases," *Physical Review Letters*, vol. 118, no. 12, p. 123401, 2017. 54, 80

[73] H. Eskes, M. B. J. Meinders, and G. A. Sawatzky, "Anomalous transfer of spectral weight in doped strongly correlated systems," *Physical Review Letters*, vol. 67, no. 8, pp. 1035–1038, 1991. 55, 68, 70, 73, 78

[74] H. Eskes, A. M. Oleś, M. B. J. Meinders, and W. Stephan, "Spectral properties of the hubbard bands," *Phys. Rev. B*, vol. 50, pp. 17980–18002, Dec 1994. 55, 73

[75] M. Kohno, "Spectral properties near the Mott transition in the one-dimensional Hubbard model," *Physical Review Letters*, vol. 105, no. 10, p. 106402, 2010. 55, 57, 70, 71, 73, 78

[76] K. Penc and F. Mila, "Phase diagram of the one-dimensional extended hubbard model with attractive and/or repulsive interactions at quarter filling," *Phys. Rev. B*, vol. 49, pp. 9670–9678, Apr 1994. 56

[77] E. Jeckelmann, "Ground-State Phase Diagram of a Half-Filled One-Dimensional Extended Hubbard Model," *Physical Review Letters*, vol. 89, no. 23, p. 236401, 2002. 56, 59, 61, 64, 66, 67

[78] J. W. Cannon, R. T. Scalettar, and E. Fradkin, "Ground-state phase diagram of the one-dimensional extended hubbard model," *Phys. Rev. B*, vol. 44, pp. 5995–6001, Sep 1991. 56

[79] P. Sengupta, A. W. Sandvik, and D. K. Campbell, "Bond-order-wave phase and quantum phase transitions in the one-dimensional extended hubbard model," *Phys. Rev. B*, vol. 65, no. 15, p. 155113, 2002. 56, 57, 59

[80] K. Sano and Y. Ōno, "Critical behavior near the metal-insulator transition in the one-dimensional extended hubbard model at quarter filling," *Phys. Rev. B*, vol. 70, p. 155102, Oct 2004. 56, 59, 68, 75

[81] S. Ejima and S. Nishimoto, "Phase diagram of the one-dimensional half-filled extended hubbard model," *Physical Review Letters*, vol. 99, no. 21, p. 216403, 2007. 56, 59, 66

[82] A. Koitzsch, S. V. Borisenko, J. Geck, V. B. Zabolotnyy, M. Knupfer, J. Fink, P. Ribeiro, B. Büchner, and R. Follath, "Current spinon-holon description of the one-dimensional charge-transfer insulator SrCu O2: Angle-resolved photoemission measurements," *Phys. Rev. B*, vol. 73, no. 20, p. 201101, 2006. 57, 61

[83] H. Benthien and E. Jeckelmann, "Spin and charge dynamics of the one-dimensional extended Hubbard model," *Phys. Rev. B*, vol. 75, no. 20, p. 205128, 2007. 57, 60

[84] M. Aichhorn, H. G. Evertz, W. Von Der Linden, and M. Potthoff, "Charge ordering in extended Hubbard models: Variational cluster approach," *Phys. Rev. B*, vol. 70, no. 23, p. 235107, 2004. 57, 59, 60, 62, 63, 77, 84

[85] Y. Ohta, K. Tsutsui, W. Koshibae, and S. Maekawa, "Exact-diagonalization study of the Hubbard model with nearest-neighbor repulsion," *Phys. Rev. B*, vol. 50, no. 18, p. 13594, 1994. 57, 65, 68, 70, 84

[86] A. Damascelli, Z. Hussain, and Z.-X. Shen, "Angle-resolved photoemission studies of the cuprate superconductors," *Rev. Mod. Phys.*, vol. 75, pp. 473–541, Apr 2003. 60

[87] M. B. J. Meinders, H. Eskes, and G. A. Sawatzky, "Spectral-weight transfer: Breakdown of low-energy-scale sum rules in correlated systems," *Phys. Rev. B*, vol. 48, no. 6, p. 3916, 1993. 68, 72

[88] B. Yan, S. a. Moses, B. Gadway, J. P. Covey, K. R. A. Hazzard, A. M. Rey, D. S. Jin, and J. Ye, "Observation of dipolar spin-exchange interactions with lattice-confined polar molecules.," *Nature*, vol. 501, no. 7468, pp. 521–5, 2013. 80

[89] M. Lu, N. Q. Burdick, and B. L. Lev, "Quantum degenerate dipolar fermi gas," *Phys. Rev. Lett.*, vol. 108, p. 215301, May 2012. 80

[90] K. Aikawa, S. Baier, A. Frisch, M. Mark, C. Ravensbergen, and F. Ferlaino, "Observation of fermi surface deformation in a dipolar quantum gas," *Science*, vol. 345, no. 6203, pp. 1484–1487, 2014. 80

[91] Y. Zhang and J. Callaway, "Extended hubbard model in two dimensions," *Phys. Rev. B*, vol. 39, pp. 9397–9404, May 1989. 80, 84

[92] H. Terletska, T. Chen, and E. Gull, "Charge ordering and correlation effects in the extended hubbard model," *Phys. Rev. B*, vol. 95, p. 115149, Mar 2017. 80, 84

[93] S. G. Bhongale, L. Mathey, S. W. Tsai, C. W. Clark, and E. Zhao, "Bond order solid of two-dimensional dipolar fermions," *Physical Review Letters*, vol. 108, no. 14, p. 145301, 2012. 80, 82

[94] E. G. Van Loon, M. I. Katsnelson, L. Chomaz, and M. Lemeshko, "Interaction-driven Lifshitz transition with dipolar fermions in optical lattices," *Physical Review B*, vol. 93, no. 19, p. 195145, 2016. 80

[95] T.-S. Zeng and L. Yin, "Supersolidity of a dipolar fermi gas in a cubic optical lattice," *Phys. Rev. B*, vol. 89, p. 174511, May 2014. 80

[96] A. L. Gadsbolle and G. M. Bruun, "Dipolar fermions in a two-dimensional lattice at nonzero temperature," *Physical Review A*, vol. 86, no. 3, p. 033623, 2012. 80

[97] S. G. Bhongale, L. Mathey, S.-W. Tsai, C. W. Clark, and E. Zhao, "Unconventional spin-density waves in dipolar fermi gases," *Phys. Rev. A*, vol. 87, p. 043604, Apr 2013. 80, 81, 82

[98] L. He and W. Hofstetter, "Supersolid phase of cold fermionic polar molecules in two-dimensional optical lattices," *Phys. Rev. A*, vol. 83, p. 053629, May 2011. 80

[99] E. G. C. P. van Loon, M. I. Katsnelson, and M. Lemeshko, "Ultralong-range order in the fermi-hubbard model with long-range interactions," *Phys. Rev. B*, vol. 92, p. 081106, Aug 2015. 81, 82

[100] F. Gerbier, S. Trotzky, S. Fölling, U. Schnorrberger, J. D. Thompson, A. Widera, I. Bloch, L. Pollet, M. Troyer, B. Capogrosso-Sansone, N. V. Prokof'ev, and B. V. Svistunov, "Expansion of a quantum gas released from an optical lattice," *Phys. Rev. Lett.*, vol. 101, p. 155303, Oct 2008. 81, 84

[101] S. Nishimoto, E. Jeckelmann, F. Gebhard, and R. M. Noack, "Application of the density matrix renormalization group in momentum space," *Phys. Rev. B*, vol. 65, p. 165114, Apr 2002. 97

[102] J. Hubbard, "Electron correlations in narrow energy bands," *Proceedings of the Royal Society of London Series A*, vol. 276, pp. 238–257, 1963. 103

[103] J. E. Hirsch, "Two-dimensional hubbard model: Numerical simulation study," *Phys. Rev. B*, vol. 31, pp. 4403–4419, Apr 1985. 106, 107

[104] S. Doniach and E. H. Sondheimer, "Green's functions for solid state physicists," 1974. 106, 107

[105] S. Sorella and E. Tosatti, "Semi-metal-insulator transition of the hubbard model in the honeycomb lattice," *EPL (Europhysics Letters)*, vol. 19, no. 8, p. 699, 1992. 107

[106] J. D. Reger, J. A. Riera, and A. P. Young, "Monte carlo simulations of the spin- 1 / 2 heisenberg antiferromagnet in two dimensions," *Journal of Physics: Condensed Matter*, vol. 1, no. 10, p. 1855, 1989. 109

[107] A. Auerbach, "Interecting electrons and quantum magnetism," 1994. 113, 114

[108] I. Affeck, M. P. Gelfand, and R. R. P. Singh, "A plane of weakly coupled heisenberg chains: theoretical arguments and numerical calculations," *Journal of Physics A: Mathematical and General*, vol. 27, no. 22, p. 7313, 1994. 116

[109] A. Sandvik, "Multichain Mean-Field Theory of Quasi-One-Dimensional Quantum Spin Systems," *Physical Review Letters*, vol. 83, no. 15, pp. 3069–3072, 1999. 116